



UNIVERSIDAD DE INVESTIGACIÓN DE TECNOLOGÍA EXPERIMENTAL YACHAY

Escuela de Ciencias Físicas y Nanotecnología

**TÍTULO: Extreme Ultraviolet wave mixing processes:
Insights from nonlinear optics**

Trabajo de integración curricular presentado como requisito para la
obtención
del título de Físico

Autor:

Villacrés Merchán Francis Germánico

Tutor:

PhD. Rojas Clara

Co-Tutores:

PhD. Krebs Dietrich

PhD. Boemer Christina

Urcuquí, Julio 2024

AUTORÍA

Yo, **Villacrés Merchán Francis Germánico**, con cédula de identidad 0926039793, declaro que las ideas, juicios, valoraciones, interpretaciones, consultas bibliográficas, definiciones y conceptualizaciones expuestas en el presente trabajo; así como, los procedimientos y herramientas utilizadas en la investigación, son de absoluta responsabilidad de el/la autora (a) del trabajo de integración curricular. Así mismo, me acojo a los reglamentos internos de la Universidad de Investigación de Tecnología Experimental Yachay.

Urcuquí, Julio 2024.

Francis Germánico Villacrés Merchán
CI: 0926039793

AUTORIZACIÓN DE PUBLICACIÓN

Yo, **Villacrés Merchán Francis Germánico**, con cédula de identidad 0926039793, cedo a la Universidad de Investigación de Tecnología Experimental Yachay, los derechos de publicación de la presente obra, sin que deba haber un reconocimiento económico por este concepto. Declaro además que el texto del presente trabajo de titulación no podrá ser cedido a ninguna empresa editorial para su publicación u otros fines, sin contar previamente con la autorización escrita de la Universidad.

Asimismo, autorizo a la Universidad que realice la digitalización y publicación de este trabajo de integración curricular en el repositorio virtual, de conformidad a lo dispuesto en el Art. 144 de la Ley Orgánica de Educación Superior

Urcuquí, Julio 2024.

Francis Germánico Villacrés Merchán
CI: 0926039793

Dedication

To the memory of my mother, Elsa Merchán Reyes

Francis G. Villacrés Merchán

Acknowledgements

I would like to express my sincere gratitude to Dr. Dietrich Krebs and Dr. Christina Boemer for their invaluable guidance, support, and mentorship throughout this thesis project. Their assistance with benchmarking the models was particularly helpful, especially the data obtained from the standard light-conversion experiment conducted at DESY (Deutsches Elektronen-Synchrotron; German Electron Synchrotron, in English). I am especially grateful to Dr. Krebs for his insightful guidance on the theoretical framework for describing pulsed wave propagation through uniaxial crystals.

I am also deeply grateful to Dr. Juan Lobos for providing the initial opportunity to conduct this research at Yachay Tech University during my time under his advisement. I am especially thankful to Dr. Clara Rojas for her support during the transition between advisors.

Linear optical material properties (using GPAW code) were computed using the Imbabura cluster at Yachay Tech University, which was purchased under contract No. 2017-024 (SIE-UI TEY-007-2017). Nonlinear optical material properties (using `Exciting` code) were computed on a personal MSI Sword A11UD-001US laptop.

Throughout this journey, I have been incredibly fortunate to have amazing friends by my side. Eder, Jorge, Antonio, Melanie, Angie, Samantha, Juan Diego, “Punto de Encuentro”, and “PAT-28” – their presence has made this stage of my life truly special. Not only have I found incredible friendships in Ecuador, but also abroad with Sarah, Diana, Maria Clara, Maria Eduarda, and Manasa. Despite being afar, their willingness to connect, even for brief calls and texting, meant the world to me.

Last but certainly not least, I deeply thank my family. Without the support of my father, grandmother, my siblings, Christine and William, and Curtiss, I do not think this project would have been completed.

Gracias totales!

Resumen

La interacción de la luz con átomos, moléculas y materiales ha dado lugar a importantes avances tanto en la teoría como en las ciencias aplicadas, incluidos campos como la nanotecnología y la ciencia de los materiales. Sin embargo, a pesar de los avances en esas áreas, nuestra comprensión de los procesos no lineales en rangos de energía como la radiación ultravioleta extrema (XUV en inglés) sigue siendo limitada.

Este trabajo se enfoca en investigar un proceso no lineal en particular: la generación de segundos armónicos, en el régimen ultravioleta extremo, utilizando el marco teórico de la óptica no lineal. La exploración comienza con conceptos establecidos sobre la propagación de ondas dentro de cristales uniaxiales, prestando especial atención al cristal niobato de litio (LiNbO_3). Posteriormente, el marco teórico desarrollado se valida experimentalmente en el régimen visible.

Tras este proceso de validación, se realizan modificaciones al modelo para incluir la absorción, un proceso físico que ocurre al trabajar con altas energías como en el XUV. Con la absorción integrada en el modelo, en esta tesis se examinan dos geometrías: la geometría de transmisión y la geometría de reflexión. Para evaluar el comportamiento del modelo en la geometría de transmisión, se realizan simulaciones de la Teoría del Funcional de Densidad para obtener los parámetros relevantes como el índice de refracción y los coeficientes no lineales. La geometría de transmisión indica que las películas delgadas de LiNbO_3 de $0.1 \mu\text{m}$ a $0.2 \mu\text{m}$ pueden generar una potencia de segundo armónico medible.

Palabras clave: Óptica no lineal, Electromagnetismo, Niobato de litio, Geometría de transmisión, Geometría de reflexión, Teoría del funcional de la densidad, Absorción.

Abstract

The interaction of light with atoms, molecules, and materials has led to significant advancements in both theory and applied science, including fields such as nanotechnology and materials science. However, despite extensive research on optical interactions, our understanding of the specific mechanisms by which light influences matter at higher energies, such as x-ray or extreme ultraviolet (XUV) processes, remains limited.

This work investigates the nonlinear process of second harmonic generation in the extreme ultraviolet (XUV) regime using the theoretical framework of nonlinear optics. The exploration begins with established concepts of wave propagation within uniaxial crystals, with particular attention given to the crystal lithium niobate (LiNbO_3). Subsequently, the developed theoretical framework is experimentally validated in the visible regime.

Following this benchmarking, modifications are made to the model to account for second harmonic generation in the XUV, which involves incorporating absorption into the theoretical framework. With absorption integrated into the model, two geometry models are developed in this thesis: transmission geometry and reflection geometry. To evaluate the behavior of the model in transmission geometry, Density Functional Theory simulations are conducted to obtain the relevant parameters, such as index of refraction and nonlinear coefficients. The transmission geometry yields that nanostructured LiNbO_3 thin films from $0.1 \mu\text{m}$ to $0.2 \mu\text{m}$ can generate measurable time-averaged second-harmonic power.

Keywords: Nonlinear optics, Electromagnetism, Lithium niobate, Transmission geometry, Reflection geometry, Density Functional Theory, Absorption.

Contents

List of Figures	x
List of Tables	xii
1 Introduction	1
1.1 Problem Statement	4
1.2 General and Specific Objectives	4
2 Preliminaries: Theoretical and Experimental Aspects	7
2.1 Basic Framework	7
2.1.1 The Wave Propagation Equation: Beam propagation in Uniaxial Crystals	11
2.2 Perturbative approach to Nonlinear Processes	15
2.2.1 The Second-order Susceptibility Tensor: $\underline{\underline{\chi}}^{(2)}(-\omega_\sigma; \omega_1, \omega_2)$	17
2.3 Modelling material properties (in brief)	20
2.3.1 Representation of the Kohn-Sham wavefunctions	25
2.3.2 Optical properties	31
3 SHG in crystals: Variations in Space and Time	37
3.1 Wave Equations with Nonlinear source	37
3.1.1 Spatial effects in wave propagation	38
3.1.2 Temporal effects in wave propagation	41
3.1.3 Considerations in Identifying Ordinary and Extraordinary Waves with Nonlinear source	46
3.1.4 Cubic systems	47
3.2 Physical insights into diffraction, walk-off, & pump depletion	47
3.3 Study case: LiNbO ₃	49
4 Wave Propagation in the XUV regime	63
4.1 Absorption in Wave Equation	63
4.2 Diffraction and Dispersion along with Absorption	66

4.3	Normal Incidence & Absorption	69
4.4	On ordinary and extraordinary waves	74
4.5	Study Case: LiNbO ₃ in XUV	75
4.6	Reflection Geometry: Semi-infinite Approximation	86
4.7	Limitations of the models and comparison with previous works	101
5	Conclusions & Outlook	105
A	The Wave Equation for Nonlinear Anisotropic Media	107
A.1	Wave propagation: insights into space	107
A.1.1	The wave equation in different coordinate systems	110
A.1.2	Ordinary and Extraordinary waves	111
A.2	Wave propagation: insights into space and time	114
A.3	More about Second-order Susceptibility tensor and Polarization	123
A.4	Visible Regime: Intermediate Calculations for Wave Propagation and Intensity	125
A.5	Study Case: calculations	128
B	Absorption & Wave Propagation	133
B.1	Absorption Criterion	133
B.2	Solutions of equations (4.22)	135
B.3	Reflection Geometry	140
C	Time-averaged Poynting vector	145
D	Two approaches towards problems in linear and nonlinear optics	149
E	Computational Details: DFT	151
	Bibliography	157
	Abbreviations & Symbols	165

List of Figures

1.1	Electromagnetic spectrum	2
1.2	Schematic representation of energy bands within solids and electronic transitions	3
2.1	Normal incidence geometry	8
2.2	Transmission, Reflection, and Scattering geometries	10
2.3	Coordinate systems for studying crystals	12
3.1	Different coordinate systems for a uniform uniaxial crystal.	40
3.2	Schematic representation of diffraction within crystals.	48
3.3	Light-conversion experiment setup for Second Harmonic Generation.	50
3.4	Second-order susceptibility tensor transformation operation	52
3.5	Cartesian components of the SHG field in the XZ plane	53
3.6	Spatially constrained plane waves	54
3.7	Index of refraction and its derivative of LiNbO_3 in the range from 1.1 eV to 3.1 eV	55
3.8	Schematic representation of the periodic Gaussian profile	57
3.9	Second-harmonic generation at normal incidence	59
4.1	Schematic representation for the different scenarios where the role of absorption and diffraction is estimated	67
4.2	SHG geometry for XUV radiation at normal incidence	70
4.3	LiNbO_3 bulk model	76
4.4	GPAW and <code>Exciting</code> calculated electronic band structures	77
4.5	Calculated dielectric function on the basis of random phase approximation	80
4.6	Linear optical parameters: index of refraction and absorption coefficient	81
4.7	LiNbO_3 non-zero second-order susceptibility components	82
4.8	Approximation criterion for the dispersion of the ordinary and extraordinary absorption coefficients	83
4.9	Time-averaged second-harmonic power (normal incidence, and absorption) in function of the size of the nonlinear medium	85
4.10	Second-harmonic generation under reflection geometry	87

4.11	Reflection geometry: vector visualization of fundamental and second-harmonic fields	92
4.12	Transmission and Reflection geometry	102
A.1	Principal coordinate system, and propagation coordinate system	109
E.1	Simple convergence tests for energy cut-off and the size of the k -mesh	153
E.2	Simple convergence tests for energy cut-off and the size of the k -mesh	154
E.3	Fit of the Birch-Murnaghan equation of state for bulk LiNbO ₃	155
E.4	LiNbO ₃ non-zero second-order susceptibility components from 30 eV to 70 eV	155

List of Tables

2.1	Relationship between the indices of the χ_{ijk} and d_{im} element	18
2.2	d -matrix for uniaxial crystals	19
3.1	Refractive indices of lithium niobate (LiNbO_3) at the visible range, for both the fundamental frequency (ω_0) and second harmonic frequency ($2\omega_0$).	51
3.2	Second-harmonic power (normal incidence) parameters	60
4.1	Parameters that characterize two different XUV light sources	83
4.2	Parameters involved in the production of SHG pulses under absorption.	84

Chapter 1

Introduction

Everyday encounters with light often involve its refraction, reflection, or absorption by various materials. In these situations, light preserves its frequency. The principles governing these phenomena find expression in the familiar laws of optics, such as Snell's law, Fresnel's equations, and Lambert-Beer's law, etc¹. These are the optical properties of matter familiar to everyone through the visual sense.

Nonetheless, as the illumination becomes sufficiently intense, certain characteristics, such as index of refraction or frequency, usually experienced as fixed, can change. Under these circumstances, light waves not only interact with the medium but also with each other, leading to the emergence of nonlinear optical effects. Experimentally, the Kerr effect*, named after John Kerr, who discovered it in 1877², was the first nonlinear optical process observed.

Following this discovery in 1883, Friedrich C. A. Pockels³ observed a modification in the refractive index that varied linearly with the electric field. (nowadays known as the linear electro-optic effect). However, it was only with the observation of Second-Harmonic Generation (SHG) by Peter Franken and colleagues that the field of nonlinear optics truly began to take shape.

Moreover, there are two reasons why one might consider second-harmonic generation (SHG) important: first, harmonic generation is achieved through either a coherent source of light, such as lasers, or ordinary light, which is less coherent⁴; second, historically, it was the first nonlinear phenomenon where a coherent output was obtained from a coherent input⁵. From the discovery of SHG, the field of nonlinear optics grew rapidly.

Today nonlinear optics is used from physics, over biology⁶ to chemistry⁷ but also in neuroscience⁸, and in surgery⁹. This research, with a focus on wave propagation in uniaxial crystals (Chapters 3 and Chapter 4), aims to contribute to the development of a future materials synthesis industry in Ecuador. Specifically, we hope that Ecuador produces crystals optimized for second-harmonic generation (SHG). The simple models developed here will provide an initial understanding of how uniaxial crystals behave under intense light from a nonlinear optics perspective.

Regarding the electromagnetic spectrum (see Fig. 1.1), the majority of second-harmonic generation experiments are conducted in the infrared, visible, and (deep) ultraviolet (UV) wavelengths¹⁰. Nowadays, there are spectroscopic

*The Kerr effect involves a change in the refractive index of a material, proportionally to the square of the applied electric field.

techniques based on second-order nonlinear processes[†] with optical and infrared radiation, to probe electronic properties of interfaces and surfaces of solid-state materials¹². In 2004, Taro Sekikawa and collaborators pointed out the lack of knowledge and explorations of the nonlinear responses in the extreme ultraviolet (XUV) and soft X-rays (SXR) regions. They reported the generation of low ninth harmonic order XUV pulses (27.9 eV) using a blue laser pulse¹³.

With the advent of X-ray free electron lasers (XFELs), the constraint highlighted by Sekikawa et al. was lifted. XFELs can deliver high-energy radiation with high brightness, ultrashort pulse duration, and high coherence. For example, the Free Electron Laser Radiation for Multidisciplinary Investigations (FERMI) at Elettra Sincrotrone Trieste, along with the Spring-8 Angstrom Compact Free Electron Laser (SACLA), operate in the ultraviolet and soft X-ray range. Concerning XUV, SACLA works with energy ranges of 25 eV to 150 eV¹⁴. However, there is a need for further contributions to theoretical explorations of nonlinear processes in the XUV.

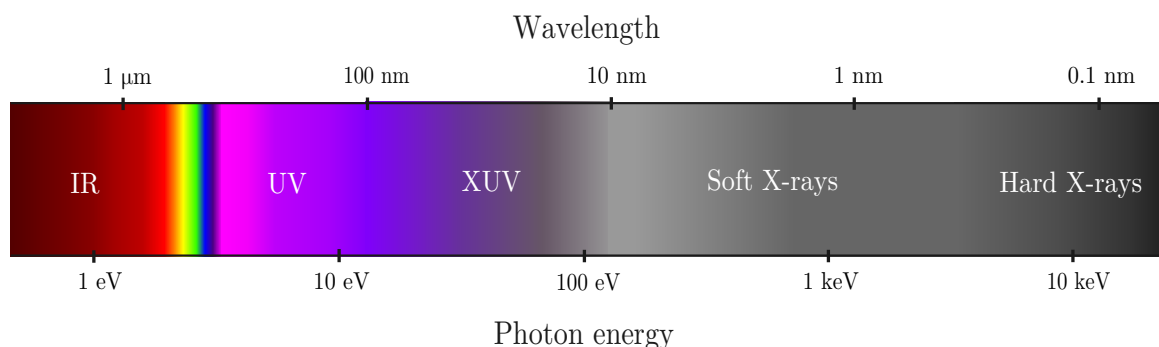


Figure 1.1: The electromagnetic spectrum extended from the infrared (IR) to the x-ray regions. Visible light is composed of wavelengths such as red (650 nm), yellow (570 nm), green (530 nm), and blue (470 nm). At shorter wavelengths, there is ultraviolet (UV) radiation, extreme ultraviolet (XUV) radiation, soft X-rays (SXR), and hard X-rays. The extreme ultraviolet is taken here as extending from photon energies of about 10 eV to about 120 eV.

In 2021, Emma Berger and collaborators¹⁵ conducted several experiments on lithium osmate (LiOsO_3) surfaces at SACLA, demonstrating that SHG-based spectroscopy at the XUV energy range can serve as a time-resolved probe of symmetry-breaking structural phase transitions on femtosecond timescales.

Additionally, Berger et al. provided a quantum-mechanical description of the process triggered by the interaction of matter with XUV pulses on the basis of Density Functional Theory (DFT). There is an emerging interest in the community in exploring the SHG nonlinear process within the XUV in crystals. For example, in addition to Berger's study, Can B. Uzundal studied lithium niobate (LiNbO_3) in the XUV regime through SHG-based spectroscopy. Exploring this nonlinear process is the main focus of this thesis.

The second harmonic generation process is a second-order nonlinear phenomenon where two incident photons with identical energy combine to produce a single photon with double the energy, expressed as $\omega + \omega = 2\omega$. As

[†]Sum-Frequency Generation, Difference-Frequency Generation, and Second-Harmonic Generation are second-order nonlinear processes¹¹.

fundamental light with frequency ω traverses a nonlinear medium, a portion of photons at frequency ω undergoes conversion to higher energy photons at 2ω .

On a microscopic level (see Fig. 1.2), as a nonlinear material absorbs photons at ω frequency, electron-hole pairs are generated. The excited electrons undergo two excitations by the fundamental light before recombining with the hole. These excited electrons can undergo two distinct excitation pathways by the incident light before recombining with the hole. These pathways are categorized as half-resonant and resonant schemes. In the former, the frequency of incident light, ω , is halfway between the ground and an excited state. In this case, the transition is facilitated by a virtual state (see Fig. 1.2 (a)-(b)). In the latter, the frequency of incident light, ω , directly excites the electron from the ground state to the excited state (see Fig. 1.2 (c)).

In Chapter 2, Section 2.3, we will provide an expression that describes the transitions occurring in the second-harmonic generation process (see equation (2.106)). According to this equation, we will find that the second-harmonic generation process takes place through either resonant or half-resonant schemes. However, equation (2.106) indicates that transitions where both the first and second excited states are simultaneously actual energy levels (i.e., eigenvalues of the Hamiltonian) do not occur. Upon recombination of electron-hole pairs, photons at frequency 2ω are emitted.

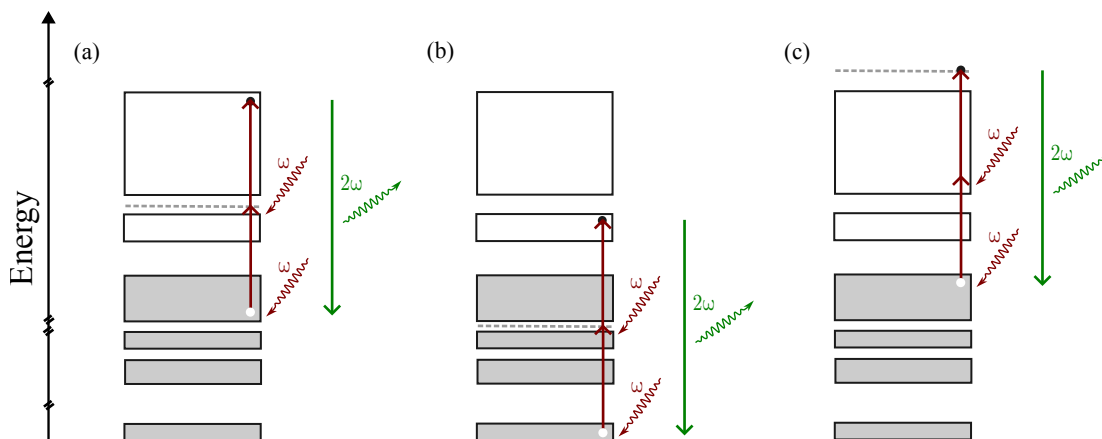


Figure 1.2: Schematic diagram (single-particle representation) of different scenarios of electronic transitions: (a)-(b) are transitions facilitated by a virtual state; (d) corresponds to a resonant scheme. Grey rectangles represent occupied states while white rectangles represent unoccupied states. Dashed lines represent virtual states. The electron is represented by a black point, while the hole is represented by a white point. The wavy arrows stand for incoming and outgoing photons. Adapted from Boyd¹¹, Fig. 1.2.1 (b).

All in all, these various scenarios represent responses of the system to an external electromagnetic field. In optics, this response is characterized by a property known as susceptibility¹¹. Typically, susceptibility is a tensor quantity, implying that both magnitude and direction are significant. Moreover, susceptibility accounts not only for the linear response of the material but also for nonlinear responses¹¹. For example, since SHG is a second-order process, the second-order susceptibility tensor characterizes this scenario. There are two means for obtaining the second-order susceptibility tensor: experimental techniques and theoretical computations. Regarding the former, a

popular experimental method for measuring the components of the second-order susceptibility tensor is known as the Maker fringes technique¹⁶. As for the latter, the second-order susceptibility tensor is generally computed using the dipole approximation¹⁷ within the Density Functional framework.

1.1 Problem Statement

Can B. Uzundal and collaborators¹⁸ conducted experimental and numerical work on second-harmonic generation from lithium niobate (LiNbO_3). They concluded that the well-established theory of nonlinear optics, in the electric-dipole approximation, is suitable to explain the observed second-order response in a bulk non-centrosymmetric material at the extreme ultraviolet regime. Given that the description of nonlinear optics is compatible with experiments conducted within the XUV region, the description of wave propagation through non-centrosymmetric materials in the XUV, based on nonlinear optics, is also plausible.

However, this task is challenging due to nonlinearity, crystal anisotropy, and the lack of theoretical and experimental data on the second-order susceptibility tensor in the XUV region. Additionally, factors such as diffraction and absorption increase the degrees of freedom, hence adding complexity. Consequently, there is a theoretical and numerical challenge to verify the plausibility of studying nonlinear wave propagation based on nonlinear optics theory.

1.2 General and Specific Objectives

The primary goal of this thesis is to comprehend SHG within LiNbO_3 starting from the well-established framework of nonlinear optics and extending it successively into the XUV regime. Furthermore, the process to attain this goal is delineated into the following specific tasks:

- Derive the nonlinear wave propagation equation in uniaxial crystals.
- Conduct an experimental benchmark of the theory for nonlinear wave propagation in LiNbO_3 .
- Explore the physical mechanisms underlying second-harmonic generation (SHG) in the extreme ultraviolet (XUV) regime
- Perform numerical simulations to calculate optical parameters required for studying second-harmonic generation (SHG) in the extreme ultraviolet (XUV) regime.

Having presented this introduction, the thesis revolves around a theoretical preamble chapter (2), two main chapters (3) - (4), followed by a concluding chapter (5).

Mainly, this thesis focuses on modeling SHG experiments in crystals from a pulsed source of light. To this end, in Chapter 2, we provide a broad description of crystals, experimental geometries, and theoretical details, especially electromagnetism within crystals, to pave the way for deriving the essential equations needed to evaluate wave

propagation within uniaxial crystals. At the end of Chapter 2, we provide details on modelling material properties with an emphasis on Density Functional Theory (DFT).

In Chapter 3, we develop the basic framework of wave propagation within uniaxial crystals incorporating spatial and temporal effects. Subsequently, within this chapter, we provide several criteria to approximate the model. The theory, along with the approximations, is benchmarked against a transmission geometry experiment conducted in the visible light regime.

Converging onto our central objective, in Chapter 4, we explore the XUV regime based on our theoretical model. Moreover, reflection geometry is explored in this chapter. Chapter 5 closes with general conclusions and outlooks.

In this thesis, vector quantities are represented in bold roman and script typefaces. Tensor quantities are denoted in underlined bold script typeface, where the number of underlines indicates the rank of the tensor. Additionally, we occasionally use the index notation to write vectors and tensors. A single index represents a vector, a double index represents a second-rank tensor, and triple indices represent a third-rank tensor, and so on.

Finally, SI units (International System of Units) have been used throughout this work unless stated otherwise.

Chapter 2

Preliminaries: Theoretical and Experimental Aspects

This chapter focuses on light propagation through crystals, offering perspectives from experiments and theory, with particular attention given to uniaxial crystals. The chapter then shifts its focus to nonlinear optics, introducing the fundamental principles of this field. Chapter 2 lays the groundwork for Chapter 3 and Chapter 4 to explore second harmonic generation (SHG) in more detail. Finally, the chapter concludes with a concise introduction to Density Functional Theory (DFT), along with approximations to model the optical properties of solid-state materials.

2.1 Basic Framework

When considering the light incident on the nonlinear medium, it is an electromagnetic wave, composed of electric and magnetic fields, denoted as $\mathbf{E}(\mathbf{r}, t)$ and $\mathbf{H}(\mathbf{r}, t)$, respectively. Mainly, the propagation of light is characterized by defining its electric field due to the fact that the magnetic field is related to the electric field through Maxwell's equations¹⁹. In reference to Fig. 2.1, as long as light propagates outside the crystal, the electric and magnetic fields are fully characterized by the following set of equations (SI units):

$$\nabla \cdot \mathbf{E} = \frac{\rho}{\epsilon_0} \quad (2.1a)$$

$$\nabla \cdot \mathbf{B} = 0 \quad (2.1b)$$

$$\nabla \times \mathbf{E} = -\frac{\partial \mathbf{B}}{\partial t} \quad (2.1c)$$

$$\nabla \times \mathbf{B} = \mu_0 \left(\mathbf{J} + \epsilon_0 \frac{\partial \mathbf{E}}{\partial t} \right) \quad (2.1d)$$

where \mathbf{E} , \mathbf{B} , \mathbf{J} , ρ are the electric field, magnetic induction, current density, and charge density, respectively. ϵ_0 and μ_0 are the permittivity and permeability* of free space. Purposely, these equations are the fundamental laws of

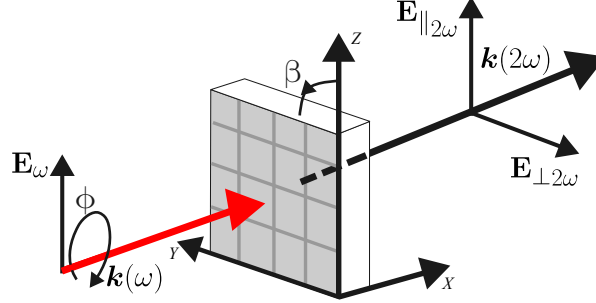


Figure 2.1: Experimental geometry where the beam is normally incident upon the sample. $\mathbf{k}(\omega)$ and $\mathbf{k}(2\omega)$ are wave vectors for the fundamental and second-harmonic waves, respectively. ϕ stands for the azimuthal angle that defines the orientation of the polarization plane of the fundamental wave \mathbf{E}_ω while β is the sample azimuthal angle. The resulted second-harmonic wave can be polarized either parallel $\mathbf{E}_{\parallel 2\omega}$ or perpendicular $\mathbf{E}_{\perp 2\omega}$ with respect to the polarization direction of the fundamental wave. Adapted from the work: “Optical third-harmonic spectroscopy of the magnetic semiconductor EuTe”²⁰.

electricity and magnetism. The electric field and magnetic field within the crystal are described by the following equations,

$$\nabla \cdot \mathbf{E} = \frac{1}{\epsilon_0}(\rho_f + \rho_b) = \frac{1}{\epsilon_0}(\rho_f - \nabla \cdot \mathbf{P}) \quad (2.2a)$$

$$\nabla \cdot \mathbf{B} = 0 \quad (2.2b)$$

$$\nabla \times \mathbf{E} = -\frac{\partial \mathbf{B}}{\partial t} \quad (2.2c)$$

$$\nabla \times \mathbf{B} = \mu_0 \left(\nabla \times \mathbf{M} + \frac{\partial \mathbf{P}}{\partial t} + \mathbf{J}_f \right) + \mu_0 \epsilon_0 \frac{\partial \mathbf{E}}{\partial t} \quad (2.2d)$$

where ρ_f , ρ_b , \mathbf{M} , \mathbf{J}_f , \mathbf{P} are the free charge density, bound charge density, magnetization, free current density, and polarization density, respectively. Provided that the magnetic induction $B_i = \mu_{ij}H_j = \mu_0(H_i + M_i)$, and displacement field $D_i = \epsilon_{ij}E_j = \epsilon_0E_i + P_i$ (These expressions are written in index notation. μ_{ij} and ϵ_{ij} are the

* $\mu_0 = 1.25664 \times 10^{-6} \text{N}\cdot\text{A}^{-2}$, $\epsilon_0 = 8.85 \times 10^{-12} \text{F/m}$

dielectric 2nd-rank tensor and permeability 2nd-rank tensor), this collection of equations becomes:

$$\nabla \cdot \mathbf{D} = \rho_f \quad (2.3a)$$

$$\nabla \cdot \mathbf{B} = 0 \quad (2.3b)$$

$$\nabla \times \mathbf{E} = -\frac{\partial \mathbf{B}}{\partial t} \quad (2.3c)$$

$$\nabla \times \mathbf{H} = \mu_0 \left(\mathbf{J}_f + \frac{\partial \mathbf{D}}{\partial t} \right) \quad (2.3d)$$

The number of underlines stands for the order of the tensor. Finally, in addition to the assumption of the lack of a macroscopic magnetization (\mathbf{M}), for the majority of situations considered in nonlinear optics, the medium is assumed to be electrically neutral and nonconducting ($\rho_f = 0 = \mathbf{J}_f$).

An ansatz for solutions of the electric field for the Maxwell's equations is given by:

$$\begin{aligned} \mathbf{E}(\mathbf{r}, t) &= \frac{1}{2} \mathbf{e} \mathcal{E}(\mathbf{r}, t) \exp(i[\mathbf{k} \cdot \mathbf{r} - \omega t]) + \text{c.c} \\ &= \frac{1}{2} \mathcal{E}(\mathbf{r}, t) \exp(i[\mathbf{k} \cdot \mathbf{r} - \omega t]) + \text{c.c} \end{aligned} \quad (2.4)$$

where \mathbf{k} is the wave vector of propagation, and ω is the circular frequency. In contrast to the rapidly varying components of the oscillating wave, the envelope, denoted as $\mathcal{E}(\mathbf{r}, t)$ [†], is a slowly varying function. Furthermore, this envelope is predominantly complex, involving both magnitude (i.e., amplitude) and phase information.

The direction of the electric field, indicating the polarization of the wave, is represented by \mathbf{e} , which can be either real or complex. In the former scenario, it corresponds to a plane-polarized wave, while in the latter, it implies that the wave is elliptically polarized. Finally, the notation "c.c." implies the complex conjugate. It is included in the definition of equation (2.4) since the electric field is a real quantity. The numerical factor 1/2 is a convention[‡].

Moreover, it is worth noting that the envelope in equation (2.4) depends not only on space but also on time. This functional form aligns with a description of pulses. Pulses refer to flashes of light, typically produced by lasers and delivered in the form of beams.

In Chapter 3, temporal effects are formally incorporated into the theory of wave propagation; however, some features characterizing pulses are provided in this section. Naturally, using pulsed radiation in optical experiments is a common practice not only in the visible light regime but also in the XUV and X-ray spectra²¹.

To develop a simple model of pulsed radiation, one should be aware of certain parameters that characterize this type of light emission. To begin with, the duration of light pulses, commonly called pulse length or pulse width, is often defined in terms of the full width at half-maximum (FWHM) of the optical power versus time. For instance, when considering a Gaussian temporal profile, the power can be described by $\mathbb{P} \sim \exp(-t^2/\tau^2)$. In this context, the pulse length, denoted as τ , is approximately the full width at half-maximum (FWHM) duration multiplied by $\frac{1}{2\sqrt{\ln 2}}$ (i.e., $\tau = \frac{\tau_{\text{FWHM}}}{2\sqrt{\ln 2}}$). In addition, along with pulse width, another significant parameter is the pulse repetition

[†]This quantity can be represented in vector form as follows: $\mathcal{E}(\mathbf{r}, t) = \mathbf{e} \mathcal{E}(\mathbf{r}, t)$.

[‡]When summing up a complex number ($z = x + iy$) with its complex conjugate, the outcome is as follows: $z + z^* = x + iy + x - iy = 2x$. Including a 1/2 factor results in x rather than $2x$.

rate. This rate is defined as the number of emitted pulses per second. In addition to the pulsed emission of light, lasers can emit a continuous beam of light without any interruptions; hence, continuous-wave (CW) lasers. In such cases, the envelope becomes independent of time.

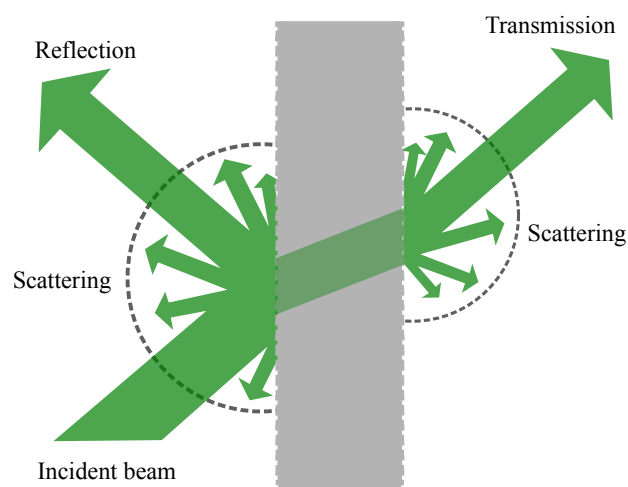


Figure 2.2: Schematic representation of three different geometries commonly used in experiments: transmission, reflection and scattering. The gray region represents the material under study. Adapted from Ref. 22 .

In addition to the type of light source, various experimental geometries can be explored, including transmission geometry, reflection geometry, and scattering geometry. As shown in Fig. 2.2, the signal of interest depends on the chosen geometry. For instance, in transmission geometry, we are interested in the transmitted signal, while in reflection geometry, the reflected signal is of interest. In scattering geometry, the scattered signal is the primary focus.

Moreover, regardless of the chosen geometry, light can strike the sample either through normal incidence or oblique incidence. In connection with second-harmonic generation experiments, both transmission²¹ and reflection²³ geometries are commonly used. For instance, Fig. 2.1 illustrates the transmission geometry under normal incidence for a SHG experiment. In this scenario, the space is partitioned into three regions. Light initially travels through air (or vacuum), then it traverses a crystal, which serves as the nonlinear medium, and ultimately returns to air where the detector is located.

Purposely, since the rapidly varying frequencies are unfeasible to be recorded by detectors, the quantity measured experimentally is the time-averaged field flux, where the average is over several cycles. Hence, one is interested in the intensity (irradiance). We are interested in understanding the behavior of light as it propagates through the nonlinear medium, ultimately characterizing the propagation with intensity.

2.1.1 The Wave Propagation Equation: Beam propagation in Uniaxial Crystals

Generally, the nonlinear medium studied in SHG experiments involves crystals. In crystalline materials, constituent atoms are arranged in a repeating configuration. Roughly speaking, crystals entail groups of atoms that are not only identical, but also oriented and aligned in all three dimensions. Each group serves as a parallelepiped-shaped building block. Such building block is called a unit cell²⁴. There are seven types of unit cells: cubic, tetrahedral, orthorhombic, monoclinic, triclinic, trigonal, and hexagonal. The edges of the unit cell define a coordinate system known as the crystallographic coordinate system. The axes of this coordinate system are denoted by the letters a , b , and c .

Depending on the type of the unit cell, these axes are either mutually orthogonal, as in the case of cubic or orthorhombic systems, or not mutually orthogonal, as in trigonal, hexagonal, triclinic or monoclinic crystal systems. In the latter case, a convention, IEEE/ANSI Std. 176²⁵, is followed to establish a trio of Cartesian axes XYZ relative to the unit cell geometry. IEEE/ANSI Std. 176 defines XYZ frame for more convenient reporting of tensor crystallographic properties (crystal physics coordinate system). Purposely, there is a special rectangular frame that is unique in the sense that in this frame, the dielectric tensor, a second-rank tensor property of materials, is diagonal. This frame is referred to as the principal (dielectric) coordinate system, $x_1x_2x_3$ (See Fig. 2.3 (a)).

Crystals can be classified into three groups (isotropic, uniaxial, an biaxial), depending on the relations between ϵ_{11} , ϵ_{22} , and ϵ_{33} , where they are the entries of the diagonalized dielectric tensor represented in the principal coordinate system ($x_1x_2x_3$):

$$\underline{\underline{\epsilon}} = \begin{pmatrix} \epsilon_{11} & 0 & 0 \\ 0 & \epsilon_{22} & 0 \\ 0 & 0 & \epsilon_{33} \end{pmatrix} \quad (2.5)$$

When the dielectric permittivity entries are equivalent, the material has an isotropic symmetry, such as cubic structure. However, when $\epsilon_{11} = \epsilon_{22} \neq \epsilon_{33}$, the material has uniaxial symmetries. Purposely, uniaxial materials often crystallize in tetragonal, trigonal, or hexagonal phases. The discrepancy in tensor components leads to a phenomenon referred to as birefringence.

In this case, light encounters different refractive indices or exhibits varying phase velocities based on the direction of the electric fields. The two waves are categorized as ordinary and extraordinary waves, with their electric fields being either perpendicular to the optic axis or having non-zero projections along the optic axis. The optic axis in uniaxial crystals corresponds to the axis with highest symmetry.

For example, LiNbO_3 belongs to the trigonal crystal class where there is an axis of threefold symmetry which is labeled by c , which is one of the axis in the crystallographic coordinate system. Furthermore, regarding uniaxial materials, the principal coordinate system ($x_1x_2x_3$) coincides with the crystal physics coordinate system (XYZ), where Z aligns parallel to c and X aligns with a . Y is oriented to form a right-handed system (see Fig. 2.3 (b)). Finally, the dielectric permittivity entries in the biaxial crystals are distinct along all three directions, $\epsilon_{11} \neq \epsilon_{22} \neq \epsilon_{33}$. In this thesis, uniaxial crystals are of interest[§].

[§]Readers interested in isotropic and/or biaxial crystals are encouraged to refer to “Laser Beam Propagation in Nonlinear Optical Media” by

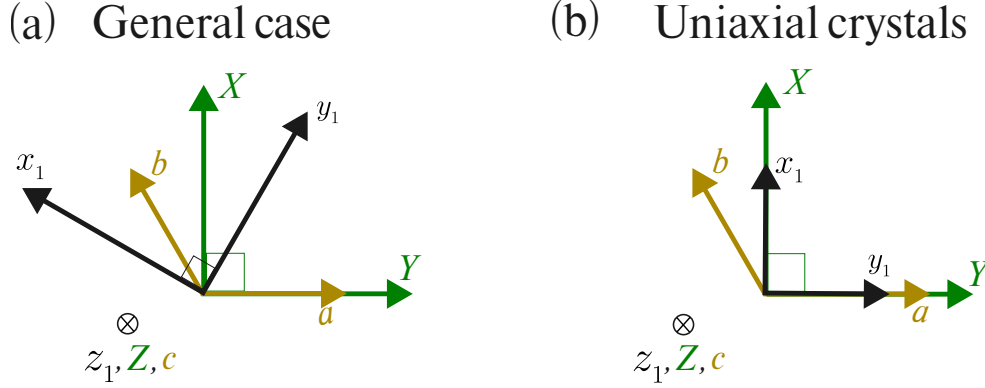


Figure 2.3: Schematic for different coordinate systems for studying crystals. In a general scenario, there are three coordinate systems: (a, b, c) , (X, Y, Z) , (x_1, y_2, z_3) , which are the crystallographic coordinate systems, principal, and crystal physics, respectively. When the crystal belongs to the uniaxial class, the crystal physics coordinate system is equivalent to the principal coordinate system.

J. Fleck and M. Feit²⁷ developed a theory to describe the propagation of light in uniform anisotropic media. Here, a re-derivation of the set of generalized wave equations governing propagation in uniform anisotropic media is presented. While CGS units were adopted in Ref. 27., SI units are used in this case. This analysis of wave propagation in anisotropic media demonstrates a key characteristic: the electric field exhibits distinct behaviors corresponding to ordinary and extraordinary polarizations.

In this context, the electric field satisfies the following differential equation 2.3:

$$\nabla \times \nabla \times \mathbf{E} = -\frac{1}{c^2 \epsilon_0} \frac{\partial^2 \mathbf{D}}{\partial t^2} \quad (2.6)$$

To obtain this equation, we apply rotation to equation (2.3c) and then use equation (2.3d). This equation can be written for a single-frequency component ω [‡]:

$$\nabla^2 \mathcal{E} - \nabla (\nabla \cdot \mathcal{E}) = -\frac{\omega^2}{c^2 \epsilon_0} \mathcal{D} \quad (2.7)$$

The displacement field can be written as follows¹¹:

$$\mathcal{D} = \epsilon_0 \underline{\underline{\epsilon}} \cdot \mathcal{E} \quad (2.8)$$

J. Fleck and M. Feit²⁷ develop the wave propagation equation with respect to the principal system XYZ . Within

Shekhar Guha and Leonel P. Gonzalez²⁶.

[‡]In this case, this single-frequency representation is given by the following expression: $\mathbf{E}(\mathbf{r}, t) = \frac{1}{2} \mathcal{E}(\mathbf{r}) \exp(-i\omega t) + \text{c.c.}$, and $\mathcal{D}(\mathbf{r}, t) = \frac{1}{2} \mathcal{D}(\mathbf{r}) \exp(-i\omega t) + \text{c.c.}$. In this case, \mathcal{E} and \mathcal{D} are vectors that only depend on spatial coordinates

such coordinate system, $\underline{\underline{\epsilon}}$ is a second-order tensor written in diagonal matrix form as follows:

$$\underline{\underline{\epsilon}} = \begin{pmatrix} \epsilon_{xx} & 0 & 0 \\ 0 & \epsilon_{xx} & 0 \\ 0 & 0 & \epsilon_{zz} \end{pmatrix} \quad (2.9)$$

In order to develop equation (2.7), J. Fleck and M. Feit²⁷ find an expression for $\nabla \cdot \mathcal{E}$:

$$\begin{aligned} \nabla \cdot \mathcal{E} &= \left(1 - \frac{\epsilon_{zz}}{\epsilon_{xx}} \right) \frac{\partial \mathcal{E}_z}{\partial Z} \\ &= \left(1 - \frac{n_{zz}^2}{n_{xx}^2} \right) \frac{\partial \mathcal{E}_z}{\partial Z} \end{aligned} \quad (2.10)$$

This expression is derived by combining equation (2.3a) (assuming $\rho_f = 0$) with equation (2.8). It applies to a uniform anisotropic material, where ϵ_{xx} and ϵ_{zz} are position-independent. Notably, n_{xx} and n_{zz} represent the refractive indices along the principal directions X and Z , respectively. These indices are commonly referred to as the ordinary refractive index (n_o) and the extraordinary refractive index (n_e), respectively.

In equation (2.10), the dependence on the Z -direction stems from our definition of the dielectric tensor, which implicitly assumes the Z -axis aligns with the optical axis. While the axis label itself is arbitrary, the alignment with the optical axis is crucial. Thus far, equation (2.7) can be written as follows^{||}:

$$\frac{\partial^2 \mathcal{E}_X}{\partial X^2} + \frac{\partial^2 \mathcal{E}_Y}{\partial Y^2} + \frac{\partial^2 \mathcal{E}_Z}{\partial Z^2} - \left(1 - \frac{n_e^2}{n_o^2} \right) \frac{\partial^2 \mathcal{E}_Z}{\partial X \partial Z} + \frac{n_o^2 \omega^2}{c^2} \mathcal{E}_X = 0 \quad (2.11a)$$

$$\frac{\partial^2 \mathcal{E}_X}{\partial X^2} + \frac{\partial^2 \mathcal{E}_Y}{\partial Y^2} + \frac{\partial^2 \mathcal{E}_Z}{\partial Z^2} - \left(1 - \frac{n_e^2}{n_o^2} \right) \frac{\partial^2 \mathcal{E}_Z}{\partial Y \partial Z} + \frac{n_o^2 \omega^2}{c^2} \mathcal{E}_Y = 0 \quad (2.11b)$$

$$\frac{\partial^2 \mathcal{E}_X}{\partial X^2} + \frac{\partial^2 \mathcal{E}_Y}{\partial Y^2} + \frac{\partial^2 \mathcal{E}_Z}{\partial Z^2} - \left(1 - \frac{n_e^2}{n_o^2} \right) \frac{\partial^2 \mathcal{E}_Z}{\partial Z^2} + \frac{n_e^2 \omega^2}{c^2} \mathcal{E}_Z = 0 \quad (2.11c)$$

We will now approach this set of equations through the plane-wave ansatz. Readers interested in the derivation of linear wave equations for paraxial beams should refer to Section 4 of Fleck and Feit's work²⁷. In Chapter 3, the focus will be on the derivation of the wave equation for uniaxial crystal class taking into consideration nonlinear effects.

The plane-wave ansatz is taken as follows^{**}:

$$\mathcal{E}(\mathbf{r}) = \mathbf{F} \exp(i\mathbf{k} \cdot \mathbf{r}) \quad (2.12)$$

^{||}J. Fleck and M. Feit (Ref. 27) derived Equation (2.11).

^{**}Thus far, we have developed equation with respect to the coordinate system XYZ . Therefore, the term $\mathbf{k} \cdot \mathbf{r}$ expands to $k_X X + k_Y Y + k_Z Z$ in this coordinate system.

In this context, \mathbf{F} is a constant vector. Plugging the expression (2.12) into the equations (2.11) yields:

$$\left[-(k_X^2 + k_Y^2 + k_Z^2) + \frac{n_o^2 \omega^2}{c^2} \right] F_X + \left(1 - \frac{n_e^2}{n_o^2} \right) k_X k_Z F_Z = 0 \quad (2.13a)$$

$$\left[-(k_X^2 + k_Y^2 + k_Z^2) + \frac{n_o^2 \omega^2}{c^2} \right] F_Y + \left(1 - \frac{n_e^2}{n_o^2} \right) k_Y k_Z F_Z = 0 \quad (2.13b)$$

$$\left[-(k_X^2 + k_Y^2 + \frac{n_e^2}{n_o^2} k_Z^2) + \frac{n_e^2 \omega^2}{c^2} \right] F_Z = 0 \quad (2.13c)$$

The condition for nontrivial solutions for F_X , F_Y , and F_Z is,

$$\left[-(k_X^2 + k_Y^2 + k_Z^2) + \frac{n_o^2 \omega^2}{c^2} \right]^2 \left[-(k_X^2 + k_Y^2 + \frac{n_e^2}{n_o^2} k_Z^2) + \frac{n_e^2 \omega^2}{c^2} \right] = 0 \quad (2.14)$$

The two solutions from equation (2.14) are denoted as the ordinary and extraordinary waves, respectively.

Regarding the ordinary-wave solution, we have the following:

$$k_X^2 + k_Y^2 + k_Z^2 = \frac{n_o^2 \omega^2}{c^2} \quad (2.15)$$

In this scenario, we have that the components of the ordinary electric field satisfy the following relations:

$$F_Z = 0 \quad (2.16a)$$

$$(F_X^2 + F_Y^2) \neq 0 \quad (2.16b)$$

Finally, through equations (2.10), (2.12), and (2.16a), the relationship between F_X and F_Y is given by:

$$F_Y = -\frac{k_X}{k_Y} F_X \quad (2.17)$$

If the electric field lacks a Z -component, this electric field is polarized perpendicular to both the Z -axis and the direction of wave propagation.

Regarding the extraordinary wave, which is the second solution of equation (2.14), we have the following relation:

$$k_X^2 + k_Y^2 + \frac{n_e^2}{n_o^2} k_Z^2 = \frac{n_e^2 \omega^2}{c^2} \quad (2.18)$$

By taking into account equation (2.18), the following relations are determined from the equations (2.11):

$$F_Z \neq 0 \quad (2.19a)$$

$$F_X = -\frac{\left(1 - \frac{n_e^2}{n_o^2} \right) k_X k_Z}{n_o^2 \omega^2 / c^2 - (k_X^2 + k_Y^2 + k_Z^2)} F_Z \quad (2.19b)$$

$$F_Y = -\frac{\left(1 - \frac{n_e^2}{n_o^2} \right) k_Y k_Z}{n_o^2 \omega^2 / c^2 - (k_X^2 + k_Y^2 + k_Z^2)} F_Z \quad (2.19c)$$

Equations (2.16a) - (2.17) and (2.19) suggest orthogonality between the ordinary and extraordinary waves. This is because the solution for the extraordinary wave involves the Z -component, while the ordinary wave solution entails the X -component. Finally, the dispersion relation for extraordinary waves is given by the following relations,

$$k_X^2 + k_X^2 + k_X^2 = \frac{n^2 \omega^2}{c^2} \quad (2.20a)$$

$$\frac{k_X^2 + k_Y^2}{n^2 \omega^2 / c^2} = \sin^2 \theta \quad (2.20b)$$

$$\frac{k_Z^2}{n^2 \omega^2 / c^2} = \cos^2 \theta \quad (2.20c)$$

where θ stands for the angle between \mathbf{k} and the Z -axis. These relations (2.20) reduce equation (2.18) to:

$$\frac{1}{n^2(\theta)} = \frac{\sin^2 \theta}{n_e^2} + \frac{\cos^2 \theta}{n_o^2} \quad (2.21)$$

Equation 2.21 shows the role of propagation direction in the index of refraction. For example, when light propagates at $\pi/2$, the ordinary refractive index that characterizes the propagation is denoted as ordinary. When $\theta = 0$, the index of refraction turns out to be extraordinary.

In connection with the experimental geometry in Fig. 2.1, the incident radiation (fundamental wave) can be linearly polarized, being either an ordinary or an extraordinary wave, while the outgoing polarization direction is chosen to be either parallel (\mathbf{E}_{\parallel}) or perpendicular (\mathbf{E}_{\perp}) to the incident polarization direction. This distinction between refractive indices is relevant when calculating SHG intensities.

The next section focuses on characterizing how materials respond under high intensities of light.

2.2 Perturbative approach to Nonlinear Processes

Generally, polarization involves both linear and nonlinear contributions. However, the nonlinear term does not play a significant role when the intensity of light is low. If the intensity is sufficiently high, nonlinear processes become relevant and require description:

$$\mathbf{P} = \mathbf{P}^{(1)} + \mathbf{P}^{\text{NL}} \quad (2.22)$$

where \mathbf{P}^{NL} is a nonlinear function of the applied field. Given that $\mathbf{D} = \underline{\underline{\epsilon}} \cdot \mathbf{E} = \epsilon_0 \mathbf{E} + \mathbf{P}$, then equation (2.6) becomes:

$$\nabla \times \nabla \times \mathbf{E} + \frac{1}{c^2} \frac{\partial^2 \mathbf{E}}{\partial t^2} + \frac{1}{c^2 \epsilon_0} \frac{\partial^2 \mathbf{P}^{(1)}}{\partial t^2} = -\frac{1}{c^2 \epsilon_0} \frac{\partial^2 \mathbf{P}^{\text{NL}}}{\partial t^2} \quad (2.23)$$

In most applications of nonlinear optics¹¹, \mathbf{P}^{NL} is expanded in a power series of applied fields:

$$\mathbf{P}^{\text{NL}} = \mathbf{P}^{(2)} + \mathbf{P}^{(3)} + \dots \quad (2.24)$$

Equation (2.24) can be written in index notation as follows:

$$P_i^{\text{NL}} = P_i^{(2)} + P_i^{(3)} + \dots$$

where,

$$P_i^{(2)}(\mathbf{r}, t) = \epsilon_0 \int_{-\infty}^{\infty} dt' \int_{-\infty}^{\infty} dt'' \chi_{ijk}^{(2)}(t-t', t-t'') E_j(\mathbf{r}, t') E_k(\mathbf{r}, t'') \quad (2.25a)$$

$$P_i^{(3)}(\mathbf{r}, t) = \epsilon_0 \int_{-\infty}^{\infty} dt' \int_{-\infty}^{\infty} dt'' \int_{-\infty}^{\infty} dt''' \chi_{ijkq}^{(3)}(t-t', t-t'', t-t''') E_j(\mathbf{r}, t') E_k(\mathbf{r}, t'') E_q(\mathbf{r}, t''') \quad (2.25b)$$

where $\chi_{ijk}^{(2)}$ and $\chi_{ijkq}^{(3)}$ are the 3rd- and 4th-order dielectric response. Remarkably, the field in the equations above is the total field, which can result from a superposition of quasi-monochromatic (or monochromatic) fields at different frequencies:

$$\mathbf{E}(\mathbf{r}, t) = \sum_{\omega_j} \frac{1}{2} \mathcal{E}_{\omega_j}(\mathbf{r}, t) \exp(-i\omega_j t) + \text{c.c.} \quad (2.26)$$

The sum is over waves with frequencies ω_j ²⁸. Moreover, when considering the nonlinear polarization as a small perturbation to the total polarization, it can be expressed as:

$$\mathbf{P}^{\text{NL}}(\mathbf{r}, t) = \sum_{\omega_j} \frac{1}{2} \mathcal{P}_{\omega_j}^{\text{NL}}(\mathbf{r}, t) \exp(-i\omega_j t) + \text{c.c.} \quad (2.27)$$

In the case of a superposition of quasi-monochromatic fields, the Fourier components of the nonlinear polarization are expressed as follows^{28, pp. 19}:

$$\tilde{\mathcal{P}}_{i\omega_\sigma}^{(n)}(\mathbf{r}, \omega_\sigma) = \epsilon_0 K(-\omega_\sigma; \omega_1, \dots, \omega_n) \chi_{ij\dots q}^{(n)}(-\omega_\sigma; \omega_1, \dots, \omega_n) \tilde{\mathcal{E}}_{j\omega_1}(\mathbf{r}, \omega_1) \dots \tilde{\mathcal{E}}_{q\omega_n}(\mathbf{r}, \omega_n) \quad (2.28)$$

where repeated indices entails summation. $\chi_{ij\dots q}^{(n)}(-\omega_\sigma; \omega_1, \dots, \omega_n)$ is the n -th order susceptibility, and $\omega_\sigma = \omega_1 + \dots + \omega_n$. Additionally, $\tilde{\mathcal{E}}_{q\omega_n}$ stands for the temporal slowly envelope part of the electric field at frequency ω_n in the frequency domain.

In this context, $K(\omega_\sigma, \omega_1, \dots, \omega_n)$ is a numerical factor that takes into account degeneracy²⁹:

$$K(-\omega_\sigma; \omega_1, \dots, \omega_n) = 2^{l+m-n} p \quad (2.29)$$

where $l = 1$ when $\omega_\sigma \neq 0$, otherwise $l = 0$, m stands for the number of sets of n frequencies $(\omega_1, \dots, \omega_n)$ that are zero, n is the order of nonlinearity, and p stands for the number of distinct permutations of $(\omega_1, \dots, \omega_n)$. The adopted convention for frequency ordering in $\chi_{ij\dots k}^{(n)}(-\omega_\sigma, \dots, \omega_n)$ is that the first entry is the frequency of the nonlinear polarization followed by the frequencies of the inputs. The signs on frequencies must be such that algebraic sum of all frequencies is zero: $-\omega_\sigma + \omega_1 + \omega_2 + \dots + \omega_n = 0$ (i.e., conservation of energy).

In the case when the electric field results from a superposition of monochromatic waves, the Fourier components of the nonlinear polarizations are given by^{29, pp. 25}:

$$\tilde{\mathcal{P}}_{i\omega_\sigma}^{(n)}(\mathbf{r}) = \epsilon_0 K(-\omega_\sigma; \omega_1, \dots, \omega_n) \chi_{ip\dots q}^{(n)}(-\omega_\sigma; \omega_1, \dots, \omega_n) \tilde{\mathcal{E}}_{p\omega_1}(\mathbf{r}) \dots \tilde{\mathcal{E}}_{q\omega_n}(\mathbf{r}) \quad (2.30)$$

We will now embark on a concise exploration of the so-called second-order susceptibility tensor (or second-order dielectric tensor). This is a property of materials necessary for studying second harmonic generation (SHG).

2.2.1 The Second-order Susceptibility Tensor: $\underline{\underline{\chi}}^{(2)}(-\omega_\sigma; \omega_1, \omega_2)$

In general, $\chi_{ij\dots k}^{(n)}(-\omega_\sigma; \omega_1, \dots, \omega_n)$ exhibits various types of symmetry, including permutation symmetry, and spatial symmetry¹¹. While this subsection primarily focuses on $\chi_{ijk}^{(2)}(-\omega_\sigma; \omega_1, \omega_2)$, the following symmetry operations are applicable to any n th-order susceptibility tensor. Regarding permutation symmetry, $\chi_{ijk}^{(2)}(-\omega_\sigma; \omega_1, \omega_2)$ is invariant under the permutations of the pairs $(j, \omega_1), (k, \omega_2)$ ²⁸:

$$\chi_{ijk}^{(2)}(-\omega_\sigma; \omega_1, \omega_2) = \chi_{ikj}^{(2)}(-\omega_\sigma; \omega_2, \omega_1) \quad (2.31)$$

In other words, there is no difference physically, in which order the electric fields are applied with respect to the material.

Moreover, permutations that include the additional pair $(i, -\omega_\sigma)$ lead to a change in sign of the frequency arguments $(-\omega_\sigma; \omega_1, \omega_2) \longleftrightarrow (-(-\omega_1); -\omega_\sigma, \omega_2) \longleftrightarrow (\omega_1; -\omega_\sigma, \omega_2)$; hence²⁸:

$$\begin{aligned} \chi_{ijk}^{(2)}(-\omega_\sigma; \omega_1, \omega_2) &= \chi_{jik}^{(2)}(\omega_1; -\omega_\sigma, \omega_2) \\ \chi_{ijk}^{(2)}(-\omega_\sigma; \omega_1, \omega_2) &= \chi_{kji}^{(2)}(\omega_2; \omega_1, -\omega_\sigma) \end{aligned} \quad (2.32)$$

Given that the nonlinear polarization is a real quantity, the complex conjugate entails a change in sign of frequency. For example, this sign change influences the outcome of the following index permutation operation²⁸:

$$\chi_{ijk}^{(2)}(-\omega_\sigma; \omega_1, \omega_2) = \chi_{jik}^{(2)*}(-\omega_1; \omega_\sigma, -\omega_2) \quad (2.33)$$

Generally, these expressions hold when the susceptibilities are complex, indicating that any frequency or combination of frequencies is near a natural resonance frequency of the material. However, susceptibilities can be treated as real quantities when all the frequencies involved are far removed from the transition frequencies of the nonlinear medium²⁸. Then equation 2.33 becomes:

$$\chi_{ijk}^{(2)}(-\omega_\sigma; \omega_1, \omega_2) = \chi_{jik}^{(2)}(-\omega_1; \omega_\sigma, -\omega_2) \quad (2.34)$$

This is the full permutation symmetry (or overall permutation symmetry²⁹, pp. 122).

When the susceptibility exhibits negligible dispersion over the entire frequency range of interest, the cartesian subscripts and frequencies are decoupled, and consequently they could be permuted independently without changing the susceptibility:

$$\begin{aligned} \chi_{ijk}^{(2)}(-\omega_\sigma; \omega_1, \omega_2) &= \chi_{jki}^{(2)}(-\omega_\sigma; \omega_1, \omega_2) = \chi_{kij}^{(2)}(-\omega_\sigma; \omega_1, \omega_2) = \chi_{ijk}^{(2)}(-\omega_\sigma; \omega_1, \omega_2) \\ &= \chi_{ikj}^{(2)}(-\omega_\sigma; \omega_1, \omega_2) = \chi_{jki}^{(2)}(-\omega_\sigma; \omega_1, \omega_2) = \chi_{kij}^{(2)}(-\omega_\sigma; \omega_1, \omega_2) \end{aligned} \quad (2.35)$$

This is known as the Kleinman symmetry. Besides frequencies being far from any material resonance, this symmetry requires that there be no resonance between any of the frequencies, such as an absorption line.

Moreover, for the process of second harmonic generation, the nonlinear optics community generally writes the nonlinear polarization density in terms of a third-rank tensor²⁹ $d_{ijk}^{(2)}$, which is often defined^{††} as follows

$$d_{ijk}(-\omega_\sigma; \omega_1, \omega_2) = \frac{1}{2} \chi_{ijk}^{(2)}(-\omega_\sigma; \omega_1, \omega_2) \quad (2.36)$$

$\chi_{ijk}^{(2)}$ has 27 components, however, symmetry properties^{‡‡} lead to a decrease in the number of its components. Due to the intrinsic permutation symmetry, the pairs of indices (j, ω_1) and (k, ω_2) in $\chi_{ijk}^{(2)}(-\omega_\sigma; \omega_1, \omega_2)$ are freely interchangeable. In addition, the susceptibility is invariant to the permutation of j and k indices for the second harmonic generation process. Hence, for SHG processes, the third-rank tensor $d_{ijk}(-2\omega; \omega, \omega)$ could be expressed as a 3×6 matrix $d_{im}(-2\omega; \omega, \omega)$. Thus there are 18 independent components of the $d_{ijk}(-2\omega; \omega, \omega) = d_{im}(-2\omega; \omega, \omega)$ where the index m takes the values 1-6 with the following correspondence to the pairs of cartesian-axis labels:

Table 2.1: Relationship between the indices of the χ_{ijk} and d_{im} element. The index m is defined in terms of the indices j and k . For, example, $\frac{1}{2}\chi_{XXZ} = d_{XXZ} = d_{15}$ where $m = 5$ when $j = X$ and $k = Z$

m	1	2	3	4	5	6
jk	XX	YY	ZZ	ZY YZ	ZX XZ	XY YX

Regarding the spatial symmetry, nonlinear susceptibilities also reflect the structural symmetry of the material. Table 2.2 shows different d-matrix for different symmetry classes of uniaxial crystals. This table is useful for calculating the nonlinear polarization vector. Finally, all materials that possess a center of inversion symmetry (centrosymmetric materials) do not display second-order nonlinearities except in regions of discontinuity such as surfaces or interfaces.^{§§}

The following section^{¶¶} will focus on the application of Density Functional Theory (DFT) to model solid-state materials, exploring the underlying physics and associated approximations.

^{††}There are several similar definitions in the literature, see for example Ref. 26, pp. 67.

^{‡‡}There are several properties^{11 26} of the nonlinear susceptibility that relate the various components of $\underline{\underline{\chi}}^{(2)}$, such as the reality of the fields and intrinsic permutation symmetry. When the oscillation frequencies of the interacting electric fields are far away from any material resonances, the components of $\underline{\underline{\chi}}^{(2)}$ are mainly frequency-independent. This scenario allows us to apply two additional symmetry properties: overall permutation symmetry and Kleinman's symmetry, which have been mentioned earlier.

^{§§}This is a consequence of deriving the susceptibility in the dipole approximation within the perturbation Hamiltonian. In liquids and vapors, isotropic materials with centers of symmetry, a second-order process may occur when a transition matrix element between two states of equal parity—states that are forbidden in the electric dipole approximation—is nonzero, owing to an electric quadrupole-allowed transition. However, such transition is very weak.

^{¶¶}While this section emphasizes the quantum mechanical description of solids, it is important to note that many of the concepts discussed can be applied to molecules as well.

Table 2.2: d -Matrix ($d_{im} = \frac{1}{2}\chi_{ijk}^{(2)}$) for uniaxial crystals.

Symmetry Class	General conditions	Kleinman
3	$\begin{pmatrix} d_{11} & -d_{11} & 0 & d_{14} & d_{15} & -d_{22} \\ -d_{22} & d_{22} & 0 & d_{15} & -d_{14} & -d_{11} \\ d_{31} & d_{31} & d_{33} & 0 & 0 & 0 \end{pmatrix}$	$\begin{pmatrix} d_{11} & -d_{11} & 0 & 0 & d_{15} & -d_{22} \\ -d_{22} & d_{22} & 0 & d_{15} & 0 & -d_{11} \\ d_{15} & d_{15} & d_{33} & 0 & 0 & 0 \end{pmatrix}$
3m	$\begin{pmatrix} 0 & 0 & 0 & 0 & d_{15} & -d_{22} \\ -d_{22} & d_{22} & 0 & d_{15} & 0 & 0 \\ d_{31} & d_{31} & d_{33} & 0 & 0 & 0 \end{pmatrix}$	$\begin{pmatrix} 0 & 0 & 0 & 0 & d_{15} & -d_{22} \\ -d_{22} & d_{22} & 0 & d_{15} & 0 & 0 \\ d_{15} & d_{15} & d_{33} & 0 & 0 & 0 \end{pmatrix}$
$\bar{6}$	$\begin{pmatrix} d_{11} & -d_{11} & 0 & 0 & 0 & -d_{22} \\ -d_{22} & d_{22} & 0 & 0 & 0 & -d_{11} \\ 0 & 0 & 0 & 0 & 0 & 0 \end{pmatrix}$	$\begin{pmatrix} d_{11} & -d_{11} & 0 & 0 & 0 & -d_{22} \\ -d_{22} & d_{22} & 0 & 0 & 0 & -d_{11} \\ 0 & 0 & 0 & 0 & 0 & 0 \end{pmatrix}$
$\bar{6}m2$	$\begin{pmatrix} 0 & 0 & 0 & 0 & 0 & -d_{22} \\ -d_{22} & d_{22} & 0 & 0 & 0 & 0 \\ 0 & 0 & 0 & 0 & 0 & 0 \end{pmatrix}$	$\begin{pmatrix} 0 & 0 & 0 & 0 & 0 & -d_{22} \\ -d_{22} & d_{22} & 0 & 0 & 0 & 0 \\ 0 & 0 & 0 & 0 & 0 & 0 \end{pmatrix}$
6,4	$\begin{pmatrix} 0 & 0 & 0 & d_{14} & d_{15} & 0 \\ 0 & 0 & 0 & d_{15} & -d_{14} & 0 \\ d_{31} & d_{31} & d_{33} & 0 & 0 & 0 \end{pmatrix}$	$\begin{pmatrix} 0 & 0 & 0 & 0 & d_{15} & 0 \\ 0 & 0 & 0 & d_{15} & 0 & 0 \\ d_{15} & d_{15} & d_{33} & 0 & 0 & 0 \end{pmatrix}$
6mm,4mm	$\begin{pmatrix} 0 & 0 & 0 & 0 & d_{15} & 0 \\ 0 & 0 & 0 & d_{15} & 0 & 0 \\ d_{31} & d_{31} & d_{33} & 0 & 0 & 0 \end{pmatrix}$	$\begin{pmatrix} 0 & 0 & 0 & 0 & d_{15} & 0 \\ 0 & 0 & 0 & d_{15} & 0 & 0 \\ d_{15} & d_{15} & d_{33} & 0 & 0 & 0 \end{pmatrix}$
622, 422	$\begin{pmatrix} 0 & 0 & 0 & d_{14} & 0 & 0 \\ 0 & 0 & 0 & 0 & -d_{14} & 0 \\ 0 & 0 & 0 & 0 & 0 & 0 \end{pmatrix}$	$\begin{pmatrix} 0 & 0 & 0 & 0 & 0 & 0 \\ 0 & 0 & 0 & 0 & 0 & 0 \\ 0 & 0 & 0 & 0 & 0 & 0 \end{pmatrix}$
$\bar{4}$	$\begin{pmatrix} 0 & 0 & 0 & d_{14} & d_{15} & 0 \\ 0 & 0 & 0 & -d_{15} & d_{14} & 0 \\ d_{31} & -d_{31} & 0 & 0 & 0 & d_{36} \end{pmatrix}$	$\begin{pmatrix} 0 & 0 & 0 & d_{14} & d_{15} & 0 \\ 0 & 0 & 0 & -d_{15} & d_{14} & 0 \\ d_{15} & -d_{15} & 0 & 0 & 0 & d_{14} \end{pmatrix}$
32	$\begin{pmatrix} d_{11} & -d_{11} & 0 & d_{14} & 0 & 0 \\ 0 & 0 & 0 & 0 & -d_{14} & -d_{11} \\ 0 & 0 & 0 & 0 & 0 & 0 \end{pmatrix}$	$\begin{pmatrix} d_{11} & -d_{11} & 0 & d_{14} & 0 & 0 \\ 0 & 0 & 0 & 0 & -d_{14} & -d_{11} \\ 0 & 0 & 0 & 0 & 0 & 0 \end{pmatrix}$
$\bar{4}2m$	$\begin{pmatrix} 0 & 0 & 0 & d_{14} & 0 & 0 \\ 0 & 0 & 0 & 0 & d_{14} & 0 \\ 0 & 0 & 0 & 0 & 0 & d_{36} \end{pmatrix}$	$\begin{pmatrix} 0 & 0 & 0 & d_{14} & 0 & 0 \\ 0 & 0 & 0 & 0 & d_{14} & 0 \\ 0 & 0 & 0 & 0 & 0 & d_{14} \end{pmatrix}$

2.3 Modelling material properties (in brief)

A solid-state material (or, a solid) is a collection of heavy, positively charged particles (nuclei) and lighter, negatively charged particles (electrons). Having N nuclei implies dealing with a problem of $N + ZN$ electromagnetically interacting particles (Z represents atomic number); this is a many-body problem. In fact, modelling materials in an atomic level requires quantum mechanics, which leads to a quantum many-body problem. The exact many-particle Hamiltonian for this system is:

$$\begin{aligned} \hat{H} = & -\frac{\hbar^2}{2} \sum_i \frac{\nabla_{\mathbf{R}_i}^2}{M_i} - \frac{\hbar^2}{2} \sum_i \frac{\nabla_{\mathbf{r}_i}^2}{m_e} \\ & - \frac{1}{4\pi\epsilon_0} \sum_{i,j} \frac{Z_i e^2}{\|\mathbf{R}_i - \mathbf{r}_j\|} + \frac{1}{8\pi\epsilon_0} \sum_{i \neq j} \frac{e^2}{\|\mathbf{r}_i - \mathbf{r}_j\|} + \frac{1}{8\pi\epsilon_0} \sum_{i \neq j} \frac{Z_i Z_j e^2}{\|\mathbf{R}_i - \mathbf{r}_j\|} \end{aligned} \quad (2.37)$$

Here, the mass of the nucleus at \mathbf{R}_i is M_i , the electrons have mass m_e and are at \mathbf{r}_i . Additionally, \hbar is the reduced Planck constant, and Z_i represents the atomic number of the nucleus i . Equation (2.37) involves five terms: the first term is the kinetic energy operator for the nuclei, the second for the electrons; the last three terms describe the Coulomb interaction between electrons and nuclei, between electrons and other electrons, and between nuclei and other nuclei. It is a common practice to write equation (2.37) using atomic units (i.e., $m_e = e = a_0 = \hbar = 1$):

$$\begin{aligned} \hat{H} = & -\frac{1}{2} \sum_i \frac{\nabla_{\mathbf{R}_i}^2}{M_i} - \frac{1}{2} \sum_i \frac{\nabla_{\mathbf{r}_i}^2}{m_e} \\ & - \sum_{i,j} \frac{Z_i}{\|\mathbf{R}_i - \mathbf{r}_j\|} + \frac{1}{2} \sum_{i \neq j} \frac{1}{\|\mathbf{r}_i - \mathbf{r}_j\|} + \frac{1}{2} \sum_{i \neq j} \frac{Z_i Z_j}{\|\mathbf{R}_i - \mathbf{r}_j\|} \end{aligned} \quad (2.38)$$

Having defined the Hamiltonian, we can study the evolution of the quantum many-body system through the so-called time-dependent Schrödinger equation³⁰:

$$i \frac{\partial}{\partial t} \Psi(\mathbf{x}, t) = \hat{H} \Psi(\mathbf{x}, t) \quad (2.39)$$

Here, $\mathbf{x} \equiv \{\mathbf{r}_1, s_1, \dots, \mathbf{r}_N, s_N; \mathbf{R}_1, S_1, \dots, \mathbf{R}_M, S_M\}$ represents all the position coordinates and spins of all nuclei and electrons.

Because the potential only depends on the position but not on time, the wavefunction Ψ is separable into a time-dependent and a time-independent part with separation constant E . The time-independent Schrödinger equation for the many-problem is then:

$$\hat{H} \psi(\mathbf{x}) = E \psi(\mathbf{x}) \quad (2.40)$$

This equation has an infinite collection of solutions ψ_κ with eigenvalue E_κ . Then the general solution is a linear combination of the separable solutions:

$$\Psi(\mathbf{x}, t) = \sum_{\kappa}^{+\infty} C_{\kappa} \psi_{\kappa}(\mathbf{x}) \exp\left(-i \frac{E_{\kappa}}{\hbar} t\right) \quad (2.41)$$

where C_{κ} is a coefficient of this series.

In quantum mechanics, every physical situation that one wants to study is completely defined by its Hamiltonian

\hat{H} . Every stationary solution, for example equation (2.40), of such a problem is described by a state ψ_κ that is an eigenstate of that Hamiltonian³¹. We can rewrite equation (2.40) in order to be in agreement with the previous statement:

$$\hat{H}\psi_\kappa(\mathbf{x}) = E_\kappa\psi_\kappa(\mathbf{x}) \quad (2.42)$$

Physical systems always have boundary conditions, leading to a discrete but infinite set of eigenvalues. The symbols κ stands for one or more quantum numbers. A common approximation is to assume periodic boundary conditions, which treats crystals as infinitely repeating units. Bloch's theorem tells how this can be done for a Hamiltonian that has a lattice periodicity²⁴. The theorem says: Any eigenfunction $\psi(\mathbf{r})$ can be written as a product of a plane wave and a function with the periodicity of the Bravais lattice:

$$\psi_{n,\mathbf{k}}(\mathbf{r}) = \exp(i\mathbf{k} \cdot \mathbf{r}) u_{n,\mathbf{k}}(\mathbf{r}) \quad (2.43)$$

where

$$u_{n,\mathbf{k}}(\mathbf{r} + \mathbf{R}) = u_{n,\mathbf{k}}(\mathbf{r}) \quad (2.44)$$

Bloch states of equation (2.43) are defined by two indices n and \mathbf{k} which represent the band index and the crystal momentum, respectively. The dependence of the Bloch states which respect to \mathbf{k} can be limited to the first Brillouin zone (FBZ) of the reciprocal space without any loss of information²⁴. The index n corresponds to the appearance of independent eigenstates of different energies but with the same \mathbf{k} . \mathbf{R} is a translation vector that characterizes the crystal. This vector is a linear combination of the three vectors of the unit cell, which reads as follows:

$$\mathbf{R} = n_1\mathbf{a}_1 + n_2\mathbf{a}_2 + n_3\mathbf{a}_3 \quad (2.45)$$

Here, the coefficients n_1, n_2, n_3 are integers, and the periodicity of the lattice is dictated by the primitive lattice vectors $\mathbf{a}_1, \mathbf{a}_2, \mathbf{a}_3$. Purposely, equation (2.45) provides insights into the lattice space that characterizes the crystals. As we have primitive lattice vectors, there are reciprocal lattice vectors \mathbf{G} :

$$\mathbf{G} = m_1\mathbf{b}_1 + m_2\mathbf{b}_2 + m_3\mathbf{b}_3 \quad (2.46)$$

The coefficients m_1, m_2, m_3 are integers, and \mathbf{b}_i are the reciprocal vectors that characterize the reciprocal space. They can be calculated from the lattice vectors as follows:

$$\mathbf{b}_i = \frac{2\pi}{\Omega} \mathbf{a}_j \times \mathbf{a}_k \quad (2.47)$$

where Ω is the volume of the unit cell. From equations (2.45) and (2.47), we can easily get the following relation:

$$\mathbf{a}_i \cdot \mathbf{b}_j = 2\pi\delta_{ij} \quad (2.48)$$

Regarding the periodic boundary condition, it is known as the Born-von Karman boundary condition²⁴. The condition can be stated as:

$$\psi(\mathbf{r} + N_i\mathbf{a}_i) = \psi(\mathbf{r}) \quad (2.49)$$

where \mathbf{a}_i are the primitive lattice vectors and N_i are integers of order $N^{1/3}$ where $N = N_1 N_2 N_3$ is the total number of primitive cells in the crystal. The quantum number \mathbf{k} can be composed from the reciprocal lattice vectors with (non-integer) coefficients x_i :

$$\mathbf{k} = x_1 \mathbf{b}_1 + x_2 \mathbf{b}_2 + x_3 \mathbf{b}_3 \quad (2.50)$$

Through relation (2.48), the Bloch's theorem then gives $\exp(i2\pi x_i N_i) = 1$. Thus, $x_i = \frac{m_i}{N_i}$. Consequently, the allowed Bloch wave vectors are given by:

$$\mathbf{k} = \sum_{i=1}^3 \frac{m_i}{N_i} \mathbf{b}_i \quad (2.51)$$

with m_i integers.

The calculation of many properties requires the evaluation of integrals over the Brillouin zone in reciprocal space. Within such discrete domain, the integral of a function $f(\mathbf{k})$ is approximated as follows:

$$\frac{1}{\Omega_{\text{BS}}} \int f(\mathbf{k}) d\mathbf{k} \approx \sum_{\mathbf{k}} w_{\mathbf{k}} f(\mathbf{k}) \quad (2.52)$$

where Ω_{BS} is the volume of the Brillouin zone. This integral is approximately equal to the weighted sum over the \mathbf{k} -points of the first Brillouin zone.

Coming back to equation (2.39), all the physical observables of the system can be deduced from the eigenfunctions and eigenvalues of this equation. However, calculating such eigenfunctions and eigenvalues is not such a straightforward task. In order to find acceptable solutions, we will need to make approximations at 3 different levels: Born-Oppenheimer approximation; Density Functional Theory; and solving the equation.

The Born-Oppenheimer approximation: Since the nuclei are much heavier and therefore much slower than electrons, we can “freeze” them at fixed positions and assume the electrons to be in instantaneous equilibrium with them. Consequently, we can regard nuclei as “external” to the electron cloud. We now deal with a collection of NZ interacting negative particles moving in the external potential of the nuclei. With this approximation, we can rewrite the Hamiltonian as follows:

$$\hat{H} = \hat{T} + \hat{V} + \hat{V}_{ext} \quad (2.53)$$

We are left with the kinetic energy of the electron gas, the potential energy due to electron-electron interactions and the potential energy of the electrons in the (now external) potential of the nuclei.

Density Functional Theory: While the Born-Oppenheimer approximation eases the complexity of the quantum many-body problem for solids, Density Functional Theory (DFT) reduce equation (2.53) to an approximate but tractable form. DFT has been formally established in 1964 by two theorems due to Hohenberg and Kohn³²:

(1) There is a **one-to-one** correspondence between the ground-state density $\rho(\mathbf{r})$ of a many-electron system (atom, molecule, solid) and the external potential \hat{V}_{ext} . An immediate consequence is that the ground-state expectation value of any observable \hat{O} is a unique functional of the exact ground-state electron density:

$$\langle \Psi | \hat{O} | \Psi \rangle = O[\rho] \quad (2.54)$$

(2) For \hat{O} being the Hamiltonian \hat{H} , the ground-state total energy functional $H[\rho] \equiv E_{V_{ext}}[\rho]$ is of the form:

$$E_{V_{ext}}[\rho] = \underbrace{\langle \Psi | \hat{T} + \hat{V} | \Psi \rangle}_{F_{HK}[\rho]} + \langle \Psi | \hat{V}_{ext} | \Psi \rangle \quad (2.55)$$

$$= F_{HK}[\rho] + \langle \Psi | \hat{V}_{ext} | \Psi \rangle \quad (2.56)$$

where the Hohenberg-Kohn density functional $F_{HK}[\rho]$ is **universal** for any many-electron system. $E_{V_{ext}}[\rho]$ reaches its **minimal** value (equal to the ground-state total energy) for the ground-state density corresponding to V_{ext} .

The one-to-one correspondence secures that the electron density contains as much information as the wavefunctions. Hence, solely using the density, we can retrieve all observable quantities. Second, the universality of $F_{HK}[\rho]$. Because $F_{HK}[\rho]$ does not contain information on the nuclei and their position, it is a universal functional for any many-electron system. Third, the second theorem implies using the variational principle of Rayleigh-Ritz³³ in order to find the ground-state density. Out of the infinite number of possible densities, the one which minimizes $E_{V_{ext}}[\rho]$ is the ground-state density corresponding to the external potential V_{ext} . $F_{HK}[\rho]$ should be known in order to find the ground-state density. To circumvent this situation, there is an alternative procedure to obtain the ground state density: the equations of Kohn-Sham (KS)³⁴:

The exact ground-state density $\rho(\mathbf{r})$ of an N -electron system is:

$$\rho(\mathbf{r}) = 2 \sum_{\mathbf{i}}^{N_e/2} \varphi_{\mathbf{i}}^*(\mathbf{r}) \varphi_{\mathbf{i}}(\mathbf{r}) \quad (2.57)$$

where the single-particle wavefunctions $\varphi_{\mathbf{i}}(\mathbf{r})$ are the $N_e/2$ lowest-energy solutions of the Kohn-Sham equation (N_e is the number of electrons):

$$\hat{H}_{KS} \varphi_{\mathbf{i}}(\mathbf{r}) = \varepsilon_{\mathbf{i}} \varphi_{\mathbf{i}}(\mathbf{r}) \quad (2.58)$$

where the Kohn-Sham Hamiltonian is given by:

$$\begin{aligned} \hat{H}_{KS} &= \hat{T}_0 + \hat{V}_H + \hat{V}_{xc} + \hat{V}_{ext} \\ &= -\frac{1}{2} \nabla_{\mathbf{i}}^2 + \int d\mathbf{r}' \frac{\rho(\mathbf{r}')}{\|\mathbf{r} - \mathbf{r}'\|} + V_{xc} + V_{ext} \end{aligned} \quad (2.59)$$

\hat{T}_0 represents the kinetic energy operator of a non-interacting electron gas, \hat{V}_H is the Hartree potential operator, \hat{V}_{ext} is the external potential operator, and \hat{V}_{xc} is the exchange-correlation potential operator. The exchange-correlation potential is written in terms of the functional derivative:

$$V_{xc} = \frac{\delta E_{xc}[\rho]}{\delta \rho} \quad (2.60)$$

In the KS approach, the many body problem of interacting electrons and nuclei is mapped to a one-electron reference system that leads to the same density as the real system.

Aside from the Born-Oppenheimer approximation, no other approximations are considered. Up to this point, the Kohn-Sham approach, described earlier, is exact. However, it relies on the exchange-correlation functional, which

is unfortunately unknown in its exact form. This is where approximations become necessary. In the case where we assume that the exchange energy is completely local, i.e., it depends only on the density at the same location, we obtain the local density approximation (LDA). In this case, the exchange-correlation functional has the following form:

$$E_{xc}^{\text{LDA}}[\rho] = \int d\mathbf{r} \rho(\mathbf{r}) \varepsilon_{xc}(\rho(\mathbf{r})) \quad (2.61)$$

The function ε_{xc} describes the exchange-correlation (xc) energy of a homogeneous electron gas, and is numerically known³⁵. The Local Density Approximation (LDA) makes a simplifying assumption about the exchange-correlation functional. It proposes that the exchange-correlation energy for a specific electron density can be calculated by breaking the material down into tiny volumes, each with a constant density. Each of these tiny volumes contributes an amount equal to the exchange-correlation energy of an identical volume filled with a homogeneous electron gas.

In order to take into account non-homogeneities in the electron density, a semi-local approximation that depends on the gradient of the density is often used. Improve on LDA entails to include the exchange-correlation contribution of every infinitesimal volume not only dependent on the local density in that volume, but also on the density in the neighbouring volumes. This approximation is therefore called the Generalized Gradient Approximation (GGA). GGA functionals have often been parameterized by fitting experimental data, but were then restricted in their application to certain systems.

However, parameter-free functionals can be used in a wide range of systems. Some of the most commonly used examples of such *ab-initio* functionals are those developed by Perdew, Burke, and Ernzerhof (PBE)³⁶. Purposely, the general form of a GGA functional reads as follows:

$$E_{xc}^{\text{GGA}}[\rho] = \int d\mathbf{r} \rho(\mathbf{r}) \varepsilon_{xc}(\rho(\mathbf{r})) R_{xc}(\rho, \nabla\rho) \quad (2.62)$$

where R_{xc} is the enhancement factor that depends on the electron density and its gradient.

The equations presented for the exchange-correlation functional, (2.61) and (2.62), intentionally focus on the spin-unpolarized case. However, it is important to note that spin-polarized versions of these equations can be derived³⁶.

Solving the equations: We end up with an infinite set of one-electron equations of the following type:

$$\left(-\frac{1}{2}\nabla^2 + \int d\mathbf{r}' \frac{\rho(\mathbf{r}')}{\|\mathbf{r} - \mathbf{r}'\|} + V_{xc} + V_{ext} \right) \varphi_{n\mathbf{k}}(\mathbf{r}) = \varepsilon_{n\mathbf{k}} \varphi_{n\mathbf{k}}(\mathbf{r}) \quad (2.63)$$

where the exchange-correlation potential is given by LDA, GGA, or another approximation. The band index n is of the order of the number of electrons per unit cell. $\varepsilon_{n\mathbf{k}}$ are the eigenvalues (energies) of the Kohn-Sham Hamiltonian. To solve equation (2.63), we mainly focus on finding coefficients $C_{i,p}$ needed to express φ_i in a given basis set ϕ_p :

$$\varphi_{n\mathbf{k}} = \sum_{p=1}^P C_{n,p}^{\mathbf{k}} \phi_p \quad (2.64)$$

The wavefunctions $\varphi_{n\mathbf{k}}$ belong to a function space which has an infinite dimension, P is therefore in principle infinite. In practice, one works with a limited set of basis functions. Such a limited basis will never be able to

describe $\varphi_{n\mathbf{k}}$ exactly, but one could try to find a basis that can generate a function that is “close” to $\varphi_{n\mathbf{k}}$. Finally, this scenario reduces to a diagonalization matrix problem.

The Kohn-Sham equations involve a self-consistency problem because both the Hartree operator (\hat{V}_H) and the exchange-correlation operator (\hat{V}_{xc}) depend on the electron density ($\rho(\mathbf{r})$). This density, in turn, is determined by the Kohn-Sham orbitals ($\phi_{n\mathbf{k}}$) we are solving for. In simpler terms, the solutions ($\phi_{n\mathbf{k}}$) influence the Hamiltonian (\hat{H}_{KS}), creating a situation where the equation cannot be written down and solved definitively before its solution is known. An iterative procedure is needed to escape from the paradox. First, some starting density ρ_0 is guessed, and a Hamiltonian \hat{H}_{KS_1} is constructed with it. The eigenvalue problem is solved, and results in a set of $\{\phi_{n\mathbf{k}}\}_1$ from which a density ρ_1 can be derived. Most probably ρ_0 will differ from ρ_1 . Now ρ_1 is used to construct \hat{H}_{KS_2} , which will yield a ρ_2 , and so on until a tolerance value is satisfied. The final density that fulfills the tolerance criterion is then consistent with the Hamiltonian.

2.3.1 Representation of the Kohn-Sham wavefunctions

In DFT calculations, we generally encounter these three representations of the KS wavefunctions: real space (RS), plane waves (PWs), and linear combinations of atomic orbitals (LCAOs). For RS representations, the wavefunctions are directly calculated at a specific number of grid points within the material. In contrast, in PW and LCAO modes, wavefunctions are expanded in a plane-wave basis set and an atomic orbital basis set, respectively. To calculate the material properties of LiNbO₃, we will focus on two key representations: PW and LCAO.

In the PW representation, all cell-periodic functions are expanded in plane waves (i.e., Fourier analysis); for example, $u_{i\mathbf{k}}$ can be written as follows:

$$u_{n\mathbf{k}} = \frac{1}{\sqrt{\Omega}} \sum_{\mathbf{G}} C_{n\mathbf{G}}^{\mathbf{k}} \exp(i\mathbf{G} \cdot \mathbf{r}) \quad (2.65)$$

where Ω is the volume of the unit cell. Consequently, the expansion of the wavefunction in the same basis is then:

$$\varphi_{n\mathbf{k}} = \frac{1}{\sqrt{\Omega}} \sum_{\mathbf{G}} C_{n\mathbf{G}}^{\mathbf{k}} \exp(i(\mathbf{G} + \mathbf{k}) \cdot \mathbf{r}) \quad (2.66)$$

In practice we cannot work with an infinite basis set, and will have to limit it somehow. For plane waves, we can simply choose all \mathbf{G} with $\|\mathbf{G}\| < \|\mathbf{G}_{\max}\|$. This corresponds to a sphere with radius $\|\mathbf{G}_{\max}\|$ centered at the origin of reciprocal space. All reciprocal lattice vectors that are inside this sphere are taken into the basis set. Instead of $\|\mathbf{G}_{\max}\|$, the free electron energy corresponding to $|\mathbf{G} + \mathbf{k}|$ is specified as a criterion to determine the number of plane-wave basis functions:

$$\frac{1}{2} |\mathbf{G} + \mathbf{k}|^2 < E_{\text{cutoff}} \quad (2.67)$$

This is called the cut-off energy. In order to represent Kohn-Sham (KS) wavefunctions using Bloch waves, we will need a finite number of points in the reciprocal space. A Monkhorst-Pack sampling of special \mathbf{k} -points^{37,38} is

performed as it is an unbiased method to select these points in an equally spaced mesh:

$$\mathbf{k}(n_1, n_2, n_3) = \sum_{i=1}^3 \frac{2n_i - N_i - 1}{2N_i} \mathbf{b}_i \quad (2.68)$$

Wavefunctions are particularly sharp when they are located close to the nuclei since valence wavefunctions must oscillate rapidly in order to satisfy the orthogonality condition with core wavefunctions. This requires a very fine grid or many plane waves to accurately describe these sharp features.

One way to avoid this problem is to use pseudopotentials³⁹. These replace the core electrons and nuclei with a smoother potential, allowing calculations to focus only on the valence electrons. This significantly reduces the number of basis set functions.

Additionally, this method reduces the number of wavefunctions to be calculated, since the pseudopotentials only have to be calculated and tabulated once for each type of atom, so that only calculations on the valence states are needed. Within the pseudopotential approach, we can neglect relativistic effects since valence electrons are non-relativistic. The pseudopotentials describing core states are of course constructed with full consideration of relativistic effect. However, this method obscures the information of the wavefunctions near the nucleus. The picture of the full wavefunction close the nuclei is lost.

The augmented-plane-wave (APW) method⁴⁰ tackles the challenge of efficiently describing full electron wavefunctions. The method achieves this by dividing space into two key regions: atom-centered augmentation spheres, and bonding region outside the sphere. In the former, the wavefunctions are treated like atomic-like partial waves. Regarding the latter, envelope functions are used to describe the wavefunctions.

An alternative approach exists: the projector augmented wave (PAW) method⁴¹. The PAW method offers a more powerful framework that encompasses the augmented plane wave (APW) method as a specific case, and the pseudopotential method as a well-defined approximation⁴². This means that PAW can handle a wider range of electronic structure problems while incorporating the strengths of both these established methods.

The PAW method establishes a linear transformation \hat{T} that maps an auxiliary smooth wavefunction $|\tilde{\varphi}_\kappa\rangle$ onto the Kohn-Sham single particle wavefunction $|\varphi_\kappa\rangle$:

$$|\varphi_\kappa\rangle = \hat{T} |\tilde{\varphi}_\kappa\rangle \quad (2.69)$$

where κ is the quantum state label, containing a \mathbf{k} index, a band index, and a spin index. This transformation yields the transformed KS equations:

$$\hat{T}^\dagger \hat{H}_{\text{KS}} \hat{T} |\tilde{\varphi}_\kappa\rangle = \varepsilon_\kappa \hat{T}^\dagger \hat{T} |\tilde{\varphi}_\kappa\rangle \quad (2.70)$$

which needs to be solved instead of the usual KS equation. To ensure clarity and maintain consistency with established Projector Augmented Wave (PAW) literature, this chapter employs the tilde symbol to represent quantities associated with auxiliary terms, such as $|\tilde{\varphi}_\kappa\rangle$, within the PAW method. This distinction is crucial to avoid ambiguity with Chapters 3 and 4, where the tilde conventionally signifies the Fourier transform in the time domain.

The transformation operator is given by the following expression:

$$\hat{T} = 1 + \sum_a \sum_i (|\phi_i^\alpha\rangle + |\tilde{\phi}_i^\alpha\rangle) \langle \tilde{p}_i^\alpha | \quad (2.71)$$

where α is an atom index. We obtain the all electron KS wavefunction $\varphi_\kappa(\mathbf{r}) = \langle \mathbf{r} | \varphi_\kappa \rangle$ from the transformation:

$$\varphi_\kappa(\mathbf{r}) = \tilde{\varphi}_\kappa(\mathbf{r}) + \sum_\alpha \sum_i (\phi_i^\alpha(\mathbf{r}) + \tilde{\phi}_i^\alpha(\mathbf{r})) \langle \tilde{p}_i^\alpha | \tilde{\varphi}_\kappa \rangle \quad (2.72)$$

where the smooth (and thereby numerically convenient) auxiliary wavefunction is calculated through solving the eigenvalue equation (2.70). Equation (2.72) entails three components: partial waves $\phi_i^\alpha(\mathbf{r})$; the smooth partial waves $\tilde{\phi}_i^\alpha(\mathbf{r})$; and the smooth projector function $\tilde{p}_i^\alpha(\mathbf{r})$. $\phi_i^\alpha(\mathbf{r})$ are the atom-centered partial waves used to expand the all-electron wavefunction within the augmentation region:

$$|\varphi_\kappa^\alpha\rangle = \sum_i \langle \tilde{p}_i^\alpha | \tilde{\varphi}_\kappa \rangle |\phi_i^\alpha\rangle, \text{ for } |\mathbf{r} - \mathbf{R}^\alpha| < r_c^\alpha \quad (2.73)$$

The cut-off radii, r_c^α should be chosen such that there is no overlap of the augmentation spheres. Regarding the smooth partial waves $|\tilde{\phi}_i^\alpha\rangle$, they expand the auxiliary smooth wavefunction $|\tilde{\varphi}_\kappa\rangle$:

$$|\tilde{\varphi}_\kappa^\alpha\rangle = \sum_i \langle \tilde{p}_i^\alpha | \tilde{\varphi}_\kappa \rangle |\tilde{\phi}_i^\alpha\rangle, \text{ for } |\mathbf{r} - \mathbf{R}^\alpha| < r_c^\alpha \quad (2.74)$$

Purposely, the smooth projector function satisfies the following condition in order to ensure that the one center expansion of the smooth all electron wave function $|\tilde{\varphi}_\kappa^\alpha\rangle$ reduce to $|\tilde{\varphi}_\kappa\rangle$ itself inside the augmentation sphere defined by α :

$$\sum_i |\tilde{\phi}_i^\alpha\rangle \langle \tilde{p}_i^\alpha| = 1 \quad (2.75)$$

Having separated the different types of waves (i.e., rapid oscillations in some parts of space, and smooth behavior in other parts of space), these can be treated individually. To improve computational efficiency, the PAW method separates the wave functions into two components. Localized, atom-centered parts, denoted by a superscript α , are well-suited for representation on fine radial grids around each atom. Delocalized parts, lacking the superscript α , are inherently smooth and can be efficiently represented using coarser Fourier- or real space grids.

Finally, for the PAW method to prove to be practical, approximations such as the frozen core approximation are considered. This approach assumes that core electron states naturally stay close to their corresponding atoms within the defined spheres. In other words, when atoms come together to form molecules or solids, the core electron states essentially behave the same way they did in the individual atoms. Thus the core KS states are identical to the atomic cores states:

$$|\varphi_\kappa^c\rangle = |\phi_\beta^{\alpha,\text{core}}\rangle \quad (2.76)$$

where the index κ on the left hand site refers to both a specific atom, α , and an atomic state, β . Consequently, in this approximation, only valence states are included in the expansions of $|\varphi_\kappa^\alpha\rangle$ and $|\tilde{\varphi}_\kappa^\alpha\rangle$.

We will now focus on the augmented plane wave (APW) method and its successors: linearized augmented plane wave method (LAPW) and augmented plane Wave method and local orbitals (LAPW+lo).

APW, LAPW, and APW+lo

The APW method is based on the idea that in the region far away from the nuclei, the electrons are more or less “free”. Free electrons are described by plane waves. Close to the nuclei, the electrons behave quite as they were in

a free atom, and they could be described more efficiently by atomic-like functions. Consequently, we can explicitly partition the space into interstitial (I) and muffin-tin (MT) regions, where the wavefunctions are described differently. The MT s are sphere of radii R_{MT} centered on atoms labeled α at positions \mathbf{R}_α . Purposely, R_{MT} can be different for different atoms. With this spatial partition, we can expand the KS wavefunctions as follows:

$$\varphi_{n\mathbf{k}}(\mathbf{r}) = \sum_{\mathbf{G}} C_{n\mathbf{G}}^{\mathbf{k}} \phi_{\mathbf{G}+\mathbf{k}}(\mathbf{r}) \quad (2.77)$$

where the sum runs over the reciprocal lattice vectors $\mathbf{G}(\mathbf{r})$. The basis functions $\phi_{\mathbf{G}+\mathbf{k}}$ are defined as follows:

$$\phi_{\mathbf{G}+\mathbf{k}} = \begin{cases} \sum_{l,m} A_{lm\alpha}^{\mathbf{G}+\mathbf{k}} u_{l\alpha}(r_\alpha) Y_{lm}(\hat{\mathbf{r}}_\alpha) & r_\alpha \leq R_{MT} \\ \frac{1}{\sqrt{\Omega}} \exp(i(\mathbf{G} + \mathbf{k}) \cdot \mathbf{r}) & \mathbf{r} \in I \end{cases} \quad (2.78)$$

Within $\mathbf{r}_\alpha = \mathbf{r} - \mathbf{R}_\alpha \leq R_{MT}$, the MT part of $\phi_{\mathbf{G}+\mathbf{k}}(\mathbf{r})$ is expanded in terms of spherical harmonic $Y_{lm}(\hat{\mathbf{r}}_\alpha)$ and radial functions $u_{l\alpha}(r_\alpha)$. The length of \mathbf{r}_α is r_α , and the angles θ and ϕ specifying the direction of \mathbf{r}_α in spherical coordinates, are indicated as $\hat{\mathbf{r}}_\alpha$. $A_{lm\alpha}^{\mathbf{G}+\mathbf{k}}$ are coefficients that ensure continuity at the sphere boundary.

Additionally, we can approximate the KS potential within the MT region. Since the shape of the potential is heavily influenced by the nearness of the nucleus, we can assume that the KS potential is spherically symmetric within the MT region. Thus, to a good approximation, we replace the KS potential by its spherical average V_0 . The $u_{l\alpha}(r_\alpha)$ are solutions to the radial part of the Schrödinger equation for a free atom α , and this at the energy $\varepsilon_{n\mathbf{k}}$:

$$\left[-\frac{1}{2} \frac{d^2}{dr^2} + \frac{l(l+1)}{2r^2} + V_0(r) - \varepsilon_{n\mathbf{k}} \right] (ru_{l\alpha}(r)) = 0 \quad (2.79)$$

where the parameter $\varepsilon_{n\mathbf{k}}$ corresponds to an eigenvalue in equation (2.63), and l is the angular quantum number³¹.

Because a discontinuous eigenfunction would lead to an undefined kinetic energy, such a scenario is physically impossible. Consequently, the plane wave function outside the augmentation sphere must match the function inside the sphere across its entire surface (in terms of value, but not necessarily its derivative).

Intuitively, matching a smooth, localized function inside the sphere with an oscillating plane wave extending infinitely might seem incongruous. After all, plane waves have a defined direction and inherent oscillation, contrasting with the spherical symmetry of the function within the sphere. However, through a clever approach, we can overcome this apparent mismatch. By expanding the plane wave in spherical harmonics about the origin of the sphere of atom α , we obtain the following:

$$\frac{1}{\sqrt{\Omega}} \exp(i(\mathbf{G} + \mathbf{k}) \cdot \mathbf{r}) = \frac{4\pi}{\sqrt{\Omega}} \exp(i(\mathbf{G} + \mathbf{k}) \cdot \mathbf{r}_\alpha) \sum_{l,m} i^l j_l(\|\mathbf{G} + \mathbf{k}\| r_\alpha) Y_{lm}^*(\widehat{\mathbf{G} + \mathbf{k}}) Y_{lm}(\hat{\mathbf{r}}_\alpha) \quad (2.80)$$

with the spherical Bessel functions⁴³ $j_l(kr)$. We can easily obtain an expression for $A_{lm\alpha}^{\mathbf{G}+\mathbf{k}}$ by requiring equation (2.80) at $\mathbf{r} = \mathbf{R}_\alpha$ to be equal to the lm -part of equation (2.78):

$$A_{lm\alpha}^{\mathbf{G}+\mathbf{k}} = \frac{4\pi i^l}{\sqrt{\Omega} u_{l\alpha}(r_\alpha)} \exp(i(\mathbf{G} + \mathbf{k}) \cdot \mathbf{R}_\alpha) j_l(\|\mathbf{G} + \mathbf{k}\| R_\alpha) Y_{lm}^*(\widehat{\mathbf{G} + \mathbf{k}}) \quad (2.81)$$

We can visualize the meaning of a single APW $\phi_{\mathbf{G}+\mathbf{k}}$ of equation (2.78): it is an oscillating function that runs through the unit cell. Whenever it encounters an atom on its path, the simple oscillating behaviour is changed into something more complex inside the MT region of that atom.

Having established the complete APW basis set, we can now utilize it to solve the Kohn-Sham (KS) equation and obtain the coefficients $C_{n\mathbf{G}}^{\mathbf{k}}$. To make the problem numerically tractable, we generally impose an upper limit to represent the Hamiltonian matrices and the overlap matrices: $|\mathbf{G} + \mathbf{k}| < G_{\max}$, where G_{\max} is a plane-wave cutoff. This criterion neglects the influence of varying muffin-tin (MT) sphere radii. A more appropriate approach defines the cutoff using the dimensionless parameter $R_{\text{MT}}G_{\max}$, where R_{MT} represents the smallest sphere radius among all atomic species in the system.

However, unlike the standard self-consistent approach described earlier, this process presents a significant challenge. The key issue lies in the energy dependence of the radial function, $u_{l\alpha}(r_\alpha)$, as evidenced in equation (2.79). To accurately describe an eigenstate, $\psi_{n\mathbf{k}}(\mathbf{r})$, using APWs, we would need to pre-set a radial function with the exact eigenvalue we are trying to determine (i.e., $u_{l\alpha}(r_\alpha; \varepsilon_{l\alpha})$). This circular dependency transforms the KS equation into a non-linear problem in terms of energy, making its solution far from straightforward.

The most obvious strategy is to make it linear by simply picking one energy $\varepsilon_{l\alpha}$ for each l in equation (2.79) and never vary it. This can lead to a problem when describing states that correspond to the same l , but have different principal quantum numbers n . This problem is solved by treating core and valence electrons separately. Core electrons are well localized, and we can calculate their wavefunctions independently by solving equation (2.79), or more commonly the Dirac equation⁴⁴ with atomic boundary conditions.

Additionally, the energy parameter $\varepsilon_{l\alpha}$ must be a very good approximation to the actual eigenenergy that corresponds to a state with the l -type character. Factors such as band dispersion or splitting into bonding and antibonding states prevents the energy parameter from matching all states with the l -character at the same time. To overcome this problem, the energy dependence of the basis is linearized. The radial function with the exact eigenenergy as the energy parameter ε is expressed as⁴⁵:

$$u_{l\alpha}(r_\alpha; \varepsilon) \approx u_{l\alpha}(r_\alpha; \varepsilon_{l\alpha}) + (\varepsilon_{l\alpha} - \varepsilon) \frac{\partial u_{l\alpha}(r_\alpha; \varepsilon)}{\partial \varepsilon} \quad (2.82)$$

This expression cannot be applied directly, however, it shows that the improved muffin-tin basis should contain these two terms. One possibility to implement the energy linearization are through the linearized augmented plane waves (LAPW) method. According to this method, the basis functions are defined as⁴⁵:

$$\phi_{\mathbf{G}+\mathbf{k}} = \begin{cases} \sum_{l,m} \left[A_{lm\alpha}^{\mathbf{G}+\mathbf{k}} u_{l\alpha}(r_\alpha; \varepsilon_{l\alpha}) + B_{lm\alpha}^{\mathbf{G}+\mathbf{k}} \dot{u}_{l\alpha}(r_\alpha; \varepsilon_{l\alpha}) \right] Y_{lm}(\hat{\mathbf{r}}_\alpha) & r_\alpha \leq R_{\text{MT}} \\ \frac{1}{\sqrt{\Omega}} \exp(i(\mathbf{G} + \mathbf{k}) \cdot \mathbf{r}) & \mathbf{r} \in I \end{cases} \quad (2.83)$$

where $\dot{u}_{l\alpha}(r_\alpha; \varepsilon_{l\alpha}) = \frac{\partial u_{l\alpha}(r_\alpha; \varepsilon)}{\partial \varepsilon}$, and the prefactors $A_{lm\alpha}^{\mathbf{G}+\mathbf{k}}$ and $B_{lm\alpha}^{\mathbf{G}+\mathbf{k}}$ are chosen in a such way that $\phi_{\mathbf{G}+\mathbf{k}}$ is smooth and continuous at the muffin-tin boundary.

The linearization of $u_{l\alpha}(r_\alpha; \varepsilon)$ can be performed in different manner⁴⁶. Additionally, we can define APWs with

frozen energy parameters along with new basis functions⁴⁷:

$$\phi_{\mu}(\mathbf{r}) = \begin{cases} \delta_{\alpha\alpha\mu} \delta_{ll\mu} \delta_{mm\mu} [a_{\mu} u_{l\alpha}(r_{\alpha}; \varepsilon_{l\alpha}) + b_{\mu} \dot{u}_{l\alpha}(r_{\alpha}; \varepsilon_{l\alpha})] Y_{lm}(\hat{\mathbf{r}}_{\alpha}) & r_{\alpha} \leq R_{\text{MT}} \\ 0 & \mathbf{r} \in I \end{cases} \quad (2.84)$$

where the coefficients a_{μ} and b_{μ} fulfill two conditions: $\phi_{\mu} = 0$ at the MT boundary and $\int_{\Omega} |\phi_{\mu}|^2 d\mathbf{r} = 1$. These functions are called local orbitals. A local orbital is defined for a particular l and m , and for a particular atom α . A local orbital is zero in the interstitial region and in the muffin tin spheres of other atoms, hence its name local orbital. Using this APW+lo basis, the wavefunction is represented as:

$$\varphi_{n\mathbf{k}}(\mathbf{r}) = \sum_{\mathbf{G}} C_{n\mathbf{G}}^{\mathbf{k}} \phi_{\mathbf{G}+\mathbf{k}}(\mathbf{r}) + \sum_{\mu} C_{n\mu}^{\mathbf{k}} \phi_{\mu}(\mathbf{r}) \quad (2.85)$$

The wavefunction within the MT region enclosing atom α then reads:

$$\varphi_{n\mathbf{k}}(\mathbf{r}) = \sum_{\mathbf{G}} \sum_{l,m} C_{n\mathbf{G}}^{\mathbf{k}} A_{lm\alpha}^{\mathbf{G}+\mathbf{k}} u_{l\alpha;\varepsilon_{l\alpha}}(r_{\alpha}) Y_{lm}(\hat{\mathbf{r}}_{\alpha}) + \sum_{\mu} \sum_{l,m} C_{n\mu}^{\mathbf{k}} \delta_{\alpha\alpha\mu} \delta_{ll\mu} \delta_{mm\mu} [a_{\mu} u_{l\alpha}(r_{\alpha}; \varepsilon_{l\alpha}) + b_{\mu} \dot{u}_{l\alpha}(r_{\alpha}; \varepsilon_{l\alpha})] Y_{lm}(\hat{\mathbf{r}}_{\alpha}) \quad (2.86)$$

Both APW+lo and LAPW offer significant advancements over the original APW method. While APW+lo generally achieves higher accuracy, it necessitates the introduction of additional basis functions, making it computationally less favorable for high-angular momentum (l) channels. Consequently, a practical approach utilizes APW+lo for low- l states and LAPW for high- l states. This strategy is implemented in `Exciting`⁴⁷, for instance.

Kohn-Sham (KS) equations provide a powerful framework to elucidate the electronic structure of materials. Solving these equations self-consistently grants access to KS eigenenergies and wavefunctions. These equations provide the formal machinery for finding the electron density and corresponding total energy within DFT. However, for excited-state properties, such as absorption spectra, limitations arise due to the inherent focus of DFT on the ground state.

Consequently, additional considerations become necessary for accurate descriptions. For example, we are interested in calculating the dielectric function and second-order susceptibility tensor of LiNbO3, which are excited-state properties of this material. We need an accurate description of the electronic structure, occupied and unoccupied bands, before calculating those excited-state properties. We will now explore approaches to address these limitations.

Significant theoretical effort has been devoted to the subject of correcting the excited-state spectrum of electronic systems resulting from DFT calculations⁴⁸. It is a well-known problem that the LDA or GGA utilized within the Kohn-Sham formalism leads to a substantial underestimate of calculated band gaps^{***} in semiconductors and insulators. Differences from experiment are typically about 50%, but deviations as large as 100% also occur⁴⁹.

In DFT, independent electrons interact solely via an exchange-correlation potential: “bare” electrons. To address this limitation, we can incorporate the electron “cloud” that screens the “bare” electrons, treating them as

^{***}The band gap is the difference between the conduction band minimum (CBM) and the valence band maximum.

quasiparticles. An intuitive picture of the quasiparticle concept consists in considering that when a “bare” particle (an electron or a hole) enters in a system of interacting electrons, it perturbs the other particles in its neighborhood and hence it gets “dressed” with a charged (positive or negative) cloud and hence becomes a quasiparticle.

The goal is to compute the quasiparticle corrections to the single-particle Kohn-Sham (KS) eigenvalues obtained from DFT calculations. A prominent approach for such corrections can be the Many-body perturbation theory that is based on Green’s functions (G)⁵⁰. Green’s function theory and the quasiparticle concept constitute an elegant alternative to DFT to solve the many-body problem. Here, we only focus on the 1-particle Green’s function: $G(\mathbf{r}_1, t_1, \mathbf{r}_2, t_2)$. This expression describes both the propagation of an extra electron and an extra hole. In fact, the time evolution of the Green’s function is governed by the electron addition/removal energies from the N -electron ground-state (we move from a N to $N + 1$ description).

In the GW approximation⁵¹, we obtain that the self-energy Σ in terms of the single particle Green’s function G and \bar{W} , which is defined as the difference between screened and the bare Coulomb potential (i.e., $\bar{W} = W - V$), can be truncated after the first term: $\Sigma = iG\bar{W}$, where G and \bar{W} are calculated through the Hedin’s equations⁵¹. In principle Hedin’s equations have to be solved self-consistently, where in the first iteration $G^{(0)}$ is the non-interacting Green’s function constructed with the KS eigenenergies and eigenstates. However, we can perform only one GW iteration step, which is commonly referred to the G_0W_0 method.

After calculating the self-energy $\Sigma^{(0)}$, we can calculate the quasiparticle spectrum⁵²:

$$\varepsilon_{n\mathbf{k}}^{\text{QP}} = \varepsilon_{n\mathbf{k}} + Z_{n\mathbf{k}} \text{Re} \langle \varphi_{n\mathbf{k}} | \Sigma^{(0)}(\varepsilon_{n\mathbf{k}}) + V_x - V_{xc} | \varphi_{n\mathbf{k}} \rangle \quad (2.87)$$

where V_{xc} is the Kohn-Sham exchange-correlation potential, V_x is the nonlocal Hartree-Fock exchange potential (“bare” potential), and the renormalization factor $Z_{n\mathbf{k}}$ is given by:

$$Z_{n\mathbf{k}} = \left(1 - \text{Re} \langle \varphi_{n\mathbf{k}} | \frac{\partial}{\partial \omega} \Sigma^{(0)}(\omega) |_{\omega=\varepsilon_{n\mathbf{k}}} | \varphi_{n\mathbf{k}} \rangle \right)^{-1} \quad (2.88)$$

Finally, the orbital energies are updated from $\varepsilon_{n\mathbf{k}}$ to ε^{QP} . All in all, we map the true problem of N interacting electrons on a 1-body “quasiparticle” equation with a “self-energy”.

The scissor correction is another widely employed technique to address the discrepancy of band gaps⁵³. The scissor correction can be applied by referencing the band gap to either a more reliable theoretical value from G_0W_0 calculations⁵⁴ or an experimental value derived from optical measurements⁵⁵. The conduction band ground-state (GS) orbital energies are shifted by $\Delta\varepsilon^{\text{Scissor}}$:

$$\varepsilon_{n\mathbf{k}} = \varepsilon_{n\mathbf{k}}^{\text{DFT}} + (1 - f_{n\mathbf{k}}) \Delta\varepsilon^{\text{Scissor}} \quad (2.89)$$

where $f_{n\mathbf{k}}$ is the Fermi occupation factor equal to one for occupied states and zero for unoccupied states.

2.3.2 Optical properties

With a better description of energy orbitals by either using G_0W_0 or scissor operator, we can now focus on the methods to calculate optical responses of materials.

We can extend DFT in order to calculate excited states and time-dependent processes, such as transport phenomena and conduction⁵⁶, this approach is known as time-dependent density functional theory (TD-DFT). The generalization of the basic formalism of DFT to the time-dependent case is due to Runge, Gross and Kohn⁵⁷, who developed a method similar to the Hohenberg-Kohn-Sham theory for time-dependent potentials. This theorem establishes a one-to-one correspondence between the time-dependent electron density $\rho(\mathbf{r}, t)$ and the external potential $V_{ext}(\mathbf{r}, t)$. This implies that all observable properties of the system can be derived as functionals of the time-dependent density. Additionally, we can find the time-dependent Kohn-Sham equations⁵⁸:

$$\left[-\frac{1}{2}\nabla^2 + V_{tot}(\mathbf{r}, t) \right] \varphi_{n\mathbf{k}}(\mathbf{r}, t) = i \frac{\partial}{\partial t} \varphi_{n\mathbf{k}}(\mathbf{r}, t) \quad (2.90)$$

where

$$V_{tot}(\mathbf{r}, t) = V_{ext}(\mathbf{r}, t) + \int d\mathbf{r}' \frac{\rho(\mathbf{r}', t)}{\|\mathbf{r} - \mathbf{r}'\|} + V_{xc}(\mathbf{r}, t) + V_{ext}(\mathbf{r}, t) \quad (2.91)$$

We can use the linear response theory to study the effect of a small perturbation $V_{ext}(\mathbf{r}, t)$ on the system. In the linear approximation, the induced charge density is related to the external potential⁵⁹:

$$\rho_{ind}(\mathbf{r}, t) = \int d\mathbf{r}' \int dt' \chi_{\rho\rho}^{(1)}(\mathbf{r}, \mathbf{r}', t - t') V_{ext}(\mathbf{r}', t') \quad (2.92)$$

Here, $\chi_{\rho\rho}^{(1)}(\mathbf{r}, \mathbf{r}', t - t')$ is the microscopic, linear density response function, specifically formulated for the electron density in Time-Dependent Density Functional Theory (TD-DFT). It is important to note that TD-DFT deals primarily with longitudinal (scalar) perturbations, leading to a longitudinal response⁶⁰. A key distinction exists between the macroscopic susceptibility, $\chi_{ij}^{(1)}$, and the microscopic density response function, $\chi_{\rho\rho}^{(1)}$. While $\chi_{ij}^{(1)}$ captures both the longitudinal and transverse macroscopic responses, $\chi_{\rho\rho}^{(1)}$ only accounts for the longitudinal response at the microscopic level. We will explore how to extract both the longitudinal and transverse macroscopic responses from the microscopic longitudinal density response function.

In condensed matter theory, we frequently study systems represented by an independent-particle electronic structure subject to an external perturbation. In this case, the non-interacting density response function $\chi_{\rho\rho}^{(0)}$ is given by the following expression⁵⁹:

$$\chi_{\rho\rho}^{(0)}(\mathbf{r}, \mathbf{r}', \omega) = \sum_{\mathbf{k}, \mathbf{q}} \sum_{n, n'}^{\text{BZ}} \frac{f_{n\mathbf{k}} - f_{n'\mathbf{k}+\mathbf{q}}}{\omega + \varepsilon_{n\mathbf{k}} - \varepsilon_{n'\mathbf{k}+\mathbf{q}} + i\eta} \varphi_{n\mathbf{k}}^*(\mathbf{r}) \varphi_{n'\mathbf{k}+\mathbf{q}}(\mathbf{r}) \varphi_{n\mathbf{k}}(\mathbf{r}') \varphi_{n'\mathbf{k}+\mathbf{q}}^*(\mathbf{r}'), \quad (2.93)$$

where $f_{n\mathbf{k}}$ is the occupation number of the single-particle orbital. $\chi_{\rho\rho}^{(0)}$ describes the linear response of the non-interacting Kohn-Sham system, where $\varphi_{n\mathbf{k}}$ is the Kohn-Sham wave functions. We can express $\chi_{\rho\rho}^{(0)}$ in a plane-wave representation for translation invariant systems, where the Fourier coefficients, derived by Adler⁶¹ and Wiser⁶², are given by:

$$\left[\chi_{\rho\rho}^{(0)}(\mathbf{q}, \omega) \right]_{\mathbf{G}\mathbf{G}'} = \frac{1}{\Omega} \sum_{\mathbf{k}} \sum_{n, m}^{\text{BZ}} \frac{f_{n\mathbf{k}} - f_{m\mathbf{k}+\mathbf{q}}}{\omega + \varepsilon_{n\mathbf{k}} - \varepsilon_{m\mathbf{k}+\mathbf{q}} + i\eta} \langle \varphi_{n\mathbf{k}} | e^{-i(\mathbf{q}+\mathbf{G})\cdot\mathbf{r}} | \varphi_{m\mathbf{k}+\mathbf{q}} \rangle \langle \varphi_{m\mathbf{k}+\mathbf{q}} | e^{i(\mathbf{q}+\mathbf{G}')\cdot\mathbf{r}'} | \varphi_{n\mathbf{k}} \rangle \quad (2.94)$$

The interacting density response function $\chi_{\rho\rho}^{(1)}$ is connected to the non-interacting response function via the Dyson-like equation⁵⁸:

$$\chi_{\rho\rho}^{(1)} = \chi_{\rho\rho}^{(0)} + \chi_{\rho\rho}^{(0)} (V + f_{xc}) \chi_{\rho\rho}^{(1)} \quad (2.95)$$

This can be written more explicitly as:

$$\begin{aligned} \chi_{\rho\rho}^{(1)}(\mathbf{r}, \mathbf{r}', \omega) &= \chi_{\rho\rho}^{(0)}(\mathbf{r}, \mathbf{r}', \omega) \\ &+ \int d\mathbf{r}'' \int d\mathbf{r}''' \left[\chi_{\rho\rho}^{(0)}(\mathbf{r}, \mathbf{r}'', \omega) \left(V(\mathbf{r}'', \mathbf{r}''') + f_{xc}(\mathbf{r}'', \mathbf{r}''', \omega) \right) \chi_{\rho\rho}^{(1)}(\mathbf{r}''', \mathbf{r}', \omega) \right] \end{aligned} \quad (2.96)$$

Here, V and f_{xc} represent the Coulomb and exchange-correlation interaction. A frequently used approximation to solve equation (2.95) is the Random Phase Approximation (RPA). In essence, RPA treats the exchange-correlation term, f_{xc} , as zero. This simplification leads equation (2.95) to the following form:

$$\chi_{\rho\rho}^{(1)} = \chi_{\rho\rho}^{(0)} + \chi_{\rho\rho}^{(0)} V \chi_{\rho\rho}^{(1)} \quad (2.97)$$

By Fourier transform, equation (2.96) in reciprocal space becomes⁶³:

$$\left[\chi_{\rho\rho}^{(1)}(\mathbf{q}, \omega) \right]_{\mathbf{G}\mathbf{G}'} = \left[\chi_{\rho\rho}^{(0)}(\mathbf{q}, \omega) \right]_{\mathbf{G}\mathbf{G}'} + \sum_{\mathbf{G}_1\mathbf{G}_2} \left[\chi_{\rho\rho}^{(0)}(\mathbf{q}, \omega) \right]_{\mathbf{G}\mathbf{G}_1} \left(V_{\mathbf{G}_1\mathbf{G}_2}(\mathbf{q}) \right) \left[\chi_{\rho\rho}^{(1)}(\mathbf{q}, \omega) \right]_{\mathbf{G}_2\mathbf{G}'} \quad (2.98)$$

where $V_{\mathbf{G}_1\mathbf{G}_2}(\mathbf{q})$ is given by:

$$V_{\mathbf{G}_1\mathbf{G}_2}(\mathbf{q}) = \frac{4\pi}{|\mathbf{q} + \mathbf{G}_1|^2} \delta_{\mathbf{G}_1\mathbf{G}_2} \quad (2.99)$$

This is the Coulomb potential in the reciprocal space.

With a description of the full interacting response function in terms of the non-interacting response function, we can obtain the dielectric matrix through the following expression⁵⁸:

$$\left[\epsilon_{\rho\rho}^{-1}(\mathbf{q}, \omega) \right]_{\mathbf{G}\mathbf{G}'} = \delta_{\mathbf{G}\mathbf{G}'} + \frac{4\pi}{|\mathbf{q} + \mathbf{G}|^2} \left[\chi_{\rho\rho}^{(1)}(\mathbf{q}, \omega) \right]_{\mathbf{G}\mathbf{G}'} \quad (2.100)$$

Using the RPA, equation (2.100) is given in terms of the non-interacting response function as follows:

$$\left[\epsilon_{\rho\rho}^{\text{RPA}}(\mathbf{q}, \omega) \right]_{\mathbf{G}\mathbf{G}'} = \delta_{\mathbf{G}\mathbf{G}'} - \frac{4\pi}{|\mathbf{q} + \mathbf{G}|^2} \left[\chi_{\rho\rho}^{(0)}(\mathbf{q}, \omega) \right]_{\mathbf{G}\mathbf{G}'} \quad (2.101)$$

In equation (2.100), we may perform the matrix inversion of the dielectric matrix element by element. In RPA, we assume that the phase of the off-diagonal elements are randomized so that the inverse of the matrix is the inverse of its elements. Recalling the distinction between reciprocal and real space, $\left[\epsilon_{\rho\rho}^{\text{RPA}}(\mathbf{q}, \omega) \right]_{\mathbf{G}\mathbf{G}'}$ represents a matrix in reciprocal space containing coefficients of the Fourier expansion. In contrast, the real space counterpart is a scalar function, specifically the longitudinal dielectric function.

We can obtain the macroscopic longitudinal dielectric function using equation (2.101) as follows:

$$\epsilon^L(\mathbf{q}, \omega) = \frac{1}{\left[\epsilon_{\rho\rho}^{-1}(\mathbf{q}, \omega) \right]_{\mathbf{G}=0 \mathbf{G}'=0}} \quad (2.102)$$

However, equation (2.102) is not directly applicable for second-harmonic generation (SHG) because it deals with transverse electric fields. We calculate the linear optical parameters in the dipole approximation (where $\mathbf{q} \rightarrow 0$) to calculate the macroscopic transverse dielectric functions. In this limit, we can find 3 axis XYZ , defining a frame in which the macroscopic dielectric tensor is diagonal ϵ_{ij} . Applying a longitudinal field (\mathbf{E}) parallel to one of these axis leads to three quantities:

$$\epsilon_{XX}(\omega) = \lim_{\mathbf{q} \rightarrow 0} \epsilon^L(\mathbf{q}, \omega) = \lim_{\mathbf{q} \rightarrow 0} \frac{1}{[\epsilon_{\rho\rho}^{-1}(\mathbf{q}, \omega)]_{\mathbf{G}=0 \ \mathbf{G}'=0}} \quad \mathbf{E} \text{ along } X \quad (2.103a)$$

$$\epsilon_{YY}(\omega) = \lim_{\mathbf{q} \rightarrow 0} \epsilon^L(\mathbf{q}, \omega) = \lim_{\mathbf{q} \rightarrow 0} \frac{1}{[\epsilon_{\rho\rho}^{-1}(\mathbf{q}, \omega)]_{\mathbf{G}=0 \ \mathbf{G}'=0}} \quad \mathbf{E} \text{ along } Y \quad (2.103b)$$

$$\epsilon_{ZZ}(\omega) = \lim_{\mathbf{q} \rightarrow 0} \epsilon^L(\mathbf{q}, \omega) = \lim_{\mathbf{q} \rightarrow 0} \frac{1}{[\epsilon_{\rho\rho}^{-1}(\mathbf{q}, \omega)]_{\mathbf{G}=0 \ \mathbf{G}'=0}} \quad \mathbf{E} \text{ along } Z \quad (2.103c)$$

For example, when the direction of propagation is along the X -axis, ϵ_{XX} is the macroscopic longitudinal dielectric function, while ϵ_{YY} and ϵ_{ZZ} are the macroscopic transverse dielectric functions when $\mathbf{q} \rightarrow 0$.

To calculate the nonlinear optical parameters, we employ the theory developed by Sharma and Ambrosch-Draxl¹⁷. This framework allows us to express the second-order susceptibility as^{17,64}:

$$\chi_{ijk}^{(2)}(-2\omega; \omega, \omega) = \chi_{ijk}^{\text{inter}}(-2\omega; \omega, \omega) + \chi_{ijk}^{\text{intra}}(-2\omega; \omega, \omega) + \chi_{ijk}^{\text{mod}}(-2\omega; \omega, \omega) \quad (2.104)$$

where i, j, k are Cartesian coordinate, and $\chi_{ijk}^{\text{inter}}$, $\chi_{ijk}^{\text{intra}}$, and χ_{ijk}^{mod} represent the interband transitions, the intraband transitions, and the modulation of the interband terms by intraband terms.

In this case, Sharma and Ambrosch-Draxl¹⁷ obtain expressions for each of those terms by averaging based on the quantum mechanical point of view. Therefore, we can compare directly with experiment after calculating equation (2.104). Specifically, the interband term is given by⁶⁴:

$$\begin{aligned} \chi_{ijk}^{\text{inter}}(-2\omega; \omega, \omega) = & \frac{1}{\Omega} \sum_{n,m} \sum_{\substack{l \\ l \neq n,m}} \sum_{\mathbf{k}} w_{\mathbf{k}} \left[\frac{2r_{nm\mathbf{k}}^i \{r_{ml\mathbf{k}}^j r_{ln\mathbf{k}}^k\}}{(\varepsilon_{ln\mathbf{k}} - \varepsilon_{ml\mathbf{k}})(\varepsilon_{mn\mathbf{k}} - 2\omega)} \right. \\ & \left. - \frac{1}{\varepsilon_{mn\mathbf{k}} - \omega} \left[\frac{r_{lm\mathbf{k}}^k \{r_{mn\mathbf{k}}^i r_{nl\mathbf{k}}^j\}}{\varepsilon_{nl\mathbf{k}} - \varepsilon_{mn\mathbf{k}}} - \frac{r_{nl\mathbf{k}}^j \{r_{lm\mathbf{k}}^k r_{mn\mathbf{k}}^i\}}{\varepsilon_{lm\mathbf{k}} - \varepsilon_{mn\mathbf{k}}} \right] \right] \end{aligned} \quad (2.105)$$

where Ω is the unit cell volume, $w_{\mathbf{k}}$ is the weight of \mathbf{k} -point, n denotes the valence states, m the conduction states and l denotes all states ($l \neq n, m$). Additionally, $\varepsilon_{nm\mathbf{k}}$ represents the energy difference between energy orbital n and energy orbital m at \mathbf{k} : $\varepsilon_{n\mathbf{k}} - \varepsilon_{m\mathbf{k}}$. Regarding the intraband and modulation of the interband terms by intraband

terms, they are given by⁶⁴:

$$\begin{aligned} \chi_{ijk}^{\text{intra}}(-2\omega; \omega, \omega) = & \frac{1}{\Omega} \sum_{\mathbf{k}} w_{\mathbf{k}} \left[\sum_{n,m} \sum_{\substack{l \\ l \neq n,m}} \frac{1}{\varepsilon_{mn\mathbf{k}}^2 (\varepsilon_{mn\mathbf{k}} - \omega)} \left[\varepsilon_{ln\mathbf{k}} r_{nl\mathbf{k}}^j \{r_{lm\mathbf{k}}^k r_{mn\mathbf{k}}^i\} - \varepsilon_{ml\mathbf{k}} r_{lm\mathbf{k}}^k \{r_{mn\mathbf{k}}^i r_{nl\mathbf{k}}^j\} \right] \right. \\ & + 2 \sum_{n,m} \sum_{\substack{l \\ l \neq n,m}} \frac{r_{nm\mathbf{k}}^i \{r_{ml\mathbf{k}}^j r_{ln\mathbf{k}}^k\} (\varepsilon_{ml\mathbf{k}} - \varepsilon_{ln\mathbf{k}})}{\varepsilon_{mn\mathbf{k}}^2 (\varepsilon_{mn\mathbf{k}} - 2\omega)} \\ & \left. - 8i \sum_{nm} \frac{1}{\varepsilon_{mn\mathbf{k}}^2 (\varepsilon_{mn\mathbf{k}} - 2\omega)} r_{nm\mathbf{k}}^i \{r_{ml\mathbf{k}}^j r_{ln\mathbf{k}}^k\} \right] \end{aligned} \quad (2.106a)$$

$$\begin{aligned} \chi_{ijk}^{\text{mod}}(-2\omega; \omega, \omega) = & \frac{1}{\Omega} \sum_{\mathbf{k}} w_{\mathbf{k}} \left[\sum_{n,m} \sum_{\substack{l \\ l \neq n,m}} \frac{1}{\varepsilon_{mn\mathbf{k}}^2 (\varepsilon_{mn\mathbf{k}} - \omega)} \left[\varepsilon_{nl\mathbf{k}} r_{lm\mathbf{k}}^i \{r_{mn\mathbf{k}}^j r_{nl\mathbf{k}}^k\} - \varepsilon_{lm\mathbf{k}} r_{nl\mathbf{k}}^i \{r_{lm\mathbf{k}}^j r_{mn\mathbf{k}}^k\} \right] \right. \\ & \left. - i \sum_{n,m} \frac{r_{nm\mathbf{k}}^i \{r_{mn\mathbf{k}}^j \Delta_{mn\mathbf{k}}^k\}}{\varepsilon_{mn\mathbf{k}}^2 (\varepsilon_{mn\mathbf{k}} - \omega)} \right] \end{aligned} \quad (2.106b)$$

The symbols are defined as:

$$\Delta_{mn\mathbf{k}}^i = v_{mm\mathbf{k}}^i - v_{nn\mathbf{k}}^i \quad (2.107)$$

with $v_{nm\mathbf{k}}^i$ being the i component of the electron velocity given by:

$$v_{nm\mathbf{k}}^i = i\varepsilon_{nm\mathbf{k}} r_{nm\mathbf{k}}^i \quad (2.108)$$

and

$$\{r_{nm\mathbf{k}}^i r_{ml\mathbf{k}}^j\} = \frac{1}{2} \left(r_{nm\mathbf{k}}^i r_{ml\mathbf{k}}^j + r_{nm\mathbf{k}}^j r_{ml\mathbf{k}}^i \right) \quad (2.109)$$

The position matrix elements between states n and m ($r_{nm\mathbf{k}}^i$) are calculated from the momentum matrix element $p_{nm\mathbf{k}}^i$ using the relation:

$$r_{nm\mathbf{k}}^i = -i \frac{p_{nm\mathbf{k}}^i}{\varepsilon_{nm\mathbf{k}}} \quad (2.110)$$

for all $\varepsilon_{n\mathbf{k}} \neq \varepsilon_{m\mathbf{k}}$ and $r_{nm\mathbf{k}}^i = 0$ otherwise.

In principle, we can evaluate equation (2.104) on the basis of DFT. We will take this approach to obtain the second-order nonlinear susceptibility for LiNbO₃.

Upon all the descriptions provided in this chapter, the nonlinear wave propagation process in uniaxial crystals for SHG is studied in the following chapters.

Chapter 3

SHG in crystals: Variations in Space and Time

This chapter is divided into two main sections. First, a review is provided on how nonlinearity in wave propagation within uniaxial crystals is addressed, as demonstrated by D. Eimerl and collaborators⁶⁵. A re-derivation of the main results from such approach can be found in Appendix A. In addition, building upon this theory, temporal effects are considered using a perturbation approach through Taylor Series, closely following the methodology presented in "Fundamentals of Nonlinear Optics" (Chapter 10) by P. Powers and J. Haus³. Secondly, different criteria for handling space- and time-related effects are discussed, alongside the introduction of a simple model based on plane-wave geometry and an analysis of a conventional light-conversion experiment.

3.1 Wave Equations with Nonlinear source

In this section, we will establish the wave equations governing the propagation of ordinary or extraordinary waves within a uniaxial crystal, such as LiNbO₃. As previously stated in Chapter 2, we will use the Cartesian coordinate system XYZ for the principal dielectric axes of the crystal. Additionally, we will introduce a new coordinate system xyz , which will label coordinates with respect to the propagation system. For example, \mathcal{E}_X and \mathcal{E}_x denote the components of a vector $\mathcal{E}(\mathbf{r}, t)$ along the axes X and x , respectively. Purposely, a sum over repeated indices is implied.

Moreover, second harmonic generation (SHG) process mainly involves two frequencies: the fundamental frequency, denoted as $\omega_f = \omega_0$, and the harmonic frequency, denoted as $\omega_{\text{SHG}} = 2\omega_0$. Thus $\mathcal{E}_{X\omega_0}$ and $\mathcal{E}_{x\omega_0}$ denote the components of a vector \mathcal{E} along the axes X and x for the fundamental frequency, respectively. Having stated these comments on notation, we will now focus on developing wave equations with emphasis on modelling continuous (spatial effects) and pulsed (temporal effects) sources of light.

3.1.1 Spatial effects in wave propagation

Studying the production of second-harmonic waves within uniaxial crystals entails primarily the following equations for nonconducting media (see Chapter 2, Sec. 2.1.1):

$$\nabla \times \mathbf{H}(\mathbf{r}, t) - \frac{\partial}{\partial t} \mathbf{H}(\mathbf{r}, t) = 0 \quad (3.1a)$$

$$\nabla \times \mathbf{E}(\mathbf{r}, t) + \mu_0 \frac{\partial}{\partial t} \mathbf{H}(\mathbf{r}, t) = 0 \quad (3.1b)$$

$$\nabla \cdot \mathbf{D}(\mathbf{r}, t) = 0 \quad (3.1c)$$

Purposely, $\nabla \cdot \mathbf{B} = 0$ is not taken into account because the focus is on the electric field. However, if one intends to compute the wave propagation for the magnetic field, then $\nabla \cdot \mathbf{B} = 0$ should be considered instead of equation (3.1c). On elimination of \mathbf{H} from equations (3.1a) and (3.1b), one obtains:

$$\nabla \times \nabla \times \mathbf{E}(\mathbf{r}, t) + \mu_0 \frac{\partial^2}{\partial t^2} \mathbf{D}(\mathbf{r}, t) = 0 \quad (3.2)$$

Moreover, the fields \mathbf{D} and \mathbf{E} are related by the following expression:

$$\mathbf{D}(\mathbf{r}, t) = \epsilon_0 \mathbf{E}(\mathbf{r}, t) + \mathbf{P}(\mathbf{r}, t) \quad (3.3)$$

One can decompose the displacement field into its linear and nonlinear parts: $\mathbf{D} = \mathbf{D}^{(1)} + \mathbf{D}^{\text{NL}}$, where $\mathbf{D}^{(1)} = \epsilon_0 \mathbf{E} + \mathbf{P}^{(1)}$ and \mathbf{P}^{NL} is the nonlinear polarization given by the expression (2.24) up to the second-order term. Consequently, equation (3.3) becomes:

$$\mathbf{D}(\mathbf{r}, t) = \epsilon_0 \mathbf{E}(\mathbf{r}, t) + \mathbf{P}^{(1)}(\mathbf{r}, t) + \mathbf{P}^{\text{NL}}(\mathbf{r}, t) \quad (3.4)$$

In terms of this quantity, the wave equation (3.2) for nonconducting media can be written as:

$$\nabla \times \nabla \times \mathbf{E}(\mathbf{r}, t) = -\mu_0 \frac{\partial^2}{\partial t^2} \left(\epsilon_0 \mathbf{E}(\mathbf{r}, t) + \mathbf{P}^{(1)}(\mathbf{r}, t) + \mathbf{P}^{\text{NL}}(\mathbf{r}, t) \right) \quad (3.5)$$

Eimerl et al.⁶⁵ conducted a theoretical investigation into the second-harmonic process using equation (3.5) within a time-independent formulation, which entails that the envelope does not depend on time. They write the components of \mathbf{E} as follows:

$$E_j = \frac{1}{2} \sum_{\omega_\ell} \mathcal{E}_{j\omega_\ell}(\mathbf{r}) \exp(-i\omega_\ell t) + \text{c.c.} \quad (3.6)$$

where j can take the values X , Y , and Z , and ω_ℓ corresponds to the frequency component involved in the nonlinear process. In this case, $\mathcal{E}_{j\omega_\ell}$ solely depends on space (i.e., \mathbf{r}). Regarding the linear polarization, this quantity is expressed as follows:

$$P_j^{(1)} = \frac{1}{2} \epsilon_0 \sum_{\omega_\ell} \chi_{jk}^{(1)}(\omega_\ell) \mathcal{E}_{k\omega_\ell}(\mathbf{r}) \exp(-i\omega_\ell t) + \text{c.c} \quad (3.7)$$

where $j, k = X, Y, Z$. $\chi_{jk}^{(1)}(\omega_\ell)$ stands for the linear susceptibility tensor for the frequency component ω_ℓ ; in connection with the nonlinear polarization, its vector components are given by:

$$P_j^{\text{NL}} = \frac{1}{2} \epsilon_0 \sum_{\omega_\ell} \mathcal{P}_{j\omega_\ell}^{\text{NL}}(\mathbf{r}) \exp(-i\omega_\ell t) + \text{c.c} \quad (3.8)$$

Building upon equations (3.5) to (3.8), Eimerl et al. derived a system of differential equations with respect to the principal coordinate system XYZ that describes each vector component of the electric field propagating within uniaxial crystals. These equations (they are detailed in Appendix A; see equations (A.13) for reference) can be written compactly as follows:

$$\nabla^2 \mathcal{E}_{\omega_\ell} + \frac{\omega_\ell^2}{c^2} \underline{\underline{\epsilon}}(\omega_\ell) \cdot \mathcal{E}_{\omega_\ell} - \beta_{\omega_\ell} \nabla \left(\hat{Z} \cdot \nabla \right) \left(\mathcal{E}_{\omega_\ell} \cdot \hat{Z} \right) = -\frac{\omega_\ell^2}{c^2} \mathcal{P}_{\omega_\ell}^{\text{NL}} \quad (3.9)$$

In this equation, $\underline{\underline{\epsilon}}$ is the dielectric tensor. With respect to the coordinate system XYZ , this tensor can be written as follows:

$$\underline{\underline{\epsilon}}(\omega_\ell) = \begin{pmatrix} \epsilon_{XX}(\omega_\ell) & 0 & 0 \\ 0 & \epsilon_{XX}(\omega_\ell) & 0 \\ 0 & 0 & \epsilon_{ZZ}(\omega_\ell) \end{pmatrix} = \begin{pmatrix} n_o^2(\omega_\ell) & 0 & 0 \\ 0 & n_o^2(\omega_\ell) & 0 \\ 0 & 0 & n_e^2(\omega_\ell) \end{pmatrix} \quad (3.10)$$

In this context, n_e represents the extraordinary index of refraction for an electric field polarized parallel to the optical axis (n_{\parallel}), while n_o refers to the ordinary index of refraction for an electric field polarized perpendicular to the optical axis (n_{\perp}). As mentioned in Chapter 2, the dependence on the Z -direction (\hat{Z}) arises from the specification of the dielectric tensor, which entails that the Z -axis aligns with the optical axis. Although the letter Z itself is not important, aligning it with the optical axis is critical.

Moreover, the factor β_{ω_ℓ} takes into account the anisotropy of the materials through the index of refraction:

$$\beta_{\omega_\ell} = 1 - \frac{n_e^2(\omega_\ell)}{n_o^2(\omega_\ell)} \quad (3.11)$$

Eimerl et al. adopted the method of Fleck and Feit²⁷ to account for the optical anisotropy, resulting in the common factor (β_{ω_ℓ}). The β_{ω_ℓ} parameter is a consequence of the anisotropy of uniaxial materials, where we have different index of refraction when light propagates along or perpendicular to the optical axis*. However, unlike the equations presented in Chapter 2 for uniaxial crystals, the right-hand side of equation (3.9) includes a non-zero term, which is the nonlinear source.

Figure 3.1 illustrates the scenario where a fundamental wave interacts with the surface of a nonlinear medium. This interaction leads to the transmission of the fundamental wave and the generation of a harmonic wave. Eimerl et al.⁶⁵ focus on the scenario where the transmitted fundamental wave and the harmonic wave propagate collinearly, as depicted in Figure 3.1(a). Eimerl and collaborators not only express the fields in the coordinate system XYZ , but also define an additional coordinate system xyz (depicted in blue in Figure 3.1(b)) to analyze the impact of the direction of the wave vector on wave propagation in uniaxial crystals. Readers interested in the work conducted

*This relationship appears when evaluating the displacement vector in the following equation: $\nabla \cdot \mathbf{D} = 0$. See Appendix A for further details.

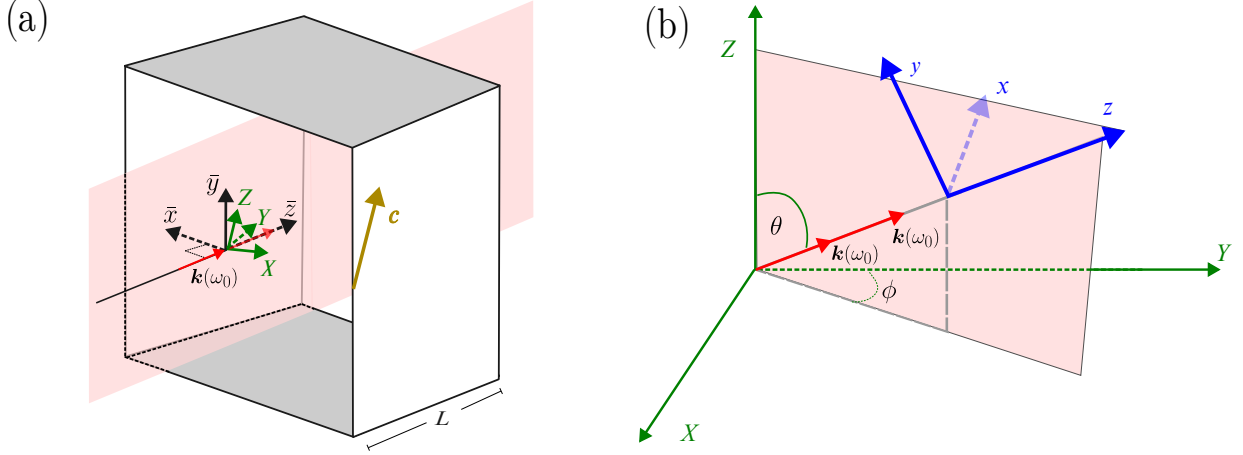


Figure 3.1: (a) The experimental geometry for second-harmonic generation (SHG) in this case is based on a plane of light incident parallel (depicted in pink) to the optical axis (c). The coordinate system $\bar{x}\bar{y}\bar{z}$ is defined as the laboratory system. $\mathbf{k}(\omega_0)$ is normal to the surface of the nonlinear medium. (b) The relationship between the plane of incidence and the diverse coordinate systems employed by Eimerl et al.⁶⁵. The XYZ coordinate system (depicted in dark green) corresponds to the principal coordinate system. The xyz coordinate system (depicted in blue) is defined in the crystal, with the z -axis aligning with the direction of propagation of the transmitted fundamental and harmonic electric field.

by Eimerl and collaborators are encouraged to refer directly to their original paper. The Appendix A in this thesis provides a detailed re-derivation of their equations, including intermediary steps omitted in the original publication.

Through a transformation operation, we can map the coordinate system XYZ to the propagation system xyz (See equation (A.14)). This transformation allows us to derive wave equations for ordinary and extraordinary waves within the xyz system. In the case of ordinary waves, the electric field vector is described completely by X and Y as pointed out in Chapter 2, Section 2.1.1. Consequently, the wave equation for ordinary waves in the xyz system simplifies to:

$$\left(\frac{\partial^2}{\partial x^2} + \frac{\partial^2}{\partial y^2}\right)F_{X\omega_\ell}^o + 2in_o(\omega_\ell)\frac{\omega_\ell}{c}\frac{\partial F_{X\omega_\ell}^o}{\partial z} \cong -\frac{\omega_\ell^2}{\epsilon_0 c^2}\mathcal{P}_{X\omega_\ell}^{\text{NL}} \exp\left(-i\frac{n_o(\omega_\ell)\omega_\ell}{c}z\right) \quad (3.12a)$$

$$\left(\frac{\partial^2}{\partial x^2} + \frac{\partial^2}{\partial y^2}\right)F_{Y\omega_\ell}^o + 2in_o(\omega_\ell)\frac{\omega_\ell}{c}\frac{\partial F_{Y\omega_\ell}^o}{\partial z} \cong -\frac{\omega_\ell^2}{\epsilon_0 c^2}\mathcal{P}_{Y\omega_\ell}^{\text{NL}} \exp\left(-i\frac{n_o(\omega_\ell)\omega_\ell}{c}z\right) \quad (3.12b)$$

where Eimerl et al.⁶⁵ parameterize ordinary waves as follows:

$$\mathcal{E}_{X\omega_\ell}(x, y, z) = F_{X\omega_\ell}^o(x, y, z) \exp\left(i\frac{n_o(\omega_\ell)\omega_\ell}{c}z\right) \quad (3.13a)$$

$$\mathcal{E}_{Y\omega_\ell}(x, y, z) = F_{Y\omega_\ell}^o(x, y, z) \exp\left(i\frac{n_o(\omega_\ell)\omega_\ell}{c}z\right) \quad (3.13b)$$

In the case of extraordinary waves, they focus on its Z -component which satisfy the following equation (refer to Appendix A for details in the derivations of this equation):

$$\begin{aligned} \frac{\partial^2 F_{Z\omega_\ell}^e}{\partial x^2} + \left[1 - \beta_{\omega_\ell} \sin^2(\theta)\right] \frac{\partial^2 F_{Z\omega_\ell}^e}{\partial y^2} + 2in_e(\omega_\ell) \frac{\omega_\ell}{c} \left[1 - \beta_{\omega_\ell} \cos^2(\theta)\right]^{\frac{1}{2}} \left[\frac{\partial F_{Z\omega_\ell}^e}{\partial z} + \rho_{\omega_\ell}(\theta) \frac{\partial \tilde{F}_{Z\omega_\ell}^e}{\partial y} \right] \\ \cong - \frac{\omega_\ell^2}{\epsilon_0 c^2} \mathcal{P}_{Z\omega_\ell}^{\text{NL}} \exp\left(-i \frac{n_e(\omega_\ell, \theta) \omega_\ell}{c} z\right) \end{aligned} \quad (3.14)$$

where n_e depends on θ because the propagation is neither parallel nor perpendicular to the optical axis, and this angle introduces a dependency on the extraordinary index of refraction (see equation (2.21)). Consequently, the parameterization for the extraordinary wave is written as follows:

$$\mathcal{E}_{Z\omega_\ell}(x, y, z) = F_{Z\omega_\ell}^e(x, y, z) \exp\left(i \frac{n_e(\omega_\ell, \theta) \omega_\ell}{c} z\right) \quad (3.15)$$

The parameter $\rho_{\omega_\ell}(\theta)$ is written in term of θ and β_{ω_ℓ} as follows:

$$\rho_{\omega_\ell}(\theta) = -\frac{\frac{\beta_{\omega_\ell}}{2} \sin(2\theta)}{1 - \beta_{\omega_\ell} \cos^2(\theta)} \quad (3.16)$$

For the sake of clarity, equations (3.12) and (3.14) illustrate the spatial evolution of waves propagating along the z -axis, taking into account factors such as diffraction, walk-off, and nonlinearity:

$$\underbrace{\left(\frac{\partial^2}{\partial x^2} + \frac{\partial^2}{\partial y^2}\right) F_{X\omega_\ell}^o + 2in_o(\omega_\ell) \frac{\omega_\ell}{c} \frac{\partial F_{X\omega_\ell}^o}{\partial z}}_{\text{Diffraction}} \cong \underbrace{- \frac{\omega_\ell^2}{\epsilon_0 c^2} \mathcal{P}_{X\omega_\ell}^{\text{NL}} \exp\left(-i \frac{n_o(\omega_\ell) \omega_\ell}{c} z\right)}_{\text{Nonlinearity}} \quad (3.17a)$$

$$\begin{aligned} \underbrace{\frac{\partial^2 F_{Z\omega_\ell}^e}{\partial x^2} + \left[1 - \beta_{\omega_\ell} \sin^2(\theta)\right] \frac{\partial^2 F_{Z\omega_\ell}^e}{\partial y^2}}_{\text{Diffraction}} + 2in_e(\omega_\ell) \frac{\omega_\ell}{c} \left[1 - \beta_{\omega_\ell} \cos^2(\theta)\right]^{\frac{1}{2}} \left[\frac{\partial F_{Z\omega_\ell}^e}{\partial z} + \underbrace{\rho_{\omega_\ell}(\theta) \frac{\partial F_{Z\omega_\ell}^e}{\partial y}}_{\text{Walk-off}} \right] \\ \cong \underbrace{- \frac{\omega_\ell^2}{\epsilon_0 c^2} \mathcal{P}_{Z\omega_\ell}^{\text{NL}} \exp\left(-i \frac{n_e(\omega_\ell, \theta) \omega_\ell}{c} z\right)}_{\text{Nonlinearity}} \end{aligned} \quad (3.17b)$$

These equations are known as the coupled amplitude equations[†]. Through nonlinear polarization, the fundamental and harmonic waves are connected with each other (see the definition of nonlinear polarization in Chapter 2). Section 3.2 provides approaches to estimate the impact of each of the indicated terms in equations (3.17).

3.1.2 Temporal effects in wave propagation[‡]

To complement the discussions in this section, Appendix A (Section A.2) provides a detailed derivation of each equation presented here. This appendix section focuses specifically on the calculations, offering a step-by-step

[†]These equations are derived using the slowly varying envelope (SVE) approximation, which is why the approximation symbol appears. Details on the SVE approximation can be found in Appendix A.

[‡]This work was performed in collaboration with Dr. Dietrich Krebs.

approach.

The wave propagation equations derived by Eimerl et al. do not incorporate temporal effects. These effects become crucial when dealing with pulsed light sources, such as pulsed lasers. To address this limitation, we incorporate the methodology developed by Peter E. Powers and Joseph W. Haus³, [pp. 348-355] within the framework established in Ref. 18. This involves redefining the parameterization of the total electric field:

$$\begin{aligned}\mathbf{E}(\mathbf{r}, t) &= \sum_{\omega_\ell} \mathbf{E}_{\omega_\ell}(\mathbf{r}, t) \\ &= \sum_{\omega_\ell} \frac{1}{2} \mathcal{E}_{\omega_\ell}(\mathbf{r}, t) \exp(-i\omega_\ell t) + \text{c.c.}\end{aligned}\quad (3.18)$$

where ω_ℓ represents the carrier frequencies involved in the nonlinear process. The carrier frequency is defined as follows³:

$$\omega_\ell = \frac{\int_0^\infty d\omega \omega |\tilde{\mathbf{E}}_{\omega_\ell}(\omega)|^2}{\int_0^\infty d\omega |\tilde{\mathbf{E}}_{\omega_\ell}(\omega)|^2} \quad (3.19)$$

where $\tilde{\mathbf{E}}_{\omega_\ell}(\omega)$ is the Fourier transform of $\mathbf{E}_{\omega_\ell}(\mathbf{r}, t)$. This equation essentially calculates a weighted average of the angular frequencies ω based on their power densities $|\tilde{\mathbf{E}}_{\omega_\ell}(\omega)|^2$.

Equation (3.18) employs a parameterization that isolates the rapidly varying temporal component of \mathbf{E}_{ω_ℓ} . This component is represented by the term $\exp(-i\omega_\ell t)$, while the remaining, slowly varying contribution is denoted by $\mathcal{E}_{\omega_\ell}(\mathbf{r}, t)$.

Building upon this new description of the electric field (3.18), we can now examine the role of time in governing wave propagation within uniaxial crystals through the wave equation:

$$\nabla \times \nabla \times \mathbf{E}(\mathbf{r}, t) = -\mu_0 \frac{\partial^2}{\partial t^2} \left(\epsilon_0 \mathbf{E}(\mathbf{r}, t) + \mathbf{P}^{(1)}(\mathbf{r}, t) + \mathbf{P}^{\text{NL}}(\mathbf{r}, t) \right) \quad (3.20)$$

The main goal is to study the contribution of the envelope $\mathcal{E}_{\omega_\ell}(\mathbf{r}, t)$ in the frequency representation of the electric field (i.e., spectral components). Hence, the strategy is to Fourier decompose the electric field, which entails decomposing the envelope:

$$\mathbf{E}(\mathbf{r}, t) = \frac{1}{2\pi} \left(\sum_{\omega_\ell} \int_{-\infty}^{+\infty} d\omega' \frac{1}{2} \tilde{\mathcal{E}}_{\omega_\ell}(\mathbf{r}, \omega') \exp(-i\omega' t) \right) \exp(-i\omega_\ell t) + \text{c.c.} \quad (3.21)$$

In line with the description of the electric field (3.18), we can represent the linear and nonlinear polarization in a similar form:

$$\mathbf{P}^{(1)}(\mathbf{r}, t) = \frac{\epsilon_0}{4} \left(\sum_{\omega_\ell} \int_{-\infty}^{+\infty} d\omega' \underline{\chi}^{(1)}(-\omega_\ell; \omega_\ell + \omega') \tilde{\mathcal{E}}_{\omega_\ell}(\mathbf{r}, \omega') \exp(-i\omega' t) \right) \exp(-i\omega_\ell t) + \text{c.c.} \quad (3.22a)$$

$$\mathbf{P}^{\text{NL}}(\mathbf{r}, t) = \frac{1}{2\pi} \left(\sum_{\omega_\ell} \int_{-\infty}^{+\infty} d\omega' \frac{1}{2} \tilde{\mathcal{P}}_{\omega_\ell}^{\text{NL}}(\mathbf{r}, \omega') \exp(-i\omega' t) \right) \exp(-i\omega_\ell t) + \text{c.c.} \quad (3.22b)$$

Building up the equations (3.21) and (3.22), we can incorporate them into the wave equation (3.18); this substitution yields the following vector representation[§]:

$$\nabla^2 \tilde{\mathcal{E}}_{\omega_\ell}(\mathbf{r}, \omega - \omega_\ell) + \frac{\omega^2}{c^2} \underline{\underline{\epsilon}}(\omega) \cdot \tilde{\mathcal{E}}_{\omega_\ell}(\mathbf{r}, \omega - \omega_\ell) - \beta'_\omega \nabla \left(\hat{Z} \cdot \nabla \right) \left(\tilde{\mathcal{E}}_{\omega_\ell}(\mathbf{r}, \omega - \omega_\ell) \cdot \hat{Z} \right) = -\frac{\omega_\ell^2}{c^2} \tilde{\mathcal{P}}_{\omega_\ell}^{\text{NL}}(\mathbf{r}, \omega - \omega_\ell) \quad (3.23)$$

where

$$\beta'_\omega = 1 - \frac{n_e^2(\omega)}{n_o^2(\omega)} \quad (3.24)$$

A crucial distinction lies between parameters β_ω and β_{ω_ℓ} (defined in equation (A.11)). While β_{ω_ℓ} has a specific value for each discrete frequency ω_ℓ , this parameter is continuous.

We can now investigate the influence of the bandwidth on equation (3.23) by performing a Taylor expansion around the carrier frequency, ω_ℓ . This analysis leads to the following equation:

$$\nabla^2 \tilde{\mathcal{E}}_{\omega_\ell}(\mathbf{r}, \omega - \omega_\ell) + \underline{\underline{\mathbf{K}}} \cdot \tilde{\mathcal{E}}_{\omega_\ell}(\mathbf{r}, \omega - \omega_\ell) - \beta'_{\omega_\ell} \nabla \left(\hat{Z} \cdot \nabla \right) \left(\tilde{\mathcal{E}}_{\omega_\ell}(\mathbf{r}, \omega - \omega_\ell) \cdot \hat{Z} \right) = -\frac{\omega_\ell^2}{c^2} \tilde{\mathcal{P}}_{\omega_\ell}^{\text{NL}}(\mathbf{r}, \omega - \omega_\ell) \quad (3.25)$$

where $\underline{\underline{\mathbf{K}}}$ is given as follows:

$$\underline{\underline{\mathbf{K}}} = \begin{pmatrix} K_{XX} & 0 & 0 \\ 0 & K_{YY} & 0 \\ 0 & 0 & K_{ZZ} \end{pmatrix} \quad (3.26a)$$

$$K_{XX} = k_o^2(\omega_\ell) + 2k_o(\omega_\ell) \frac{1}{v_g^o(\omega_\ell)} (\omega - \omega_\ell) + \frac{1}{v_g^o(\omega_\ell)^2} \left(1 - k_o(\omega_\ell) \frac{\partial v_g^o}{\partial \omega} \Big|_{\omega=\omega_\ell} \right) (\omega - \omega_\ell)^2 + \dots \quad (3.26b)$$

$$K_{YY} = k_o^2(\omega_\ell) + 2k_o(\omega_\ell) \frac{1}{v_g^o(\omega_\ell)} (\omega - \omega_\ell) + \frac{1}{v_g^o(\omega_\ell)^2} \left(1 - k_o(\omega_\ell) \frac{\partial v_g^o}{\partial \omega} \Big|_{\omega=\omega_\ell} \right) (\omega - \omega_\ell)^2 + \dots \quad (3.26c)$$

$$K_{ZZ} = k_e^2(\omega_\ell) + 2k_e(\omega_\ell) \frac{1}{v_g^e(\omega_\ell)} (\omega - \omega_\ell) + \frac{1}{v_g^e(\omega_\ell)^2} \left(1 - k_e(\omega_\ell) \frac{\partial v_g^e}{\partial \omega} \Big|_{\omega=\omega_\ell} \right) (\omega - \omega_\ell)^2 + \dots \quad (3.26d)$$

where $v_g^{o,e}$ stands for either the ordinary (o) or the extraordinary (e) group velocity. The parameter β'_ω is rewritten as β'_{ω_ℓ} , given by:

$$\beta'_{\omega_\ell} = 1 - \frac{k_e^2(\omega_\ell) + 2k_e(\omega_\ell) \frac{1}{v_g^e(\omega_\ell)} (\omega - \omega_\ell) + \frac{1}{v_g^e(\omega_\ell)^2} \left(1 - k_e(\omega_\ell) \frac{\partial v_g^e}{\partial \omega} \Big|_{\omega=\omega_\ell} \right) (\omega - \omega_\ell)^2 + \dots}{k_o^2(\omega_\ell) + 2k_o(\omega_\ell) \frac{1}{v_g^o(\omega_\ell)} (\omega - \omega_\ell) + \frac{1}{v_g^o(\omega_\ell)^2} \left(1 - k_o(\omega_\ell) \frac{\partial v_g^o}{\partial \omega} \Big|_{\omega=\omega_\ell} \right) (\omega - \omega_\ell)^2 + \dots} \quad (3.27)$$

[§]Refer to Appendix A, Section A.2, for a more in-depth discussion of these equations. Additionally, equation (A.59) provides an expanded form of this vector equation. To obtain this compact vector equation, we exploit the relationship between the dielectric tensor, denoted by $\underline{\underline{\epsilon}}(\omega)$, and the linear susceptibility tensor, denoted by $\underline{\underline{\chi}}^{(1)}(\omega)$, which is defined as follows: $\underline{\underline{\epsilon}}(\omega) = \mathbf{I} + \underline{\underline{\chi}}^{(1)}(\omega)$. This relation allows us to connect equation (3.23) with equation (A.59).

To obtain these expressions, we perform a Taylor expansion of the term $\frac{\omega}{c^2} \underline{\epsilon}(\omega)$ around the carrier frequency, ω_ℓ . This expansion, along with the relationships established in Appendix A, Section A.2, allows us to ultimately express the results in terms of the ordinary (k_o) and extraordinary (k_e) wavenumbers. In this context, the parameters k_o and k_e are defined as follows:

$$k_o(\omega) = n_o(\omega) \frac{\omega}{c} \quad (3.28a)$$

$$k_e(\omega, \theta) = n_e(\omega, \theta) \frac{\omega}{c} \quad (3.28b)$$

where n_o is the ordinary index of refraction while n_e is the extraordinary index of refraction. For equation (3.26d), we have equation (3.28b) for $\theta = \frac{\pi}{2}$, where θ is the angle between the optical axis Z and the direction of propagation.

Concerning equations (3.26a), the first term (i.e., $k_{o,e}(\omega_\ell)$) represents the conventional monochromatic scenario[¶]. The second term corresponds to the group velocity, while the final term denotes the group velocity dispersion (GVD), which is the slope of the inverse of the group velocity. Thus, each higher-order derivative corresponds to a higher-order dispersion term.

To estimate the significance of the second term compared to the first, the following considerations are provided. The question is whether or not the second term is relevant compared to the first in the Taylor expansion. Given that $\tilde{\mathcal{E}}_{\omega_\ell}(\mathbf{r}, \omega - \omega_c)$ has some limited extend around the carrier frequency ω_ℓ , we can approximate the maximum distance between the carrier frequency and points around it is approximately given by the following expression $\max(|\omega - \omega_c|) \approx \Delta\omega/2$ as long as the envelope is symmetric, such as a Gaussian profile.

To assess the relative significance of the second term in the Taylor expansion compared to the first, we consider the behavior of the function $\tilde{\mathcal{E}}_{\omega_\ell}(\mathbf{r}, \omega - \omega_\ell)$. Since this function has limited spatial extent around the carrier frequency ω_ℓ , we can approximate the maximum deviation from the carrier as $\Delta\omega/2$, assuming a symmetric envelope (e.g., Gaussian profile); symbolically, $\max(|\omega - \omega_\ell|) \approx \Delta\omega/2$. This allows us to evaluate the relative contribution of the second-order term. Moreover, the first term and the second term are defined as follows³:

$$k_{o,e}(\omega_\ell) = \frac{\omega_\ell}{v_p^{o,e}} \quad (3.29a)$$

$$\left. \frac{\partial k_{o,e}}{\partial \omega} \right|_{\omega=\omega_\ell} (\omega - \omega_\ell) = \frac{1}{v_g^{o,e}(\omega_\ell)} (\omega - \omega_\ell) \quad (3.29b)$$

where $v_p^{o,e}$ and $v_g^{o,e}$ stand for the phase velocity and the group velocity for either the ordinary or extraordinary waves, respectively. We will now compare the magnitudes of these two terms to assess their relative importance in the Taylor expansion:

$$|k_{o,e}(\omega_\ell)| = \left| \frac{\omega_\ell}{v_p^{o,e}} \right| \quad (3.30a)$$

$$\left| \left. \frac{\partial k_{o,e}}{\partial \omega} \right|_{\omega=\omega_\ell} (\omega - \omega_\ell) \right| \approx \left| \frac{1}{v_g^{o,e}(\omega_\ell)} \frac{\Delta\omega}{2} \right| \quad (3.30b)$$

[¶]The term $k_{o,e}(\omega_\ell)$ appears in the Taylor expansion for both temporal and spatial effects. However, in the temporal case, the expansion includes additional terms beyond $k_{o,e}(\omega_\ell)$. Despite this, this term remains present in both scenarios.

Comparing equations (3.30a) and (3.30b), we can see that when the phase velocity $v_p^{o,e}$ is approximately equal to the group velocity $v_g^{o,e}$, and the frequency bandwidth $\Delta\omega$ is smaller than the carrier frequency ω_ℓ ($\Delta\omega \ll \omega_c$), then equation (3.29a) dominates the expansion.

Regarding the scenario $v_p \approx v_g$, one can assess the impact of such assumption on the wave propagation within the nonlinear medium. In this regard, we can express these two quantities at the central frequency ω_ℓ as follows:

$$v_p^{o,e} = \frac{\omega_\ell}{n_{o,e}(\omega_\ell) \frac{\omega_\ell}{c}} = \frac{c}{n_{o,e}(\omega_\ell)} \quad (3.31a)$$

$$v_g^{o,e} = \frac{1}{\left. \frac{\partial k_{o,e}}{\partial \omega} \right|_{\omega=\omega_\ell}} = \frac{1}{\frac{n_{o,e}(\omega_\ell)}{c} + \frac{\omega_\ell}{c} \left. \frac{\partial n_{o,e}}{\partial \omega} \right|_{\omega=\omega_\ell}} = \frac{c}{n(\omega_\ell) + \hbar\omega_\ell \left. \frac{\partial n_{o,e}}{\partial(\hbar\omega)} \right|_{\hbar\omega=\hbar\omega_\ell}} \quad (3.31b)$$

Then, the impact is quantitatively estimated through the relative difference between these two quantities:

$$\begin{aligned} \left| \frac{v_g^{o,e} - v_p^{o,e}}{v_p^{o,e}} \right| &= \left(\frac{c}{n_{o,e}(\omega_\ell) + \hbar\omega_\ell \left. \frac{\partial n_{o,e}}{\partial(\hbar\omega)} \right|_{\hbar\omega=\hbar\omega_\ell}} - \frac{c}{n_{o,e}(\omega_\ell)} \right) \left(\frac{c}{n_{o,e}(\omega_\ell)} \right)^{-1} \\ &= \left| \frac{\hbar\omega_\ell \left. \frac{\partial n_{o,e}}{\partial(\hbar\omega)} \right|_{\hbar\omega=\hbar\omega_\ell}}{n_{o,e}(\omega_\ell) + \hbar\omega_\ell \left. \frac{\partial n_{o,e}}{\partial(\hbar\omega)} \right|_{\hbar\omega=\hbar\omega_\ell}} \right| \end{aligned} \quad (3.32)$$

where the derivative is evaluated at either the fundamental or harmonic frequency. With equation (3.32), one can quantitatively assess the impact of neglecting group velocity on wave propagation. For example, if the group velocity is significantly larger than that of the phase velocity, neglecting the term associated with the group velocity in the Taylor expansion is not advisable. Otherwise, neglecting that term may not drastically affect the outcome.

There is an advantage of neglecting higher dispersion-related terms, which is that equations (A.65) are derived analogously to the work by D. Eimerl and collaborators⁶⁵ discussed at the beginning of this chapter. The parameterization of the complex envelop $\tilde{\mathcal{E}}_{\omega_\ell}$ for both ordinary and extraordinary waves is the following:

$$\tilde{\mathcal{E}}_{q\omega_\ell}^o(\mathbf{r}, \omega - \omega_\ell) = \tilde{F}_{q\omega_\ell}^o(\mathbf{r}, \omega - \omega_\ell) \exp(ik_o(\omega_\ell)z) \quad q = X, Y \quad (3.33a)$$

$$\tilde{\mathcal{E}}_{j\omega_\ell}^e(\mathbf{r}, \omega - \omega_\ell) = \tilde{F}_{j\omega_\ell}^e(\mathbf{r}, \omega - \omega_\ell) \exp(ik_e(\omega_\ell, \theta)z) \quad j = X, Y, Z \quad (3.33b)$$

Here, the spatially slowly varying envelopes in the frequency domain are represented by $\tilde{F}_{j\omega_\ell}^o(\mathbf{r}, \omega - \omega_\ell)$ for the ordinary wave and $\tilde{F}_{j\omega_\ell}^e(\mathbf{r}, \omega - \omega_\ell)$ for the extraordinary wave. Incorporating only the dominant terms and neglecting higher-order dispersion effects, the coupled amplitude equations governing the X and Z components of the ordinary

and extraordinary waves, expressed within the principal XYZ coordinate system, can be written as:

$$\begin{aligned} \left(\frac{\partial^2}{\partial x^2} + \frac{\partial^2}{\partial y^2} \right) \tilde{F}_{X\omega_\ell}^o(\mathbf{r}, \omega - \omega_\ell) + 2in_o(\omega_\ell) \frac{\omega_\ell}{c} \frac{\partial}{\partial z} \tilde{F}_{X\omega_\ell}^o(\mathbf{r}, \omega - \omega_\ell) \\ \cong - \frac{\omega_\ell^2}{\epsilon_0 c^2} \tilde{\mathcal{P}}_{X\omega_\ell}^{\text{NL}}(\mathbf{r}, \omega - \omega_\ell) \exp\left(-in_o(\omega_\ell) \frac{\omega_\ell}{c} z\right) \end{aligned} \quad (3.34a)$$

$$\begin{aligned} \frac{\partial^2}{\partial x^2} \tilde{F}_{Z\omega_\ell}^e(\mathbf{r}, \omega - \omega_\ell) + \left[1 - \beta'_{\omega_\ell} \sin^2(\theta)\right] \frac{\partial^2}{\partial y^2} \tilde{F}_{Z\omega_\ell}^e(\mathbf{r}, \omega - \omega_\ell) + 2in_e(\omega_\ell) \frac{\omega_\ell}{c} \left[1 - \beta'_{\omega_\ell} \cos^2(\theta)\right]^{\frac{1}{2}} \\ \left[\frac{\partial}{\partial z} \tilde{F}_{Z\omega_\ell}^e(\mathbf{r}, \omega - \omega_\ell) + \rho'_{\omega_\ell}(\theta) \frac{\partial}{\partial y} \tilde{F}_{Z\omega_\ell}^e(\mathbf{r}, \omega - \omega_\ell) \right] \\ \cong - \frac{\omega_\ell^2}{\epsilon_0 c^2} \tilde{\mathcal{P}}_{Z\omega_\ell}^{\text{NL}}(\mathbf{r}, \omega - \omega_\ell) \exp\left(-in_e(\omega_\ell, \theta) \frac{\omega_\ell}{c} z\right) \end{aligned} \quad (3.34b)$$

where, β'_{ω_ℓ} and ρ'_{ω_ℓ} are given by:

$$\beta'_{\omega_\ell} = 1 - \frac{n_e^2(\omega_\ell)}{n_o^2(\omega_\ell)} \quad (3.35a)$$

$$\rho'_{\omega_\ell}(\theta) = - \frac{\frac{\beta'_{\omega_\ell}}{2} \sin(2\theta)}{1 - \beta'_{\omega_\ell} \cos^2(\theta)} \quad (3.35b)$$

The higher-order terms in the power series of $k_{o,e}$ are neglected.

3.1.3 Considerations in Identifying Ordinary and Extraordinary Waves with Nonlinear source

Leveraging the distinction between ordinary and extraordinary waves, we derive the wave equation with a nonlinear source, incorporating spatio-temporal effects. As shown in Chapter 2, this identification arises for plane-wave solutions of equations (2.11). Consequently, when the nonlinear polarization is negligible compared to the linear polarization, this identification of ordinary and extraordinary waves for plane waves remains valid even in the presence of a nonlinear polarizability. This is because the linear polarization dictates the distinction between these wave types. Mathematically, we can express this conditions as follows:

$$\begin{aligned} \|\langle \mathcal{P}_{2\omega_0}^{\text{NL}} \rangle\| \ll \|\langle \mathcal{P}_{\omega_0}^{(1)} \rangle\| \\ \left\| \left\langle \underline{\underline{\epsilon_0 \mathbf{X}^{(2)}}}(-2\omega_0; \omega_0, \omega_0) : \mathcal{E}_{\omega_0}(\mathbf{r}, t) \mathcal{E}_{\omega_0}(\mathbf{r}, t) \right\rangle \right\| \ll \left\| \left\langle \underline{\underline{\epsilon_0 \mathbf{X}^{(1)}}}(-\omega_0; \omega_0) \cdot \mathcal{E}_{\omega_0}(\mathbf{r}, t) \right\rangle \right\| \end{aligned} \quad (3.36)$$

This condition expresses that the nonlinear interaction of the fundamental wave with the medium should be much smaller than the linear interaction for the validity of the identification of ordinary and extraordinary waves. The double vertical bars $\|\cdot\|$ denote the Euclidean norm (or L^2 -norm) used to compare the time-averaged magnitudes of the linear and nonlinear polarization.

3.1.4 Cubic systems

Thus far, the theoretical framework has been focused on uniaxial crystals, characterized by two distinct indices of refraction within the principal coordinate system XYZ . This formalism can be readily adapted to accommodate simpler scenarios where the indices of refraction in the XYZ system are identical. Such scenarios occur in cubic crystal systems, where isotropy is observed with respect to the indices of refraction²⁸. Eimerl et al. introduce a term that captures the optical anisotropy of the crystal, denoted as β_{ω_ℓ} . When the indices of refraction are identical, this factor becomes zero (see equation (3.11) or equation (3.35a)).

Consequently, the term $\rho_{\omega_\ell}(\theta)$, which characterizes the walk-off effect, also vanishes (see equation (3.16)). In the time-independent formalism, the coupled amplitude equations (see equations (3.17)) become:

$$\left(\frac{\partial^2}{\partial x^2} + \frac{\partial^2}{\partial y^2}\right)F_{X\omega_\ell} + 2in(\omega_\ell)\frac{\omega_\ell}{c}\frac{\partial F_{X\omega_\ell}}{\partial z} \cong -\frac{\omega_\ell^2}{\epsilon_0 c^2}\mathcal{P}_{X\omega_\ell}^{\text{NL}} \exp\left(-in(\omega_\ell)\frac{\omega_\ell}{c}z\right) \quad (3.37a)$$

$$\left(\frac{\partial^2}{\partial x^2} + \frac{\partial^2}{\partial y^2}\right)F_{Z\omega_\ell} + 2in(\omega_\ell)\frac{\omega_\ell}{c}\frac{\partial F_{Z\omega_\ell}}{\partial z} \cong \frac{\omega_\ell^2}{\epsilon_0 c^2}\tilde{\mathcal{P}}_{Z\omega_\ell}^{\text{NL}}(\mathbf{r}, \omega - \omega_\ell) \exp\left(-in(\omega_\ell)\frac{\omega_\ell}{c}z\right) \quad (3.37b)$$

There is no need to differentiate between the ordinary and extraordinary indices of refraction or envelopes. In connection with the time-related case, the coupled amplitude equations from (3.34) are rewritten as follows:

$$\begin{aligned} \left(\frac{\partial^2}{\partial x^2} + \frac{\partial^2}{\partial y^2}\right)\tilde{F}_{X\omega_\ell}(\mathbf{r}, \omega - \omega_\ell) + 2in(\omega_\ell)\frac{\omega_\ell}{c}\frac{\partial \tilde{F}_{X\omega_\ell}(\mathbf{r}, \omega - \omega_\ell)}{\partial z} \\ \cong -\frac{\omega_\ell^2}{\epsilon_0 c^2}\tilde{\mathcal{P}}_{X\omega_\ell}^{\text{NL}}(\mathbf{r}, \omega - \omega_\ell) \exp\left(-in(\omega_\ell)\frac{\omega_\ell}{c}z\right) \end{aligned} \quad (3.38a)$$

$$\begin{aligned} \left(\frac{\partial^2}{\partial x^2} + \frac{\partial^2}{\partial y^2}\right)\tilde{F}_{Z\omega_\ell}(\mathbf{r}, \omega - \omega_\ell) + 2in(\omega_\ell)\frac{\omega_\ell}{c}\frac{\partial \tilde{F}_{Z\omega_\ell}(\mathbf{r}, \omega - \omega_\ell)}{\partial z} \\ \cong -\frac{\omega_\ell^2}{\epsilon_0 c^2}\tilde{\mathcal{P}}_{Z\omega_\ell}^{\text{NL}}(\mathbf{r}, \omega - \omega_\ell) \exp\left(-in(\omega_\ell)\frac{\omega_\ell}{c}z\right) \end{aligned} \quad (3.38b)$$

In isotropic (cubic) crystals, as opposed to the case treated by Eimerl et al., the quantity θ plays no role neither in (3.37) nor in (3.38). Therefore, direction is meaningless in isotropic crystals.

In isotropic and uniaxial crystals, waves experience dispersion and diffraction as they propagate through the material. Therefore, the following section aims to establish simple criteria for determining when it is acceptable to neglect these effects. Additionally, arguments for neglecting the walk-off effect are presented, followed by an introduction to a common approximation method for handling the coupled amplitude equations.

3.2 Physical insights into diffraction, walk-off, & pump depletion

Solving either equation (3.17) or equation (3.34) provides insight into the propagation of waves within uniaxial crystals for SHG. When diffraction, walk-off, and temporal effects are taken into account, one mainly solves such

equations through numerical methods, such as the splitting method^{26, pp. 229}. However, analytical expressions are useful for gaining insights into the physics of the phenomenon.

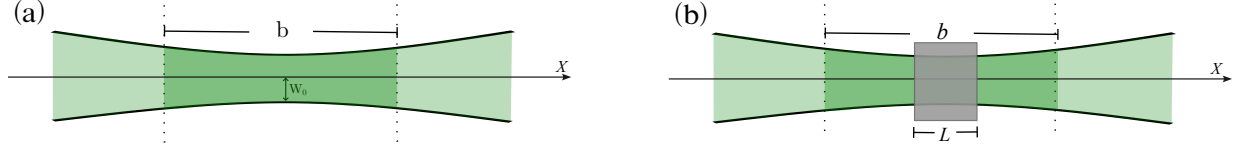


Figure 3.2: Depth of focus of a (Gaussian) beam. (a) Relation between the beam waist radius W_0 (radial size of the beam at its narrowest point.) and the confocal parameter b . (b) Comparison between the interaction length L and the confocal parameter b . The gray rectangle illustrates a nonlinear medium, such as LiNbO_3 .

In this regard, one can estimate the impact of diffraction and walk-off on the propagation of the fundamental and harmonic waves within the sample to determine whether neglecting these aspects of the scenario results in negligible changes. For example, we can assess whether or not the divergence becomes relevant on the length scale of the sample. The shape of a wave changes due to diffraction after propagating a characteristic length, which is known as the diffraction length (L_d). Commonly, the fundamental transverse electromagnetic mode (TEM_{00}) is used to model a finite beam²⁸.

In order to assess the role of diffraction, two parameters that characterize TEM_{00} are introduced: Beam waist W_0 and confocal parameter b . The former is the minimum radius of the beam²⁸, but beyond a certain distance, the beam radius starts increasing by a factor of $\sqrt{2}$; this distance is called the Rayleigh range (z_R), which is given by²⁸:

$$z_R = \frac{\pi W_0^2}{\lambda} \quad (3.39)$$

where n is the index of refraction of the medium, and λ is the wavelength within the nonlinear medium^{||}. The distance between the points $\pm z_R$ about W_0 is called the confocal parameter b (See Fig. 3.2), where $b = 2z_R$. Given that the beam radius starts increasing considerably from z_R , the confocal parameter is a good indicator of the diffraction length: $L_d \simeq b$.

Therefore, we define the following criterion for neglecting diffraction:

$$L_d \simeq b = \frac{2\pi}{\lambda} W_0^2 > L \quad (3.40)$$

where L is the interaction length (i.e., length of the sample, see Fig. 3.2(b)).

Walk-off angle

Due to the difference in the index of refraction between ordinary and extraordinary waves, the direction of wave propagation for an extraordinary wave does not typically align with the direction of energy propagation, as characterized by the Poynting vector. This phenomenon results in the extraordinary beams appearing to deviate from the axis

^{||}In this context, the wavelength within the medium, denoted by λ , is related to the vacuum wavelength, $\bar{\lambda}$, through the expression $\bar{\lambda}/n$, where n represents the refractive index. The standard notation for the vacuum wavelength is often λ_0 . However, to maintain clarity and consistency within this thesis, we will use $\bar{\lambda}$ to avoid confusion with the fundamental wavelength, already designated as λ_0 .

of the ordinary beam. This deviation is given by ρ_{ω_ℓ} for uniaxial crystal. From expression (3.16), when propagating perpendicular to the optical axis ($\theta = \pi/2$), the walk-off effect is completely negligible^{28, pp. 98}.

Therefore, as long as propagation takes places perpendicularly, the ordinary and extraordinary waves overlap, and either equations (3.17) or equations (3.34) get simplified.

Undepleted pump approximation

Under certain conditions, the fundamental wave can be considered to propagate without significant influence from nonlinear interactions. This occurs when the fundamental wave power is sufficiently high, and the efficiency of the second harmonic wave generation is low.

A specific example arises when the fundamental wave is ordinarily polarized and the second harmonic wave is extraordinarily polarized. In this scenario, the nonlinear polarization at the fundamental frequency ω_0 vanishes, represented by $\tilde{\mathcal{P}}_{X\omega_0}^{\text{NL}}(\omega - \omega_0) = 0$. Consequently, the system of coupled differential equations described by Eq. (3.34) reduces to a set of partially decoupled equations:

$$\left(\frac{\partial^2}{\partial x^2} + \frac{\partial^2}{\partial y^2}\right)\tilde{F}_{X\omega_0}^o(\mathbf{r}, \omega - \omega_0) + 2i n_o(\omega_0)\frac{\omega_0}{c}\frac{\partial}{\partial z}\tilde{F}_{X\omega_0}^o(\mathbf{r}, \omega - \omega_0) \cong 0 \quad (3.41a)$$

$$\begin{aligned} & \frac{\partial^2}{\partial x^2}\tilde{F}_{Z2\omega_0}^e(\mathbf{r}, \omega - 2\omega_0) + \left[1 - \beta'_{2\omega_0}\sin^2(\theta)\right]\frac{\partial^2}{\partial y^2}\tilde{F}_{Z2\omega_0}^e(\mathbf{r}, \omega - 2\omega_0) \\ & + 2i n_e(2\omega_0)\frac{2\omega_0}{c}\left[1 - \beta'_{2\omega_0}\cos^2(\theta)\right]^{\frac{1}{2}}\left[\frac{\partial}{\partial z}\tilde{F}_{Z2\omega_0}^e(\mathbf{r}, \omega - 2\omega_0) + \rho_{2\omega_0}(\theta)\frac{\partial}{\partial y}\tilde{F}_{Z2\omega_0}^e(\mathbf{r}, \omega - 2\omega_0)\right] \\ & \cong -\frac{(2\omega_0)^2}{\epsilon_0 c^2}\tilde{\mathcal{P}}_{Z2\omega_0}^{\text{NL}}(\mathbf{r}, \omega - 2\omega_0)\exp\left(-i n_e(\omega_{\text{SHG}}, \theta)\frac{\omega_{\text{SHG}}}{c}z\right) \end{aligned} \quad (3.41b)$$

Decouple in the sense that equation (3.41a) no longer depends on the other wave due to the weak nonlinearity. This is known as the undepleted pump approximation, and a quantitative criterion for such approximation is¹¹:

$$\eta_{\text{SHG}} = \frac{I_{2\omega}(L)}{I_\omega(0)} \ll 1 \quad (3.42)$$

where η_{SHG} represents the efficiency of second-harmonic generation (SHG). It is a dimensionless quantity defined as the ratio of the output power (intensity) of the second harmonic wave to the input power (intensity) of the fundamental wave.

3.3 Study case: LiNbO₃**

This section focuses on benchmarking the theoretical framework developed so far through a standard light-conversion experiment. The experimental setup is designed for light conversion from a pump wavelength of 1030 nm to a second

**This work was performed in collaboration with Dr. Dietrich Krebs and Dr. Christina Boemer. The standard light-conversion experiment was conducted by them at DESY (German Electron Synchrotron, in English), in Hamburg.

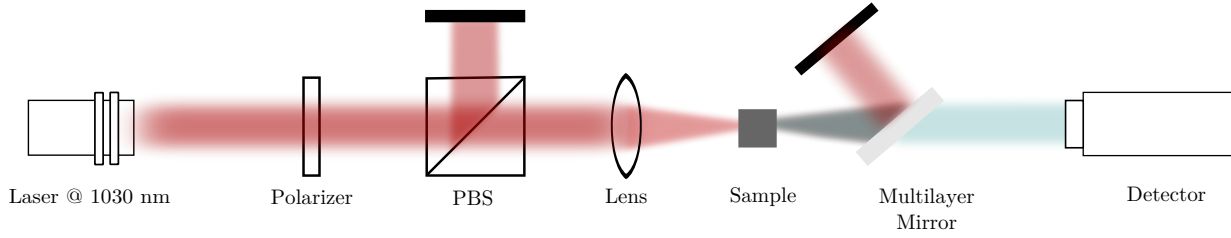


Figure 3.3: Schematic representation of the light-conversion experiment setup. The red region represents the fundamental wave, while the green region represents the second harmonic wave. PBS stands for polarizing beamsplitter.

harmonic of 515 nm, as conducted by co-advisors Dr. Dietrich Krebs and Dr. Christina Boemer (see Fig. 3.3). We employ a X -cut LiNbO_3 sample, where the X crystallographic axis is normal to the interacting surface. A polarization system, incorporating a polarizer and a polarizing beamsplitter (Fig. 3.3), is used. Through this system, the fundamental wave is polarized parallel to the tabletop.

Given that the crystal is oriented such that its optical axis is perpendicular to the tabletop, the fundamental (or input/pump) wave is linearly polarized along the Y -axis, as shown in Fig. 3.6. The beam impinges on the crystal at normal incidence. To increase the photon density within the nonlinear material, a lens is used. The sample is located at the focal point of such lens, where the beam is measured to have a width of $11 \mu\text{m}$.^{††}

Moreover, the beam power before the sample is 287 mW. The thickness of the nonlinear medium is $L = 1$ mm. After the sample, a multilayer mirror is employed since we are interested in the SHG transmitted signal (i.e., transmission geometry). This mirror fully reflects light at 1030 nm, but allows transmission of (part of) the SHG signal to the detector. The measured SHG power is 2.7 mW. Finally, regarding the light source, the laser is pulsed, which is characterized by a period-repetition time of 0.02 ms or repetition rate of 50 kHz, and a pulse length (τ) of 0.102 ps.^{‡‡}

Concerning LiNbO_3 , its transparency window, defined as the spectral region where absorption is extremely low, extends from the band edge at approximately 320 nm (3.87 eV) to multiphonon absorption in the infrared region at around 3000 nm⁶⁶. When the frequencies of the interacting electric fields are far from any material resonances (i.e., light absorption is low), the $\chi^{(2)}$ values are largely independent of frequency^{26, pp. 67}.

Structurally, LiNbO_3 is characterized by the non-centrosymmetric point group, $3m$, where the optical axis aligns with the threefold axis (or, principal symmetry axis). This symmetry class dictates the form of the susceptibility tensor (See Table 2.2). Given that the SHG process takes place within the transparency windows of the material, Kleinman symmetry is allowed. Based on the parameters of the experiments, $L_d > L$ (i.e., $L_d = 1.65$ mm, where we use expression (3.40) for $n_o(\omega_0) = 2.2339$; and $L_d = 3.29$ mm, where we use expression (3.40) for $n_e(2\omega_0) = 2.2270$). In this case, diffraction within the medium plays a minimal role since diffraction effects become significant at a length larger than the size of the crystal. The indices of refraction reported in Table 3.1 are calculated

^{††}This corresponds to a $D4\sigma$ of $44 \mu\text{m}$, which means the Gaussian $1/e$ width is $11 \mu\text{m}$.

^{‡‡}The pulse length τ is calculated from the full-width at half maximum (FWHM) measurement: $\frac{\tau_{\text{FWHM}}}{2\sqrt{\log 2}}$, where $\tau_{\text{FWHM}} = 170$ fs

Table 3.1: The ordinary index of refraction is provided for two different scenarios: $\omega_0(\lambda_0)$ and $2\omega_0(\lambda_0/2)$; the extraordinary index of refraction is given as well. Parameters used to obtain these indices of refraction from the model by U. Schalarb and K. Betzler⁶⁷: $c_{\text{Li}} = 49.65$ and $T = 25$ °C.

	ω_0 (λ_0)	$2\omega_0$ ($\lambda_0/2$)
n_o	2.2339	2.3304
n_e	2.1467	2.2270

using a generalized Sellmeier equation derived by U. Schalarb and K. Betzler⁶⁷ §§.

To analyze the response of the material to a linearly ordinary polarized incident field at the fundamental frequency (ω_0), we can determine the resulting nonlinear polarization at the second harmonic ($2\omega_0$) frequency. However, the second-order susceptibility tensor (or d -matrix) for the $3m$ symmetry class (Table 2.2) is unsuitable for X -cut LiNbO_3 . In Table 2.2, those d -matrices are formulated under the assumption that the optical axis (in this thesis, we denote the optical axis by Z) aligns with the principal symmetry axis, which in turn points along the crystallographic c -axis.

However, in the X -cut LiNbO_3 , the principal symmetry axis aligns with the b -axis. To obtain a compatible d -matrix, rotations are needed to align the Z -axis with the lattice vector \mathbf{b} . The appropriate nonlinear polarization expression for the X -cut LiNbO_3 is given as follows:

$$\mathcal{P}_{2\omega_0}^{\text{NL}}(\mathbf{r}, t) = \epsilon_0 \begin{pmatrix} -d_{33} & -d_{15} & -d_{15} & 0 & 0 & 0 \\ 0 & 0 & 0 & 0 & d_{22} & -d_{15} \\ 0 & d_{22} & -d_{22} & 0 & -d_{15} & 0 \end{pmatrix} \begin{pmatrix} \mathcal{E}_{X\omega_0}^2(\mathbf{r}, t) \\ \mathcal{E}_{Y\omega_0}^2(\mathbf{r}, t) \\ \mathcal{E}_{Z\omega_0}^2(\mathbf{r}, t) \\ 2\mathcal{E}_{Y\omega_0}(\mathbf{r}, t)\mathcal{E}_{Z\omega_0}(\mathbf{r}, t) \\ 2\mathcal{E}_{X\omega_0}(\mathbf{r}, t)\mathcal{E}_{Z\omega_0}(\mathbf{r}, t) \\ 2\mathcal{E}_{X\omega_0}(\mathbf{r}, t)\mathcal{E}_{Y\omega_0}(\mathbf{r}, t) \end{pmatrix} \quad (3.43)$$

Figure 3.4 visually depicts the transformations employed to obtain the second-order susceptibility tensor. Appendix A (Section A.3) provides further details on these transformations, ultimately leading to the expression given in equation (3.43). When the fundamental electric field is polarized along the Y -axis (i.e., ordinary (o) polarization),

§§They fitted a set of parameters to experimental data covering Li_2O compositions ranging from 47 to 50 mol%, wavelengths from 400 to 1200 nm, and temperatures from 50 to 600 K⁶⁷.

the induced nonlinear response exhibits the following components:

$$\mathcal{P}_{X2\omega_0}^{\text{NL}} = -\epsilon_0 d_{15} [\mathcal{E}_{Y\omega_0}^o(\mathbf{r}, t)]^2 \quad (3.44a)$$

$$\mathcal{P}_{Y2\omega_0}^{\text{NL}} = 0 \quad (3.44b)$$

$$\mathcal{P}_{Z2\omega_0}^{\text{NL}} = \epsilon_0 d_{22} [\mathcal{E}_{Y\omega_0}^o(\mathbf{r}, t)]^2 \quad (3.44c)$$

Under an ordinary polarized fundamental wave, the nonlinear polarization arises along the X and Z directions.

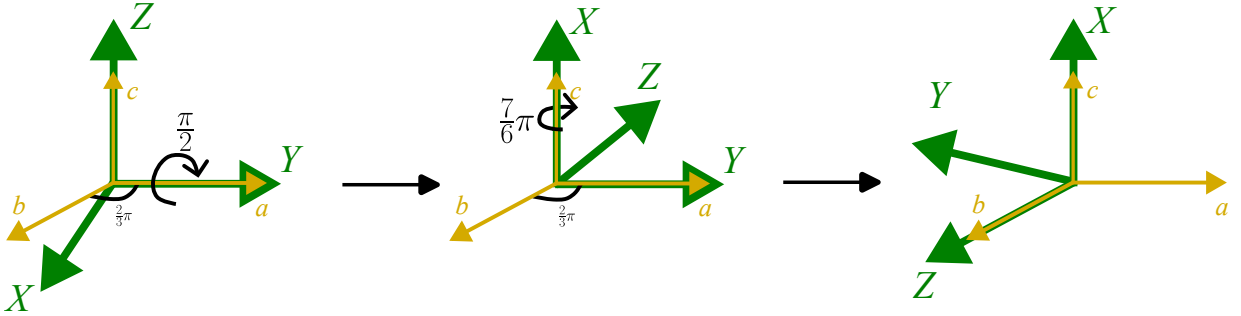


Figure 3.4: The two rotations that need to be performed to align the Z -axis (the optical axis) with the lattice vector b .

Notably, the propagation direction is along the X -axis. This geometry leads to the following key points. Due to equation (3.44c), a second-harmonic wave linearly polarized along the Z -axis propagates within the medium. If the generated second-harmonic electric field has both X and Z components (as depicted in Figure 3.5), the Poynting vector (denoted by $\mathbf{S}_{2\omega_0}$) does not align with the propagation direction vector. This contradicts the condition for zero walk-off angle when propagation is normal to the optical axis.

Therefore, considering the specific propagation direction and the governing equations, we focus on the generation and propagation of the Z -polarized second-harmonic wave induced by the Z -component of the nonlinear polarization given by equation (3.44c).

We can model this scenario using the Z projection of equation (3.25) for $\omega_\ell = 2\omega_0$, taking into consideration spatio-temporal effects:

$$\begin{aligned} \hat{Z} \cdot \left[\nabla^2 \tilde{\mathcal{E}}_{2\omega_0}(\mathbf{r}, \omega - 2\omega_0) + \underline{\mathbf{K}} \cdot \tilde{\mathcal{E}}_{2\omega_0}(\mathbf{r}, \omega - 2\omega_0) - \beta'_{2\omega_0} \nabla \left(\hat{Z} \cdot \nabla \right) \left(\tilde{\mathcal{E}}_{2\omega_0}(\mathbf{r}, \omega - 2\omega_0) \cdot \hat{Z} \right) \right] \\ = \hat{Z} \cdot \left[-\frac{(2\omega_0)^2}{c^2} \tilde{\mathcal{P}}_{2\omega_0}^{\text{NL}}(\mathbf{r}, \omega - 2\omega_0) \right] \end{aligned} \quad (3.45)$$

Regarding the fundamental field, we can also use equation (3.25) for $\omega_\ell = \omega_0$, but we focus on the projection along the Y -axis. Due to the nature of ordinary waves, the Z -component of the electric field vanishes (i.e., $\tilde{\mathcal{E}}_{\omega_0}(\mathbf{r}, \omega - \omega_0) \cdot \hat{Z} = 0$), which leads to the following expression:

$$\hat{Y} \cdot \left[\nabla^2 \tilde{\mathcal{E}}_{\omega_0}(\mathbf{r}, \omega - \omega_0) + \underline{\mathbf{K}} \cdot \tilde{\mathcal{E}}_{\omega_0}(\mathbf{r}, \omega - \omega_0) \right] = \hat{Y} \cdot \left[-\frac{\omega_0^2}{c^2} \tilde{\mathcal{P}}_{\omega_0}^{\text{NL}}(\mathbf{r}, \omega - \omega_0) \right] \quad (3.46)$$

Conveniently, we can still use the XYZ coordinate system because the propagation is perpendicular to the optical axis (Z) and along a principal axis (X). This avoids the need for the xyz propagation coordinate system and the corresponding coordinate system transformation (Appendix A, Section A.1.1). The transformation between XYZ and xyz in this case involves simple permutations due to this specific propagation geometry:

$$\begin{pmatrix} X \\ Y \\ Z \end{pmatrix} = \begin{pmatrix} 0 & 0 & 1 \\ 1 & 0 & 0 \\ 0 & 1 & 0 \end{pmatrix} \begin{pmatrix} x \\ y \\ z \end{pmatrix}$$

Therefore, we focus on the principal coordinate system XYZ as it simplifies the analysis for propagation along the

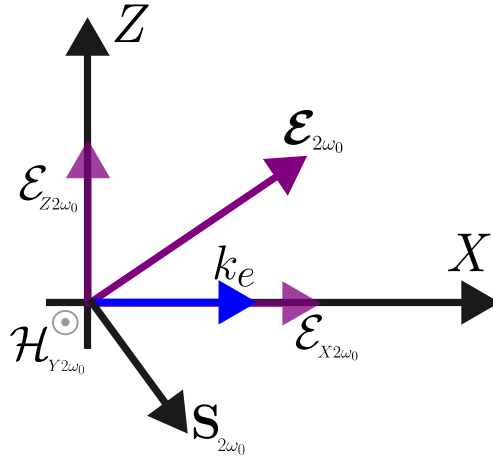


Figure 3.5: The second-harmonic electric field, denoted by $\mathcal{E}_{2\omega_0}$, is confined to the XZ plane. This plane is defined by the extraordinary wave vector, k_e , and the optical axis, which lies along the Z direction. In the time domain, the field vector components are represented without the tilde notation. The corresponding magnetic field, $\mathcal{H}_{2\omega_0}$, is oriented perpendicular to the XZ plane, pointing out of the page. $\mathcal{S}_{2\omega_0}$ represents the Poynting vector.

X -axis. We now express the components of the envelopes for both the fundamental and second-harmonic fields as follows:

$$\tilde{\mathcal{E}}_{Y\omega_0}^o(\mathbf{r}, \omega - \omega_0) = \Theta(R^{(b)} - R_{YZ}) \tilde{F}_{Y\omega_0}^o(X, \omega - \omega_0) \exp(i k_o(\omega_0) X) \quad (3.47a)$$

$$\tilde{\mathcal{E}}_{Z2\omega_0}^e(\mathbf{r}, \omega - 2\omega_0) = \Theta(R^{(b)} - R_{YZ}) \tilde{F}_{Z2\omega_0}^e(X, \omega - 2\omega_0) \exp(i k_e(2\omega_0) X) \quad (3.47b)$$

where $\Theta(R^{(b)} - R_{YZ})$ is a Heaviside function given by:

$$\Theta(R^{(b)} - R_{YZ}) = \begin{cases} 1 & , \text{ for } R^{(b)} \geq R_{YZ} \text{ where } R_{YZ} = \sqrt{Y^2 + Z^2} \\ 0 & , \text{ otherwise} \end{cases} \quad (3.48)$$

This model departs from the previously established approach based on Refs. 5 and 30 by employing a different parameterization. The prior method expresses the term $\mathbf{F}_{\omega_\ell}(\mathbf{r}, \omega - \omega_\ell)$ as a function of both spatial coordinates (represented by the three-component vector \mathbf{r}) and frequency ($\omega - \omega_\ell$). In contrast, this model simplifies the spatial dependence by considering only the longitudinal coordinate (X).

However, the transverse dependence (Y and Z) is introduced through the Heaviside function. This function acts as a mathematical switch, taking a value of one within the defined beam radius ($R^{(b)}$) and zero outside, as shown in Figure 3.6. This approach effectively captures the presence or absence of the field in different spatial regions. Furthermore, we assume the Heaviside function remains constant across the cross-section region of the beam. In this case, this assumption is justified because diffraction plays a minor role in this particular case.

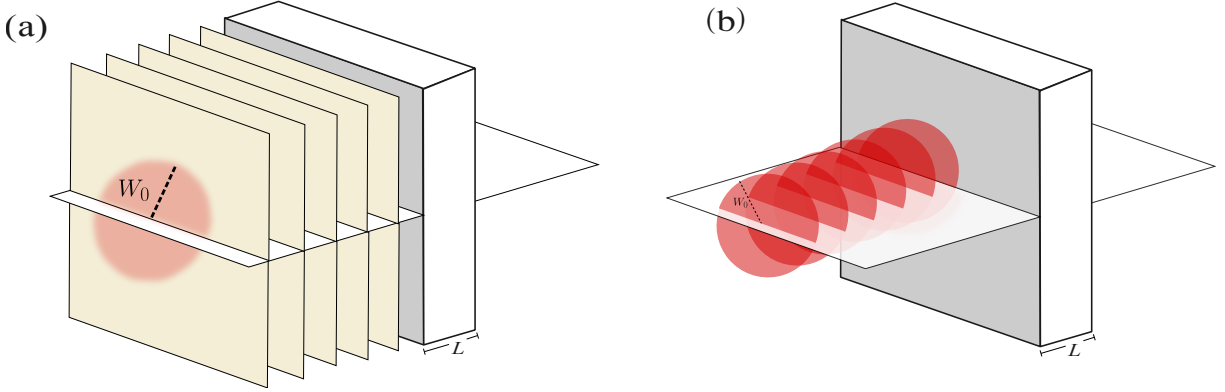


Figure 3.6: Spatially constrained plane waves. (a) Schematic representation of wavefronts for plane waves (depicted in beige), while the red spot illustrates the cross section of the pencil-like shaped beam.

Building upon this parameterization of the envelopes (3.47), we can derive the following coupled amplitude equations (The details can be found in Appendix A (Section A.4); see equations (A.80), for example):

$$\frac{\partial}{\partial X} \tilde{F}_{Y\omega_0}^o(X, \omega - \omega_0) = \Theta(R^{(b)} - R_{YZ}) \frac{i(\omega_0)^2}{2k_o(\omega_0)\epsilon_0 c^2} \tilde{\mathcal{P}}_{Y\omega_0}^{\text{NL}}(\mathbf{r}, \omega - \omega_0) \exp(-ik_o(\omega_0)X) \quad (3.49a)$$

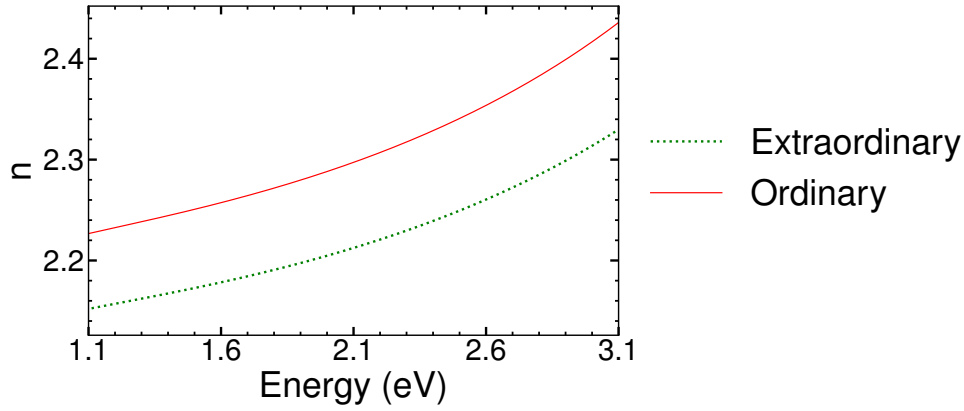
$$\frac{\partial}{\partial X} \tilde{F}_{Z2\omega_0}^e(X, \omega - 2\omega_0) = \Theta(R^{(b)} - R_{YZ}) \frac{i(2\omega_0)^2}{2k_e(2\omega_0)\epsilon_0 c^2} \tilde{\mathcal{P}}_{Z2\omega_0}^{\text{NL}}(\mathbf{r}, \omega - 2\omega_0) \exp(-ik_e(2\omega_0)X) \quad (3.49b)$$

When deriving equations (3.49), we neglect dispersion terms, such as group velocity. While this simplification streamlines the mathematical treatment, it is crucial to acknowledge the potential inaccuracies introduced. Particularly, neglecting group velocity effects can lead to deviations from the actual behavior, especially when dealing with short pulses. Equation (3.32) estimates the magnitude of the error introduced by this approximation. For clarity,

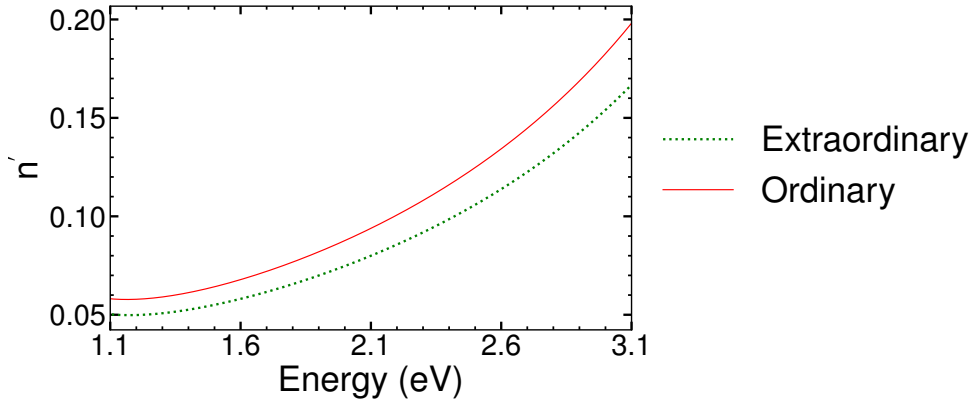
equation (3.32) is rewritten below:

$$\left| \frac{v_g^{o,e} - v_p^{o,e}}{v_p^{o,e}} \right| = \left| \frac{\hbar\omega_\ell \frac{\partial n_{o,e}}{\partial(\hbar\omega)} \Big|_{\hbar\omega=\hbar\omega_\ell}}{n_{o,e}(\omega_\ell) + \hbar\omega_\ell \frac{\partial n_{o,e}}{\partial(\hbar\omega)} \Big|_{\hbar\omega=\hbar\omega_\ell}} \right|$$

Regarding the second-harmonic frequency $\omega_\ell = \omega_{\text{SHG}} = 2\omega_0$, we can use this expression to assess the impact



(a) Ordinary and Extraordinary index of refraction.



(b) Derivative of the ordinary and extraordinary index of refraction.

Figure 3.7: Linear response of LiNbO₃ in the range from 400 nm (3.1 eV) to 1127 nm (1.1 eV). The data were obtained using the model proposed by U. Schlarb and K. Betzler⁶⁷.

on neglecting group velocity in wave propagation within this material. From the experiment, the fundamental wavelength is 1030 nm, which leads to a second-harmonic wavelength of 515 nm^{¶¶}; hence, the photon energy for

^{¶¶}The following equations tie together wavelength (λ), frequency (ω), and energy (\mathbb{E}) of light: $\omega = 2\pi \frac{c}{\lambda}$ (where c is the speed of light); and $\mathbb{E} = \hbar\omega$ (where \hbar is the reduced Planck constant).

each of these wavelengths corresponds to 1.2 eV and 2.4 eV, respectively. The index of refraction and its derivative are calculated using the Sellmeier equation proposed by U. Schlarb and K. Betzler⁶⁸. Figure 3.7 illustrates these quantities across a broad range of energy, covering wavelengths from 400 nm (3.1 eV) to 1127 nm (1.1 eV). Evaluation of equation (3.32) shows a relative difference of 3% and 9% between the phase velocity and group velocity for the fundamental ordinary and second-harmonic extraordinary waves, respectively***.

Following the description of a cylindrical-shaped beam, one can estimate the time-averaged intensity of the fundamental and harmonic signals through the following expression:

$$\langle I_{\omega_0, 2\omega_0} \rangle = \frac{\langle \mathbb{P}_{\omega_0, 2\omega_0} \rangle}{A_{\text{beam}}} = \frac{\langle \mathbb{P}_{\omega_0, 2\omega_0} \rangle}{\pi W_0^2} \quad (3.50)$$

The cross-section area for the model corresponds to the area of a circle (see Fig. 3.6 (b)), and $\langle \mathbb{P}_{\omega_0} \rangle$ and $\langle \mathbb{P}_{2\omega_0} \rangle$ represent the time-averaged power for the fundamental and harmonic waves, respectively. With this description, the criterion 3.42 is redefined as follows:

$$\eta_{\text{SHG}} = \frac{\langle I_{2\omega}(L) \rangle}{\langle I_{\omega}(0) \rangle} = \frac{\langle \mathbb{P}_{2\omega_0} \rangle}{\pi W_0^2} \left(\frac{\langle \mathbb{P}_{\omega_0} \rangle}{\pi W_0^2} \right)^{-1} = \frac{\langle \mathbb{P}_{2\omega_0} \rangle}{\langle \mathbb{P}_{\omega_0} \rangle} \ll 1 \quad (3.51)$$

During the experiment, the measured average fundamental power (282 mW) was significantly higher than the measured average second harmonic power (2.7 mW). Substituting these values into equation (3.51) results in an efficiency of 0.009. This low efficiency suggests minimal conversion of the fundamental power to the second harmonic. Consequently, the time-averaged intensity is likely unaffected as it propagates through the nonlinear medium. Thus, the condition for employing the undepleted pump approximation is satisfied. As a result, equations (3.49) become:

$$\frac{\partial}{\partial X} \tilde{F}_{Y\omega_0}^o(X, \omega - \omega_0) = 0 \quad (3.52a)$$

$$\frac{\partial}{\partial X} \tilde{F}_{Z2\omega_0}^e(X, \omega - 2\omega_0) = \Theta(R^{(b)} - R_{YZ}) \frac{i(2\omega_0)^2}{2k_e(2\omega_0)\epsilon_0 c^2} \tilde{\mathcal{P}}_{Z2\omega_0}^{\text{NL}}(\mathbf{r}, \omega - 2\omega_0) \exp(-ik_e(2\omega_0)X) \quad (3.52b)$$

This section aims to compare the theoretical prediction of the average second harmonic power with the measured value. As established in Chapter 2, intensity is the observable of interest, and within the model, it relates to power through equation (3.50). The following equation expresses the time-averaged intensity for both the fundamental and second harmonic signals:

$$\langle I_{\omega_\ell}(\mathbf{r}) \rangle = \left\| \frac{1}{T_{P\omega_\ell}} \int_{-\frac{1}{2}T_{P\omega_\ell}}^{\frac{1}{2}T_{P\omega_\ell}} dt \frac{1}{2} \text{Re} \{ \mathcal{E}_{\omega_\ell}(\mathbf{r}, t) \times \mathcal{H}_{\omega_\ell}^*(\mathbf{r}, t) \} \right\| \quad (3.53)$$

In this equation, $T_{P\omega_\ell}$ is the period-repetition time for frequency ω_ℓ involved in the nonlinear process. This process can involve frequencies like the fundamental ω_0 and its second harmonic, $2\omega_0$. Moreover, \mathcal{E} and \mathcal{H} are the slowly

***For the fundamental wave, we substitute the following parameter values into equation (3.32): $n_o(\omega_0) = 2.2337$ and $\partial n_o / \partial(\hbar\omega) = 0.0578$. Similarly, for the second-harmonic wave, we evaluate equation (3.32) using the parameters: $n_e(2\omega_0) = 2.2295$ and $\partial n_e / \partial(\hbar\omega) = 0.09616$.

varying envelope of the electric field and magnetic field for frequency ω_ℓ , respectively. The double vertical bars $\|\cdot\|$ denote the Euclidean norm. This expression is derived from the Poynting vector (see Appendix C).

Under the undepleted pump approximation, we can directly solve equation (3.52a). This solution can then be transformed back into the time domain using the Fourier transform. This transformation yields the following expression (See Appendix A , Section A.4):

$$F_{Y\omega_0}^o(X, t) = C_{Y\omega_0}^o(t) \quad (3.54)$$

Given the negligible change in average fundamental intensity within the nonlinear medium, equation (3.53) offers

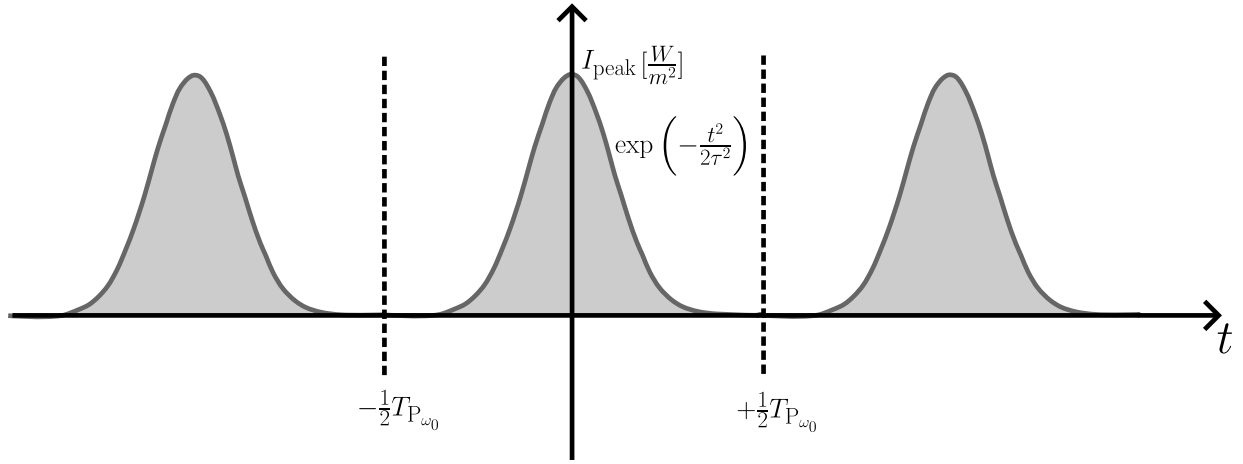


Figure 3.8: Illustration of the Gaussian profile used for modelling the pulse, where the pulse-repetition time is given by $T_{P\omega_0}$.

a convenient property. We can choose the value of $F_{Y\omega_0}^o$ arbitrarily across space (along the X -axis). This holds true regardless of the X -coordinate. However, to maintain consistency with the scenario where the laser beam starts interacting with the nonlinear material at $X = 0$, we set $F_{Y\omega_0}^o(X, t) = F_{Y\omega_0}^o(0, t)$. Consequently, equation (3.54) becomes: $C(t) = F_{Y\omega_0}^o(t)$.

Having computed the magnetic field (see equation (A.84) in Appendix A), we can evaluate equation (3.53) for the fundamental wave at $X = 0$, which yields the following:

$$\langle I_{\omega_0} \rangle = I_{\text{peak}} \frac{1}{T_{P\omega_0}} \sqrt{\pi} \tau \quad (3.55)$$

In this equation, I_{peak} represents the peak intensity (see Fig 3.8), and τ is the pulse length. To arrive at equation (3.55), we state that the fundamental envelope at $X = 0$ follows a Gaussian profile^{†††}, which is generally a first

^{†††} $F_{Y\omega_0}^o(0, t) = K \exp(-t^2/2\tau^2)$ where K is a constant with units of V/m (i.e., SI units for electric field). A more detailed explanation of how we obtained equation (3.55) can be found in Appendix A, equation (A.92).

good approximation²⁸. To determine the value of the peak intensity in expression (3.55), we can use the relationship between the time-averaged power and the time-averaged intensity, which is given by expression (3.50):

$$I_{\text{peak}} = \frac{\langle \mathbb{P}_{\omega_0} \rangle}{\sqrt{\pi} A_{\text{beam}}} \left(\frac{T_{\text{P}_{\omega_0}}}{\tau} \right) \quad (3.56)$$

Here, $\langle \mathbb{P}_{\omega_0} \rangle$ is the averaged power of the fundamental radiation, A_{beam} is the cross-section area of the laser beam. To determine the second harmonic intensity, we first solve equation (3.52b). This equation serves as a prerequisite for the subsequent calculation of the second harmonic intensity utilizing equation (3.53). However, solving equation (3.52b) requires the prior calculation of the Z -component of the nonlinear polarization $\tilde{\mathcal{P}}_{2\omega_0}^{\text{NL}}(\mathbf{r}, \omega - 2\omega_0)$.

We can perform a Fourier inverse transformation on equation (3.44c) in order to obtain the Z -component of the nonlinear polarization $\tilde{\mathcal{P}}_{2\omega_0}^{\text{NL}}(\mathbf{r}, \omega - 2\omega_0)$ (Refer to Appendix A, equation (A.87) for a detailed derivation of this expression):

$$\tilde{\mathcal{P}}_{Z2\omega_0}^{\text{NL}}(X, \omega - 2\omega_0) = \Theta(R^{(b)} - R_{YZ}) \epsilon_0 d_{22} G^o(\omega - 2\omega_0) \exp(i 2k_o(2\omega_0) X) \quad (3.57)$$

where $G^o(\omega - 2\omega_0)$ is given by:

$$G^o(\omega - 2\omega_0) = \int_{-\infty}^{+\infty} \frac{d\xi}{(2\pi)^2} \tilde{C}_{Y\omega_0}^o(\xi) \tilde{C}_{Y\omega_0}^o(\omega - 2\omega_0 - \xi)$$

Plugging equation (3.57) into equation (3.52b), we obtain the following expression:

$$\frac{\partial}{\partial X} \tilde{F}_{Z2\omega_0}^e(X, \omega - 2\omega_0) = \Theta(R^{(b)} - R_{YZ}) \frac{i(2\omega_0)^2}{2k_e(2\omega_0)c^2} d_{22} G^o(\omega - 2\omega_0) \exp(-i \Delta k X) \quad (3.58)$$

Here, the term Δk is give by:

$$\Delta k = k_e(2\omega_0) - 2k_o(\omega_0) = \frac{2\omega_0}{c} \left(n_e(2\omega_0) - n_o(\omega_0) \right) \quad (3.59)$$

Equation (3.58) can be directly integrated as follows^{†††}:

$$\tilde{F}_{Z2\omega_0}^e(X, \omega - 2\omega_0) = \Theta(R^{(b)} - R_{YZ}) \frac{i(2\omega_0)^2 X}{2k_e(2\omega_0)c^2} d_{22} G^o(\omega - 2\omega_0) \text{sinc}\left(\frac{\Delta k}{2} X\right) \exp\left(-i \frac{\Delta k}{2} X\right) \quad (3.60)$$

Finally, the time dependence of the second harmonic pulse is calculated by Fourier transforming back equation (3.60):

$$F_{Z2\omega_0}^e(X, t) = \Theta(R^{(b)} - R_{YZ}) \frac{i(2\omega_0)^2 X}{2k_e(2\omega_0)c^2} d_{22} \text{sinc}\left(\frac{\Delta k}{2} X\right) \exp\left(-i \frac{\Delta k}{2} X\right) \frac{1}{2\pi} [F_{Y\omega_0}^o(t)]^2 \quad (3.61)$$

where the inverse Fourier transformation of $G(\omega - 2\omega_0)$ is given by^{§§§}:

$$\int_{-\infty}^{+\infty} \frac{d\omega}{2\pi} G^o(\omega - 2\omega_0) \exp(-i(\omega - 2\omega_0)t) = \frac{1}{2\pi} [F_{Y\omega_0}^o(t)]^2 \quad (3.62)$$

^{†††}In this part, the identity $(\exp(-i\Delta k X) - 1) \frac{1}{\Delta k} = -iX \exp\left(\frac{-i\Delta k X}{2}\right) \text{sinc}\left(\frac{\Delta k}{2} X\right)$ is used.

^{§§§}See equation (B.33) in Appendix A, Section A.4

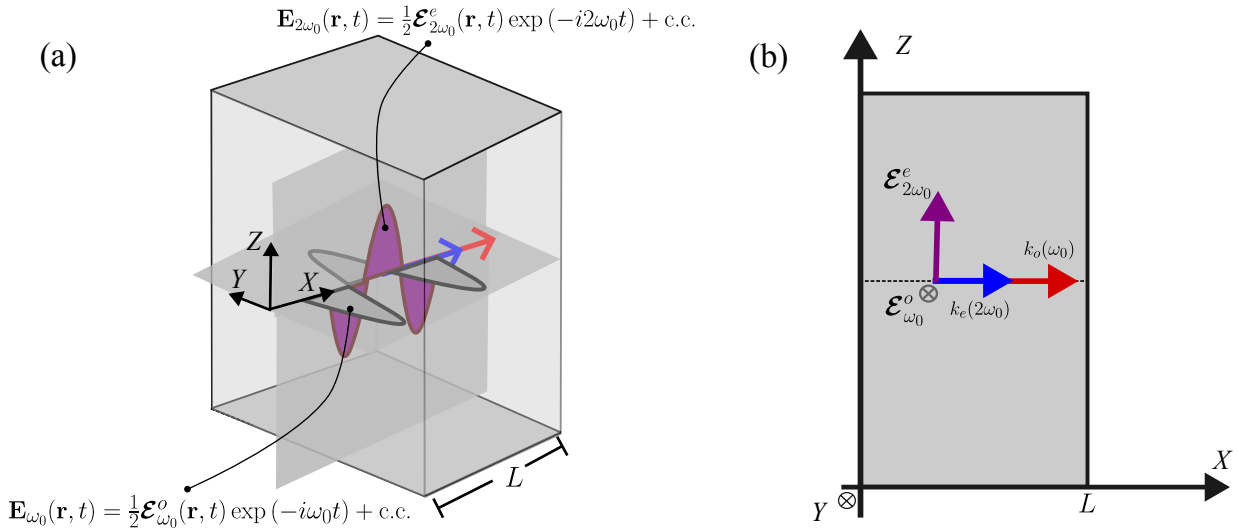


Figure 3.9: Second-harmonic generation at normal incidence: (a) Schematic representation of the interaction within the nonlinear crystal, depicting the conversion of fundamental wave (gray) to second-harmonic wave (purple). (b) Depiction of the wave vector components for the fundamental and second-harmonic waves in the XZ plane.

To compute the second-harmonic intensity, we focus on the region within the beam radius (i.e., $R_{YZ} \leq R^{(b)}$), which leads to $\Theta(R^{(b)} - R_{YZ}) = 1$. In Appendix A, Section A.5, we derive an expression for the average second-harmonic intensity at $X = L$, which is given by (see equation (A.93)):

$$\langle I_{2\omega_0} \rangle = \frac{\omega_0^2 L^2 |d_{22}|^2}{\sqrt{8\pi^5} n_e(2\omega_0) n_o^2(\omega_0) \epsilon_0 c^3} \frac{T_{P_{\omega_0}}}{\tau} \langle I_{\omega_0} \rangle^2 \text{sinc}^2\left(\frac{\Delta k}{2} L\right) \quad (3.63)$$

The average second-harmonic power of the second harmonic radiation is now computed as follows:

$$\langle P_{2\omega_0} \rangle = \langle I_{2\omega_0} \rangle \cdot A_{\text{beam}} = \frac{\omega_0^2 L^2 |d_{22}|^2}{\sqrt{8\pi^5} n_e(2\omega_0) n_o^2(\omega_0) \epsilon_0 c^3} \frac{T_{P_{\omega_0}}}{\tau} \langle I_{\omega_0} \rangle^2 \text{sinc}^2\left(\frac{\Delta k}{2} L\right) A_{\text{beam}} \quad (3.64)$$

Table 3.2 summarizes the values used to evaluate equation (3.64) for clarity. Substituting these values yields a predicted power of 3.44 mW. However, there is still a discrepancy between theory and experiment (i.e., 2.7 mW), which represents a relative error of 22%. The multilayer mirror, designed to reflect light optimally at 1030 nm, is intended to transmit all SHG signal to the detector. However, it turns out to have a finite (possible large) reflectivity at 525 nm^{¶¶¶}. This uncertainty in mirror performance can explain the remaining discrepancy between theory and experiment.

Taking into consideration the absorption of the multilayer mirror, the theoretical prediction developed in this chapter achieves quantitatively agreement with the experimental result of second harmonic generation process at infrared (IR) and visible (VIS) wavelengths.

^{¶¶¶}Communication with the manufacturer revealed a potential reflectivity range for second harmonic generation (SHG) of 10% to 89%.

Crucially, condition (3.36) needs to be considered. The model assumes that the linear contribution dominates in the expansion of the polarization density. Particularizing this condition for the scenario with a temporal Gaussian profile, we obtain the following expressions:

$$\left\| \left\langle \underline{\underline{\epsilon}}_0 \underline{\underline{\chi}}^{(2)}(-2\omega_0; \omega_0, \omega_0) : \mathcal{E}_{\omega_0}(\mathbf{r}, t) \mathcal{E}_{\omega_0}(\mathbf{r}, t) \right\rangle \right\| = \frac{\sqrt{\pi} \epsilon_0 \tau}{T_{P_{\omega_0}}} \frac{2I_{\text{peak}}}{c \epsilon_0 n_o(\omega_0)} \sqrt{|d_{15}|^2 + |d_{22}|^2} \quad (3.65a)$$

$$\left\| \left\langle \underline{\underline{\epsilon}}_0 \underline{\underline{\chi}}^{(1)}(-\omega_0; \omega_0) \cdot \mathcal{E}_{\omega_0}(\mathbf{r}, t) \right\rangle \right\| = \frac{\sqrt{2\pi} \epsilon_0 \tau}{T_{P_{\omega_0}}} |n_o^2(\omega_0) - 1| \left(\frac{2I_{\text{peak}}}{c \epsilon_0 n_o(\omega_0)} \right)^{1/2} \quad (3.65b)$$

With these two expressions, we can rewrite the condition (3.36) as follows:

$$\sqrt{|d_{15}|^2 + |d_{22}|^2} \left(\frac{2I_{\text{peak}}}{c \epsilon_0 n_o(\omega_0)} \right)^{1/2} \ll |n_o^2(\omega_0) - 1| \quad (3.66)$$

The left-hand side yields a value of 0.02, significantly smaller than the 3.97 obtained on the right-hand side, confirming that the condition is satisfied. Purposely, I_{peak} is calculated using equation (3.56). Model evaluation

Table 3.2: Parameters used to evaluate equation (3.63). The first column indicates the reference source for each parameter value. A blank entry signifies that the parameter is a known parameter.

Reference	Parameter	Value
	L	1 mm
	λ_0	1030 nm
Sánchez-Dena et al. ⁶⁹	d_{15}	5 pm/V
	d_{22}	2.5 pm/V
Schalarb and Betzler ⁶⁷	$n_o(\omega_0)$	2.2339
	$n_e(2\omega_0)$	2.2270
	$T_{P_{\omega_0}}$	0.02 ms
	τ	0.112 ps
	A_{beam}	38.01 nm
	P_{ω_0}	2.7 mW

introduces uncertainty due to material-dependent parameters, like the index of refraction and nonlinear coefficients, which are not directly measured in this study. We rely on Schalarb and Betzler's model⁶⁷ for the index of refraction and values reported by Sánchez-Dena et al.⁶⁹ for the nonlinear coefficients. This introduces the possibility of alternative parameter sets yielding similar results.

While directly measuring these parameters would be ideal, it is beyond the scope of this work. However, the derived model provides results consistent with the order of magnitude observed in experimental data. For instance,

in standard nonlinear optics books^{11,29}, one can find the following equation:

$$\mathbb{P}_{2\omega_0} = \frac{2\omega_0^2 L^2}{\epsilon_0 c^3} \frac{|d_{22}|^2}{n_{o,\omega_0}^2 n_{e,2\omega_0}} I_{\omega_0}^2 \operatorname{sinc}^2 \left(\frac{\Delta k}{2} L \right) A_{\text{beam}} \quad (3.67)$$

This expression, with the given parameters in Table 3.2, underestimates the second-harmonic power by at least three orders of magnitude (i.e., nW) compared to measured data (i.e., mW). This stark discrepancy highlights the crucial role of considering temporal effects when modeling second-harmonic generation (SHG) with pulsed light sources.

Having validated the theory for wave propagation in uniaxial crystals, the next step is to extend this framework to explore SHG within the extreme ultraviolet (XUV) regime.

Chapter 4

Wave Propagation in the XUV regime

Building on the exploration of wave propagation within uniaxial crystals in Chapter 3, which focuses on the role of spatio-temporal effects in second harmonic generation (SHG) at the infrared and visible regimes, this chapter expands the scope. We delve deeper into wave propagation within uniaxial crystals, particularly the challenges presented by the extreme ultraviolet (XUV) regime.

While the light-conversion experiment described in Chapter 3 benefits from the favorable transparency window (i.e., low absorption) of the nonlinear medium, lithium niobate (LiNbO_3), spanning 320 nm to 3000 nm⁶⁶, this advantage diminishes significantly at higher energies. For instance, at 514 nm, the linear absorption coefficient α [cm^{-1}] is 0.019 cm^{-1} for light polarized perpendicular to the optic axis, and 0.035 cm^{-1} for parallel polarization⁷⁰. This translates to 1.9% and 3.5% reduction in intensity, respectively, when light travels through a 1 cm sample. However, at XUV wavelengths, absorption becomes a dominant factor, significantly impacting light-conversion efficiency. Drawing on the spatio-temporal framework established in Chapter 3, this chapter incorporates absorption into the description of wave propagation within uniaxial crystals.

4.1 Absorption in Wave Equation

As derived in Chapter 3, Section 3.1.2, the wave equation governing propagation at frequency ω_ℓ with respect to the principal coordinate system XYZ is:

$$\nabla^2 \tilde{\mathcal{E}}_{\omega_\ell}(\mathbf{r}, \omega - \omega_\ell) + \frac{\omega^2}{c^2} \underline{\underline{\epsilon}}(\omega) \cdot \tilde{\mathcal{E}}_{\omega_\ell}(\mathbf{r}, \omega - \omega_\ell) - \beta'_\omega \nabla \left(\hat{Z} \cdot \nabla \right) \left(\tilde{\mathcal{E}}_{\omega_\ell}(\mathbf{r}, \omega - \omega_\ell) \cdot \hat{Z} \right) = -\frac{\omega_\ell^2}{c^2} \tilde{\mathcal{P}}_{\omega_\ell}^{\text{NL}}(\mathbf{r}, \omega - \omega_\ell)$$

where the dielectric tensor $\underline{\underline{\epsilon}}$ and the parameter β'_ω read as follows:

$$\underline{\underline{\epsilon}}(\omega) = \mathbf{I} + \underline{\underline{\chi}}^{(1)}(\omega)$$
$$\beta'_\omega = 1 - \frac{1 + \chi_{ZZ}^{(1)}(\omega)}{1 + \chi_{XX}^{(1)}(\omega)}$$

Here, $\underline{\underline{\chi}}^{(1)}(\omega)$ is the linear susceptibility tensor. To introduce absorption into the wave propagation equation, the linear susceptibility can be written as a complex quantity³:

$$\underline{\underline{\chi}}^{(1)}(\omega) = \text{Re}\{\underline{\underline{\chi}}^{(1)}(\omega)\} + i \text{Im}\{\underline{\underline{\chi}}^{(1)}(\omega)\} \quad (4.1)$$

Consequently, the expression for the dielectric tensor can be rewritten as follows:

$$\underline{\underline{\epsilon}}(\omega) = \mathbf{I} + \text{Re}\{\underline{\underline{\chi}}^{(1)}(\omega)\} + i \text{Im}\{\underline{\underline{\chi}}^{(1)}(\omega)\} \quad (4.2)$$

Taking into consideration expression (4.2), the wave equation becomes:

$$\begin{aligned} \nabla^2 \tilde{\mathcal{E}}_{\omega_\ell}(\mathbf{r}, \omega - \omega_\ell) + \frac{\omega^2}{c^2} \text{Re}\{\underline{\underline{\epsilon}}(\omega)\} \cdot \tilde{\mathcal{E}}_{\omega_\ell}(\mathbf{r}, \omega - \omega_\ell) - \beta'_\omega \nabla \left(\hat{Z} \cdot \nabla \right) \left(\tilde{\mathcal{E}}_{\omega_\ell}(\mathbf{r}, \omega - \omega_\ell) \cdot \hat{Z} \right) = \\ -i \frac{\omega^2}{c^2} \text{Im}\{\underline{\underline{\epsilon}}(\omega)\} \cdot \tilde{\mathcal{E}}_{\omega_\ell}(\mathbf{r}, \omega - \omega_\ell) - \frac{\omega_\ell^2}{c^2} \tilde{\mathcal{P}}_{\omega_\ell}^{\text{NL}}(\mathbf{r}, \omega - \omega_\ell) \end{aligned} \quad (4.3)$$

The real and imaginary part of the dielectric tensor are given by the following expressions:

$$\begin{aligned} \text{Re}\{\underline{\underline{\epsilon}}(\omega)\} &= \mathbf{I} + \text{Re}\{\underline{\underline{\chi}}^{(1)}(\omega)\} \\ \text{Im}\{\underline{\underline{\epsilon}}(\omega)\} &= \text{Im}\{\underline{\underline{\chi}}^{(1)}(\omega)\} \end{aligned}$$

where \mathbf{I} is the identity matrix. To analyze the wave equation (4.3) further, we can introduce convenient shorthand notation for the diagonal components of the real and imaginary parts of the dielectric tensor:

$$\begin{aligned} k_{o,e}(\omega) &= \frac{\omega}{c} \sqrt{1 + \text{Re}\{\chi_{jk}^{(1)}(\omega)\}} \\ &= \frac{\omega}{c} n_{o,e}(\omega) \end{aligned} \quad (4.4a)$$

$$g_{o,e}(\omega) = \frac{\omega}{c} \sqrt{\text{Im}\{\chi_{jk}^{(1)}(\omega)\}} \quad (4.4b)$$

The index of refraction, denoted by $n_{o,e}(\omega)$ for the ordinary and extraordinary waves respectively, relates to the real part of the linear susceptibility through the following equation²⁸:

$$n_{o,e}(\omega) = \sqrt{1 + \text{Re}\{\chi_{jk}^{(1)}(\omega)\}} \quad (4.5)$$

In this context, jk becomes XX for ordinary (o) wave and ZZ for extraordinary (e) wave. Purposely, we denote expression (4.4a) by $k_{o,e}(\omega)$ since they represent the same quantity defined in Chapter 3*. Since we express the dielectric tensor with respect to the principal coordinate system XYZ , the off-diagonal entries of the dielectric tensor

*For example, see equations (3.28) for $\theta = 0$, where θ is the angle between the wave vector and the optic axis. In this case, the quantity is real. Further on in this chapter, we will see that this quantity can be defined as a complex quantity.

are zero. Using expressions (4.4), we can rewrite equation (4.3) as follows:

$$\begin{aligned} \nabla^2 \tilde{\mathcal{E}}_{\omega_\ell}(\mathbf{r}, \omega - \omega_\ell) + \begin{pmatrix} k_o^2(\omega) & 0 & 0 \\ 0 & k_e^2(\omega) & 0 \\ 0 & 0 & k_e^2(\omega) \end{pmatrix} \cdot \tilde{\mathcal{E}}_{\omega_\ell}(\mathbf{r}, \omega - \omega_\ell) - \beta'_\omega \nabla \left(\hat{Z} \cdot \nabla \right) \left(\tilde{\mathcal{E}}_{\omega_\ell}(\mathbf{r}, \omega - \omega_\ell) \cdot \hat{Z} \right) = \\ -i \begin{pmatrix} g_o^2(\omega) & 0 & 0 \\ 0 & g_o^2(\omega) & 0 \\ 0 & 0 & g_e^2(\omega) \end{pmatrix} \cdot \tilde{\mathcal{E}}_{\omega_\ell}(\mathbf{r}, \omega - \omega_\ell) - \frac{\omega_\ell^2}{c^2} \tilde{\mathcal{P}}_{\omega_\ell}^{\text{NL}}(\mathbf{r}, \omega - \omega_\ell) \end{aligned} \quad (4.6)$$

We can gain insights into the behavior of $k_{o,e}(\omega)$ and $g_{o,e}(\omega)$ around the carrier frequency ω_ℓ by employing a Taylor series expansion:

$$k_{o,e}(\omega) = k_{o,e}(\omega_\ell) + \left. \frac{\partial k_{o,e}}{\partial \omega} \right|_{\omega=\omega_\ell} (\omega - \omega_\ell) + \left. \frac{\partial^2 k_{o,e}}{\partial \omega^2} \right|_{\omega=\omega_\ell} (\omega - \omega_\ell)^2 + \dots \quad (4.7a)$$

$$g_{o,e}(\omega) = g_{o,e}(\omega_\ell) + \left. \frac{\partial g_{o,e}}{\partial \omega} \right|_{\omega=\omega_\ell} (\omega - \omega_\ell) + \left. \frac{\partial^2 g_{o,e}}{\partial \omega^2} \right|_{\omega=\omega_\ell} (\omega - \omega_\ell)^2 + \dots \quad (4.7b)$$

Utilizing the results of the Taylor series expansion, we can transform equation (4.6) into the following form:

$$\begin{aligned} \nabla^2 \tilde{\mathcal{E}}_{\omega_\ell}(\mathbf{r}, \omega - \omega_\ell) + \underline{\underline{\mathbf{K}}} \cdot \tilde{\mathcal{E}}_{\omega_\ell}(\mathbf{r}, \omega - \omega_\ell) - \beta'_{\omega_\ell} \nabla \left(\hat{Z} \cdot \nabla \right) \left(\tilde{\mathcal{E}}_{\omega_\ell}(\mathbf{r}, \omega - \omega_\ell) \cdot \hat{Z} \right) = \\ -i \underline{\underline{\mathbf{G}}} \cdot \tilde{\mathcal{E}}_{\omega_\ell}(\mathbf{r}, \omega - \omega_\ell) - \frac{\omega_\ell^2}{c^2} \tilde{\mathcal{P}}_{\omega_\ell}^{\text{NL}}(\mathbf{r}, \omega - \omega_\ell) \end{aligned} \quad (4.8)$$

Here, we introduce $\underline{\underline{\mathbf{K}}}$ that is given by the following expression:

$$\underline{\underline{\mathbf{K}}} = \begin{pmatrix} K_{XX} & 0 & 0 \\ 0 & K_{YY} & 0 \\ 0 & 0 & K_{ZZ} \end{pmatrix}$$

$$K_{jk} = k_{o,e}^2(\omega_\ell) + \left(2k_{o,e}(\omega_\ell) \frac{1}{v_{g^{o,e}}(\omega_\ell)} \right) (\omega - \omega_\ell) + \frac{1}{v_{g^{o,e}}(\omega_\ell)^2} \left(1 - k_{o,e}(\omega_\ell) \frac{\partial v_{g^{o,e}}}{\partial \omega} \Big|_{\omega=\omega_\ell} \right) (\omega - \omega_\ell)^2 + \dots \quad (4.9)$$

Additionally, $\underline{\underline{\mathbf{G}}}$ is expressed as follows:

$$\underline{\underline{\mathbf{G}}} = \begin{pmatrix} G_{XX} & 0 & 0 \\ 0 & G_{YY} & 0 \\ 0 & 0 & G_{ZZ} \end{pmatrix}$$

$$G_{jk} = g_{o,e}^2(\omega_\ell) + 2g_{o,e}(\omega_\ell) \frac{\partial g_{o,e}}{\partial \omega} \Big|_{\omega=\omega_\ell} (\omega - \omega_\ell) + \left[\left(\frac{\partial g_{o,e}}{\partial \omega} \right)^2 \Big|_{\omega=\omega_\ell} + 2g_{o,e}(\omega_\ell) \frac{\partial^2 g_{o,e}}{\partial \omega^2} \Big|_{\omega=\omega_\ell} \right] (\omega - \omega_\ell)^2 + \dots \quad (4.10)$$

Purposely, jk can be XX and YY for ordinary (o) waves, but jk becomes ZZ for extraordinary (e) waves. In addition, $v_g^{o,e}$ represents the group velocity for either ordinary or extraordinary waves. Regarding the parameter β'_{ω_ℓ} , it is written as follows:

$$\begin{aligned}\beta'_{\omega_\ell} &= 1 - \frac{1 + \chi_{ZZ}^{(1)}(\omega)}{1 + \chi_{XX}^{(1)}(\omega)} \\ &= 1 - \frac{[k_e(\omega)]^2 + i[g_e(\omega)]^2}{[k_o(\omega)]^2 + i[g_o(\omega)]^2}\end{aligned}\quad (4.11)$$

where $k_{o,e}(\omega_\ell)$ and $g_{o,e}(\omega_\ell)$ are Taylor expanded around ω_ℓ .

All in all, equation (4.8) describes the pulse propagation with absorption. The left-hand side of this equation preserves the functional form presented in equation (3.25). Consequently, we can use the formalism developed by Eimerl and co-workers⁶⁵ to address the space-related terms in equation (4.8). We highlight that these equations are valid for isotropic crystals (i.e., $n_o = n_e$) as discussed in Chapter 3.

In isotropic crystal, the entries of the linear susceptibility tensor are identical. This means that the real and imaginary parts of each entry do not differ from one another. Consequently, $\beta'_{\omega_\ell} = 0$ from (4.11). Finally, equation (4.8) becomes:

$$\begin{aligned}\nabla^2 \tilde{\mathcal{E}}_{\sigma\omega_\ell}(\mathbf{r}, \omega - \omega_\ell) + \left(f(\omega_\ell) + \frac{\partial f}{\partial \omega} \Big|_{\omega=\omega_\ell} (\omega - \omega_\ell) + \frac{\partial^2 f}{\partial \omega^2} \Big|_{\omega=\omega_\ell} (\omega - \omega_\ell)^2 + \dots \right)^2 \tilde{\mathcal{E}}_{\sigma\omega_\ell}(\mathbf{r}, \omega - \omega_\ell) \\ = -\frac{\omega_\ell^2}{\epsilon_0 c^2} \tilde{\mathcal{P}}_{\sigma\omega_\ell}^{\text{NL}}(\mathbf{r}, \omega - \omega_\ell) - i \left(g(\omega_\ell) + \frac{\partial g}{\partial \omega} \Big|_{\omega=\omega_\ell} (\omega - \omega_\ell) + \frac{\partial^2 g}{\partial \omega^2} \Big|_{\omega=\omega_\ell} (\omega - \omega_\ell)^2 + \dots \right)^2 \tilde{\mathcal{E}}_{\sigma\omega_\ell}(\mathbf{r}, \omega - \omega_\ell)\end{aligned}\quad (4.12)$$

where $\sigma = X, Y, Z$. This compact notation is possible because direction does not play a role in wave propagation through cubic crystals.

The subsequent section revisits the arguments provided in Chapter 3 to assess the relevance of spatial-temporal effects in SHG.

4.2 Diffraction and Dispersion along with Absorption

This section focuses on estimating the impact of absorption on the various criteria introduced in Chapter 3, Section 3.2. Wave propagation of fundamental and harmonic modes in uniaxial crystals can be analyzed using equation (4.8). However, there is no such tractable, analytical, and general approach to deal with coupled nonlinear partial differential equations⁷¹.

Generally, these equations are typically tackled using numerical methods³. However, in an effort to reduce the complexity of these equations, the effect of diffraction and dispersion under absorption are estimated.

Diffraction

Similar to Chapter 3, Section 3.2, there are two characteristic lengths: the diffraction length (L_d) and the sample length (L). However, when absorption starts playing a role in wave propagation, an additional parameter emerges:

the absorption length (L_α). By definition, the imaginary part of the linear susceptibility tensor is related to a previously introduced parameter: the absorption coefficient (α). This relationship is expressed as follows²⁸:

$$\alpha_{o,e}(\omega) = \frac{\omega \operatorname{Im}\{\chi_{jk}^{(1)}(\omega)\}}{n_{o,e}(\omega)c} \quad (4.13)$$

In this expression, $\alpha_{o,e}$ corresponds to either ordinary (when jk involves XX or YY) or extraordinary (when jk corresponds to ZZ) waves. The unit of this quantity is $1/m$. The absorption length is given by: $L_{\alpha_{o,e}} = 1/\alpha_{o,e}$. This length provides an indication of the distance over which the intensity of radiation decreases significantly due to absorption in the material.

In Chapter 3 (Section 3.2), we provide the following criterion for estimating diffraction:

$$L_d \simeq b = \frac{2\pi}{\lambda} W_0^2 > L$$

where L is the length of the sample, and λ is the wavelength within the nonlinear medium. The latter is given by the following expression: $\bar{\lambda}/n_{o,e}$, where $\bar{\lambda}$ stands for the wavelength in vacuum[†], and $n_{o,e}$ corresponds to the ordinary or extraordinary index of refraction. There are two key scenarios to consider regarding the diffraction length (L_d) and the sample length (L): (1) $L_d > L$ and (2) $L_d < L$ (see Fig. 4.1).

In the former, the diffraction length, which characterizes the distance light travels before spreading significantly, is larger than the sample length. This implies that the nonlinear interaction between the light and the medium dominates in comparison with diffraction; light interacts with the medium, potentially leading to effects like second harmonic generation (SHG), before diffracting noticeably.

In the latter, the sample length is larger than the diffraction length. This signifies that diffraction occurs within the nonlinear medium. Diffraction becomes a significant factor alongside the nonlinear interaction, and both effects need to be incorporated into any model describing the light propagation.

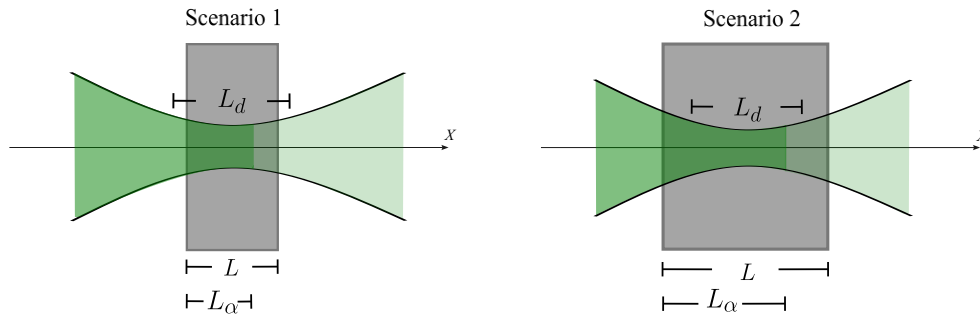


Figure 4.1: Illustration of the key characteristic lengths governing light propagation in a solid crystal, such as LiNbO_3 , considering both absorption and diffraction phenomena. We examine two main scenarios: one where diffraction plays a role (Scenario 1), and another where it does not (Scenario 2), while still considering the effects of absorption.

[†]For the convention of using $\bar{\lambda}$ for the vacuum wavelength, please refer to the footnote on page 48.

Within scenario (1), absorption can be neglected if $L_{\alpha_{o,e}}$ is larger than both L and L_d . This implies that light can propagate through the medium and interact non-linearly with the material before it is appreciably absorbed or diffracted. Conversely, when $L_{\alpha_{o,e}}$ is smaller than both L and L_d , absorption becomes dominant. This weakens the nonlinear interaction and diffraction. In extreme cases, strong absorption can completely prevent light transmission through the material. While we can potentially increase light transmission by adjusting L , it is crucial to do so cautiously. Reducing L excessively can weaken the nonlinear interaction needed for processes, such as SHG.

Therefore, maintaining a suitable sample length is essential for observing nonlinear effects in presence of absorption.

With respect to scenario (2), we can encounter three scenarios[‡]:

- $L_{\alpha_{o,e}} > L$ & $L_{\alpha_{o,e}} > L_d$
- $L_{\alpha_{o,e}} < L$ & $L_{\alpha_{o,e}} > L_d$
- $L_{\alpha_{o,e}} < L$ & $L_{\alpha_{o,e}} < L_d$

In the first case, the length scale of absorption is significantly larger than the scales at which diffraction and nonlinear processes occur. This allows us to neglect absorption in this specific scenario. However, for all other cases, absorption reduces the nonlinear interaction because it takes place within the sample length. In regimes with strong absorption, it can even dominate over nonlinear interaction, leading to a variation of the fundamental field due to the linear effect of absorption rather than any nonlinear effects.

Dispersion

Following Section 4.1, $k_{o,e}(\omega)$ captures the dispersion arising from the real part of the linear susceptibility tensor $\chi_{jk}^{(1)}(\omega)$. To quantify these dispersion effects, we perform a Taylor expansion of $k_{o,e}(\omega)$ around the carrier frequency ω_ℓ (as shown in equation (4.9)). This approach parallels the analysis in Section 3.1 of Chapter 3, allowing us to establish a similar criterion for neglecting group velocity in the expansion around ω_ℓ :

$$\left| \frac{v_g^{o,e} - v_p^{o,e}}{v_p^{o,e}} \right| = \left| \frac{\hbar\omega_\ell \frac{\partial n_{o,e}}{\partial(\hbar\omega)} \Big|_{\hbar\omega=\hbar\omega_\ell}}{n_{o,e}(\omega_\ell) + \hbar\omega_\ell \frac{\partial n_{o,e}}{d(\hbar\omega)} \Big|_{\hbar\omega=\hbar\omega_\ell}} \right| \quad (4.14)$$

For clarity, $v_p^{o,e}$ represents the ordinary/extraordinary phase velocity, and $v_g^{o,e}$ stands for the ordinary/extraordinary group velocity.

Analogous to the dispersion captured by $k_{o,e}(\omega)$ for the real susceptibility, $g_{o,e}(\omega)$ describes the dispersion associated with the imaginary part of the linear susceptibility tensor $\chi_{jk}^{(1)}(\omega)$. Similar to the expansion of $k_{o,e}(\omega)$ in (4.7b) or (4.9), we can expand $g_{o,e}(\omega)$ around the carrier frequency ω_ℓ . For simplicity, we use the expansion given

[‡]Considering the case where $L_{\alpha_{o,e}} > L$ & $L_{\alpha_{o,e}} < L_d$, a contradiction arises. This is because L cannot be both larger and smaller than L_d .

by expression (4.7b):

$$g_{o,e}(\omega) = g_{o,e}(\omega_\ell) + \frac{\partial g_{o,e}}{\partial \omega} \Big|_{\omega=\omega_\ell} (\omega - \omega_\ell) + \frac{\partial^2 g_{o,e}}{\partial \omega^2} \Big|_{\omega=\omega_\ell} (\omega - \omega_\ell)^2 + \dots$$

In this expression, the derivatives read as follows:

$$\frac{\partial g_{o,e}}{\partial \omega} \Big|_{\omega=\omega_\ell} = g_{o,e}(\omega_\ell) \left(\frac{1}{\omega_\ell} + \frac{1}{2} \frac{\partial}{\partial \omega} \left[\log_e \left(\text{Im} \{ \chi_{jk}^{(1)}(\omega_\ell) \} \right) \right] \Big|_{\omega=\omega_\ell} \right) \quad (4.15a)$$

$$\begin{aligned} \frac{\partial^2 g_{o,e}}{\partial \omega^2} \Big|_{\omega=\omega_\ell} = g_{o,e}(\omega_\ell) & \left(\frac{1}{\omega_\ell} \frac{\partial}{\partial \omega} \left[\log_e \left(\text{Im} \{ \chi_{jk}^{(1)}(\omega_\ell) \} \right) \right] \Big|_{\omega=\omega_\ell} - \frac{1}{4} g_{o,e}(\omega_\ell) \frac{\partial}{\partial \omega} \left[\text{Im} \{ \chi_{jk}^{(1)}(\omega_\ell) \} \right] \Big|_{\omega=\omega_\ell} \right. \\ & \left. + \frac{1}{2} \frac{1}{\text{Im} \{ \chi_{jk}^{(1)}(\omega_\ell) \}} \frac{\partial^2}{\partial \omega^2} \left[\text{Im} \{ \chi_{jk}^{(1)}(\omega_\ell) \} \right] \Big|_{\omega=\omega_\ell} \right) \quad (4.15b) \end{aligned}$$

where $g_{o,e}(\omega_\ell)$ is given by expression (4.4b) evaluated at the carrier frequency ω_ℓ :

$$g_{o,e}(\omega_\ell) = \frac{\omega_\ell}{c} \sqrt{\text{Im} \{ \chi_{jk}^{(1)}(\omega_\ell) \}}$$

Moreover, jk corresponds to either XX or YY for ordinary (o) waves, and jk corresponds to ZZ for extraordinary (e) waves. The aim is to develop a criterion to assess the influence of neglecting dispersion-related terms on (4.7b). We specifically focus on a system characterized by a pseudo-monochromatic field (i.e., a wave with a narrow frequency bandwidth, $\Delta\omega \ll \omega_\ell$). This implies we aim to evaluate $g_{o,e}$ at the carrier frequency, ω_ℓ . To achieve this, we establish a condition that guarantees minimal contributions from the first-order dispersion term within a Taylor series expansion, which is written as follows[§]:

$$\left| \frac{1}{4} \frac{\partial}{\partial \hbar\omega} \left[\log_e \left(\text{Im} \{ \chi_{jk}^{(1)} \} \right) \right] \Big|_{\hbar\omega=\hbar\omega_\ell} \right| \ll 1 \quad (4.16)$$

Under this condition, neglecting dispersion-related terms associated with the imaginary part of the first-order susceptibility can be neglected. The next section focuses on deriving and evaluating the SHG intensity (power) at normal incidence in the transmission geometry for X -cut LiNbO₃.

4.3 Normal Incidence & Absorption

We explicitly account for absorption within the wave equation that describes the spatio-temporal evolution of waves propagating through uniaxial crystals. This approach aligns perfectly with the fact that contemporary XUV radiation sources, like SACLA and FERMI^{15,21}, emit radiation in the form of pulses. The scenario modeled in this section is illustrated in Fig. 4.2. The nonlinear medium under consideration is the X -cut LiNbO₃. There is an incident

[§]For a detailed derivation of the absorption criterion, refer to Appendix B, Section B.1.

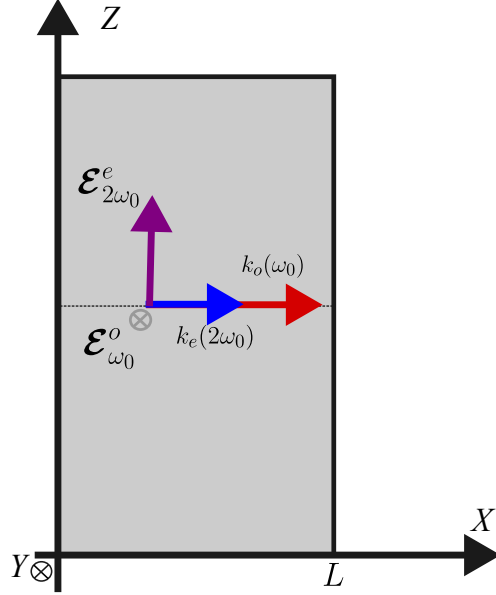


Figure 4.2: Wave propagation of the fundamental and second-harmonic waves through the nonlinear material at normal incidence.

fundamental radiation pulse at a carrier frequency ω_0 . This wave propagates along the principal axis X , while the electric field is polarized along Y . In the case where the nonlinear medium is a uniaxial crystal, the fundamental electric field, under this geometry, is ordinary polarized. The fundamental wave strikes the surface at normal incidence, transmitting into the crystal. The nonlinear response is given by the following expression:

$$\mathcal{P}_{2\omega_0}^{\text{NL}}(\mathbf{r}, t) = \epsilon_0 \begin{pmatrix} -d_{33} & -d_{31} & -d_{31} & 0 & 0 & 0 \\ 0 & 0 & 0 & 0 & d_{22} & -d_{15} \\ 0 & d_{22} & -d_{22} & 0 & -d_{15} & 0 \end{pmatrix} \begin{pmatrix} \mathcal{E}^2(\mathbf{r}, t) \\ X\omega_0 \\ \mathcal{E}^2(\mathbf{r}, t) \\ Y\omega_0 \\ \mathcal{E}^2(\mathbf{r}, t) \\ Z\omega_0 \\ 2\mathcal{E}^2(\mathbf{r}, t)_{Y\omega_0} \mathcal{E}^2(\mathbf{r}, t)_{Z\omega_0} \\ 2\mathcal{E}^2(\mathbf{r}, t)_{X\omega_0} \mathcal{E}^2(\mathbf{r}, t)_{Z\omega_0} \\ 2\mathcal{E}^2(\mathbf{r}, t)_{X\omega_0} \mathcal{E}^2(\mathbf{r}, t)_{Y\omega_0} \end{pmatrix} \quad (4.17)$$

Referring to Table 2.2, the d -matrix possesses two distinct representations. The first representation is applicable when the Kleinman symmetry is broken, whereas the second is valid under this symmetry. Due to the high energy of the employed XUV radiation, the former representation is more appropriate because of the absorption within the material. As discussed in Chapter 3, we rotate the d -matrix for the $3m$ crystal class in Table 2.2 to accurately describe this quantity for the X -cut LiNbO_3 . In the particular case that the fundamental field is polarized along Y

(ordinary o), the components of the nonlinear polarization in equation (4.17) become:

$$\mathcal{P}_{X2\omega_0}^{\text{NL}} = -\epsilon_0 d_{31} [\mathcal{E}_{Y\omega_0}^o(\mathbf{r}, t)]^2 \quad (4.18a)$$

$$\mathcal{P}_{Y2\omega_0}^{\text{NL}} = 0 \quad (4.18b)$$

$$\mathcal{P}_{Z2\omega_0}^{\text{NL}} = \epsilon_0 d_{22} [\mathcal{E}_{Y\omega_0}^o(\mathbf{r}, t)]^2 \quad (4.18c)$$

We solely consider the Z component of the nonlinear response (Eq. 4.18c) because only the second-harmonic wave polarized along the optical axis propagates effectively through the nonlinear medium. This is further elaborated in Chapter 3, where we conclude that the generated second-harmonic wave only propagates when aligned with the optical axis.

In analyzing equation (4.8), we employ the same parameterization for both the fundamental and second-harmonic waves as presented in Chapter (3):

$$\tilde{\mathcal{E}}_{Y\omega_0}^o(\mathbf{r}, \omega - \omega_0) = \Theta(R^{(b)} - R_{YZ}) \tilde{F}_{Y\omega_0}^o(X, \omega - \omega_0) \exp(i k_o(\omega_0) X) \quad (4.19a)$$

$$\tilde{\mathcal{E}}_{Z2\omega_0}^e(\mathbf{r}, \omega - 2\omega_0) = \Theta(R^{(b)} - R_{YZ}) \tilde{F}_{Z2\omega_0}^e(X, \omega - 2\omega_0) \exp(i k_e(2\omega_0) X) \quad (4.19b)$$

where $\Theta(R^{(b)} - R_{YZ})$ is a Heaviside function given by:

$$\Theta(R^{(b)} - R_{YZ}) = \begin{cases} 1 & , \text{ for } R^{(b)} \leq R_{YZ} \text{ where } R_{YZ} = \sqrt{Y^2 + Z^2} \\ 0 & , \text{ otherwise} \end{cases} \quad (4.20)$$

In equations (4.19), the fundamental wave polarized along the Y-axis is denoted as o , while the generated second-harmonic wave polarized along the Z-axis is denoted as e . This distinction between ordinary (o) and extraordinary (e) waves is inherent to this model, as established in Chapter 3. Section 4.4 will demonstrate that this distinction remains valid even when considering nonlinear effects, as the identification is determined by linear effects.

As a reminder from Chapter 2, ordinary waves exhibit polarizations perpendicular to the plane formed by the wave vector and the optical axis, which in this case coincides with the XZ plane. Conversely, waves polarized within this plane are referred to as extraordinary waves.

We will now focus on the area where the distance from the beam center (denoted by R_{YZ}) is less than or equal to the beam radius $R^{(b)}$. Within this region, the Heaviside function equals unity. Additionally, the diffraction, and absorption criteria are assumed to be valid. Later, we will re-visit these criteria.

There is a crucial distinction between the scenario explored in Chapter 3 and the current case when considering the applicability of the approximation based on the criterion (4.14). In Chapter 3, we established that the phase velocity did not deviate considerably from the group velocity. This allowed us to simplify the Taylor series expansion (refer to equation (3.26a)) by focusing solely on the term associated with the phase velocity. For clarity, the phase

velocity and the group velocity are given below:

$$v_p^{o,e} = \frac{c}{n_{o,e}(\omega_\ell)} \quad (4.21a)$$

$$v_g^{o,e} = \frac{c}{n(\omega_\ell) + \hbar\omega_\ell \left. \frac{\partial n_{o,e}}{\partial(\hbar\omega)} \right|_{\hbar\omega=\hbar\omega_\ell}} \quad (4.21b)$$

Wavefront propagation describes the movement of a specific phase (crest, trough, for instance) of a wave, traveling at the phase velocity. However, the information carried by the wave, often represented by the peak of a pulse, propagates at a different speed known as the group velocity⁷². As discussed in Chapter 3, when the difference between group and phase velocities is minimal, we can calculate the time-averaged second-harmonic power using the phase velocity.

Notably, since both the ordinary and extraordinary refractive indices are greater than one, the phase velocity in this case was slower than the speed of light. However, this behavior differs in the XUV region for LiNbO₃ since the index of refraction is less than unity (see Section 4.5, Fig. 4.6). This necessitates including the second term in the Taylor expansion presented in equation (4.9) in order to incorporate explicitly the group velocity. Then, using expressions (4.19), equation (4.8) for $\omega_\ell = \omega_0$ and $\omega_\ell = 2\omega_0$ become:

$$\begin{aligned} \frac{\partial}{\partial X} \tilde{F}_{Y\omega_0}^o(X, \omega - \omega_0) + \frac{1}{2} \alpha_o(\omega_0) \tilde{F}_{Y\omega_0}^o(X, \omega - \omega_0) - \frac{i(\omega - \omega_0)}{v_g^o} \tilde{F}_{Y\omega_0}^o(X, \omega - \omega_0) \\ = \frac{i(\omega_0)^2}{2k_o(\omega_0)\epsilon_0 c^2} \tilde{\mathcal{P}}_{Y\omega_0}^{\text{NL}}(\mathbf{r}, \omega - \omega_0) \exp(-i k_o(\omega_0) X) \end{aligned} \quad (4.22a)$$

$$\begin{aligned} \frac{\partial}{\partial X} \tilde{F}_{Z2\omega_0}^e(X, \omega - 2\omega_0) + \frac{1}{2} \alpha_e(2\omega_0) \tilde{F}_{Z2\omega_0}^e(X, \omega - 2\omega_0) - \frac{i(\omega - 2\omega_0)}{v_g^e} \tilde{F}_{Z2\omega_0}^e(X, \omega - 2\omega_0) \\ = \frac{i(2\omega_0)^2}{2k_e(\omega_0)\epsilon_0 c^2} \tilde{\mathcal{P}}_{Z2\omega_0}^{\text{NL}}(\mathbf{r}, \omega - 2\omega_0) \exp(-i k_e(2\omega_0) X) \end{aligned} \quad (4.22b)$$

The derivation of these equations follows a similar approach to that detailed in Appendix A, Section A.4. These extended equations account for absorption in both the fundamental wave (denoted by $\alpha_o(\omega_0)$) and the second-harmonic wave (denoted by $\alpha_e(2\omega_0)$) wave. One potential simplification arises when the second-order material response is significantly weaker than the absorption experienced by the fundamental wave.

Within the nonlinear medium, the interaction with the second harmonic wave (SHG) minimally modifies the fundamental wave compared to the attenuation caused by absorption. Under this assumption, equation (4.22a) can be reduced to:

$$\frac{\partial}{\partial X} \tilde{F}_{Y\omega_0}^o(X, \omega - \omega_0) + \frac{1}{2} \alpha_o(\omega_0) \tilde{F}_{Y\omega_0}^o(X, \omega - \omega_0) - \frac{i(\omega - \omega_0)}{v_g^o} \tilde{F}_{Y\omega_0}^o(X, \omega - \omega_0) \approx 0 \quad (4.23)$$

This assumption enables the decoupling of the fundamental wave from the harmonic wave, leading to a simplified form of Equation (4.22a). In many SHG experiments, a common scenario arises: the nonlinear crystal is illuminated solely by fundamental light, with no second harmonic radiation present at the beginning of the nonlinear medium

($X = 0$). Mathematically, this statement is expressed as follows:

$$F_{Y\omega_0}^o(0, t) = K \exp\left(-\frac{t^2}{2\tau^2}\right) \quad (4.24a)$$

$$F_{Z2\omega_0}^e(0, t) = 0 \quad (4.24b)$$

Building on Chapter 3, we again consider a Gaussian temporal profile at the interface for the fundamental wave, where K is a constant with units of V/m. Additionally, τ represents the pulse length. The solution to equation (4.23) in the time-domain is then given by:

$$F_{Y\omega_0}^o(X, t) = K \exp\left(-\frac{\alpha_o(\omega_0)}{2}X\right) \exp\left(-\frac{1}{2\tau^2}\left(t - \frac{1}{v_g^o}X\right)^2\right) \quad (4.25)$$

In Appendix B, Section B.2, we obtain the solution of equation (4.22b) under the boundary condition (4.24):

$$F_{Z2\omega_0}^e(X, t) = \frac{i\omega_0 d_{22} G^o(\omega - 2\omega_0) \exp(i\theta)}{n_e(2\omega_0) c \sqrt{\frac{\alpha_e(2\omega_0)}{2} - \alpha_o(\omega_0) - i\Delta k}} \left[\exp\left([- \alpha_o(\omega_0) - i\Delta k]X\right) - \exp\left(-\frac{1}{2}\alpha_e(2\omega_0)X\right) \right] \frac{1}{2\pi} (F_{Y\omega_0}^o(t))^2 \quad (4.26)$$

where θ is given by:

$$\theta = \pi + \arctan\left[\left(\frac{\alpha_e(2\omega_0)}{2} - \alpha_o(\omega_0)\right)/\Delta k\right] \quad (4.27)$$

In Appendix B, Section B.2, we employ the narrow-band approximation to derive expression (4.26). This approximation assumes that deviations from the central frequency are significantly smaller than the central frequency itself.

Having computed the fundamental (4.25) and second-harmonic (4.26) envelopes, we will now focus on deriving an expression for the time-averaged fundamental and second-harmonic intensity (power). We are interested in the time-averaged fundamental intensity at the beginning of the nonlinear medium. We obtain an expression for the time-averaged fundamental intensity through the following expression which is derived in Appendix C:

$$\langle I_{\omega_0} \rangle = \left\| \frac{1}{T_{P\omega_0}} \int_{-\frac{1}{2}T_{P\omega_0}}^{+\frac{1}{2}T_{P\omega_0}} dt \frac{1}{2} \operatorname{Re}\{\mathcal{E}_{\omega_0}(X, t) \times \mathcal{H}_{\omega_0}^*(X, t)\} \right\| \quad (4.28)$$

Here, $T_{P\omega_0}$ stands for the period-repetition time. Appendix B, Section B.2, details the derivation of expression (B.11), culminating in the following expression:

$$\langle I_{\omega_0} \rangle = I_{\text{peak}} \frac{1}{T_{P\omega_0}} \sqrt{\pi} \tau \quad (4.29)$$

where I_{peak} is given by the following expression:

$$I_{\text{peak}} = \frac{\langle \mathbb{P}_{\omega_0} \rangle}{\sqrt{\pi} A_{\text{beam}}} \left(\frac{T_{P\omega_0}}{\tau} \right) \quad (4.30)$$

The expression (4.29) is obtained using equation (3.50) introduced in Chapter 3. For clarity, we write equation (3.50) below:

$$\langle I_{\omega_0, 2\omega_0} \rangle = \frac{\langle \mathbb{P}_{\omega_0, 2\omega_0} \rangle}{A_{\text{beam}}} = \frac{\langle \mathbb{P}_{\omega_0, 2\omega_0} \rangle}{\pi W_0^2} \quad (4.31)$$

Finally, we calculate the time-averaged second-harmonic intensity (power) through the following expression:

$$\langle I_{2\omega_0} \rangle = \left\| \frac{1}{T_{\text{P}\omega_0}} \int_{-\frac{1}{2}T_{\text{P}\omega_0}}^{+\frac{1}{2}T_{\text{P}\omega_0}} dt \frac{1}{2} \text{Re} \{ \mathcal{E}_{2\omega_0}(X, t) \times \mathcal{H}_{2\omega_0}^*(X, t) \} \right\| \quad (4.32)$$

Analogous to the derivation of the time-averaged fundamental intensity, we can obtain an expression for the time-averaged second-harmonic intensity using equation (4.32); evaluating such expression at $X = L$ yields:

$$\langle I_{2\omega_0} \rangle = \frac{\omega_0^2 |d_{22}|^2}{\sqrt{8\pi^5} n_o^2(\omega_0) n_e(2\omega_0) c^3 \epsilon_0} \left(\frac{T_{\text{P}\omega_0}}{\tau} \right) \langle I_{\omega_0} \rangle^2 \mathcal{F}(L) \quad (4.33)$$

Here, $\mathcal{F}(L)$ is given by the following expression:

$$\mathcal{F}(L) = \frac{\sin^2 \left(\frac{\Delta k}{2} L \right) + \sinh^2 \left(\left[\frac{1}{2} \alpha_o(\omega_0) - \frac{1}{4} \alpha_e(2\omega_0) \right] L \right)}{\left[\left(\alpha_o(\omega_0) - \frac{\alpha_e(2\omega_0)}{2} \right) \frac{L}{2} \right]^2 + \left(\frac{\Delta k}{2} L \right)^2} L^2 \exp \left(- \left[\alpha_o(\omega_0) + \frac{1}{2} \alpha_e(2\omega_0) \right] L \right) \quad (4.34)$$

The time-averaged second-harmonic power reads as follows:

$$\langle \mathbb{P}_{2\omega_0} \rangle = \frac{\omega_0^2 |d_{22}|^2}{\sqrt{8\pi^5} n_o^2(\omega_0) n_e(2\omega_0) c^3 \epsilon_0} \left(\frac{T_{\text{P}\omega_0}}{\tau} \right) \langle I_{\omega_0} \rangle^2 A_{\text{beam}} \mathcal{F}(L) \quad (4.35)$$

Compared to the expression for the time-averaged second-harmonic power derived in Chapter 3 (equation 3.64), equation (4.35) shows a key difference. Equation (4.35) shows a distinct dependence on the length (L) of the nonlinear medium. In contrast to equation (3.64), it shows an exponential decay of the second-harmonic signal with increasing length (L).

Additionally, when absorption is present, the nonlinear coefficient d_{22} becomes a complex quantity. In contrast, in equation (3.64), d_{22} is a real coefficient. In the next section, we will revisit the validity condition introduced in Chapter 3 for using ordinary and extraordinary waves in the context of nonlinear effects.

4.4 On ordinary and extraordinary waves

We derive the wave propagation equation incorporating absorption, distinguishing between ordinary and extraordinary waves. This distinction is based on the linear polarization density. Therefore, we implicitly assume that the nonlinear interaction of the fundamental wave with the medium is significantly weaker than the linear interaction:

$$\begin{aligned} & \left\| \langle \mathcal{P}_{2\omega_0}^{\text{NL}} \rangle \right\| \ll \left\| \langle \mathcal{P}_{\omega_0}^{(1)} \rangle \right\| \\ & \left\| \left\langle \epsilon_0 \underline{\underline{\chi}}^{(2)}(-2\omega_0; \omega_0, \omega_0) : \mathcal{E}_{\omega_0}(\mathbf{r}, t) \mathcal{E}_{\omega_0}(\mathbf{r}, t) \right\rangle \right\| \ll \left\| \left\langle \epsilon_0 \underline{\underline{\chi}}^{(1)}(-\omega_0; \omega_0) \cdot \mathcal{E}_{\omega_0}(\mathbf{r}, t) \right\rangle \right\| \end{aligned} \quad (4.36)$$

This condition is introduced specifically in Chapter 3. Building upon the approach presented there, we develop condition (4.36) in this section. Similar to Chapter 3, we assume the fundamental wave follows a Gaussian profile in time. Additionally, the fundamental wave is polarized along the Y -axis (ordinary wave) propagating along the X -axis. Consequently, condition (4.36) becomes:

$$\sqrt{|d_{31}|^2 + |d_{22}|^2} \left(\frac{2I_{\text{peak}}}{c\epsilon_0 n_o(\omega_0)} \right)^{1/2} \ll \sqrt{(\text{Re}\{\epsilon_{YY}(\omega_0) - 1\})^2 + (\text{Im}\{\epsilon_{YY}(\omega_0)\})^2} \quad (4.37)$$

This condition differs from the one presented in Chapter 3 since it incorporates absorption. This is achieved by considering the imaginary part of the dielectric function.

With the time-averaged second-harmonic power expression derived, we can now evaluate this model. However, material-dependent parameters are crucial for this evaluation, including the nonlinear coefficients and refractive indices. These parameters will be addressed in the following section.

4.5 Study Case: LiNbO₃ in XUV

This section focuses on applying the theory developed thus far to the study of wave propagation within a uniaxial medium, specifically in the XUV regime. The aim is to provide a collection of parameters necessary to evaluate the formalism. These parameters fall into two categories: material-dependent parameters, such as nonlinear coefficients (d_{22}) and refractive indices (n_o and n_e); and light source parameters (i.e., laser), such as the period-repetition time and pulse width. We are interested in the following energy range: 32 eV - 72 eV.

Building upon the foundational concepts of Density Functional Theory (DFT) introduced in Chapter 2, this section focuses on the practical aspects of material property simulations. We will utilize the GPAW^{73,74} code to calculate the dielectric function of LiNbO₃, while `Exciting`⁴⁷ will be employed to calculate the nonlinear coefficients. The underlying physical principles and approximations employed by these codes are detailed in Chapter 2.

Material-dependent parameters

There are various methods for obtaining optical parameters of materials, including experimental approaches and numerical simulations. Furthermore, databases are available to retrieve information on optical parameters of different materials. For instance, when operating at high energies such as XUV or X-rays, the Center for X-Ray Optics provides a database of refractive indices in the XUV and X-ray regions⁷⁵. However, in the case of LiNbO₃, there is no information regarding whether the values reported in that database correspond to either ordinary or extraordinary refractive indices. Since our formalism requires distinguishing between the indices of refraction, we must choose between an experimental or numerical approach.

Regarding the latter, Density Functional Theory (DFT) is a popular modeling method to investigate the properties of materials; several software packages based on DFT are available to carry out theoretical calculations, such as GPAW (Grid-based Projector-Augmented Wave)^{73,74}, VASP (Vienna Ab initio Simulation Package)⁷⁶, Elk⁷⁷, and `Exciting`⁴⁷. As stated previously, we use GPAW to compute the dielectric tensor elements, while `Exciting` is

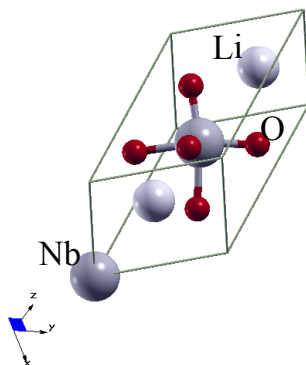


Figure 4.3: LiNbO_3 is depicted in its primitive cell, which represents the smallest unit of bulk LiNbO_3 . In this configuration, LiNbO_3 is described with two niobium (Nb) atoms, two lithium (Li) atoms, and six oxygen (O) atoms.

employed to calculate the nonlinear coefficients.

GPAW is based on the projector-augmented wave (PAW) method⁷³. Through the PAW method, GPAW is able to calculate all-electron properties efficiently. GPAW offers three approaches to study properties of materials: plane-wave⁷³, real-space uniform grids⁷⁸, and atom-centered basis functions⁷⁹. In this section, the plane-wave mode⁷³ is used to calculate the dielectric tensor⁸⁰.

Regarding the calculations of the second-order susceptibility tensor elements, we use the `Exciting` code, which is a full potential all-electron augmented linearized plane wave package. GPAW and `Exciting` work in plane-wave mode to treat valence electrons, but the latter does not rely on the PAW method to simulate all-electron properties. Instead, `Exciting` is based on the linearized augmented plane wave (LAPW) method⁸¹, explicitly taking into consideration not only valence but also core electrons. `Exciting` deals with core electrons through a different basis set, which utilizes spherical harmonic functions. This is why `Exciting` is more computationally demanding.

In the simulations conducted in this section, the treatment of exchange and correlation, accounting for the interactions between electrons within a material, is represented by the generalized gradient approximation (GGA) using the Perdew-Burke-Ernzerhof (PBE)³⁶ functional in both GPAW and `Exciting` codes.

We aim at simulating the linear and nonlinear optical response of LiNbO_3 using the software packages GPAW and `Exciting`. The crystallographic structure of LiNbO_3 is retrieved from the Open Quantum Materials Database (OQMD)^{82,83}. The system can be described using a rhombohedral 10-atom unit cell with space group $R3c$. The projector-augmented-wave (PAW) method⁴² is used to model the electron-ion interaction in the GPAW calculations. In this study, PAW setups are used for each element: Li $1s^22s^1$, Nb $4s^24p^64d^45s^1$, and O $2s^2p^4$. They correspond to the valence states. These configurations align with the standard species file used by the `Exciting` code for both the muffin-tin and interstitial regions. Maintaining a consistent description across these codes minimizes

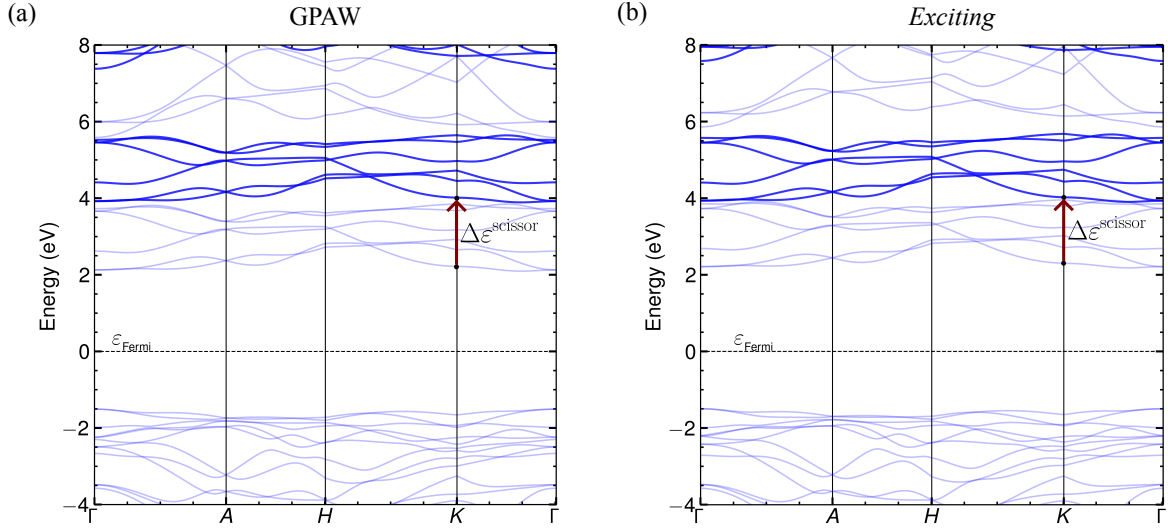


Figure 4.4: Electronic band structure of (bulk) LiNbO_3 calculated using (a) GPAW and (b) `Exciting` codes. The Kohn-Sham (KS) energies are plotted along high-symmetry lines of the Brillouin zone. Fading blue lines represent the KS energies before applying a scissor operator to the unoccupied (conduction band) levels, depicted as solid blue lines. Energies are relative to the Fermi energy.

discrepancies in the calculated electronic structures.

In simulating properties of materials, achieving a converged ground-state calculation is the critical first step. This involves considering two key parameters: number of basis functions, and the Brillouin zone sampling. The former involves the number of basis (linearized augmented) plane-wave functions used to expand the electron wave functions while the latter determines the size of the mesh used to sample the Brillouin zone of the system. Many properties of a solid, including the total energy, are represented as integrals, performed over all possible \mathbf{k} -vectors. Obviously, the direct calculation of these integrals is very demanding. Therefore, the integrals are approximated by sums performed on a set of \mathbf{k} -points distributed on a finite grid.

We detail the convergence test performed in Appendix E to ensure a good description of the ground-state calculations. We achieve this by fixing the \mathbf{k} -mesh size and analyzing how increasing the basis set dimension impacts the total energy per atom. As the difference in energy between calculations with increasing basis functions progressively decreases (see Figs. E.1 in Appendix E), this difference serves as an estimate for the accuracy of the calculated energy. In GPAW, we achieve an accuracy of 1 meV. Once a basis set size is chosen within this accuracy, we vary the \mathbf{k} -mesh size. In this case, the total energy per atom shows minimal variation, indicating that the chosen \mathbf{k} -mesh size has a negligible impact on the total energy calculation.

Using GPAW, we calculate the relaxed ground-state geometry and determine a lattice constant of $a = 5.562 \text{ \AA}$. However, the GGA-PBE functional can slightly overestimate lattice constants⁸⁴. This is indeed observed here, as the experimental lattice constant⁶⁹ is 5.492 \AA . This translates to an overestimation of around 1.3%, which can be attributed

to the limitations of the chosen functional. We use this relaxed geometry in `Exciting` to perform the convergence tests of the total energy. `Exciting` achieves an accuracy of 0.01 eV (see Fig. ??`Exciting_convergencefig` : `Exciting_convergencependix E`).

To quantify how the discrepancy in total energy per atom impacts the electronic structure, we directly compare the band structures obtained using GPAW and `Exciting` (see Fig. 4.4). Both methods exhibit qualitatively similar band structures, as shown by the semi-transparent blue lines in the figure. Notably, in both calculations, the valence-band maximum (VBM) is located at the Γ point, while the conduction-band minimum (CBM) lies along the $K-\Gamma$ path. This observation aligns well with previous theoretical studies^{84,85}. Within the single-particle approximation, LiNbO_3 exhibits an indirect band gap of 3.60 eV and 3.66 eV for GPAW and `Exciting`, respectively. These values are in good agreement with each other, and also align well with other DFT calculations reporting band gaps of 3.61 eV⁸⁵, 3.60 eV⁵⁴, 3.48 eV⁸⁴, and 3.50 eV⁸⁶.

While both GPAW and `Exciting` offer comparable electronic structures within this level of theory, a more precise description of the occupied and unoccupied bands is crucial for calculating the dielectric function and non-linear coefficients. Since DFT often underestimates band gaps⁴⁴, a correction to the calculated band gap for LiNbO_3 is necessary before calculating the optical response.

DFT-GGA underestimates the optical gap because it neglects important physical phenomena. These phenomena include the interaction between electrons and holes (excitonic effects) and the influence of electronic self-energy effects (quasi-particle corrections)⁵⁴. Arthur Riefer and collaborators⁸⁷ utilize the G_0W_0 approach, a non-self-consistent method, to calculate the quasi-particle spectrum of LiNbO_3 . This approach yields a band gap value of 5.4 eV. However, they acknowledge the influence of polar nature of this material on band gap calculations, as highlighted in prior work by Schmidt and co-workers⁸⁴.

The polar character of LiNbO_3 gives rise to longitudinal optical phonons, which can generate macroscopic electric fields that impact excited electrons and holes. Schmidt et al. estimate that electron-phonon coupling could potentially increase the band gap to a range between 5.4 and 6.5 eV. Riefer et al.⁵⁴ revisit this topic in a more comprehensive study, employing a quasiparticle self-consistent approach. Additionally, they explicitly incorporate thermal effects to account for lattice vibrations. This refined approach yields a band gap of 5.4 eV for LiNbO_3 . They conclude that the previous reported band gaps^{84,87} rely on a fortuitous error cancellation between the simplified evaluation of the self-energy and the neglect of lattice vibrations.

We shift the calculated KS unoccupied states with respect to a quasi-particle G_0W_0 band gap of 5.4 eV using the scissor operator, as described in Chapter 2. This value is chosen based on our review of previous literature on LiNbO_3 band gap calculations, as discussed earlier. This approach leads to scissor operator values of $(\Delta\epsilon^{\text{Scissor}})$ 1.8 and 1.73 eV for the GPAW and `Exciting` band gaps, respectively.

The application of the scissor operator is depicted in Fig. 4.4. In this thesis, we do not take into consideration excitonic effects when modelling the band gap. Consequently, we overestimate the optical band gap. This overestimation becomes more significant when the energy range under study approaches the optical band gap of the material.

Having incorporated the self-energy corrections, we aim to model the optical response of the material. A total of 213 empty states are included to account for excitation up to twice the incoming photon energy for both linear and nonlinear responses. The transition energy from the valence band maximum to the highest energy unoccupied eigenstate with the scissor operator yields 89 eV and 88.72 eV for GPAW and `Exciting`, respectively.

The dielectric tensor is calculated based on the Random-Phase Approximation (RPA)⁸⁰, while the second-order susceptibility tensor is evaluated using the formalism outlined by Sharma and Ambrosch-Draxl¹⁷, as implemented within `Exciting`. The level of theory employed in the linear response calculation is kept consistent with the second harmonic response calculation. Both RPA and Sharma and Ambrosch-Draxl's method are particle-independent approximations. The calculations of the dielectric tensor components are depicted in Fig. 4.5. Comparing with experimental data extracted from Ref. 18, the calculated imaginary part of the dielectric function shows a qualitative agreement with the experimental data, except for an overestimation of the peak located around 37 eV and a red-shifted of the calculated spectrum with respect to the experimental data.

As previously noted in another study¹⁸, this characteristic peak is common at this level of theory (i.e., in the particle-independent approximation). This pronounced peak appears not only in the imaginary part but also in the real part of the dielectric tensor components. This peak is attributed to the transition metal oxides: the NbO₆ octahedron. The transition metal ion (Nb) is surrounded by an octahedral cage of six oxygen ions, the so-called ligands, which create a crystal field with cubic symmetry acting on the *d*-electrons of the transition metal atom: *t_{2g}* and *e_g*. This pronounced peak around 37 eV is attributed to *t_{2g}* orbitals. To properly sample the *t_{2g}* peak, many-body effects would need to be included.

Additionally, while adjusting the broadening parameter can improve the fit to experimental data, it can also obscure the difference between the ordinary and extraordinary dielectric functions. From the real and imaginary part of the dielectric function, we can compute the ordinary and extraordinary index of refraction as follows⁸⁸:

$$n_{o,e} = \left[\frac{1}{2} \left(\sqrt{\text{Re}\{\epsilon_{ij}\}^2 + \text{Im}\{\epsilon_{ij}\}^2} + \text{Re}\{\epsilon_{ij}\} \right) \right]^{1/2} \quad (4.38)$$

In this context, *jk* becomes *XX* for ordinary (*o*) and *ZZ* for extraordinary. As previously stated in Chapter 2, uniaxial crystals are optically anisotropic as pointed out in equation (2.9):

$$\underline{\underline{\epsilon}} = \begin{pmatrix} \epsilon_{XX} & 0 & 0 \\ 0 & \epsilon_{XX} & 0 \\ 0 & 0 & \epsilon_{ZZ} \end{pmatrix}$$

Within the material, the linear interaction between the medium and light can be categorized as ordinary or extraordinary. Ordinary refers to the linear response of the material when light propagates perpendicular to the optical axis (i.e, *X*-axis or *Y*-axis). Conversely, extraordinary describes the linear response along the optical axis (i.e., *Z*-axis).

The ordinary and extraordinary absorption coefficients can also be computed from the dielectric tensor components as follows⁸⁸:

$$\alpha_{o,e} = \frac{\sqrt{2}\omega}{c} \left[\sqrt{\text{Re}\{\epsilon_{ij}\}^2 + \text{Im}\{\epsilon_{ij}\}^2} - \text{Re}\{\epsilon_{ij}\} \right]^{1/2} \quad (4.39)$$

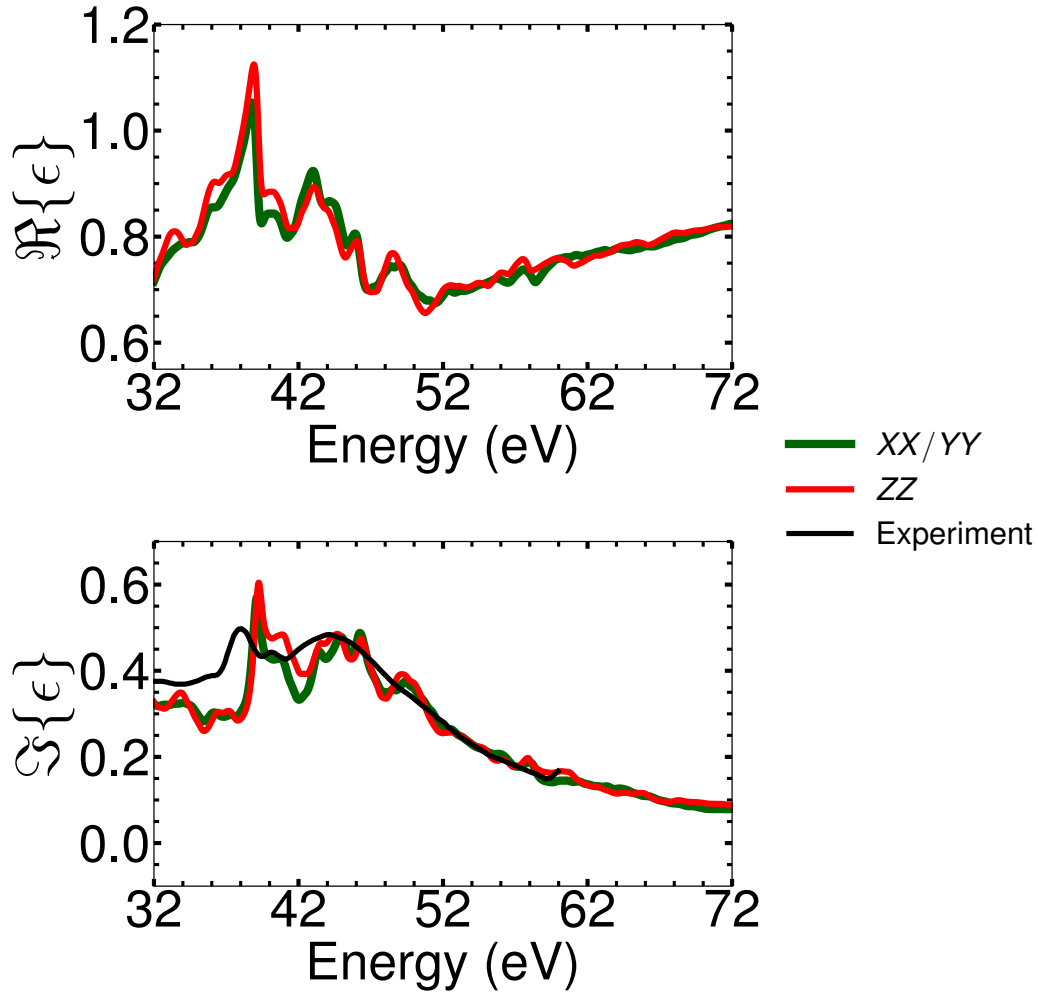


Figure 4.5: Visualization of the calculated real part and the imaginary part of the dielectric tensor components of LiNbO_3 along the X and Z axes. In the bottom, the black solid line represents experimental data extracted from the work of Can B. Uzundal and collaborators¹⁸. A broadening of 0.25 eV is applied.

The refractive indices and absorption coefficients, as derived from equations (4.38) and (4.39), are illustrated in Fig. 4.6. The calculated refractive indices generally follow the experimental trend, but significantly overestimate the peak around 37 eV. This overestimation likely originates from the real and imaginary parts of the dielectric function, which are also overestimated in this region. Consequently, we will exclude the data from 36 to 50 eV when selecting values for the index of refraction and absorption coefficient.

The calculated modulus of the non-zero elements of the second-order susceptibility tensor components for LiNbO_3 are shown in Fig. 4.7. Notably, four non-vanishing nonlinear coefficients are observed. This is consistent

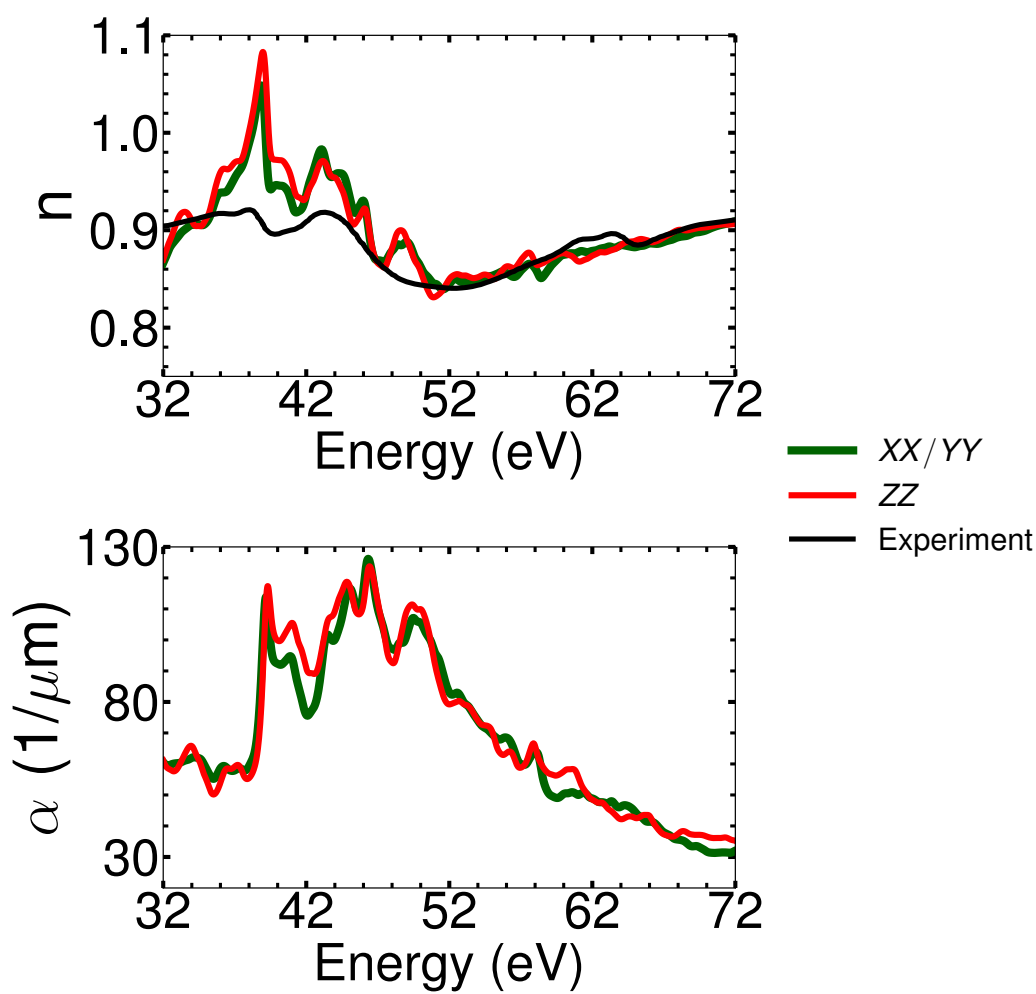


Figure 4.6: Visualization of the ordinary and extraordinary indices of refraction, and the ordinary and extraordinary absorption coefficients for LiNbO_3 . Experimental data of index of refraction extracted from the work of Can B. Uzundal and collaborators¹⁸ is included along with the calculated indices of refraction.

with the case where Kleinman symmetry does not hold. Additionally, the parameter L , representing the length of the crystal, is further discussed later in this section.

Light Source Parameters

Conducting experiments within a photon energy range of 32 to 72 eV entails specialized facilities. For example, Emma Berger and her collaborators¹⁵ conducted several experiments on XUV SHG spectroscopy at the BL1 beamline of the SPring-8 Angstrom Compact Free Electron Laser (SACLA). The BL1 beamline covers photon

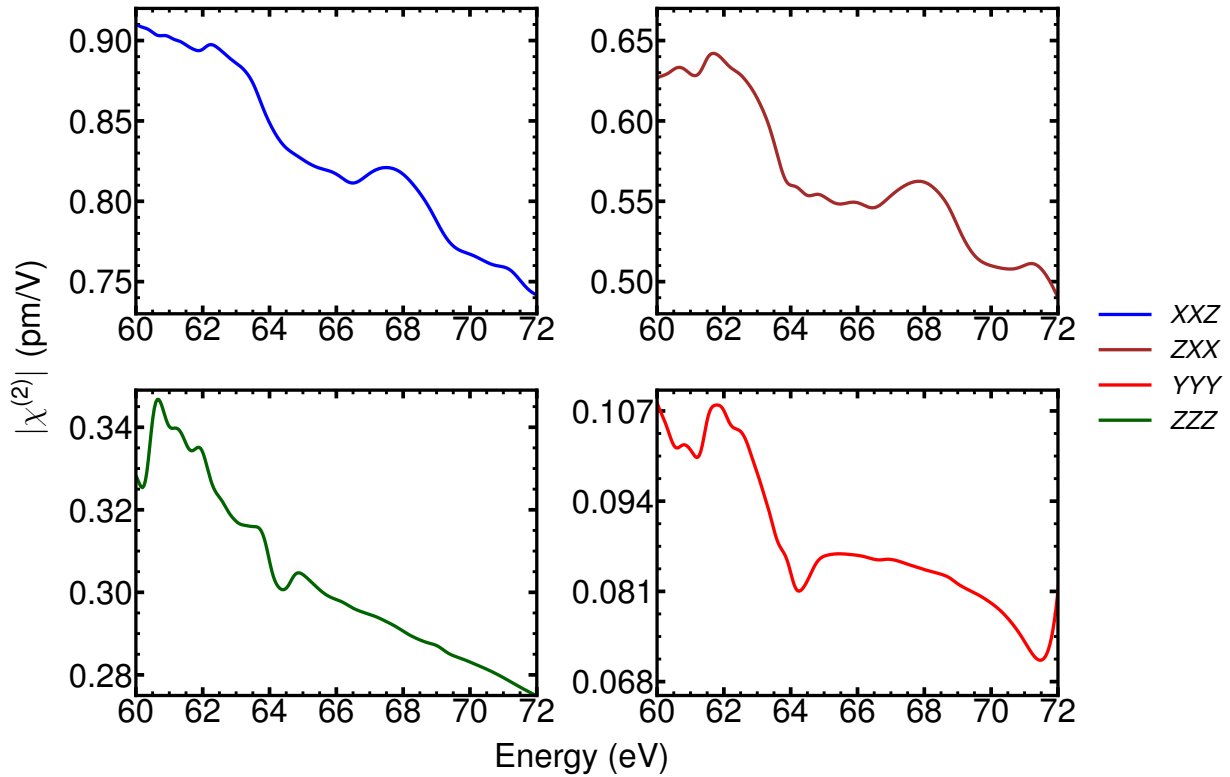


Figure 4.7: Visualization of the modulus of the non-zero second-order nonlinear susceptibility components of LiNbO_3 . Shown in a clockwise direction from the upper left quadrant are the components: XXZ , ZXX , YYY , and ZZZ . A broadening of 0.025 eV is applied.

energies approximately ranging from 25 eV to 150 eV¹⁴. This spectrum aligns with the photon energy range used to calculate the optical parameters of LiNbO_3 based on DFT. Another facility operating in the ultraviolet range is the Free Electron Laser Radiation for Multidisciplinary Investigations (FERMI). Additionally, in these facilities, the pulses are tunable in discrete steps of 0.5 eV.

The parameters characterizing the generation of photons in these facilities are provided in Table 4.1. We can finally evaluate the time-averaged second-harmonic power model (4.35) using these light source parameters and the optical material properties. However, the model is developed based on several approximation criteria (see Sec. 4.2). We will now focus on these approximations and the evaluation of the model.

Approximations and Evaluation

Special attention is given to the dispersion-related approximations. The scenario involves a fundamental wave with Y -axis polarization propagating along the X -axis. undergoes normal incidence transmission through the nonlinear

Table 4.1: Parameters that characterize two different XUV light sources: BL1 at SACLA and FEL1 at FERMI. λ_0 is the carrier wavelength; T_p is the pulse-repetition time; τ is the pulse width reported with respect to the full width at half maximum (FWHM); and $\langle \mathbb{P}_{\omega_0} \rangle$ stands for the averaged power.

Beamline	Parameter	Values
BL1 (SACLA) ^{14, 89}	λ_0	8 - 49 nm
	$T_{p_{\omega_0}}$	0.02 s
	τ_{FWHM}	50 - 70 fs
	Pulse energy	1 - 100 μJ
	$\langle \mathbb{P}_{\omega_0} \rangle$	50 μW - 5 mW
FEL1 (FERMI) ^{90, 91}	λ_0	20 - 100 nm
	$T_{p_{\omega_0}}$	0.02 s
	τ_{FWHM}	10 - 100 fs
	Maximum pulse energy	0.1 mJ
	$\langle \mathbb{P}_{\omega_0} \rangle$	5 mW

medium, generating a second-harmonic wave polarized along the Z -axis. Equation (4.16) is evaluated based on the quantities calculated through DFT. For clarity, equation (4.16) is rewritten below:

$$|\Delta_{ij}| = \left| \frac{1}{4} \frac{\partial}{\partial \hbar\omega} \left[\log_e \left(\text{Im} \left\{ \chi_{jk}^{(1)} \right\} \right) \right] \right|_{\hbar\omega = \hbar\omega_\ell} \quad (4.40)$$

In deriving equation (4.35), we assume negligible variation in the absorption coefficient around the central frequencies

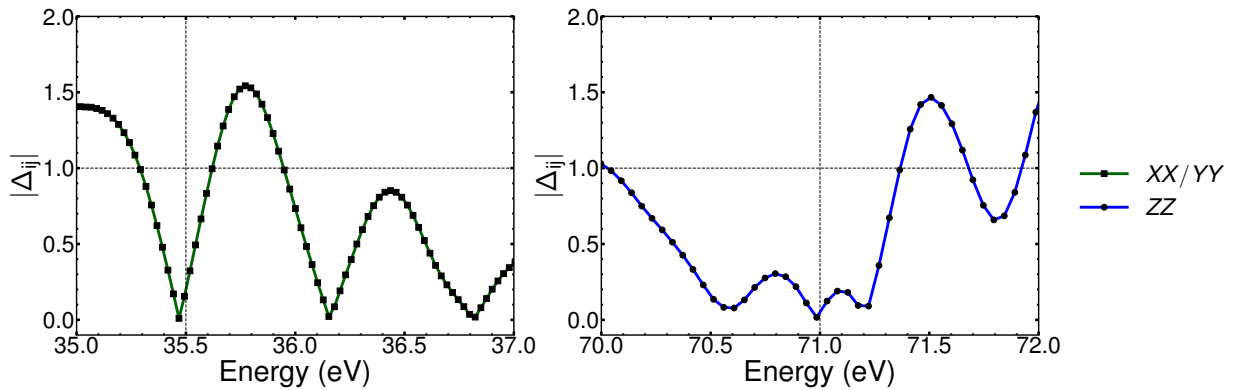


Figure 4.8: The left and right figures depict the approximation criterion, equation (4.40), for the dispersion of the ordinary (XX/YY) and extraordinary (ZZ) absorption coefficients, respectively.

(fundamental and second harmonic). This simplification is valid when the quantity given in equation (4.40) is much less than unity (see Section 4.2).

In Figure 4.8, we evaluate equation (4.40) for the ordinary and extraordinary case. The plot focuses on a specific energy range for each case: 35 to 37 eV for the ordinary and 70 to 72 eV for the extraordinary. Within these ranges, the criterion is satisfied around 35.5 eV for the ordinary case and 71 eV for the extraordinary case. For the sake of clarity, the parameters used to evaluate equation (4.35) are stated in Table 4.2. The length parameter (L) of the

Table 4.2: Parameters involved in the production of SHG pulses under absorption.

Parameter	Value
$\mathbb{E}_0(\lambda_0)$	35.5 eV (~ 34.925 nm)
$d_{22} (d_{22})$	$\sim 0.0736 + i 0.0035$ (0.0737) pm/V
$n_o(\omega_0)$	~ 0.9237
$n_e(2\omega_0)$	~ 0.9059
$\alpha_o(\omega_0)$	$\sim 55.1940 \frac{1}{\mu m}$
$\alpha_e(2\omega_0)$	$\sim 36.1404 \frac{1}{\mu m}$
$T_{P_{\omega_0}}$	0.02 s
τ	30.02 fs
$A_{\text{beam}} (W_0)$	1.96 nm^2 ($25 \mu m$)
$\langle \mathbb{P}_{\omega_0} \rangle$	5 mW

crystal is omitted in Table 4.2 because its effect on the second-harmonic power is analyzed using the other parameters listed.

Figure 4.9 shows the time-averaged second-harmonic power for different crystal lengths. While the power peaks around $0.03 \mu m$, a crystal of this size would not be effective. The fundamental wavelength (λ_0) is larger than the crystal length, resulting in minimal interaction with the medium and negligible second harmonic generation. Considering this limitation, we evaluate the second harmonic power for a range of crystal lengths (L) between $0.1 \mu m$ and $0.2 \mu m$. The results, as shown in Figure 4.9, demonstrate a decrease in power with increasing length. The second harmonic power goes from 0.447 nW at $0.1 \mu m$ to 0.013 nW at $0.2 \mu m$.

In order to assess the practicality of measuring such low power, we can begin by estimating the number of photons associated with the second-harmonic power. The number of photons can be calculated by dividing the energy of a pulse by the energy of one photon within the pulse. The energy pulse can be computed as the product between the average power (i.e., $\langle P_{2\omega_0} \rangle$) and the pulse-repetition time (i.e., $T_{P_{\omega_0}}$). For example, consider a crystal with a length of $0.1 \mu m$, the SHG pulse energy is given by $E_P = \langle P_{2\omega_0} \rangle T_P = 8.935 \text{ pJ} = 55.772 \text{ MeV}$. Since the energy of one photon within the SHG pulse is given by $E_{\text{photon}} = 71 \text{ eV}$, the number of photons in this scenario is $N_{\text{photon}} \approx 7 \times 10^5$.

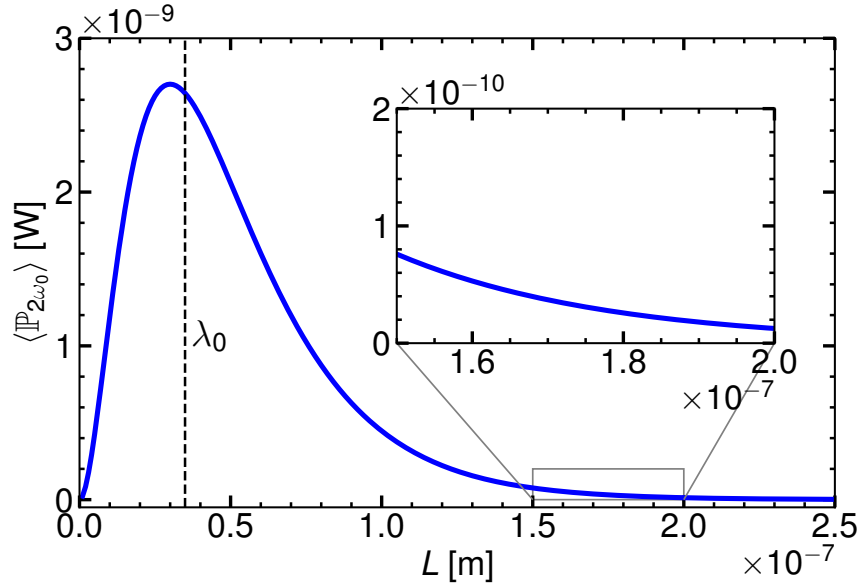


Figure 4.9: Role of the length of the nonlinear medium in the time-averaged second-harmonic power. The vertical dashed line represents the value of the fundamental wavelength.

Regarding the case when the length of the nonlinear medium is $0.2 \mu\text{m}$, the number of photons is given by $N_{\text{photon}} \approx 0.2 \times 10^5$. For such low-intensity radiation, down to 10^5 photons per pulse, Sorokin and collaborators⁹² develop detectors operable under these circumstances, called huge-aperture open electron multiplier (HAMP) detectors. However, a crucial drawback is that FERMI and SACLA currently lack HAMP detectors, limiting their applicability in these facilities.

Lam et al. investigate second-harmonic generation (SHG) in graphite thin films at FERMI²¹. They use normally incident light on films with thicknesses ranging from 100 to 720 nm. Interestingly, they measure SHG at low photon numbers per pulse, ranging from 10^5 to 10^6 . To achieve this, they employ an XUV spectrometer available at FERMI⁹³. This portable instrument utilizes a grating and a charge-coupled device (CCD) detector for signal detection. This XUV spectrometer, which is operational within the desired energy range of 35.5 – 71 eV, is well-suited for measuring the second-harmonic signal generated in LiNbO_3 at normal incidence in transmission geometry.

Regarding the length of the nonlinear medium, there are nanostructured LiNbO_3 thin films^{94,95} with thickness from 45 nm to 193 nm. LiNbO_3 thin films can be good candidates to use in a transmission geometry SHG experiment. Given the parameters in Table 4.2, we find that a crystal with a thickness of $0.1 \mu\text{m}$ can potentially generate experimentally measurable averaged power for second-harmonic generation in transmission geometry. To mitigate sample damage, the area of the sample can be scanned during the experiment²¹.

The analysis considers two further key criteria: diffraction length (equation (4.14)) and the ordinary-extraordinary (*o-e*) distinction condition (equation (4.37)). For diffraction, the fundamental wave exhibits a diffraction length of

0.10 m, while the second-harmonic wave diffracts over a longer distance of 0.20 m. Given the specific context, these diffraction lengths do not play a role within the nonlinear medium. (i.e., $L = 0.1 \mu\text{m}$). Similarly, the *o-e* distinction analysis reveals a dominance of the linear process (i.e., 0.33) compared to the second-harmonic contribution (i.e., 0.016). This aligns with the fact that we focus on inefficient second-harmonic generation. Therefore, within this specific energy regime, the concept of ordinary and extraordinary waves remains a valid and applicable framework for this work.

In addition to transmission geometry, we can encounter scenarios where the focus is on the reflected SHG radiation. This situation is explored in the subsequent section.

4.6 Reflection Geometry: Semi-infinite Approximation

The transmission geometry is a popular configuration for conducting optical experiments. Similarly, the reflection geometry is useful for scenarios where absorption is strong within the medium, while our interest lies in the reflected wave. This section focuses on conducting a theoretical analysis of the reflection geometry under oblique incidence.

In 1969, J. Jerphagnon and S. Kurtz presented a comprehensive account of SHG in nonabsorbing isotropic and uniaxial crystals²³, a theory readily accessible in standard nonlinear optics books^{11,28}. In 1994, W. Herman and L. Hayden⁹⁶ extended the theory beyond propagation along special directions within the crystal to include birefringence. Furthermore, they exclusively focused on accounting for absorption in isotropic materials.

A common feature shared between these two works is the consideration of the finite size of the sample, with particular attention given to the thickness of the crystal. In contrast, this section is centered around the semi-infinite approximation, neglecting the reflection at the back surface of the crystal. This choice is grounded in the fact that the strong absorption within the crystal prevents waves from reaching the back surface.

Figure 4.10 illustrates the geometry of the system. Unprimed parameters refer to the medium the fundamental wave strikes from, while primed parameters correspond to those within the nonlinear medium. The propagation takes place in a plane perpendicular to the optical axis. The quantity θ_i denotes the incidence angle of the fundamental wave on the crystal. Upon encountering the crystal, the fundamental wave undergoes partial reflection and partial transmission. Upon transmission through the medium, the source wave undergoes a nonlinear interaction, generating a polarization source wave at the doubled frequency $2\omega_0$. This second-harmonic polarization source (denoted by subscript *s*) then radiates light at the same frequency $2\omega_0$. Notably, these two second-harmonic waves typically propagate in different directions²⁸. Additionally, the nonlinear interaction can also generate a reflected second-harmonic wave.^{97, 11 (pp. 124 - 126)}

This reflected second-harmonic wave is collinear (i.e., their corresponding wave vectors point in the same direction) with the reflected fundamental wave. This will become evident when deriving an expression for the reflected and transmitted fields.

To describe the propagation of the second-harmonic wave within the crystal, we need to define the wave propagation equation for this geometry under absorption. There is no reason why we cannot use the wave propagation we derived previously in this chapter. However, we find it easier to deal with the dielectric tensor rather than the

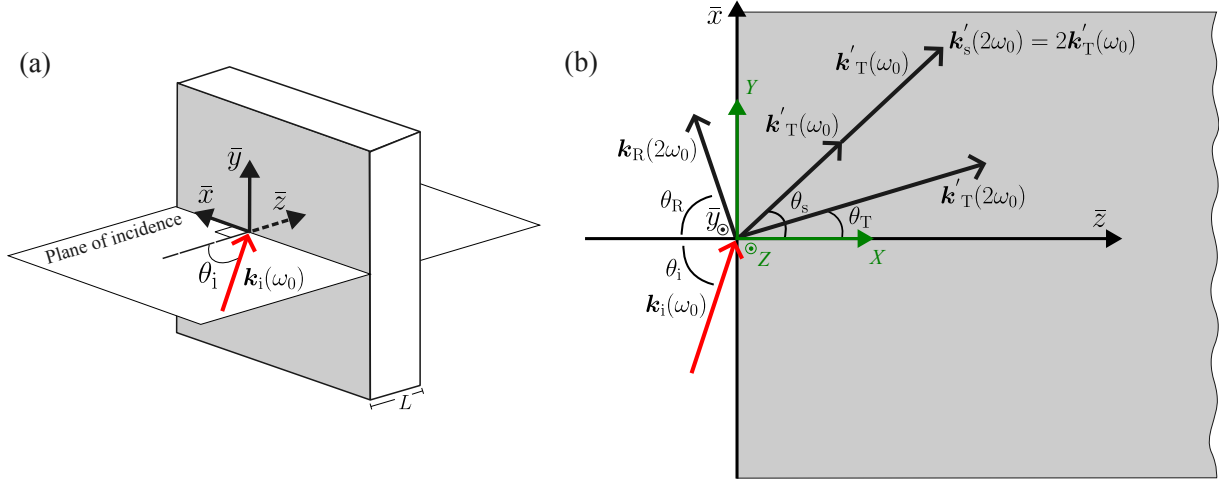


Figure 4.10: The experimental geometry for second-harmonic generation (SHG) involves the oblique incidence at an angle θ_i of fundamental radiation onto the surface of a nonlinear crystal with thickness L . The plane of incidence (white) is perpendicular to the optical axis. The coordinate system $\bar{x}\bar{y}\bar{z}$ is defined as the laboratory system, and the red vector represents the wave vector of the fundamental electric field. (b) This is a representation of the intersection between the plane of incidence and the crystal. The XYZ coordinate system corresponds to the principal coordinate system.

linear susceptibility for this case. Hence, the starting point is the following equation derived in Chapter 3, Sec. 3.1.2:

$$\nabla^2 \tilde{\mathcal{E}}_{\omega_\ell}(\mathbf{r}, \omega - \omega_\ell) + \frac{\omega^2}{c^2} \underline{\underline{\epsilon}}(\omega) \cdot \tilde{\mathcal{E}}_{\omega_\ell}(\mathbf{r}, \omega - \omega_\ell) - \beta'_\omega \nabla \left(\hat{Z} \cdot \nabla \right) \left(\tilde{\mathcal{E}}_{\omega_\ell}(\mathbf{r}, \omega - \omega_\ell) \cdot \hat{Z} \right) = -\frac{\omega_\ell^2}{c^2} \tilde{\mathcal{P}}_{\omega_\ell}^{\text{NL}}(\mathbf{r}, \omega - \omega_\ell) \quad (4.41)$$

We choose this equation as the starting point because the treatment of the spatial coordinate differs from the previous cases treated thus far in this thesis. Since we propagate radiation in a plane perpendicular to the optical axis, we implicitly choose to work with respect to the principal coordinate system XYZ . Therefore, the dielectric tensor is in its diagonal representation:

$$\nabla^2 \tilde{\mathcal{E}}_{\omega_\ell}(\mathbf{r}, \omega - \omega_\ell) + \frac{\omega^2}{c^2} \begin{pmatrix} \epsilon_{XX}(\omega) & 0 & 0 \\ 0 & \epsilon_{XX}(\omega) & 0 \\ 0 & 0 & \epsilon_{ZZ}(\omega) \end{pmatrix} \cdot \tilde{\mathcal{E}}_{\omega_\ell}(\mathbf{r}, \omega - \omega_\ell) - \beta'_\omega \nabla \left(\hat{Z} \cdot \nabla \right) \left(\tilde{\mathcal{E}}_{\omega_\ell}(\mathbf{r}, \omega - \omega_\ell) \cdot \hat{Z} \right) = -\frac{\omega_\ell^2}{c^2} \tilde{\mathcal{P}}_{\omega_\ell}^{\text{NL}}(\mathbf{r}, \omega - \omega_\ell) \quad (4.42)$$

We have two orthogonal coordinate system: the principal coordinate system XYZ and the laboratory coordinate

system $\bar{x}\bar{y}\bar{z}$. From Fig. 4.10, these two coordinate systems are related to each other as follows:

$$\begin{pmatrix} \bar{x} \\ \bar{y} \\ \bar{z} \end{pmatrix} = \begin{pmatrix} 0 & 1 & 0 \\ 0 & 0 & 1 \\ 1 & 0 & 0 \end{pmatrix} \begin{pmatrix} X \\ Y \\ Z \end{pmatrix} \quad (4.43)$$

Using this matrix transformation operation, the dielectric tensor in the laboratory coordinate system $\bar{x}\bar{y}\bar{z}$ from the principal coordinate system XYZ is given by:

$$\begin{aligned} \begin{pmatrix} \epsilon_{\bar{x}\bar{x}}(\omega) & 0 & 0 \\ 0 & \epsilon_{\bar{y}\bar{y}}(\omega) & 0 \\ 0 & 0 & \epsilon_{\bar{z}\bar{z}}(\omega) \end{pmatrix} &= \begin{pmatrix} 0 & 1 & 0 \\ 0 & 0 & 1 \\ 1 & 0 & 0 \end{pmatrix} \begin{pmatrix} \epsilon_{XX}(\omega) & 0 & 0 \\ 0 & \epsilon_{XX}(\omega) & 0 \\ 0 & 0 & \epsilon_{ZZ}(\omega) \end{pmatrix} \begin{pmatrix} 0 & 1 & 0 \\ 0 & 0 & 1 \\ 1 & 0 & 0 \end{pmatrix}^T \\ &= \begin{pmatrix} \epsilon_{YY}(\omega) & 0 & 0 \\ 0 & \epsilon_{ZZ}(\omega) & 0 \\ 0 & 0 & \epsilon_{XX}(\omega) \end{pmatrix} \end{aligned} \quad (4.44)$$

The dielectric tensor in the laboratory coordinate system $\bar{x}\bar{y}\bar{z}$ remains diagonal. Subsequently, every equation, vector, and tensor is defined with respect to the laboratory coordinate system. In transmission geometry, the transformation between the principal axes and the laboratory frame simplifies to a rearrangement of the principal directions. Since this rearrangement has no effect on the results, we can conveniently ignore it.

Conversely, reflection geometry necessitates a transformation because measurements are typically referenced to the surface normal of the sample, which generally differs from the principal axes. However, for an X -cut LiNbO_3 crystal, the principal axis X coincides with the surface normal. This fortunate alignment allows us to use the principal coordinate system for analysis, but we will express the results in the laboratory frame for consistency with a general description. Equation (4.42) can be expressed in terms of its vector components as follows:

$$\begin{aligned} \nabla_{\sigma 2\omega_0}^2 \tilde{\mathcal{E}}(\mathbf{r}, \omega - 2\omega_0) + \frac{\omega^2}{c^2} \epsilon_{\sigma\sigma}(\omega) \tilde{\mathcal{E}}(\mathbf{r}, \omega - 2\omega_0) - \beta'_\omega \nabla_\sigma (\bar{y} \cdot \nabla) \left(\tilde{\mathcal{E}}(\mathbf{r}, \omega - 2\omega_0) \cdot \bar{y} \right) = \\ - \frac{(2\omega_0)^2}{c^2} \tilde{\mathcal{P}}_{2\omega_0}^{\text{NL}}(\mathbf{r}, \omega - 2\omega_0) \end{aligned} \quad (4.45)$$

where $\sigma = \bar{x}, \bar{y}, \bar{z}$. In this case, we set $\omega_\ell = 2\omega_0$. Similarly to the transmission geometry case, the dielectric tensor becomes a complex quantity to account for absorption. Additionally, we approach dispersion through the Taylor expansion of the following term: $\frac{\omega}{c} \sqrt{\epsilon_{\sigma\sigma}(\omega)}$:

$$\begin{aligned} \frac{\omega}{c} \sqrt{\epsilon_{\sigma\sigma}(\omega)} &= \frac{2\omega_0}{c} \sqrt{\epsilon_{\sigma\sigma}(2\omega_0)} \\ &+ \left[\frac{1}{c} \sqrt{\epsilon_{\sigma\sigma}(2\omega_0)} + \frac{\omega}{c} \sqrt{\epsilon_{\sigma\sigma}(2\omega_0)} \frac{\partial}{\partial \omega} \log_e \left(\epsilon_{\sigma\sigma}(\omega) \right) \right] \Bigg|_{\omega=2\omega_0} (\omega - 2\omega_0) + \dots \end{aligned} \quad (4.46)$$

In order to be consistent with the previous derivations, we solely focus on the pseudo-monochromatic term. Consequently, equation (4.45) becomes:

$$\begin{aligned} \nabla^2 \tilde{\mathcal{E}}_{\sigma 2\omega_0}(\mathbf{r}, \omega - 2\omega_0) + \frac{(2\omega_0)^2}{c^2} \epsilon_{\sigma\sigma}(2\omega_0) \tilde{\mathcal{E}}_{\sigma 2\omega_0}(\mathbf{r}, \omega - 2\omega_0) - \beta'_{2\omega_0} \nabla_{\sigma} (\tilde{\mathbf{y}} \cdot \nabla) \left(\tilde{\mathcal{E}}_{\sigma 2\omega_0}(\mathbf{r}, \omega - 2\omega_0) \cdot \tilde{\mathbf{y}} \right) = \\ - \frac{(2\omega_0)^2}{c^2} \tilde{\mathcal{P}}_{2\omega_0}^{\text{NL}}(\mathbf{r}, \omega - 2\omega_0) \end{aligned} \quad (4.47)$$

To simplify the analysis, we neglect the depletion of the fundamental wave at ω_0 due to nonlinear processes. This is justified because absorption in the medium is typically much stronger than these nonlinear effects. Additionally, we consider a scenario where the propagation directions of the second-harmonic wave and the nonlinear polarization wave are not the same. This spatial separation further weakens the interaction between the fundamental and second-harmonic waves.

The solution of the wave equation 4.47 consists of the sum of a solution to the homogeneous wave equation (i.e., when $\tilde{\mathcal{P}}_{2\omega_0}^{\text{NL}}(\mathbf{r}, \omega - 2\omega_0) = 0$) and a particular solution of the inhomogeneous wave equation (i.e., when $\tilde{\mathcal{P}}_{2\omega_0}^{\text{NL}}(\mathbf{r}, \omega - 2\omega_0) \neq 0$). These waves are commonly referred to as the free wave and the bound wave, respectively. Given that the right side of the interface is lossy, the dielectric function of such a lossy medium is specified by its real and imaginary parts²⁸: $\epsilon'_{\sigma\sigma} = \text{Re}\{\epsilon'_{\sigma\sigma}\} + i \text{Im}\{\epsilon'_{\sigma\sigma}\}$. As a different means of characterizing the lossy medium, the wavenumber $\gamma'_{\nu, \omega_{\ell}}$ is introduced, taking the form of a complex number:

$$\gamma'_{\nu, \omega_{\ell}} = \beta'_{\nu, \omega_{\ell}} + i\alpha'_{\nu, \omega_{\ell}} = \frac{\omega_{\ell}}{c} \sqrt{\epsilon'_{\nu}(\omega_{\ell})} = \frac{\omega_{\ell}}{c} n'_{\nu}(\omega_{\ell}) \quad (4.48)$$

Here, $\nu = \perp, \parallel$ (i.e., perpendicular ($\tilde{\mathbf{y}}$), and parallel ($\tilde{\mathbf{x}}, \tilde{\mathbf{z}}$) to the plane of incidence) and $\omega_{\ell} = \omega_0, 2\omega_0$ (ω_0 refers to the fundamental wave while $2\omega_0$ refers to the harmonic wave). The dielectric function is related to the index of refraction as follows: $n'_{\nu}(\omega_{\ell}) = \sqrt{\epsilon'_{\nu}(\omega_{\ell})}$.

Purposely, regarding the left side of the interface, where there is no absorption, one can introduce a real-valued wavenumber: γ_{ν} :

$$\gamma_{\nu, \omega_{\ell}} = \beta_{\nu, \omega_{\ell}} = \frac{j}{c} \sqrt{\epsilon_{\nu}(\omega_{\ell})} = \frac{\omega_{\ell}}{c} n_{\nu}(\omega_{\ell}) \quad (4.49)$$

Naturally, equation (4.47) can be rewritten as:

$$\begin{aligned} \nabla^2 \tilde{\mathcal{E}}_{\sigma 2\omega_0}(\mathbf{r}, \omega - 2\omega_0) + (\gamma'_{\nu, 2\omega_0})^2 \tilde{\mathcal{E}}_{\sigma 2\omega_0}(\mathbf{r}, \omega - 2\omega_0) - \beta'_{2\omega_0} \nabla_{\sigma} (\tilde{\mathbf{y}} \cdot \nabla) \left(\tilde{\mathcal{E}}_{\sigma 2\omega_0}(\mathbf{r}, \omega - 2\omega_0) \cdot \tilde{\mathbf{y}} \right) = \\ - \frac{(2\omega_0)^2}{c^2} \tilde{\mathcal{P}}_{2\omega_0}^{\text{NL}}(\mathbf{r}, \omega - 2\omega_0) \end{aligned} \quad (4.50)$$

As noted in previous works^{98,99}, the form of the reflected and transmitted harmonic wave differs depending on whether $\tilde{\mathcal{P}}_{2\omega_0}^{\text{NL}}$ lies within or is perpendicular to the plane of incidence. In this section, we focus on a p -polarized (i.e., parallel to the plane of incidence) fundamental electric field and $\tilde{\mathcal{P}}_{2\omega_0}^{\text{NL}}$ perpendicular (\mathbf{p}_{\perp}) to the plane of incidence.

To obtain an expression for p_{\perp} , we begin with the expression for the nonlinear polarization for an X -cut LiNbO_3 given in equation (3.43):

$$\mathcal{P}_{2\omega_0}^{\text{NL}}(\mathbf{r}, t) = \epsilon_0 \begin{pmatrix} -d_{33} & -d_{31} & -d_{31} & 0 & 0 & 0 \\ 0 & 0 & 0 & 0 & d_{22} & -d_{15} \\ 0 & d_{22} & -d_{22} & 0 & -d_{15} & 0 \end{pmatrix} \begin{pmatrix} \mathcal{E}_{X\omega_0}^2(\mathbf{r}, t) \\ \mathcal{E}_{Y\omega_0}^2(\mathbf{r}, t) \\ \mathcal{E}_{Z\omega_0}^2(\mathbf{r}, t) \\ 2\mathcal{E}_{Y\omega_0}(\mathbf{r}, t)\mathcal{E}_{Z\omega_0}(\mathbf{r}, t) \\ 2\mathcal{E}_{X\omega_0}(\mathbf{r}, t)\mathcal{E}_{Z\omega_0}(\mathbf{r}, t) \\ 2\mathcal{E}_{X\omega_0}(\mathbf{r}, t)\mathcal{E}_{Y\omega_0}(\mathbf{r}, t) \end{pmatrix} \quad (4.51)$$

In this case, the transmitted fundamental radiation leads to the nonlinear response. Hence, we need to know its form in order to evaluate equation (4.51). The incident fundamental field in frequency domain is given by:

$$\tilde{\mathcal{E}}_{\omega_0 i}(\mathbf{r}, \omega - \omega_0) = \begin{pmatrix} \cos(\theta_i) \\ 0 \\ -\sin(\theta_i) \end{pmatrix} \Theta \left(R^{(b)} - r_{\bar{x}\bar{y}}^i \right) \tilde{F}_{\omega_0 i}(\omega - \omega_0) \exp\{i\mathbf{k}_i(\omega_0) \cdot \mathbf{r}\} \quad (4.52)$$

The transmitted fundamental field is expressed as follows:

$$\tilde{\mathcal{E}}'_{\omega_0 T}(\mathbf{r}, \omega - \omega_0) = \begin{pmatrix} \cos(\theta'_s) \\ 0 \\ -\sin(\theta'_s) \end{pmatrix} \Theta \left(R^{(b)} - r_{\bar{x}\bar{y}}^s \right) \tilde{F}'_{\omega_0 T}(\omega - \omega_0) \exp\left(i\mathbf{k}'_T(\omega_0) \cdot \mathbf{r}\right) \quad (4.53)$$

Here, $\Theta \left(R^{(b)} - r_{\bar{x}\bar{y}}^{\zeta} \right)$ is a Heaviside function given by:

$$\Theta \left(R^{(b)} - r_{\bar{x}\bar{y}}^{\zeta} \right) = \begin{cases} 1 & , \text{ for } R^{(b)} \geq r_{\bar{x}\bar{y}} \text{ where } r_{\bar{x}\bar{y}} = \sqrt{\sec^2(\theta_{\zeta}) \bar{x}^2 + \bar{y}^2} \\ 0 & , \text{ otherwise} \end{cases} \quad (4.54)$$

where ζ can be either i or s , and $R^{(b)}$ is the radius of beam. Since both the nonlinear source wave and the transmitted fundamental wave travel in the same direction, θ'_s appears in equation (4.53).

To account for the finite size of the beam, we model it using spatially confined plane waves restricted to a cylindrical region. This confinement naturally results in a beam with a circular cross-section. Additionally, we introduce angles within the equation (4.54) to account for the specific directions of both the incident and transmitted fundamental waves.

Through standard Snell's law and Fresnel's formulas from linear optics^{19,28}, the connection between the incident angle θ_i and the refraction angle θ'_T can be determined:

$$n'_{\parallel}(\omega_0) \sin(\theta'_s) = n_{\parallel}(\omega_0) \sin(\theta_i) \quad (4.55)$$

Since the incident field is p -polarized, we choose the index of refraction parallel to the plane of incidence n_{\parallel} . Additionally, the transmitted envelope is related to the incident envelope, described by the following relations:

$$\tilde{F}'_{\omega_{0T}}(\omega - \omega_0) = t^{\{s,p\}} \tilde{F}_{\omega_{0i}}(\omega - \omega_0) \quad (4.56a)$$

where $t^{\{s,p\}}$ is the standard Fresnel transmission coefficient²⁸. For the transmitted wave, we focus specifically on the case where the incident electric field, $\tilde{\mathcal{E}}_{\omega_{0i}}(\omega - \omega_0)$, lies parallel to the plane of incidence. This corresponds to p -polarization (or TM polarization). In this scenario, the Fresnel coefficient for transmission takes the following form:

$$t^{\{p\}} = \frac{2n_{\parallel}(\omega_0) \cos(\theta_i)}{n_{\parallel}(\omega_0) \cos(\theta'_s) + n'_{\parallel}(\omega_0) \cos(\theta_i)} \quad (4.57a)$$

Therefore, the transmitted fundamental wave is written as follows:

$$\tilde{\mathcal{E}}'_{\omega_{0T}}(\mathbf{r}, \omega - \omega_0) = \begin{pmatrix} \cos(\theta'_s) \\ 0 \\ -\sin(\theta'_s) \end{pmatrix} \Theta \left(R^{(b)} - r_{\bar{x}\bar{y}}^s \right) t^{\{p\}} \tilde{F}_{\omega_{0i}}(\omega - \omega_0) \exp \left(i\mathbf{k}'_T(\omega_0) \cdot \mathbf{r} \right) \quad (4.58)$$

By Fourier transforming back equation (4.58), we obtain the following expression:

$$\tilde{\mathcal{E}}'_{\omega_{0T}}(\mathbf{r}, t) = \begin{pmatrix} \cos(\theta'_s) \\ 0 \\ -\sin(\theta'_s) \end{pmatrix} \Theta \left(R^{(b)} - r_{\bar{x}\bar{y}}^s \right) t^{\{p\}} F_{\omega_{0i}}(t) \exp \left(i\mathbf{k}'_T(\omega_0) \cdot \mathbf{r} \right) \quad (4.59)$$

Since equation (4.59) is expressed with respect to $\bar{x}\bar{y}\bar{z}$, we have to transform it to the principal coordinate system XYZ in order to evaluate it in (4.51):

$$\left[\tilde{\mathcal{E}}'_{\omega_{0T}} \right]_{XYZ}(\mathbf{r}, t) = \begin{pmatrix} -\sin(\theta'_s) \\ \cos(\theta'_s) \\ 0 \end{pmatrix} \Theta \left(R^{(b)} - r_{\bar{x}\bar{y}}^s \right) t^{\{p\}} F_{\omega_{0i}}(t) \exp \left(i\mathbf{k}'_T(\omega_0) \cdot \mathbf{r} \right) \quad (4.60)$$

Then, plugging the corresponding components of (4.60) into equation (4.51) yields:

$$\mathcal{P}_{X2\omega_0}^{\text{NL}} = -\epsilon_0 \left[d_{33} \sin^2(\theta'_s) + d_{31} \cos^2(\theta'_s) \right] \Theta \left(R^{(b)} - r_{\bar{x}\bar{y}}^s \right) \left[t^{\{p\}} \right]^2 F_{\omega_{0i}}^2(t) \exp \left(i2\mathbf{k}'_T(\omega_0) \cdot \mathbf{r} \right) \quad (4.61a)$$

$$\mathcal{P}_{Y2\omega_0}^{\text{NL}} = -\epsilon_0 \left[2d_{15} \sin(\theta'_s) \cos(\theta'_s) \right] \Theta \left(R^{(b)} - r_{\bar{x}\bar{y}}^s \right) \left[t^{\{p\}} \right]^2 F_{\omega_{0i}}^2(t) \exp \left(i2\mathbf{k}'_T(\omega_0) \cdot \mathbf{r} \right) \quad (4.61b)$$

$$\mathcal{P}_{Z2\omega_0}^{\text{NL}} = \epsilon_0 \left[d_{22} \cos^2(\theta'_s) \right] \Theta \left(R^{(b)} - r_{\bar{x}\bar{y}}^s \right) \left[t^{\{p\}} \right]^2 F_{\omega_{0i}}^2(t) \exp \left(i2\mathbf{k}'_T(\omega_0) \cdot \mathbf{r} \right) \quad (4.61c)$$

Finally, in the principal coordinate system XYZ , p_{\perp} corresponds to the Z -component of the nonlinear polarization in (4.61). Conveniently, the Z axis aligns with the \bar{y} axis in the laboratory coordinate system, thereby p_{\perp} in the

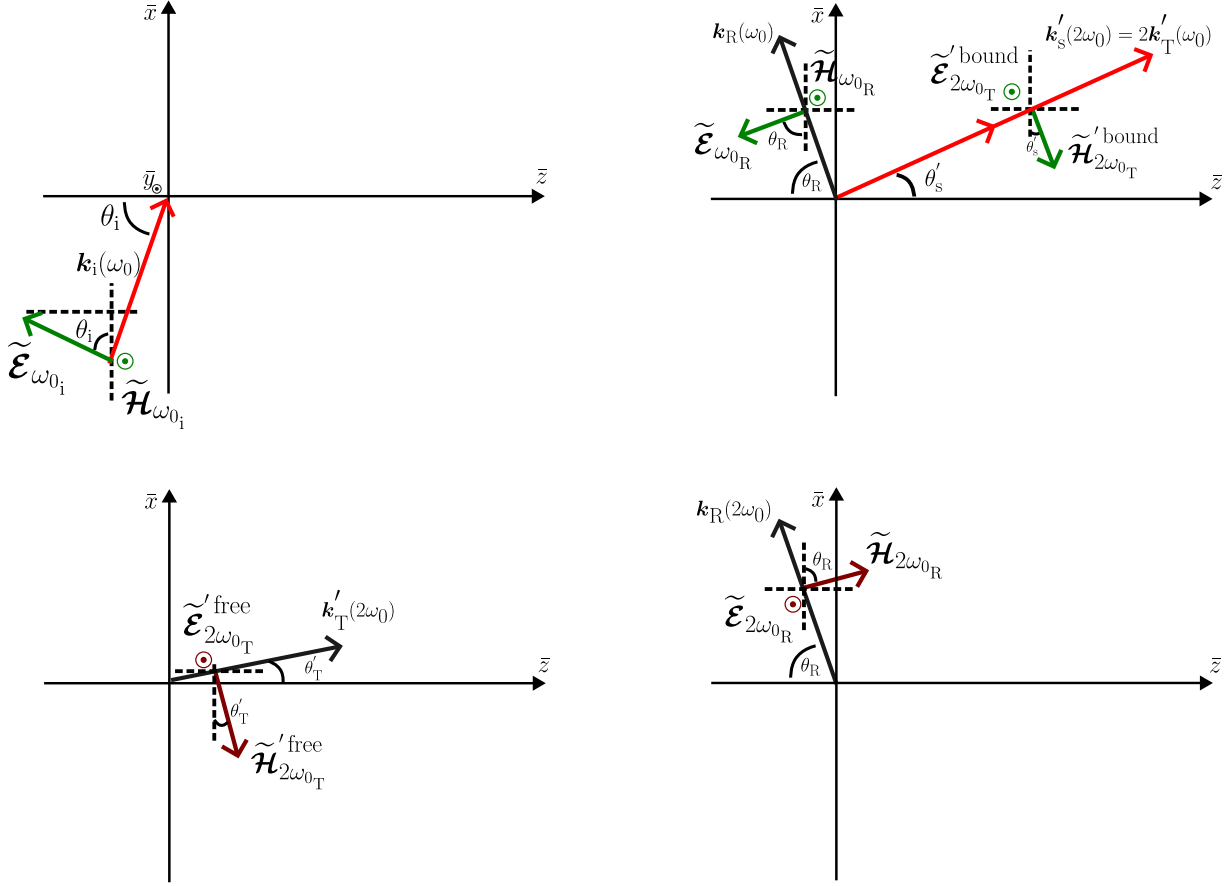


Figure 4.11: Polarization directions of fundamental and second-harmonic fields in reflection SHG.

laboratory coordinate system is given as follows:

$$P_{\perp 2\omega_0}(\mathbf{r}, t) = P_{\bar{y}2\omega_0}^{\text{NL}} = P_{Z2\omega_0}^{\text{NL}} = \epsilon_0 \left[d_{22} \cos^2(\theta'_s) \right] \Theta \left(R^{(b)} - r_{\bar{x}\bar{y}}^s \right) \left[t^{\{p\}} \right]^2 F_{\omega_0}^2(t) \exp \left(i 2\mathbf{k}'_T(\omega_0) \cdot \mathbf{r} \right) \quad (4.62)$$

This equation can be written in the frequency domain as follows:

$$\tilde{P}_{\perp 2\omega_0}(\mathbf{r}, \omega - 2\omega_0) = \epsilon_0 \left[d_{22} \cos^2(\theta'_s) \right] \Theta \left(R^{(b)} - r_{\bar{x}\bar{y}}^s \right) \left[t^{\{p\}} \right]^2 \exp \left(i 2\mathbf{k}'_T(\omega_0) \cdot \mathbf{r} \right) G(\omega - 2\omega_0) \quad (4.63)$$

Here, $G(\omega - 2\omega_0)$ is given by the following expression:

$$G(\omega - 2\omega_0) = \int_{-\infty}^{+\infty} \frac{d\xi}{(2\pi)^2} \tilde{F}_{\omega_0}(\xi) \tilde{F}_{\omega_0}(\omega - 2\omega_0 - \xi)$$

Building upon the analogous steps detailed in Appendix A, Section A.4, we can arrive at equation (4.63).

In this specific geometry, the slowly varying envelopes of the electric and magnetic fields can be expressed as follows:

$$\tilde{\mathcal{E}}_{\omega_0 i}(\mathbf{r}, \omega - \omega_0) = \begin{pmatrix} \cos(\theta_i) \\ 0 \\ -\sin(\theta_i) \end{pmatrix} \Theta \left(R^{(b)} - r_{\bar{x}\bar{y}}^i \right) \tilde{F}_{\omega_0 i}(\omega - \omega_0) \exp(i\mathbf{k}_i(\omega_0) \cdot \mathbf{r}) \quad (4.64a)$$

$$\tilde{\mathcal{H}}_{\omega_0 i}(\mathbf{r}, \omega - \omega_0) = \begin{pmatrix} 0 \\ 1 \\ 0 \end{pmatrix} \frac{1}{\mu_0 \omega_0} \gamma_{\parallel, \omega_0} \Theta \left(R^{(b)} - r_{\bar{x}\bar{y}}^i \right) \tilde{F}_{\omega_0 i}(\omega - \omega_0) \exp(i\mathbf{k}_i(\omega_0) \cdot \mathbf{r}) \quad (4.64b)$$

$$\tilde{\mathcal{E}}_{2\omega_0 R}(\mathbf{r}, \omega - 2\omega_0) = \begin{pmatrix} 0 \\ 1 \\ 0 \end{pmatrix} \Theta \left(R^{(b)} - r_{\bar{x}\bar{y}}^R \right) \tilde{F}_{2\omega_0 R}(\omega - 2\omega_0) \exp(i\mathbf{k}_R(2\omega_0) \cdot \mathbf{r}) \quad (4.64c)$$

$$\tilde{\mathcal{H}}_{2\omega_0 R}(\mathbf{r}, \omega - 2\omega_0) = \begin{pmatrix} \cos(\theta_R) \\ 0 \\ \sin(\theta_R) \end{pmatrix} \frac{1}{\mu_0 2\omega_0} \gamma_{\perp, 2\omega_0} \Theta \left(R^{(b)} - r_{\bar{x}\bar{y}}^R \right) \tilde{F}_{2\omega_0 R}(\omega - 2\omega_0) \exp(i\mathbf{k}_R(2\omega_0) \cdot \mathbf{r}) \quad (4.64d)$$

$$\begin{aligned} \tilde{\mathcal{E}}'_{2\omega_0 T}(\mathbf{r}, \omega - 2\omega_0) &= \begin{pmatrix} 0 \\ 1 \\ 0 \end{pmatrix} \Theta \left(R^{(b)} - r_{\bar{x}\bar{y}}^T \right) \tilde{F}'_{2\omega_0 T}(\omega - 2\omega_0) \exp(i\mathbf{k}'_T(2\omega_0) \cdot \mathbf{r}) \\ &+ \begin{pmatrix} 0 \\ 1 \\ 0 \end{pmatrix} \frac{(2\omega_0)^2}{c^2} \frac{d_{22} \cos^2(\theta'_T) [t\{p\}]^2}{(2\gamma'_{\parallel, \omega_0})^2 - \gamma'^2_{\perp, 2\omega_0}} \Theta \left(R^{(b)} - r_{\bar{x}\bar{y}}^s \right) G(\omega - 2\omega_0) \\ &\exp(i2\mathbf{k}'_T(\omega_0) \cdot \mathbf{r}) \end{aligned} \quad (4.64e)$$

$$\begin{aligned} \tilde{\mathcal{H}}_{2\omega_0 T}(\mathbf{r}, \omega - 2\omega_0) &= \begin{pmatrix} -\cos(\theta'_T) \\ 0 \\ \sin(\theta'_T) \end{pmatrix} \frac{\gamma'_{\perp, 2\omega_0}}{\mu_0 2\omega_0} \Theta \left(R^{(b)} - r_{\bar{x}\bar{y}}^T \right) \tilde{F}'_{2\omega_0 T}(\omega - 2\omega_0) \exp(i\mathbf{k}'_T(2\omega_0) \cdot \mathbf{r}) \\ &+ \begin{pmatrix} -\cos(\theta'_s) \\ 0 \\ \sin(\theta'_s) \end{pmatrix} \frac{\gamma'_{\parallel, \omega_0}}{\mu_0 \omega_0} \frac{(2\omega_0)^2}{c^2} \frac{d_{22} \cos^2(\theta'_T) [t\{p\}]^2}{(2\gamma'_{\parallel, \omega_0})^2 - \gamma'^2_{\perp, 2\omega_0}} \Theta \left(R^{(b)} - r_{\bar{x}\bar{y}}^s \right) G(\omega - 2\omega_0) \\ &\exp(i2\mathbf{k}'_T(\omega_0) \cdot \mathbf{r}) \end{aligned} \quad (4.64f)$$

$\Theta \left(R^{(b)} - r_{\bar{x}\bar{y}}^\zeta \right)$ is given by equation (4.54). Here, ζ can be i (incident wave), R (reflected wave), T (SH refraction

wave), and s (fundamental/nonlinear source wave).

In Figure 4.11, we define the following angles: θ_i for incidence, θ_R for reflection, θ'_T for the generated second-harmonic wave, and θ'_s for the transmitted fundamental wave (and the nonlinear source wave). Figure 4.11 illustrates equations (4.64).

Equations (4.64e) and (4.64f) decompose the wave solutions into “free” and “bound” components. The first term in each equation represents the “free” solution, while the second term captures the “bound” solution of equation (4.50). Additionally, the wave vectors are given as follows:

$$\mathbf{k}_i(\omega_0) = \gamma_{\parallel, \omega_0} \begin{pmatrix} \sin(\theta_i) \\ 0 \\ \cos(\theta_i) \end{pmatrix} \quad (4.65a)$$

$$\mathbf{k}_R(2\omega_0) = \gamma_{\perp, 2\omega_0} \begin{pmatrix} \sin(\theta_R) \\ 0 \\ -\cos(\theta_R) \end{pmatrix} \quad (4.65b)$$

$$\mathbf{k}'_T(2\omega_0) = \gamma'_{\perp, 2\omega_0} \begin{pmatrix} \sin(\theta'_T) \\ 0 \\ \cos(\theta'_T) \end{pmatrix} \quad (4.65c)$$

$$\mathbf{k}'_s(2\omega_0) = 2\mathbf{k}'_T(\omega_0) = 2\gamma'_{\parallel, \omega_0} \begin{pmatrix} \sin(\theta'_s) \\ 0 \\ \cos(\theta'_s) \end{pmatrix} \quad (4.65d)$$

In equations (4.64), we utilize plane waves as an ansatz for solving equation (4.50). This entails that either \mathbf{F} or \mathbf{F}' does not depend on spatial variables. We adopt this approach for several reasons. In the transmission geometry, the slowly varying envelope approximation (in space) simplifies equation (4.50) as the primary interest lies in the forward-propagating wave. However, this approximation is unsuitable for studying the second-harmonic reflected wave because it inherently excludes backward-propagating solutions²⁸. Therefore, we do not approach this geometry using the slowly varying envelope approximation (in space).

While equation (4.50) offers a framework for analyzing wave propagation with reflection, its complexity increases significantly for scenarios beyond purely plane-wave ansatz. Here, we justify the use of plane waves as a valuable initial approximation. Firstly, the reflected second-harmonic generated by the nonlinear interaction primarily propagates outside the nonlinear medium, which prevents the second-harmonic envelope being spatially modulated. Secondly, for transmitted waves in a strong absorption regime, the envelopes decay spatially due to linear effects, such as absorption (i.e., complex wavenumber). Consequently, nonlinearities have a negligible effect on their envelope modulation.

Therefore, plane waves offer a robust starting point for further analysis, simplifying the problem without compromising the key aspects of the wave propagation with reflection in a nonlinear medium.

We will now focus on regions where $r_{\bar{x}\bar{y}}^{\zeta} \leq R^{(b)}$ in order to evaluate the boundary conditions. In connection with the

electric fields, the continuity of the tangential components (\bar{y} -components) of the electric field ($2\omega_0$) at the interface (i.e., $\bar{z} = 0$) yields:

$$\begin{aligned} \tilde{F}_{2\omega_0\text{R}}(\omega - 2\omega_0) \exp(i\gamma_{\perp,2\omega_0} \sin(\theta_{\text{R}})\bar{x}) &= \tilde{F}'_{2\omega_0\text{T}}(\omega - 2\omega_0) \exp(i\gamma'_{\perp,2\omega_0} \sin(\theta'_{\text{T}})\bar{x}) \\ &+ \frac{(2\omega_0)^2}{c^2} \frac{d_{22} \cos^2(\theta'_{\text{T}}) [t^{\{p\}}]^2}{(2\gamma'_{\parallel,\omega_0})^2 - \gamma'^2_{\perp,2\omega_0}} G(\omega - 2\omega_0) \\ &\exp(i2\gamma'_{\parallel,\omega_0} \sin(\theta'_s)\bar{x}) \end{aligned} \quad (4.66)$$

For the two sides to match at all points on the interface, the phase factors must be equal to each other; hence,

$$\begin{aligned} \exp(i\gamma_{\perp,2\omega_0} \sin(\theta_{\text{R}})\bar{x}) &= \exp(i\gamma'_{\perp,2\omega_0} \sin(\theta'_{\text{T}})\bar{x}) = \exp(i2\gamma'_{\parallel,\omega_0} \sin(\theta'_s)\bar{x}) \\ \gamma_{\perp,2\omega_0} \sin(\theta_{\text{R}}) &= \gamma'_{\perp,2\omega_0} \sin(\theta'_{\text{T}}) = 2\gamma'_{\parallel,\omega_0} \sin(\theta'_s) \end{aligned} \quad (4.67)$$

These relationships are regarded as the nonlinear optical generalization of Snell's law¹¹. Purposely, we can rewrite equation (4.55) using equations (4.48) and (4.49):

$$\gamma'_{\parallel,\omega_0} \sin(\theta'_s) = \gamma_{\parallel,\omega_0} \sin(\theta_i) \quad (4.68)$$

which allows to relate θ_i with θ'_{T} , θ_{R} , and θ'_s :

$$2\gamma_{\parallel,\omega_0} \sin(\theta_i) = \gamma_{\perp,2\omega_0} \sin(\theta_{\text{R}}) = \gamma'_{\perp,2\omega_0} \sin(\theta'_{\text{T}}) = 2\gamma'_{\parallel,\omega_0} \sin(\theta'_s) \quad (4.69)$$

Due to these relationships, a key finding is that the incident angle (θ_i) and the reflected angle (θ_{R}) of the second-harmonic wave are equal in vacuum (as $n_{\perp}(\omega_0) = n_{\perp}(2\omega_0) = 1$). This is approximately true if the medium of incidence is air.

If the relation (4.69) holds, equation (4.66) is expressed as follows:

$$\tilde{F}_{2\omega_0\text{R}}(\omega - 2\omega_0) = \tilde{F}'_{2\omega_0\text{T}}(\omega - 2\omega_0) + \frac{(2\omega_0)^2}{c^2} \frac{d_{22} \cos^2(\theta'_{\text{T}}) [t^{\{p\}}]^2}{(2\gamma'_{\parallel,\omega_0})^2 - \gamma'^2_{\perp,2\omega_0}} G(\omega - 2\omega_0) \quad (4.70)$$

Furthermore, the condition for the continuity of the tangential components (i.e., \bar{x} -components) of the magnetic fields at the interface ($\bar{z} = 0$) leads to the following relation:

$$\begin{aligned} \cos(\theta_{\text{R}}) \frac{1}{\mu_0 2\omega_0} \gamma_{\perp,2\omega_0} \tilde{F}_{2\omega_0\text{R}}(\omega - 2\omega_0) &= -\cos(\theta'_{\text{T}}) \frac{\gamma'_{\perp,2\omega_0}}{\mu_0 2\omega_0} \tilde{F}'_{2\omega_0\text{T}}(\omega - 2\omega_0) - \cos(\theta'_s) \frac{\gamma'_{\parallel,\omega_0}}{\mu_0 \omega_0} \frac{(2\omega_0)^2}{c^2} \\ &\frac{d_{22} \cos^2(\theta'_{\text{T}}) [t^{\{p\}}]^2}{(2\gamma'_{\parallel,\omega_0})^2 - \gamma'^2_{\perp,2\omega_0}} G(\omega - 2\omega_0) \end{aligned} \quad (4.71)$$

Here, we use relation (4.67) to arrive at this equation. There are two unknowns $F_{2\omega_0\text{R}}(\omega - 2\omega_0)$ and $F'_{2\omega_0\text{T}}(\omega - 2\omega_0)$,

and we have two equations (4.70) and (4.71). The solutions of this system of equation are given as follows:

$$\tilde{F}_{2\omega_0\text{R}}(\omega - 2\omega_0) = \frac{(2\omega_0)^2}{c^2} \frac{d_{22} \cos^2(\theta'_T) [t\{p\}]^2}{(2\gamma'_{\parallel,\omega_0})^2 - (\gamma'_{\perp,2\omega_0})^2} \left(\frac{\gamma'_{\perp,2\omega_0} \cos(\theta'_T) - 2\gamma'_{\parallel,\omega_0} \cos(\theta'_s)}{\gamma_{\perp,2\omega_0} \cos(\theta_R) + \gamma'_{\perp,2\omega_0} \cos(\theta'_T)} \right) G(\omega - 2\omega_0) \quad (4.72a)$$

$$\tilde{F}'_{2\omega_0\text{T}}(\omega - 2\omega_0) = -\frac{(2\omega_0)^2}{c^2} \frac{d_{22} \cos^2(\theta'_T) [t\{p\}]^2}{(2\gamma'_{\parallel,\omega_0})^2 - (\gamma'_{\perp,2\omega_0})^2} \left(\frac{\gamma_{\perp,2\omega_0} \cos(\theta_R) + 2\gamma'_{\parallel,\omega_0} \cos(\theta'_s)}{\gamma_{\perp,2\omega_0} \cos(\theta_R) + \gamma'_{\perp,2\omega_0} \cos(\theta'_T)} \right) G(\omega - 2\omega_0) \quad (4.72b)$$

These are the transmitted and reflected envelopes of the SHG radiation. Particularly, we are interested in the reflected signal since, as we know from the previous section, the signal in transmission geometry is low. Naturally, the next step is mainly the derivation of an expression for the SHG intensity from equation (4.72b).

There is a feature worth noting in equations (4.72): complex angles. From equation (4.55), θ'_s implicitly takes complex values since the primed index of refraction is complex as well. Building on the previously established relations (4.69), we can infer that θ'_T is complex as well. In order to avoid dealing with complex angles, we adopt the methodology presented by Orfanidis¹⁰⁰ to re-express $\cos(\theta'_s)$ and $\cos(\theta'_T)$ in terms of other quantities.

First, from the relation (4.69), we can establish a relationship between the \bar{x} -components of the following wave vectors. The \bar{x} -component of equation (4.65d) can be related to the \bar{x} -component of equation (4.65a) as follows:

$$k'_{s,\bar{x}}(2\omega_0) = 2\gamma'_{\parallel,\omega_0} \sin(\theta'_s) = 2\gamma_{\parallel,\omega_0} \sin(\theta_i) = 2k_{i,\bar{x}}(\omega_0) \quad (4.73)$$

Similarly, the \bar{x} -component of equation (4.65c) can be related to the \bar{x} -component of equation (4.65a):

$$k'_{T,\bar{x}}(2\omega_0) = \gamma'_{\perp,2\omega_0} \sin(\theta'_T) = 2\gamma_{\parallel,\omega_0} \sin(\theta_i) = 2k_{i,\bar{x}}(\omega_0) \quad (4.74)$$

These two equations guarantee that the \bar{x} components of \mathbf{k}'_s and \mathbf{k}'_T are real. However, the \bar{z} -components are written as complex numbers:

$$k'_{s,\bar{z}}(2\omega_0) = 2\gamma'_{\parallel,\omega_0} \cos(\theta'_s) = a_{\omega_0} + ib_{\omega_0} \quad (4.75a)$$

$$k'_{T,\bar{z}}(2\omega_0) = \gamma'_{\perp,2\omega_0} \cos(\theta'_T) = c_{2\omega_0} + id_{2\omega_0} \quad (4.75b)$$

To solve for unknowns a_{ω_0} , b_{ω_0} , $c_{2\omega_0}$, and $d_{2\omega_0}$, we utilize the following relations: $\mathbf{k}'_s(2\omega_0) \cdot \mathbf{k}'_s(2\omega_0) = 4(\gamma'_{\parallel,\omega_0})^2$, and $\mathbf{k}'_T(2\omega_0) \cdot \mathbf{k}'_T(2\omega_0) = (\gamma'_{\perp,2\omega_0})^2$. These relations will allow us to derive the following expression[¶]:

$$a_{\omega_\ell}, b_{\omega_\ell} \text{ or } c_{\omega_\ell}, d_{\omega_\ell} = \left(\frac{\sqrt{A_{\nu,\omega_\ell}^2 + B_{\nu,\omega_\ell}^2} \pm A_{\nu,\omega_\ell}}{2} \right)^{1/2} \quad (4.76)$$

We consider two indices: ν representing the polarization (parallel or perpendicular), and ω_ℓ representing the frequency (fundamental ω_0 or second-harmonic $2\omega_0$). For the first set of elements (a_{ω_ℓ} and b_{ω_ℓ}), ν corresponds

[¶]The detailed derivations for obtaining these equations are provided in Appendix B, Section B.3.

to the parallel polarization and ω_ℓ to the fundamental frequency. Additionally, a_{ω_0} is associated with the positive sign, while b_{ω_0} has the negative sign. Similarly, for the second set of elements (c_{ω_ℓ} and d_{ω_ℓ}), ν represents the perpendicular polarization and ω_ℓ represents the second-harmonic frequency. Here, $c_{2\omega_0}$ carries the positive sign, and $d_{2\omega_0}$ has the negative sign. We will now define A_{ν,ω_ℓ} and B_{ν,ω_ℓ} as follows:

$$A_{\nu,\omega_\ell} = \frac{(2\omega_0)^2}{c^2} \left(\operatorname{Re}\{\epsilon'_\nu(\omega_\ell)\} - \epsilon_{\parallel,\omega_0}(\omega_0) \sin(\theta_1) \right) \quad (4.77a)$$

$$B_{\nu,\omega_\ell} = \frac{(2\omega_0)^2}{c^2} \operatorname{Im}\{\epsilon'_\nu(\omega_\ell)\} \quad (4.77b)$$

Finally, we can re-express $\cos(\theta'_T)$ and $\cos(\theta'_s)$ in terms of a_{ω_0} , b_{ω_0} and $c_{2\omega_0}$, $d_{2\omega_0}$ as follows:

$$\cos(\theta'_s) = \frac{k'_{s,\bar{z}}(2\omega_0)}{2[\mathbf{k}'_T(\omega_0) \cdot \mathbf{k}'_T(\omega_0)]^{1/2}} = \frac{k'_{s,\bar{z}}(2\omega_0)}{2\gamma'_{\parallel,\omega_0}} = \frac{a_{\omega_0} + ib_{\omega_0}}{2\gamma'_{\parallel,\omega_0}} \quad (4.78a)$$

$$\cos(\theta'_T) = \frac{k'_{T,\bar{z}}(2\omega_0)}{[\mathbf{k}'_T(2\omega_0) \cdot \mathbf{k}'_T(2\omega_0)]^{1/2}} = \frac{k'_{T,\bar{z}}(2\omega_0)}{\gamma'_{\perp,2\omega_0}} = \frac{c_{2\omega_0} + id_{2\omega_0}}{\gamma'_{\perp,2\omega_0}} \quad (4.78b)$$

Equation (4.72a) is re-written without the complex angles as follows:

$$\tilde{F}_{2\omega_{0R}}(\omega - 2\omega_0) = \frac{(2\omega_0)^2}{c^2} \frac{a + ib}{2\gamma'_{\parallel,\omega_0}} \frac{d_{22} [t\{p\}]^2}{(2\gamma'_{\parallel,\omega_0})^2 - (\gamma'_{\perp,2\omega_0})^2} \left(\frac{(c - a) + i(d - b)}{\gamma_{\perp,2\omega_0} \cos(\theta_R) + c + id} \right) G(\omega - 2\omega_0) \quad (4.79)$$

To facilitate the derivation of the average second-harmonic power in reflection, we will first revisit some crucial aspects of the model.

Comments on the transmitted fundamental intensity

To determine the intensity of the transmitted fundamental wave, we can calculate the magnitude of the Poynting vector, which is given by the following equation (see Appendix C):

$$\langle I_{\omega_{0T}}(\mathbf{r}) \rangle = \left\| \frac{1}{T_{P\omega_0}} \int_{-\frac{1}{2}T_{P\omega_0}}^{\frac{1}{2}T_{P\omega_0}} dt \frac{1}{2} \operatorname{Re}\left\{ \mathcal{E}_{2\omega_{0T}}(\mathbf{r}, t) \times \mathcal{H}_{2\omega_{0T}}^*(\mathbf{r}, t) \right\} \right\| \quad (4.80)$$

where $T_{P\omega_0}$ is the pulse-repetition time of the incident pulse. $\mathcal{E}_{\omega_{0i}}$ is given in equation (4.59). $\mathcal{H}_{\omega_{0T}}^*$ is given by the following expression:

$$\mathcal{H}_{\omega_{0T}}^*(\mathbf{r}, t) = \begin{pmatrix} 0 \\ 1 \\ 0 \end{pmatrix} \frac{1}{\mu_0 \omega_0} \gamma'^*_{\parallel,\omega_0} t\{p\}^* F_{\omega_{0i}}^*(t) \exp\left(-i\mathbf{k}'_T(\omega_0) \cdot \mathbf{r}\right) \quad (4.81)$$

By plugging equations (4.59) and (4.81) into equation (4.80) and developing it, we arrive at the following expression for the transmitted average intensity:

$$\begin{aligned} \langle I_{\omega_0\tau}(\bar{z}) \rangle &= \sqrt{\gamma_{\parallel,\omega_0}^2 \sin^2(\theta_i) \left[(\beta'_{\parallel,\omega_0})^2 - (\alpha'_{\parallel,\omega_0})^2 \right]^2 + \frac{1}{4} \left[a(\beta'_{\parallel,\omega_0})^2 - a(\alpha'_{\parallel,\omega_0})^2 + 2b\beta'_{\parallel,\omega_0}\alpha'_{\parallel,\omega_0} \right]^2} \\ &\quad \frac{1}{2\mu_0\omega_0} \frac{\sqrt{\pi} |t^{\{p\}}|^2}{(\beta'_{\parallel,\omega_0})^2 + (\alpha'_{\parallel,\omega_0})^2} \frac{\tau}{T_{P\omega_0}} |K|^2 \exp(-b\bar{z}) \end{aligned} \quad (4.82)$$

Equation (4.82) includes the term $|K|^2$ because we assume a Gaussian profile for $F_{\omega_0_i}(t)$ as established throughout this thesis. This profile is defined as $F_{\omega_0_i}(t) = Kf(t)$, where $f(t) = \exp(-t^2/2\tau^2)$ and K is a factor with units of V/m. τ is the pulse length. In the equation, we can combine all terms except the decaying exponential function into a single term, denoted by $I_{\bar{z}\rightarrow 0^+}$:

$$\langle I_{\omega_0\tau}(\bar{z}) \rangle = I_{\bar{z}\rightarrow 0^+} \exp(-b\bar{z})$$

We introduce the notation $I_{\bar{z}\rightarrow 0^+}$ to denote the average fundamental intensity in the immediate vicinity of the vacuum (or air)–LiNbO₃ interface.

Following the calculation of the transmitted average intensity, we can similarly obtain the incident average intensity. The expression for the incident average intensity is given by:

$$\langle I_{\omega_0_i} \rangle = I_{\bar{z}\rightarrow 0^-} \frac{\tau}{T_{P\omega_0}} \sqrt{\pi} \quad (4.83)$$

Here, $I_{\bar{z}\rightarrow 0^-}$ represents the intensity at the boundary (\bar{z} approaches 0 from the negative side) and is given by:

$$I_{\bar{z}\rightarrow 0^-} = \frac{\epsilon_0 c}{2} n_{\parallel}(\omega_0) |K|^2 \quad (4.84)$$

This K term is the same as the one appearing in equation (4.82) due to the chosen Gaussian profile for $F_{\omega_0_i}(t)$. Furthermore, $I_{\bar{z}\rightarrow 0^-}$ can be related to the incident average power as follows:

$$I_{\bar{z}\rightarrow 0^-} = \left(\frac{T_{P\omega_0}}{\tau} \right) \frac{\langle P_{\omega_0_i} \rangle}{\sqrt{\pi} A_{\text{beam}}} \quad (4.85)$$

where the cross-section area of the beam is given by $A_{\text{beam}} = \pi W_0^2$ with W_0 representing the radius of the beam.

Finally, using equation (4.84) in equation (4.82), we can relate $I_{\bar{z}\rightarrow 0^-}$ with $I_{\bar{z}\rightarrow 0^+}$ as follows:

$$\begin{aligned} I_{\bar{z}\rightarrow 0^+} &= \sqrt{\gamma_{\parallel,\omega_0}^2 \sin^2(\theta_i) \left[(\beta'_{\parallel,\omega_0})^2 - (\alpha'_{\parallel,\omega_0})^2 \right]^2 + \frac{1}{4} \left[a(\beta'_{\parallel,\omega_0})^2 - a(\alpha'_{\parallel,\omega_0})^2 + 2b\beta'_{\parallel,\omega_0}\alpha'_{\parallel,\omega_0} \right]^2} \\ &\quad \frac{\sqrt{\pi} |t^{\{p\}}|^2}{(\beta'_{\parallel,\omega_0})^2 + (\alpha'_{\parallel,\omega_0})^2} \frac{\tau}{T_{P\omega_0}} \frac{c}{\omega_0 n_{\parallel}(\omega_0)} I_{\bar{z}\rightarrow 0^-} \end{aligned} \quad (4.86)$$

This equation quantifies the relationship between the transmitted and incident fundamental intensities at the interface, incorporating the effect of absorption within the medium. Notably, under the absence of absorption (i.e., $\alpha'_{\parallel,\omega_0} = 0$)

and transmission geometry condition (i.e., $\theta_i = 0$), equation (4.86) reduces to the expected outcome of transmission geometry in the absence of absorption developed in Chapter 3: $I_{\bar{z} \rightarrow 0^+} = \sqrt{\pi} |t\{p\}|^2 \frac{\tau}{T_{P\omega_0}} I_{\bar{z} \rightarrow 0^-} \cdot |t\{p\}|^2$ does appear in Chapter 3 as we do not take into consideration backward-travelling waves since there are not compatible with the slowing-varying approximation. This provides confidence in the methodology followed for deriving the model. We will now focus on deriving an expression for the average second-harmonic intensity.

Reflected average second-harmonic intensity

We compute the reflected average second-harmonic intensity, using the following expression:

$$\langle I_{2\omega_{0R}}(\mathbf{r}) \rangle = \left\| \frac{1}{T_{P\omega_0}} \int_{-\frac{1}{2}T_{P\omega_0}}^{\frac{1}{2}T_{P\omega_0}} dt \frac{1}{2} \operatorname{Re} \left\{ \mathcal{E}_{2\omega_{0R}}(\mathbf{r}, t) \times \mathcal{H}_{2\omega_{0R}}^*(\mathbf{r}, t) \right\} \right\| \quad (4.87)$$

We evaluate this equation using (4.64c) and (4.64d) for $\mathcal{H}_{2\omega_{0R}}^*$ and $\mathcal{H}_{2\omega_{0R}}$, respectively. This evaluation requires an expression for $F_{2\omega_{0R}}(t)$. Obtaining this expression involves transforming equation (4.79) into the time domain, which yields the following:

$$F_{2\omega_{0R}}(t) = \frac{(2\omega_0)^2}{c^2} \frac{a + ib}{2\gamma'_{\parallel, \omega_0}} \frac{d_{22} [t\{p\}]^2}{(2\gamma'_{\parallel, \omega_0})^2 - (\gamma'_{\perp, 2\omega_0})^2} \left(\frac{(c - a) + i(d - b)}{\gamma_{\perp, 2\omega_0} \cos(\theta_R) + c + id} \right) \frac{1}{2\pi} F_{\omega_{0i}}^2(t) \quad (4.88)$$

The details on the developing of equation (4.87) are omitted, but provided in Appendix (B), Section B.3. The reflected average second-harmonic intensity is expressed as follows:

$$\langle I_{2\omega_{0R}} \rangle = \frac{16 \omega_0^3 \gamma_{\perp, 2\omega_0}}{\epsilon_0 c^4 \sqrt{2\pi^3}} \frac{(a_{\omega_0}^2 + b_{\omega_0}^2) |d_{22}|^2}{(\beta'_{\parallel, \omega_0})^2 + (\alpha'_{\parallel, \omega_0})^2} \frac{n_{\parallel}^2(\omega_0) \cos^4(\theta_i)}{[p'^2 + q'^2]^2} \frac{(c_{2\omega_0} - a_{\omega_0})^2 + (d_{2\omega_0} - b_{\omega_0})^2}{(\gamma_{\perp, 2\omega_0} \cos 2\omega_0(\theta_i) + c_{2\omega_0})^2 + d_{2\omega_0}^2} \frac{1}{p^2 + q^2} \frac{\tau}{T_{P\omega_0}} I_{\bar{z} \rightarrow 0^-}^2 \quad (4.89)$$

The parameters a_{ω_0} , b_{ω_0} , $c_{2\omega_0}$, and $d_{2\omega_0}$ are given by equation (4.76). We can also provide expressions for $\beta'_{\nu, \omega_\ell}$ and $\alpha'_{\nu, \omega_\ell}$ with $\nu = \perp, \parallel$ and $\omega_\ell = \omega_0, 2\omega_0$ in terms of the dielectric function:

$$\beta'_{\nu, \omega_\ell}, \alpha'_{\nu, \omega_\ell} = \left(\frac{\sqrt{C_{\nu, \omega_\ell}^2 + D_{\nu, \omega_\ell}^2} \pm C_{\nu, \omega_\ell}}{2} \right)^{1/2} \quad (4.90)$$

Here, C_{ν, ω_ℓ} and D_{ν, ω_ℓ} are given by the following expressions:

$$C_{\nu, \omega_\ell} = \frac{(\omega_\ell)^2}{c^2} \operatorname{Re} \left\{ \epsilon'_{\nu}(\omega_\ell) \right\} \quad (4.91a)$$

$$D_{\nu, \omega_\ell} = \frac{(\omega_\ell)^2}{c^2} \operatorname{Im} \left\{ \epsilon'_{\nu}(\omega_\ell) \right\} \quad (4.91b)$$

Finally, the parameters p , q , p' , and q' read as follows:

$$p = 8\beta'_{\parallel,\omega_0}\alpha'_{\parallel,\omega_0} - 2\beta'_{\perp,2\omega_0}\alpha'_{\perp,2\omega_0} \quad (4.92a)$$

$$q = 4(\beta'_{\parallel,\omega_0})^2 + (\alpha'_{\perp,2\omega_0})^2 - (\beta'_{\perp,2\omega_0})^2 - 4(\alpha'_{\parallel,\omega_0})^2 \quad (4.92b)$$

$$p' = \frac{1}{2} \frac{n_{\parallel}(\omega_0)}{(\beta'_{\parallel,\omega_0})^2 + (\alpha'_{\parallel,\omega_0})} \left(b_{\omega_0}\beta'_{\parallel,\omega_0} - a_{\omega_0}\alpha'_{\parallel,\omega_0} \right) + \text{Im}\{n_{\parallel}(\omega_0)\} \cos(\theta_i) \quad (4.92c)$$

$$q' = \frac{1}{2} \frac{n_{\parallel}(\omega_0)}{(\beta'_{\parallel,\omega_0})^2 + (\alpha'_{\parallel,\omega_0})} \left(a_{\omega_0}\beta'_{\parallel,\omega_0} + b_{\omega_0}\alpha'_{\parallel,\omega_0} \right) + \text{Re}\{n_{\parallel}(\omega_0)\} \cos(\theta_i) \quad (4.92d)$$

Comments on average second-harmonic power

We can compute the reflected average second-harmonic power through the following expression:

$$\begin{aligned} \langle P_{2\omega_0\text{R}} \rangle &= \langle I_{2\omega_0\text{R}} \rangle A_{\text{beam}} \\ &= \frac{16\omega_0^3 \gamma_{\perp,2\omega_0}}{\epsilon_0 c^4 \sqrt{2\pi^3}} \frac{(a_{\omega_0}^2 + b_{\omega_0}^2) |d_{22}|^2}{(\beta'_{\parallel,\omega_0})^2 + (\alpha'_{\parallel,\omega_0})^2} \frac{n_{\parallel}^2(\omega_0) \cos^4(\theta_i)}{[p'^2 + q'^2]^2} \frac{(c_{2\omega_0} - a_{\omega_0})^2 + (d_{2\omega_0} - b_{\omega_0})^2}{(\gamma_{\perp,2\omega_0} \cos 2\omega_0(\theta_i) + c_{2\omega_0})^2 + d_{2\omega_0}^2} \\ &\quad \frac{1}{p^2 + q^2} \frac{\tau}{T_{\text{P}\omega_0}} I_{\bar{z} \rightarrow 0^-}^2 A_{\text{beam}} \end{aligned} \quad (4.93)$$

This is the main result of this section. For the sake of comparison, we write the SHG power for transmission geometry below:

$$\langle \mathbb{P}_{2\omega_0} \rangle = \frac{\omega_0^2 |d_{22}|^2}{\sqrt{8\pi^5} n_o^2(\omega_0) n_e(2\omega_0) c^3 \epsilon_0} \left(\frac{T_{\text{P}\omega_0}}{\tau} \right) \langle I_{\omega_0} \rangle^2 A_{\text{beam}} \mathcal{F}(L) \quad (4.94)$$

The main difference between equation (4.93) and equation (4.94) is that we do not have to deal with the decaying function \mathcal{F} in terms of the length of the crystal (see equation (4.34)). This is evident as we justify that the role of the length of the crystal is minimal in this scenario. In this reflection geometry model, absorption is taken into consideration through the different parameters that depend on the imaginary part of the dielectric function.

There is a detail to mention regarding this reflection geometry model, which is that we assume the propagation of the fundamental wave to be parallel to the plane of incidence, which we consider orthogonal to the optical axis. Additionally, we assume the SHG wave to be polarized perpendicular to the plane of incidence. Importantly, this is not the only scenario; we can encounter other cases where the fundamental wave is polarized perpendicular to the plane of incidence (s -polarized) while the harmonic wave is polarized parallel to the plane of incidence (p -polarized).

In fact, there are in total 4 configurations that can be used in an experiment: ss , sp , ps , pp . In this thesis, we only consider the ps case. We choose this simple case in order to explore the possibility of reflection geometry and derive a simple framework in order to deal with absorption encoded in complex dielectric functions (complex refractive indices). Additionally, we can now follow the framework developed in this thesis in order to derive an expression for the other cases.

We cannot evaluate our reflection model as in the case of transmission geometry since we do not have information of the optical parameters for LiNbO₃. The calculated material parameters for the transmission geometry are not

suitable for evaluating the reflection model since those parameters describe the bulk optical properties of LiNbO₃. Equation (4.93) focuses on the region around the surface of the sample. In this case, surface contributions predominate in comparison with the bulk contribution of the material.

In this regard, we need to calculate the surface optical properties of LiNbO₃ in order to have a better description of the linear and nonlinear optical parameters (i.e., index of refraction and nonlinear coefficients). Simone Sanna and Wolf Gero Schmidt¹⁰¹ propose slab models for different surfaces of LiNbO₃. However, these models revolve around a large number of atoms (i.e., 120 atoms). For our current computation resources[‡], simulating with `Exciting` the surface nonlinear optical properties of LiNbO₃ is impractical. Nevertheless, this model paves the way for further explorations in reflection geometry to study materials at energies where absorption is relevant, such as in XUV. We will now discuss the extend and limitations of the developed transmission and reflection models, contrasting them with previous approaches.

4.7 Limitations of the models and comparison with previous works

The plane-wave ansatz forms the foundation for both the transmission and reflection models presented here. While this approach is commonly explored in nonlinear optics books^{11,28,29}, we can find its applicability extends beyond books^{65,102,103}. For example, Bringuier and Bourdon¹⁰³ develop a travelling-plane-wave model to study second-harmonic generation in lossy media, such as GaSe and InSe. To study the second-harmonic generation process, they make the approximation of slowly varying envelope approximation, and they consider the depletion of the fundamental wave during the process. Additionally, they focus on studying the role of standing waves with GaSe and InSe by going beyond the slowly varying envelope approximation. However, they do not take into consideration temporal effects as the laser used generates pulses at a low rate (40 pulses/second).

We develop the transmission model under the slowly varying envelope approximation in space, and incorporate temporal effects under the narrow-band approximation. To evaluate the model, we perform DFT calculations to obtain linear and nonlinear optical parameters (index of refraction and d -coefficients). We observe that LiNbO₃ undergoes strong absorption within the energy range under study. This suggests the possibility that the slowly varying envelope approximation cannot be satisfied. The condition used to incorporate this approximation into the model is given by the following expression (see Appendix A):

$$\left| \frac{\partial^2 F_{i\omega_\ell}}{\partial X^2} \right| \ll \frac{4\pi}{\lambda_{f,\text{SHG}}} \left| \frac{\partial F_{i\omega_\ell}}{\partial X} \right| \quad (4.95)$$

where i corresponds to Cartesian coordinates, and $\lambda_{f,\text{SHG}}$ stands for either the fundamental or second-harmonic wavelength. We can evaluate this condition using equation (4.26) and (4.25) with the parameters provided in Table 4.2. We find that the condition (4.95) is fulfilled for both the fundamental and second-harmonic waves**.

Additionally, a key consideration for the transmission model lies in its evaluation for the X -cut LiNbO₃. Despite

[‡]We ran the `Exciting` code on a conventional 8-core laptop to calculate the nonlinear coefficients of LiNbO₃ (10-atom system). Simulating a 120-atom system within the all-electron GGA-PBE framework is not possible with this computational resource. In fact, 120-atom systems can be challenging to model using high-performance facilities with the `Exciting` code because of the explicit treatment of both cores and valence

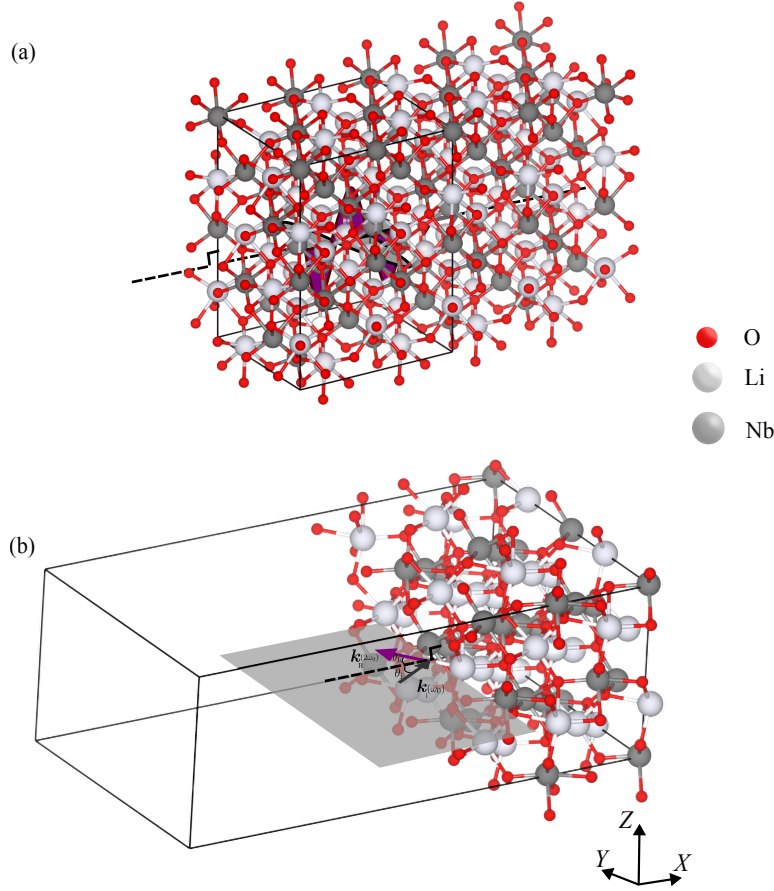


Figure 4.12: Second-harmonic generation geometry models: (a) Transmission geometry, and (b) Reflection geometry.

focusing on the X-cut, the model is evaluated using bulk LiNbO_3 properties obtained from DFT calculations. This approach might raise concerns about neglecting surface effects on the calculated second-harmonic power.

However, Philippe Guyot-Sionnest and collaborators¹⁰⁴ conclude that surface contribution to the electric field is overwhelmed by bulk contribution when the bulk medium has no center of symmetry, such as LiNbO_3 . In line with Guyot-Sionnest et al., the calculated linear and nonlinear optical material parameters are evaluated safe in the transmission model.

To visualize the two geometries (transmission and reflection) considered in this thesis, refer to Fig. 4.12 which

electrons. We believe that simulating the linear response using GPAW with 120-atom systems is possible in high-performance facilities.

**Our analysis of the fundamental and second-harmonic waves reveals a substantial difference between the left-hand side (LHS) and right-hand side (RHS) values. For the fundamental wave, the LHS yields 2.8×10^7 , while the RHS yields 3.6×10^8 . This difference of one order of magnitude is crucial in the context of our scenario, as it likely indicates that condition (A.23) is satisfied. Similarly, for the second-harmonic wave, the LHS value of 4.3×10^{13} is significantly smaller compared to the RHS value of 2×10^{15} .

presents a schematic representation. Regarding the reflection geometry, we incorporate the time dependence on the basis of the narrow-band approximation. Previous studies have extensively explored second-harmonic generation (SHG) in reflection geometry. Jerphagnon and Kurtz established a theory for isotropic and uniaxial crystals (propagation perpendicular to the optical axis), which is well documented in standard nonlinear optics texts^{11,28}.

Herman and Hayden subsequently extended this theory to encompass birefringence in uniaxial crystals (propagation at an angle θ with respect to the optical axis). They also addressed isotropic materials with absorption⁹⁶. Notably, both these works considered crystals with finite thickness. In contrast, we adopt the semi-infinite approximation, neglecting back surface reflection due to the strong absorption characteristics of LiNbO_3 ^{††}.

Moreover, Figure 4.12 illustrates the simplification employed in the second-harmonic generation (SHG) for both transmission and reflection geometries. Here, we restrict the focus to light propagating strictly perpendicular to the optical axis (Z -direction). This limitation confines the applicability of the models to specific experimental scenarios. Consequently, while the model can handle wave propagation in uniaxial materials with the $3m$ symmetry class, it is only valid for light propagating perpendicular to the optical axis.

We note in closing, that prior research on the time dependence of second-harmonic generation, such as the study of Glenn¹⁰⁵ on second-harmonic generation by picosecond pulses, often neglects the absorption of both the fundamental and second-harmonic radiation. We incorporate absorption while accounting for dispersion effects. We achieve this within the framework of the narrow-band approximation using a Taylor series expansion. To justify neglecting higher-order dispersion terms, we introduce an approximation criterion (detailed in equation (4.40) and Figure 4.8) that allows us to evaluate absorption solely at the central frequencies of the fundamental and generated second-harmonic pulses.

^{††}To ensure clarity within this section, we revisit information previously mentioned in Section 4.6.

Chapter 5

Conclusions & Outlook

This work focused on exploring the second harmonic generation process from the framework of nonlinear optics in an unexplored energy regime, denoted as the extreme ultraviolet. The nonlinear medium under consideration was the uniaxial crystal lithium niobate LiNbO_3 . The preliminary step revolves around understanding the propagation of light throughout uniaxial crystals, which requires taking into considerations optical anisotropies encoded in the indices of refraction.

In this stage, we derived two versions of the wave propagation equation: a time-independent wave and time-dependent propagation equation, and we found that under special circumstances we can neglect higher-order dispersion parameters in the dispersion relation of the linear susceptibility. Additionally, spatial effects such as diffraction and walk-off were also neglected based on developed criteria. We established intensity or power as the observable to compare theoretical estimation and experiments.

In addition, we provided explicit criteria to estimate the impact of neglecting higher-order dispersion terms. We experimentally benchmarked our theoretical formalism in the visible regime under transmission geometry. The theoretical estimation of the power (3.44 mW) showed fair quantitative agreement with the actual measured power (2.7 mW) within the uncertainties involved in the model evaluation (see Chapter 3, Section 3.3).

From this benchmarked theoretical framework, we moved our efforts towards exploration of wave propagation in the XUV regime within this benchmarked theoretical formalism as the starting point.

The first modification introduced in our model was absorption. In addition, we extended the criteria to neglect higher-order dispersion terms to include absorption. In order to assess the practicality of the dispersion criterion for the absorption coefficient, we carried out DFT simulations because of the lack of experimental data for LiNbO_3 in XUV regime. We found that at 35.5 eV and 71 eV, higher-order dispersion terms have a negligible impact on the absorption coefficient. This allows us to use our theoretical formalism to study wave propagation in the XUV regime. Additionally, the refractive indices calculated using DFT and RPA agree qualitatively with experimental data from Ref. 18 (See Chapter 4, Section 4.5).

We focused on a particular case with these two energies: the fundamental wave at 35.5 eV was ordinary polarized

and the generated second harmonic wave at 71 eV was extraordinary polarized. In this geometry, photon energies and particular material and laser source parameters, we found that nanostructured LiNbO₃ thin films from 0.1 μm to 0.2 μm can generate measurable, but weak, time-averaged second-harmonic power. (See Chapter 4, Section 4.5).

Finally, as an alternative to the transmission geometry model, we developed a framework to model reflection geometry. This model represents a first step towards future explorations of role of experimental geometry in the SHG process within the XUV regime. The transmission and reflection models we developed in this thesis can be employed to study other uniaxial crystals, they are not limited to only LiNbO₃. In this way our results will contribute to step towards second-harmonic generation in the extreme ultraviolet regime using uniaxial crystals.

Our current approach has limitations for a comprehensive description of second-harmonic generation (SHG) in the extreme ultraviolet (XUV) regime. The current criteria for neglecting higher-order dispersion terms only holds for a restricted range of energies. Including these terms is crucial for a broader description of SHG intensity/power across the XUV regime. Additionally, accurately describing material properties requires moving beyond the single-particle approximation used in density functional theory (DFT). This would allow for a more realistic picture of the physics within the crystals, but necessitates significant computational resources.

All in all, this work explores the limitations and opportunities to understand second-harmonic generation experiments using simple models (and Density Functional Theory) within the framework of nonlinear optics.

Appendix A

The Wave Equation for Nonlinear Anisotropic Media

This derivation closely follows the work by Eimerl et al.⁶⁵ up to page 114.

A.1 Wave propagation: insights into space

To begin with, from the Maxwell's equations for a charge neutral non-magnetic medium along with the use of the relation $\mathbf{D} = \epsilon_0 \mathbf{E} + \mathbf{P}$, we can derive the following equation:

$$\nabla^2 \mathbf{E} - \frac{1}{c^2} \frac{\partial^2}{\partial t^2} \mathbf{E} - \nabla(\nabla \cdot \mathbf{E}) = \frac{1}{\epsilon_0 c^2} \frac{\partial^2}{\partial t^2} \mathbf{P} \quad (\text{A.1})$$

where \mathbf{E} is the total electric field. The vector components of such total electric field, denoted by E_j , are given by the following equation:

$$E_j = \frac{1}{2} \sum_{\omega_\ell} \mathcal{E}_{j\omega_\ell}(\mathbf{r}) \exp(-i\omega_\ell t) + \text{c.c} \quad (\text{A.2})$$

where ω_ℓ correspond to frequency components involved in the nonlinear process. Equation (A.1) can be expressed in components as follows:

$$\frac{1}{2} \sum_{\omega_\ell} \left[\nabla^2 \mathcal{E}_{j\omega_\ell} + \frac{\omega_\ell^2}{c^2} \mathcal{E}_{j\omega_\ell} - \frac{\partial}{\partial x_j} \left(\frac{\partial \mathcal{E}_{\sigma\omega_\ell}}{\partial x_\sigma} \right) \right] \exp(-i\omega_\ell t) = \frac{1}{\epsilon_0 c^2} \frac{\partial^2}{\partial t^2} P_j \quad (\text{A.3})$$

A summation over repeated indices (represented by the Greek letter sigma, σ) is implicit. We can decompose the polarization density, P_j , into its linear, $P_j^{(1)}$, and nonlinear, P_j^{NL} , contributions. The former, $P_j^{(1)}$, typically reflects linear dispersion effects, while the latter, P_j^{NL} , captures processes like second harmonic generation (SHG) that arise from nonlinearities in the material response. The linear and nonlinear polarization density ($P_j^{(1)}$ and P_j^{NL}) are

expressed as the sums of frequency components:

$$P_j^{(1)} = \frac{1}{2} \epsilon_0 \sum_{\omega_\ell} \chi_{j\sigma}^{(1)}(\omega_\ell) \mathcal{E}_{\sigma\omega_\ell} \exp(-i\omega_\ell t) + \text{c.c} \quad (\text{A.4a})$$

$$P_j^{\text{NL}} = \frac{1}{2} \epsilon_0 \sum_{\omega_\ell} \mathcal{P}_{j\omega_\ell}^{\text{NL}} \exp(-i\omega_\ell t) + \text{c.c} \quad (\text{A.4b})$$

where $\chi_{jk}^{(1)}(\omega_\ell)$ stands for the linear susceptibility tensor at the frequency component ω_ℓ ; hence, plugging these two expressions into equation A.3 yields the following:

$$\frac{1}{2} \sum_{\omega_\ell} \left[\nabla^2 \mathcal{E}_{j\omega_\ell} + \frac{\omega_\ell^2}{c^2} (\delta_{j\sigma} + \chi_{j\sigma}^{(1)}) \mathcal{E}_{\sigma\omega_\ell} - \frac{\partial}{\partial x_j} \left(\frac{\partial \mathcal{E}_{\sigma\omega_\ell}}{\partial x_\sigma} \right) + \frac{\omega_\ell^2}{\epsilon_0 c^2} \mathcal{P}_{j\omega_\ell}^{\text{NL}} \right] \exp(-i\omega_\ell t) = 0 \quad (\text{A.5})$$

To satisfy this equation for any arbitrary frequency component ω_ℓ , the coefficient accompanying each harmonic term (i.e., $\exp(-i\omega_\ell t)$) must vanish. In other words:

$$\nabla^2 \mathcal{E}_{j\omega_\ell} + \frac{\omega_\ell^2}{c^2} (\delta_{j\sigma} + \chi_{j\sigma}^{(1)}) \mathcal{E}_{\sigma\omega_\ell} - \frac{\partial}{\partial x_j} \left(\frac{\partial \mathcal{E}_{\sigma\omega_\ell}}{\partial x_\sigma} \right) = -\frac{\omega_\ell^2}{\epsilon_0 c^2} \mathcal{P}_{j\omega_\ell}^{\text{NL}} \quad (\text{A.6})$$

where $\delta_{j\sigma} + \chi_{j\sigma}^{(1)}$ corresponds to the relative dielectric tensor: $\epsilon_{j\sigma}$. This equation is coordinate-free, which entails being valid in any Cartesian coordinate system. In the principal coordinate system XYZ (see Figure A.1), the tensor ϵ is diagonal. In addition, the entries ϵ_{XX} and ϵ_{YY} are identical for a uniaxial crystal, such as LiNbO_3 . In this coordinate system, the resulting X -component of $\mathcal{E}_{\omega_\ell}$ reads in equation A.5 as follows:

$$\nabla^2 \mathcal{E}_{X\omega_\ell} + \frac{\omega_\ell^2}{c^2} \epsilon_{XX}(\omega_\ell) \mathcal{E}_{X\omega_\ell} - \frac{\partial}{\partial X} \left(\frac{\partial \mathcal{E}_{X\omega_\ell}}{\partial X} + \frac{\partial \mathcal{E}_{Y\omega_\ell}}{\partial Y} + \frac{\partial \mathcal{E}_{Z\omega_\ell}}{\partial Z} \right) = -\frac{\omega_\ell^2}{\epsilon_0 c^2} \mathcal{P}_{X\omega_\ell}^{\text{NL}} \quad (\text{A.7})$$

In insulators, where free charges are absent, the electric displacement field, \mathbf{D} , is divergence-free. In this case, the displacement field is given by the following expression:

$$\mathbf{D} = \sum_{\omega_\ell} \mathbf{D}_{\omega_\ell} \quad (\text{A.8})$$

where $\mathbf{D}_{\omega_\ell} = \epsilon_0 \epsilon(\omega_\ell) \cdot \mathbf{E}_{\omega_\ell}$ for each frequency component. We can exploit such relationship between \mathbf{D}_{ω_ℓ} and \mathbf{E}_{ω_ℓ} to derive the following expression:

$$\begin{aligned} \nabla \cdot \mathbf{D} &= \sum_{\omega_\ell} \frac{\partial D_{\sigma\omega_\ell}}{\partial X_\sigma} \\ &= \sum_{\omega_\ell} \frac{\partial}{\partial X_\sigma} [\epsilon_0 \epsilon_{\sigma j} E_{j\omega_\ell}] \\ &= \sum_{\omega_\ell} \epsilon_0 \epsilon_{XX}(\omega_\ell) \left[\frac{\partial E_{X\omega_\ell}}{\partial X} + \frac{\partial E_{Y\omega_\ell}}{\partial Y} \right] + \epsilon_0 \epsilon_{ZZ}(\omega_\ell) \frac{\partial E_{Z\omega_\ell}}{\partial Z} = 0 \end{aligned}$$

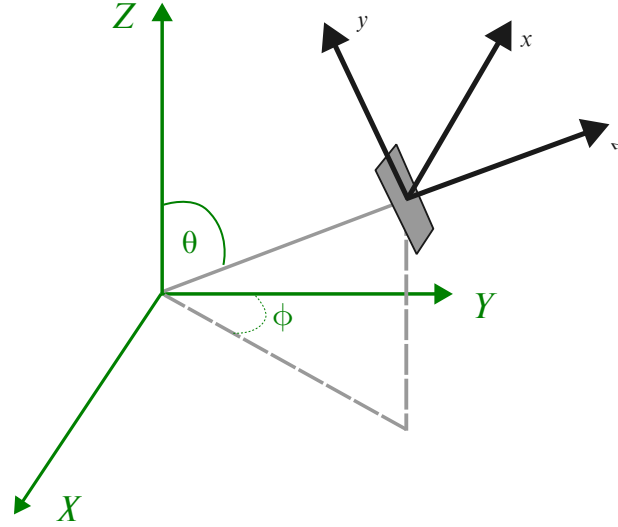


Figure A.1: Coordinate systems used to understand the wave propagation within uniaxial crystals. XYZ is the principal dielectric coordinate system while xyz is the propagation coordinate system ($Z =$ optical axis, and $z =$ direction of propagation). Reproduced from Ref. 65, Fig. 1.

We can rewrite this expression to obtain:

$$\sum_{\omega_\ell} \frac{\partial E_{X\omega_\ell}}{\partial X} + \frac{\partial E_{Y\omega_\ell}}{\partial Y} + \frac{n_e^2(\omega_\ell)}{n_o^2(\omega_\ell)} \frac{\partial E_{Z\omega_\ell}}{\partial Z} = 0 \quad (\text{A.9})$$

Furthermore, by utilizing (A.2) and the fact that exponential functions with distinct arguments are linearly independent, we can simplify equation (A.9) to:

$$\frac{\partial \mathcal{E}_{X\omega_\ell}}{\partial X} + \frac{\partial \mathcal{E}_{Y\omega_\ell}}{\partial Y} = -\frac{n_e^2(\omega_\ell)}{n_o^2(\omega_\ell)} \frac{\partial \mathcal{E}_{Z\omega_\ell}}{\partial Z} \quad (\text{A.10})$$

where

$$\beta_{\omega_\ell} = 1 - \frac{n_e^2(\omega_\ell)}{n_o^2(\omega_\ell)} \quad (\text{A.11})$$

Plugging equation A.10 into equation A.7 leads to the following expression:

$$\nabla^2 \mathcal{E}_{X\omega_\ell} + \frac{\omega_\ell^2}{c^2} n_o^2(\omega_\ell) \mathcal{E}_{X\omega_\ell} - \beta_{\omega_\ell} \frac{\partial^2 \mathcal{E}_{Z\omega_\ell}}{\partial X \partial Z} = -\frac{\omega_\ell^2}{\epsilon_0 c^2} \mathcal{P}_{X\omega_\ell}^{NL} \quad (\text{A.12})$$

Following the same procedure, we can derive the corresponding propagation equation for the Y -component and the Z -component. Therefore, the differential equations governing each vector component are given by:

$$\nabla^2 \mathcal{E}_{X \omega_\ell} + \frac{\omega_\ell^2}{c^2} n_o^2(\omega_\ell) \mathcal{E}_{X \omega_\ell} - \beta_{\omega_\ell} \frac{\partial^2 \mathcal{E}_{Z \omega_\ell}}{\partial X \partial Z} = -\frac{\omega_\ell^2}{\epsilon_0 c^2} \mathcal{P}_{X \omega_\ell}^{\text{NL}} \quad (\text{A.13a})$$

$$\nabla^2 \mathcal{E}_{Y \omega_\ell} + \frac{\omega_\ell^2}{c^2} n_o^2(\omega_\ell) \mathcal{E}_{Y \omega_\ell} - \beta_{\omega_\ell} \frac{\partial^2 \mathcal{E}_{Z \omega_\ell}}{\partial Y \partial Z} = -\frac{\omega_\ell^2}{\epsilon_0 c^2} \mathcal{P}_{Y \omega_\ell}^{\text{NL}} \quad (\text{A.13b})$$

$$\nabla^2 \mathcal{E}_{Z \omega_\ell} + \frac{\omega_\ell^2}{c^2} n_e^2(\omega_\ell) \mathcal{E}_{Z \omega_\ell} - \beta_{\omega_\ell} \frac{\partial^2 \mathcal{E}_{Z \omega_\ell}}{\partial Z^2} = -\frac{\omega_\ell^2}{\epsilon_0 c^2} \mathcal{P}_{Z \omega_\ell}^{\text{NL}} \quad (\text{A.13c})$$

A.1.1 The wave equation in different coordinate systems

The equations governing the wave propagation, as expressed in equations (A.13), are currently written with respect to the principal coordinate system. However, it is also useful to consider a different coordinate system; in this case, the coordinate system xyz . To relate these two systems and enable expressing either the differential operators or the vector components with respect to the xyz system, we introduce a transformation matrix, \mathcal{O} . This matrix explicitly defines the transformation between the propagation coordinate system xyz and the principal coordinate system XYZ (refer to Fig. A.1 for a visual representation):

$$\begin{pmatrix} x \\ y \\ z \end{pmatrix} = \mathcal{O} \begin{pmatrix} X \\ Y \\ Z \end{pmatrix} \quad (\text{A.14})$$

$$\begin{pmatrix} x \\ y \\ z \end{pmatrix} = \begin{pmatrix} -\cos(\phi) & \sin(\phi) & 0 \\ -\cos(\theta) \sin(\phi) & -\cos(\theta) \cos(\phi) & \sin(\theta) \\ \sin(\theta) \sin(\phi) & \sin(\theta) \cos(\phi) & \cos(\theta) \end{pmatrix} \begin{pmatrix} X \\ Y \\ Z \end{pmatrix}$$

In addition, the inverse transformation matrix is given by:

$$\mathcal{O}^{-1} = \mathcal{O}^T = \begin{pmatrix} -\cos(\phi) & -\cos(\theta) \sin(\phi) & \sin(\theta) \sin(\phi) \\ \sin(\phi) & -\cos(\theta) \cos(\phi) & \sin(\theta) \cos(\phi) \\ 0 & \sin(\theta) & \cos(\theta) \end{pmatrix} \quad (\text{A.15})$$

The gradient operator in the principal coordinate system is written as follows:

$$\nabla = \hat{X} \frac{\partial}{\partial X} + \hat{Y} \frac{\partial}{\partial Y} + \hat{Z} \frac{\partial}{\partial Z} \quad (\text{A.16})$$

By applying the mathematical rules of coordinate transformation (A.15), we obtain the gradient operator in the mixed coordinate representation:

$$\begin{aligned} \nabla = \hat{X} & \left[-\cos(\phi) \frac{\partial}{\partial x} - \sin(\phi) \cos(\theta) \frac{\partial}{\partial y} + \sin(\theta) \sin(\phi) \frac{\partial}{\partial z} \right] \\ & + \hat{Y} \left[\sin(\phi) \frac{\partial}{\partial x} - \cos(\phi) \cos(\theta) \frac{\partial}{\partial y} + \cos(\phi) \sin(\theta) \frac{\partial}{\partial z} \right] \\ & + \hat{Z} \left[\sin(\theta) \frac{\partial}{\partial x} + \cos(\theta) \frac{\partial}{\partial z} \right] \end{aligned} \quad (\text{A.17})$$

Therefore, the partial derivatives with respect to the XYZ coordinate system can be expressed in terms of the xyz system as follows:

$$\frac{\partial}{\partial X} = -\cos(\phi) \frac{\partial}{\partial x} - \sin(\phi) \cos(\theta) \frac{\partial}{\partial y} + \sin(\theta) \sin(\phi) \frac{\partial}{\partial z} \quad (\text{A.18a})$$

$$\frac{\partial}{\partial Y} = \sin(\phi) \frac{\partial}{\partial x} - \cos(\phi) \cos(\theta) \frac{\partial}{\partial y} + \cos(\phi) \sin(\theta) \frac{\partial}{\partial z} \quad (\text{A.18b})$$

$$\frac{\partial}{\partial Z} = \sin(\theta) \frac{\partial}{\partial x} + \cos(\theta) \frac{\partial}{\partial z} \quad (\text{A.18c})$$

We will now describe the propagation equation for ordinary and extraordinary waves. The field components are defined in the XYZ coordinate system, while the differential operators are expressed in terms of the xyz system.

A.1.2 Ordinary and Extraordinary waves

For ordinary waves, which are polarized perpendicular to the optic axis, the propagation of the field components defined in the XYZ coordinate system within the xyz system is described by the following expressions:

$$\mathcal{E}_{X \omega_\ell}(x, y, z) = F_{X \omega_\ell}^o(x, y, z) \exp\left(i n_o(\omega_\ell) \frac{\omega_\ell}{c} z\right) \quad (\text{A.19a})$$

$$\mathcal{E}_{Y \omega_\ell}(x, y, z) = F_{Y \omega_\ell}^o(x, y, z) \exp\left(i n_o(\omega_\ell) \frac{\omega_\ell}{c} z\right) \quad (\text{A.19b})$$

Within these expressions, the parameter $k_o(\omega_\ell)$ can be introduced as follows:

$$k_o(\omega_\ell) = n_o(\omega_\ell) \frac{\omega_\ell}{c} \quad (\text{A.20})$$

where $n_o(\omega_\ell)$ is the refractive index of the ordinary wave, c is the speed of light, and ω_ℓ is the an angular frequency. Furthermore, $F_{X \omega_\ell}^o$ and $F_{Y \omega_\ell}^o$ are slowly varying functions with respect to z . Purposely, for ordinary waves, by definition, $\mathcal{E}_{Z \omega_\ell} = 0$ (see Chapter 2, Section 2.1.1).

By substituting equation (A.17) for the gradient operator in equation (A.13a), we obtain the following expression:

$$\left(\frac{\partial^2}{\partial x^2} + \frac{\partial^2}{\partial y^2} + \frac{\partial^2}{\partial z^2} \right) \mathcal{E}_{X \omega_\ell} + \frac{\omega_\ell^2}{c^2} n_o^2(\omega_\ell) \mathcal{E}_{X \omega_\ell} = -\frac{\omega_\ell^2}{\epsilon_0 c^2} \mathcal{P}_{X \omega_\ell}^{\text{NL}} \quad (\text{A.21})$$

Because the Laplacian operator is a scalar, it remains invariant (or independent) of the coordinate system used. From equation (A.19a), we see that second-order partial derivatives in x and y only affect $F_{X \omega_\ell}^o$ within the electric field component $\mathcal{E}_{X \omega_\ell}$. Therefore, we will now focus on the z -dependence by examining the second-order derivative with respect to z in equation (A.19a):

$$\frac{\partial^2 \mathcal{E}_{X \omega_\ell}}{\partial z^2} = \left[\frac{\partial^2 F_{X \omega_\ell}^o}{\partial z^2} + 2i n_o(\omega_\ell) \frac{\omega_\ell}{c} \frac{\partial F_{X \omega_\ell}^o}{\partial z} - n_o^2(\omega_\ell) \frac{\omega_\ell^2}{c^2} F_{X \omega_\ell}^o \right] \exp\left(i n_o(\omega_\ell) \frac{\omega_\ell}{c} z\right) \quad (\text{A.22})$$

A common approximation technique, known as the slowly varying envelope (SVE) approximation¹¹, allows us to neglect the first term on the right side of this equation. This simplification is valid when:

$$\left| \frac{\partial^2 F_{X \omega_\ell}^o}{\partial z^2} \right| \ll \left| 2i n_o(\omega_\ell) \frac{\omega_\ell}{c} \frac{\partial F_{X \omega_\ell}^o}{\partial z} \right| = \frac{4\pi}{\lambda} \left| \frac{\partial F_{X \omega_\ell}^o}{\partial z} \right| \quad (\text{A.23})$$

One can see that the fractional change of $\frac{\partial}{\partial x} F_{X\omega_\ell}^o$ must be smaller than the inverse of wavelength. Under the SVA approximation, the second-order partial derivative with respect to x becomes:

$$\frac{\partial^2 \mathcal{E}_{X\omega_\ell}}{\partial z^2} \cong \left[2in_o(\omega_\ell) \frac{\omega_\ell}{c} \frac{\partial F_{X\omega_\ell}^o}{\partial z} - n_o^2(\omega_\ell) \frac{\omega_\ell^2}{c^2} F_{X\omega_\ell}^o \right] \exp\left(i n_o(\omega_\ell) \frac{\omega_\ell}{c} z\right) \quad (\text{A.24})$$

Then equation A.21 reduces to

$$\left(\frac{\partial^2}{\partial x^2} + \frac{\partial^2}{\partial y^2} \right) F_{X\omega_\ell}^o + 2in_o(\omega_\ell) \frac{\omega_\ell}{c} \frac{\partial F_{X\omega_\ell}^o}{\partial z} \cong -\frac{\omega_\ell^2}{\epsilon_0 c^2} \mathcal{P}_{X\omega_\ell}^{\text{NL}} \exp\left(-i n_o(\omega_\ell) \frac{\omega_\ell}{c} z\right) \quad (\text{A.25})$$

Analogously to the X component, we can derive an equation for the Y component of the ordinary wave:

$$\left(\frac{\partial^2}{\partial x^2} + \frac{\partial^2}{\partial y^2} \right) F_{Y\omega_\ell}^o + 2in_o(\omega_\ell) \frac{\omega_\ell}{c} \frac{\partial F_{Y\omega_\ell}^o}{\partial z} \cong -\frac{\omega_\ell^2}{\epsilon_0 c^2} \mathcal{P}_{Y\omega_\ell}^{\text{NL}} \exp\left(-i n_o(\omega_\ell) \frac{\omega_\ell}{c} z\right) \quad (\text{A.26})$$

In connection with the extraordinary waves, the refractive indices vary with θ (the angle between the wave vector and the optic axis Z ; see Fig. A.1). In this case, the vector components are expressed as follows:

$$\mathcal{E}_{X\omega_\ell}(x, y, z) = F_{X\omega_\ell}^e(x, y, z) \exp\left(i n_e(\omega_\ell, \theta) \frac{\omega_\ell}{c} z\right) \quad (\text{A.27a})$$

$$\mathcal{E}_{Y\omega_\ell}(x, y, z) = F_{Y\omega_\ell}^e(x, y, z) \exp\left(i n_e(\omega_\ell, \theta) \frac{\omega_\ell}{c} z\right) \quad (\text{A.27b})$$

$$\mathcal{E}_{Z\omega_\ell}(x, y, z) = F_{Z\omega_\ell}^e(x, y, z) \exp\left(i n_e(\omega_\ell, \theta) \frac{\omega_\ell}{c} z\right) \quad (\text{A.27c})$$

Similar to the ordinary case, within these expressions, the parameter $k_e(\omega_\ell, \theta)$ can be introduced as follows:

$$k_e(\omega_\ell, \theta) = n_e(\omega_\ell, \theta) \frac{\omega_\ell}{c} \quad (\text{A.28})$$

Eimerl et al. focused on the Z -component of the extraordinary field because they studied geometries where the Z -component is only involved.

Using expression (A.17) for ∇^2 and expression (A.18c) for $\frac{\partial^2}{\partial z^2}$, equation (A.13c) can be re-written as follows:

$$\begin{aligned} \left(\frac{\partial^2}{\partial x^2} + \frac{\partial^2}{\partial y^2} + \frac{\partial^2}{\partial z^2} \right) \mathcal{E}_{Z\omega_\ell} + \frac{\omega_\ell^2}{c^2} n_e^2(\omega_\ell) \mathcal{E}_{Z\omega_\ell} - \beta_{\omega_\ell} \left[\sin^2(\theta) \frac{\partial^2}{\partial y^2} + \cos^2(\theta) \frac{\partial^2}{\partial z^2} \right. \\ \left. + \sin(2\theta) \frac{\partial^2}{\partial y \partial z} \right] \mathcal{E}_{Z\omega_\ell} = -\frac{\omega_\ell^2}{\epsilon_0 c^2} \mathcal{P}_{Z\omega_\ell}^{\text{NL}} \end{aligned} \quad (\text{A.29})$$

To simplify the above equation, we approach it using the SVA approximation as follows:

$$\begin{aligned} \frac{\partial^2 \mathcal{E}_{Z\omega_\ell}}{\partial z^2} &= \frac{\partial^2}{\partial z^2} \left[F_{Z\omega_\ell}^e \exp\left(i n_e(\omega_\ell, \theta) \frac{\omega_\ell}{c} z\right) \right] \\ &\cong \left[2in_e(\omega_\ell, \theta) \frac{\omega_\ell}{c} \frac{\partial F_{Z\omega_\ell}^e}{\partial z} - n_e^2(\omega_\ell, \theta) \frac{\omega_\ell^2}{c^2} F_{Z\omega_\ell}^e \right] \exp\left(i n_e(\omega_\ell, \theta) \frac{\omega_\ell}{c} z\right) \end{aligned} \quad (\text{A.30})$$

Building upon this approximation, we can approach the mixed partial derivative in the following manner:

$$\begin{aligned}
\frac{\partial^2 \mathcal{E}_{Z\omega_\ell}}{\partial y \partial z} &= \frac{\partial^2}{\partial y \partial z} \left[F_{Z\omega_\ell}^e \exp\left(i n_e(\omega_\ell, \theta) \frac{\omega_\ell}{c} z\right) \right] \\
&= \left(\frac{\partial^2 F_{Z\omega_\ell}^e}{\partial y \partial z} \right) \exp\left(i n_e(\omega_\ell, \theta) \frac{\omega_\ell}{c} z\right) + i \frac{\omega_\ell}{c} n_e(\omega_\ell, \theta) \exp\left(i n_e(\omega_\ell, \theta) \frac{\omega_\ell}{c} z\right) \frac{\partial F_{Z\omega_\ell}^e}{\partial y} \\
&\cong i \frac{\omega_\ell}{c} n_e(\omega_\ell, \theta) \exp\left(i n_e(\omega_\ell, \theta) \frac{\omega_\ell}{c} z\right) \frac{\partial F_{Z\omega_\ell}^e}{\partial y}
\end{aligned} \tag{A.31}$$

While the latter uses a variation of the slowing varying envelope approximation in the form of $\left| \frac{\partial^2 F_{Z\omega_\ell}^e}{\partial z \partial x} \right| \ll \left| \frac{F_{Z\omega_\ell}^e}{\partial z} \right|$, the latter is the analog of equation A.24. Plugging back expressions (A.30) and (A.31) into (A.29), it reduces to:

$$\begin{aligned}
\frac{\partial^2 F_{Z\omega_\ell}^e}{\partial x^2} + \left[1 - \beta_{\omega_\ell} \sin^2(\theta) \right] \frac{\partial^2 F_{Z\omega_\ell}^e}{\partial y^2} - i \beta_{\omega_\ell} \frac{\omega_\ell}{c} n_e(\omega_\ell, \theta) \sin(2\theta) \frac{\partial F_{Z\omega_\ell}^e}{\partial y} \\
+ 2i n_e(\omega_\ell, \theta) \frac{\omega_\ell}{c} \left[1 - \beta_{\omega_\ell} \cos^2(\theta) \right] \frac{\partial F_{Z\omega_\ell}^e}{\partial z} \\
= -\frac{\omega_\ell^2}{\epsilon_0 c^2} \mathcal{P}_{Z\omega_\ell}^{\text{NL}} \exp\left(-i n_e(\omega_\ell, \theta) \frac{\omega_\ell}{c} z\right)
\end{aligned} \tag{A.32}$$

Using the dispersion relation for $n_e(\omega_\ell, \theta)$ (See Section 2.1.1), one obtains the following relationship between $n_e(\omega_\ell)$ and $n_e(\omega_\ell, \theta)$:

$$\begin{aligned}
\frac{1}{n_e^2(\omega_\ell, \theta)} &= \frac{\sin^2(\theta)}{n_e^2(\omega_\ell)} + \frac{\cos^2(\theta)}{n_o^2(\omega_\ell)} \\
n_e^2(\omega_\ell) &= n_e^2(\omega_\ell, \theta) \left[1 - \left(1 - \frac{n_e^2(\omega_\ell)}{n_o^2(\omega_\ell)} \right) \cos^2(\theta) \right] \\
n_e^2(\omega_\ell) &= n_e^2(\omega_\ell, \theta) \left[1 - \beta_{\omega_\ell} \cos^2(\theta) \right] \\
n_e(\omega_\ell) \left[1 - \beta_{\omega_\ell} \cos^2(\theta) \right]^{\frac{1}{2}} &= n_e(\omega_\ell, \theta) \left[1 - \beta_{\omega_\ell} \cos^2(\theta) \right]
\end{aligned}$$

This relationship allows us to re-write equation (A.32) as follows:

$$\begin{aligned}
\frac{\partial^2 F_{Z\omega_\ell}^e}{\partial x^2} + \left[1 - \beta_{\omega_\ell} \sin^2(\theta) \right] \frac{\partial^2 F_{Z\omega_\ell}^e}{\partial y^2} + 2i n_e(\omega_\ell) \frac{\omega_\ell}{c} \left[1 - \beta_{\omega_\ell} \cos^2(\theta) \right]^{\frac{1}{2}} \\
\left[\frac{\partial F_{Z\omega_\ell}^e}{\partial z} - \left(\frac{\beta_{\omega_\ell}}{2} \sin(2\theta) \right) \frac{\partial F_{Z\omega_\ell}^e}{\partial y} \right] \\
= -\frac{\omega_\ell^2}{\epsilon_0 c^2} \mathcal{P}_{Z\omega_\ell}^{\text{NL}} \exp\left(-i n_e(\omega_\ell, \theta) \frac{\omega_\ell}{c} z\right)
\end{aligned} \tag{A.33}$$

We can introduce an additional parameter that groups together the factor β_{ω_ℓ} and θ as follows:

$$\rho_{\omega_\ell}(\theta) = -\frac{\frac{\beta_{\omega_\ell}}{2} \sin(2\theta)}{1 - \beta_{\omega_\ell} \cos^2(\theta)} \quad (\text{A.34})$$

Finally, equation A.33 becomes:

$$\begin{aligned} \frac{\partial^2 F_{Z\omega_\ell}^e}{\partial x^2} + \left[1 - \beta_{\omega_\ell} \sin^2(\theta)\right] \frac{\partial^2 F_{Z\omega_\ell}^e}{\partial y^2} + 2in_e(\omega_\ell) \frac{\omega_\ell}{c} \left[1 - \beta_{\omega_\ell} \cos^2(\theta)\right]^{\frac{1}{2}} \left[\frac{\partial F_{Z\omega_\ell}^e}{\partial z} + \rho_{\omega_\ell}(\theta) \frac{\partial F_{Z\omega_\ell}^e}{\partial y} \right] \\ = -\frac{\omega_\ell^2}{\epsilon_0 c^2} \mathcal{P}_{Z\omega_\ell}^{\text{NL}} \exp\left(-in_e(\omega_\ell, \theta) \frac{\omega_\ell}{c} z\right) \end{aligned} \quad (\text{A.35})$$

A.2 Wave propagation: insights into space and time

We will now provide the detailed intermediate steps for the derivations outlined in Section 3.1.2 of Chapter 3. The parameterization of the total electric field is written as follows:

$$\begin{aligned} \mathbf{E}(\mathbf{r}, t) &= \sum_{\omega_\ell} \mathbf{E}_{\omega_\ell}(\mathbf{r}, t) \\ &= \sum_{\omega_\ell} \frac{1}{2} \mathcal{E}_{\omega_\ell}(\mathbf{r}, t) \exp(-i\omega_\ell t) + \text{c.c.} \end{aligned} \quad (\text{A.36})$$

where ω_ℓ is the carrier frequency. We proceed to compute the Fourier transforms of several quantities, such as the electric field and polarization, as introduced in Section 3.1.2. The Fourier transform of the electric field described by equation (A.36) is:

$$\begin{aligned} \tilde{\mathbf{E}}(\mathbf{r}, \omega) &= \int_{-\infty}^{+\infty} dt \mathbf{E}(\mathbf{r}, t) \exp(i\omega t) \\ &= \sum_{\omega_\ell} \frac{1}{2} \int_{-\infty}^{+\infty} dt \left(\mathcal{E}_{\omega_\ell}(\mathbf{r}, t) \exp(-i\omega_\ell t) \exp(i\omega t) + \mathcal{E}_{\omega_\ell}^*(\mathbf{r}, t) \exp(i\omega_\ell t) \exp(i\omega t) \right) \\ &= \sum_{\omega_\ell} \frac{1}{2} \int_{-\infty}^{+\infty} dt \mathcal{E}_{\omega_\ell}(\mathbf{r}, t) \exp(i(\omega - \omega_\ell)t) + \frac{1}{2} \int_{-\infty}^{+\infty} dt \mathcal{E}_{\omega_\ell}^*(\mathbf{r}, t) \exp(i(\omega + \omega_\ell)t) \\ &= \frac{1}{2} \left(\sum_{\omega_\ell} \tilde{\mathcal{E}}_{\omega_\ell}(\mathbf{r}, \omega - \omega_\ell) + \tilde{\mathcal{E}}_{\omega_\ell}^*(\mathbf{r}, \omega + \omega_\ell) \right) \end{aligned} \quad (\text{A.37})$$

where the envelopes have some limited extend around the carrier frequencies at $\pm\omega_\ell$. The Fourier pair of (A.37) can be written as follows:

$$\begin{aligned} \mathbf{E}(\mathbf{r}, t) &= \frac{1}{2\pi} \int_{-\infty}^{+\infty} d\omega \tilde{\mathbf{E}}(\mathbf{r}, \omega) \exp(-i\omega t) \\ &= \frac{1}{2\pi} \int_{-\infty}^{+\infty} d\omega \frac{1}{2} \left(\sum_{\omega_\ell} \tilde{\mathcal{E}}_{\omega_\ell}(\mathbf{r}, \omega - \omega_\ell) + \tilde{\mathcal{E}}_{\omega_\ell}^*(\mathbf{r}, \omega + \omega_\ell) \right) \exp(-i\omega t) \end{aligned} \quad (\text{A.38})$$

Through a variable substitution $\omega' = \omega \pm \omega_\ell$, we can re-write equation (A.38) as two integrals:

$$\begin{aligned} \mathbf{E}(\mathbf{r}, t) &= \frac{1}{2\pi} \left(\sum_{\omega_\ell} \int_{-\infty}^{+\infty} d\omega' \frac{1}{2} \tilde{\mathcal{E}}_{\omega_\ell}(\mathbf{r}, \omega') \exp(-i\omega' t) \right) \exp(-i\omega_\ell t) \\ &+ \frac{1}{2\pi} \left(\sum_{\omega_\ell} \int_{-\infty}^{+\infty} d\omega' \frac{1}{2} \tilde{\mathcal{E}}_{\omega_\ell}^*(\mathbf{r}, \omega') \exp(-i\omega' t) \right) \exp(i\omega_\ell t) \\ &= \frac{1}{2\pi} \left(\sum_{\omega_\ell} \int_{-\infty}^{+\infty} d\omega' \frac{1}{2} \tilde{\mathcal{E}}_{\omega_\ell}(\mathbf{r}, \omega') \exp(-i\omega' t) \right) \exp(-i\omega_\ell t) + \text{c.c.} \end{aligned} \quad (\text{A.39})$$

Because $\mathbf{E}(\mathbf{r}, t)$ is a real quantity, the second term in equation (A.39) must be the complex conjugate of the first term to ensure the entire expression remains real. Unlike equation (3.6), which describes a time-independent total electric field, the relationship between polarization, $\mathbf{P}^{(1)}(\mathbf{r}, t)$, and the electric field, $\mathbf{E}(\mathbf{r}, t)$, in this context can depend on past history of the field. This dependence is captured by the following equation:

$$\mathbf{P}^{(1)}(\mathbf{r}, t) = \epsilon_0 \int_{-\infty}^{+\infty} d\tau \underline{\underline{\chi}}^{(1)}(\tau) \cdot \mathbf{E}(\mathbf{r}, t - \tau) \quad (\text{A.40})$$

where $\underline{\underline{\chi}}^{(1)}$ is a linear response function. Taking the inverse Fourier transform of $\mathbf{E}(\mathbf{r}, t)$ and substituting it into equation (A.40), we obtain:

$$\begin{aligned} \mathbf{P}^{(1)}(\mathbf{r}, t) &= \epsilon_0 \int_{-\infty}^{+\infty} d\tau \underline{\underline{\chi}}^{(1)}(\tau) \cdot \int_{-\infty}^{+\infty} \frac{d\omega}{2\pi} \tilde{\mathbf{E}}(\mathbf{r}, \omega) \exp(-i\omega(t - \tau)) \\ &= \frac{\epsilon_0}{2\pi} \int_{-\infty}^{+\infty} d\omega \left(\int_{-\infty}^{+\infty} d\tau \underline{\underline{\chi}}^{(1)}(\tau) \exp(i\omega\tau) \right) \cdot \tilde{\mathbf{E}}(\mathbf{r}, \omega) \exp(-i\omega t) \\ &= \frac{\epsilon_0}{2\pi} \int_{-\infty}^{+\infty} d\omega \underline{\underline{\chi}}^{(1)}(-\omega_\sigma; \omega) \cdot \tilde{\mathbf{E}}(\mathbf{r}, \omega) \exp(-i\omega t) \end{aligned} \quad (\text{A.41})$$

where $\omega_\sigma = \omega$, and

$$\underline{\underline{\chi}}^{(1)}(-\omega_\sigma; \omega) = \int_{-\infty}^{+\infty} d\tau \underline{\underline{\chi}}^{(1)}(\tau) \exp(i\omega\tau)$$

Moreover, $\underline{\underline{\chi}}^{(1)}(\tau)$ must vanish when τ is negative in order to ensure that $\mathbf{P}^{(1)}(\mathbf{r}, t)$ depends only on values of the field for times before t ; hence causality condition. Plugging equation (A.37) into equation (A.41) and making the

same substitution $\omega' = \omega \pm \omega_\ell$, the linear polarization is finally written as follows:

$$\begin{aligned}
\mathbf{P}^{(1)}(\mathbf{r}, t) &= \frac{\epsilon_0}{2\pi} \int_{-\infty}^{+\infty} d\omega \underline{\underline{\chi}}^{(1)}(-\omega_\sigma; \omega) \cdot \tilde{\mathbf{E}}(\mathbf{r}, \omega) \exp(-i\omega t) \\
&= \frac{\epsilon_0}{2\pi} \int_{-\infty}^{+\infty} d\omega \underline{\underline{\chi}}^{(1)}(-\omega_\sigma; \omega) \cdot \frac{1}{2} \left(\sum_{\omega_\ell} \tilde{\mathcal{E}}_{\omega_\ell}(\mathbf{r}, \omega - \omega_\ell) + \tilde{\mathcal{E}}_{\omega_\ell}^*(\mathbf{r}, \omega + \omega_\ell) \right) \exp(-i\omega t) \\
&= \frac{\epsilon_0}{4} \left(\sum_{\omega_\ell} \int_{-\infty}^{+\infty} d\omega' \underline{\underline{\chi}}^{(1)}(-\omega_\sigma; \omega_\ell + \omega') \tilde{\mathcal{E}}_{\omega_\ell}(\mathbf{r}, \omega') \exp(-i\omega' t) \right) \exp(-i\omega_\ell t) \\
&\quad + \frac{\epsilon_0}{4} \left(\sum_{\omega_\ell} \int_{-\infty}^{+\infty} d\omega' \underline{\underline{\chi}}^{(1)}(-\omega_\sigma; \omega_\ell - \omega') \tilde{\mathcal{E}}_{\omega_\ell}^*(\mathbf{r}, \omega') \exp(-i\omega' t) \right) \exp(i\omega_\ell t) \\
&= \frac{\epsilon_0}{4} \left(\sum_{\omega_\ell} \int_{-\infty}^{+\infty} d\omega' \underline{\underline{\chi}}^{(1)}(-\omega_\sigma; \omega_\ell + \omega') \tilde{\mathcal{E}}_{\omega_\ell}(\mathbf{r}, \omega') \exp(-i\omega' t) \right) \exp(-i\omega_\ell t) + \text{c.c.}
\end{aligned} \tag{A.42}$$

By analogy with the electric field, the second term in expression (A.42) is the complex conjugate of the first term; purposely, in this case, $\omega_\sigma = \omega_\ell \pm \omega'$.

The nonlinear polarization term is expressed as a power series expansion of the total electric field:

$$\begin{aligned}
\mathbf{P}^{\text{NL}}(\mathbf{r}, t) &= \epsilon_0 \int_{-\infty}^{+\infty} d\tau_1 \int_{-\infty}^{+\infty} d\tau_2 \underline{\underline{\chi}}^{(2)}(t - \tau_1, t - \tau_2) : \mathbf{E}(\mathbf{r}, \tau_1) \mathbf{E}(\mathbf{r}, \tau_2) \\
&\quad + \epsilon_0 \int_{-\infty}^{+\infty} d\tau_1 \int_{-\infty}^{+\infty} d\tau_2 \int_{-\infty}^{+\infty} d\tau_3 \underline{\underline{\chi}}^{(3)}(t - \tau_1, t - \tau_2, t - \tau_3) : \mathbf{E}(\mathbf{r}, \tau_1) \mathbf{E}(\mathbf{r}, \tau_2) \mathbf{E}(\mathbf{r}, \tau_3) + \dots
\end{aligned} \tag{A.43}$$

In the context of this thesis, solely second-order terms are taken into consideration. In addition, the causality condition requires that $\underline{\underline{\chi}}^{(2)}(t - \tau_1, t - \tau_2) = 0$ when either τ_1 or τ_2 is negative. In the expression (A.43), for the second-order term, we can express the total electric field in terms of its inverse Fourier transform as follows:

$$\mathbf{P}^{\text{NL}}(\mathbf{r}, t) = \epsilon_0 \int_{-\infty}^{+\infty} \frac{d\omega_1}{2\pi} \int_{-\infty}^{+\infty} \frac{d\omega_2}{2\pi} \underline{\underline{\chi}}^{(2)}(-\omega_\sigma; \omega_1, \omega_2) : \tilde{\mathbf{E}}(\mathbf{r}, \omega_1) \tilde{\mathbf{E}}(\mathbf{r}, \omega_2) e^{-i(\omega_1 + \omega_2)t} \tag{A.44}$$

where $\omega_\sigma = \omega_1 + \omega_2$, and $\underline{\underline{\chi}}^{(2)}(-\omega_\sigma; \omega_1, \omega_2)$ is the second-order susceptibility:

$$\underline{\underline{\chi}}^{(2)}(-\omega_\sigma; \omega_1, \omega_2) = \int_{-\infty}^{+\infty} d\tau_1 \int_{-\infty}^{+\infty} d\tau_2 \underline{\underline{\chi}}^{(2)}(\tau_1, \tau_2) e^{i(\omega_1 \tau_1 + \omega_2 \tau_2)} \tag{A.45}$$

To gain insight into the frequency components at play in second-order nonlinear processes, we can substitute equation (A.37) into equation (A.45):

$$\begin{aligned}
\mathbf{P}^{\text{NL}}(\mathbf{r}, t) &= \epsilon_0 \int_{-\infty}^{+\infty} \frac{d\omega_1}{2\pi} \int_{-\infty}^{+\infty} \frac{d\omega_2}{2\pi} \underline{\chi}^{(2)}(-\omega_\sigma; \omega_1, \omega_2) : \tilde{\mathbf{E}}(\mathbf{r}, \omega_1) \tilde{\mathbf{E}}(\mathbf{r}, \omega_2) e^{-i(\omega_1 + \omega_2)t} \\
&= \frac{\epsilon_0}{4} \sum_{\omega_p} \sum_{\omega_q} \int_{-\infty}^{+\infty} \frac{d\omega_1}{2\pi} \int_{-\infty}^{+\infty} \frac{d\omega_2}{2\pi} \chi_{ijk}^{(2)}(-\omega_\sigma; \omega_1, \omega_2) \left(\tilde{\mathcal{E}}_{j\omega_p}(\mathbf{r}, \omega_1 - \omega_p) + \tilde{\mathcal{E}}_{j\omega_p}^*(\mathbf{r}, \omega_1 + \omega_p) \right) \\
&\quad \left(\tilde{\mathcal{E}}_{k\omega_q}(\mathbf{r}, \omega_2 - \omega_q) + \tilde{\mathcal{E}}_{k\omega_q}^*(\mathbf{r}, \omega_2 + \omega_q) \right) \exp(-i(\omega_1 + \omega_2)t) \\
&= \frac{\epsilon_0}{4} \left(\sum_{\omega_p} \sum_{\omega_q} \int_{-\infty}^{+\infty} \frac{d\omega''}{2\pi} \int_{-\infty}^{+\infty} \frac{d\omega'''}{2\pi} \chi_{ijk}^{(2)}(-\omega_\sigma; \omega'' + \omega_p, \omega''' + \omega_q) \tilde{\mathcal{E}}_{j\omega_p}(\mathbf{r}, \omega'') \tilde{\mathcal{E}}_{k\omega_q}(\mathbf{r}, \omega''') \right) \\
&\quad \exp(-i(\omega'' + \omega''')t) \Big) \exp(-i(\omega_p + \omega_q)t) \\
&\quad + \frac{\epsilon_0}{4} \left(\sum_{\omega_p} \sum_{\omega_q} \int_{-\infty}^{+\infty} \frac{d\omega''}{2\pi} \int_{-\infty}^{+\infty} \frac{d\omega'''}{2\pi} \chi_{ijk}^{(2)}(-\omega_\sigma; \omega'' + \omega_p, \omega''' - \omega_q) \tilde{\mathcal{E}}_{j\omega_p}(\mathbf{r}, \omega'') \tilde{\mathcal{E}}_{k\omega_q}^*(\mathbf{r}, \omega''') \right) \\
&\quad \exp(-i(\omega'' + \omega''')t) \Big) \exp(-i(\omega_p - \omega_q)t) \\
&\quad + \frac{\epsilon_0}{4} \left(\sum_{\omega_p} \sum_{\omega_q} \int_{-\infty}^{+\infty} \frac{d\omega''}{2\pi} \int_{-\infty}^{+\infty} \frac{d\omega'''}{2\pi} \chi_{ijk}^{(2)}(-\omega_\sigma; \omega'' - \omega_p, \omega''' + \omega_q) \tilde{\mathcal{E}}_{j\omega_p}^*(\mathbf{r}, \omega'') \tilde{\mathcal{E}}_{k\omega_q}(\mathbf{r}, \omega''') \right) \\
&\quad \exp(-i(\omega'' + \omega''')t) \Big) \exp(-i(\omega_q - \omega_p)t) \\
&\quad + \frac{\epsilon_0}{4} \left(\sum_{\omega_p} \sum_{\omega_q} \int_{-\infty}^{+\infty} \frac{d\omega''}{2\pi} \int_{-\infty}^{+\infty} \frac{d\omega'''}{2\pi} \chi_{ijk}^{(2)}(-\omega_\sigma; \omega'' - \omega_p, \omega''' - \omega_q) \tilde{\mathcal{E}}_{j\omega_p}^*(\mathbf{r}, \omega'') \tilde{\mathcal{E}}_{k\omega_q}^*(\mathbf{r}, \omega''') \right) \\
&\quad \exp(-i(\omega'' + \omega''')t) \Big) \exp(i(\omega_p + \omega_q)t)
\end{aligned} \tag{A.46}$$

where we introduce the following changes of variable: $\omega'' = \omega_1 \pm \omega_p$ and $\omega''' = \omega_2 \pm \omega_q$.

Similar to (A.36), the polarization $\mathbf{P}^{\text{NL}}(\mathbf{r}, t)$ can be written as:

$$\mathbf{P}^{\text{NL}}(\mathbf{r}, t) = \sum_{\omega_\ell} \frac{1}{2} \mathcal{P}_{\omega_\ell}^{\text{NL}}(\mathbf{r}, t) \exp(-i\omega_\ell t) + \text{c.c.} \tag{A.47}$$

By analyzing the relationship between equations (A.47) and (A.46), we can derive an expression for $\mathcal{P}_{\omega_\ell}^{\text{NL}}$ depending on the specific value of ω_ℓ :

$$\begin{aligned} \mathcal{P}_{i\omega_\ell} &= \frac{\epsilon_0}{2} \sum_{\omega_p} \sum_{\omega_q} \int_{-\infty}^{+\infty} \frac{d\omega''}{2\pi} \int_{-\infty}^{+\infty} \frac{d\omega'''}{2\pi} \chi_{ijk}^{(2)}(-\omega_\sigma; \omega'' + \omega_p, \omega''' + \omega_q) \tilde{\mathcal{E}}_{j\omega_p}(\mathbf{r}, \omega'') \tilde{\mathcal{E}}_{k\omega_q}(\mathbf{r}, \omega''') \\ &\quad \exp\left(-i(\omega'' + \omega''')t\right) \end{aligned} \quad \text{for } \omega_\ell = \omega_p + \omega_q \quad (\text{A.48a})$$

$$\begin{aligned} \mathcal{P}_{i\omega_\ell} &= \frac{\epsilon_0}{2} \sum_{\omega_p} \sum_{\omega_q} \int_{-\infty}^{+\infty} \frac{d\omega''}{2\pi} \int_{-\infty}^{+\infty} \frac{d\omega'''}{2\pi} \chi_{ijk}^{(2)}(-\omega_\sigma; \omega'' + \omega_p, \omega''' - \omega_q) \tilde{\mathcal{E}}_{j\omega_p}(\mathbf{r}, \omega'') \tilde{\mathcal{E}}_{k\omega_q}^*(\mathbf{r}, \omega''') \\ &\quad \exp\left(-i(\omega'' + \omega''')t\right) \end{aligned} \quad \text{for } \omega_\ell = \omega_p - \omega_q \quad (\text{A.48b})$$

$$\begin{aligned} \mathcal{P}_{i\omega_\ell} &= \frac{\epsilon_0}{2} \sum_{\omega_p} \sum_{\omega_q} \int_{-\infty}^{+\infty} \frac{d\omega''}{2\pi} \int_{-\infty}^{+\infty} \frac{d\omega'''}{2\pi} \chi_{ijk}^{(2)}(-\omega_\sigma; \omega'' - \omega_p, \omega''' + \omega_q) \tilde{\mathcal{E}}_{j\omega_p}^*(\mathbf{r}, \omega'') \tilde{\mathcal{E}}_{k\omega_q}(\mathbf{r}, \omega''') \\ &\quad \exp\left(-i(\omega'' + \omega''')t\right) \end{aligned} \quad \text{for } \omega_\ell = \omega_q - \omega_p \quad (\text{A.48c})$$

$$\begin{aligned} \mathcal{P}_{i\omega_\ell} &= \frac{\epsilon_0}{2} \sum_{\omega_p} \sum_{\omega_q} \int_{-\infty}^{+\infty} \frac{d\omega''}{2\pi} \int_{-\infty}^{+\infty} \frac{d\omega'''}{2\pi} \chi_{ijk}^{(2)}(-\omega_\sigma; \omega'' - \omega_p, \omega''' - \omega_q) \tilde{\mathcal{E}}_{j\omega_p}^*(\mathbf{r}, \omega'') \tilde{\mathcal{E}}_{k\omega_q}^*(\mathbf{r}, \omega''') \\ &\quad \exp\left(-i(\omega'' + \omega''')t\right) \end{aligned} \quad \text{for } \omega_\ell = -\omega_p - \omega_q \quad (\text{A.48d})$$

Since the envelopes, $\mathcal{E}_{\omega_\ell}$ possess a narrow bandwidth, the evaluation of the nonlinear second-order susceptibility in equations (A.48) is conveniently performed at the carrier frequencies. This simplification arises because the narrow bandwidth can imply minimal variation in the susceptibility across a limited frequency range. Consequently, equation (A.48a), for example, becomes:

$$\begin{aligned} \mathcal{P}_{i\omega_\ell} &= \frac{\epsilon_0}{2} \sum_{\omega_p} \sum_{\omega_q} \chi_{ijk}^{(2)}(-\omega_\sigma; \omega_p, \omega_q) \int_{-\infty}^{+\infty} \frac{d\omega''}{2\pi} \int_{-\infty}^{+\infty} \frac{d\omega'''}{2\pi} \tilde{\mathcal{E}}_{j\omega_p}(\mathbf{r}, \omega'') \tilde{\mathcal{E}}_{k\omega_q}(\mathbf{r}, \omega''') \\ &\quad \exp\left(-i(\omega'' + \omega''')t\right) \end{aligned} \quad \text{for } \omega_\ell = \omega_p + \omega_q \quad (\text{A.49})$$

We focus on second-harmonic generation (SHG), a nonlinear process where light fields of specific frequencies, ω_p and ω_q , interact to generate a second-order polarization at ω_ℓ that satisfies the condition $\omega_\ell = \pm\omega_p \pm \omega_q$. The summations in equations (A.48) account for all possible combinations of ω_p and ω_q that fulfill this relationship. However, in designing SHG experiments, researchers typically avoid this complexity. Most often, there is only one desired set of ω_p and ω_q that will produce the target ω_ℓ . This simplifies the experimental setup and avoids ambiguity in the interpretation of the results. Therefore, we typically focus on a single set of input frequencies. In this case (SHG), both ω_p and ω_q become equal to a common carrier frequency, ω_0 . This simplification allows us to directly

obtain the second harmonic frequency, $\omega_\ell = 2\omega_0$, using equation (A.49) as follows:

$$\begin{aligned}
\mathcal{P}_{i2\omega_0} &= \frac{\epsilon_0}{2} \chi_{ijk}^{(2)}(-\omega_\sigma; \omega_0, \omega_0) \int_{-\infty}^{+\infty} \frac{d\omega''}{2\pi} \int_{-\infty}^{+\infty} \frac{d\omega'''}{2\pi} \tilde{\mathcal{E}}_{j\omega_0}(\mathbf{r}, \omega'') \tilde{\mathcal{E}}_{k\omega_0}(\mathbf{r}, \omega''') \\
&\quad \exp\left(-i(\omega'' + \omega''')t\right) \\
&= \frac{\epsilon_0}{2} \chi_{ijk}^{(2)}(-\omega_\sigma; \omega_0, \omega_0) \int_{-\infty}^{+\infty} \frac{d\omega''}{2\pi} \tilde{\mathcal{E}}_{j\omega_0}(\mathbf{r}, \omega'') \exp\left(-i\omega''t\right) \\
&\quad \int_{-\infty}^{+\infty} \frac{d\omega'''}{2\pi} \tilde{\mathcal{E}}_{k\omega_0}(\mathbf{r}, \omega''') \exp\left(-i\omega'''t\right) \\
&= \frac{\epsilon_0}{2} \chi_{ijk}^{(2)}(-\omega_\sigma; \omega_0, \omega_0) \mathcal{E}_{j\omega_0}(\mathbf{r}, t) \mathcal{E}_{k\omega_0}(\mathbf{r}, t)
\end{aligned} \tag{A.50}$$

where $\omega_\sigma = 2\omega_0$.

After having developed expressions for the field and polarizations, they are then substituted into the wave equation:

$$\nabla \times \nabla \times \mathbf{E}(\mathbf{r}, t) = -\mu_0 \frac{\partial^2}{\partial t^2} \left(\epsilon_0 \mathbf{E}(\mathbf{r}, t) + \mathbf{P}^{(1)}(\mathbf{r}, t) + \mathbf{P}^{\text{NL}}(\mathbf{r}, t) \right) \tag{A.51}$$

To illustrate how this equation can be further developed, we will now break it down step-by-step. Plugging equation (A.39) and equation (A.42) into the two first terms on the right-hand side of (A.51) yields:

$$\begin{aligned}
\epsilon_0 \mu_0 \frac{\partial^2}{\partial t^2} \mathbf{E}(\mathbf{r}, t) + \mu_0 \frac{\partial^2}{\partial t^2} \mathbf{P}^{(1)}(\mathbf{r}, t) &= \frac{1}{2c^2} \frac{\partial^2}{\partial t^2} \left(\sum_{\omega_\ell} \int_{-\infty}^{+\infty} \frac{d\omega'}{2\pi} \left[\mathbf{I} + \underline{\underline{\chi}}^{(1)}(\omega_\ell + \omega') \right] \cdot \tilde{\mathcal{E}}_{\omega_\ell}(\mathbf{r}, \omega') \right. \\
&\quad \left. \exp\left(-i(\omega_\ell + \omega')t\right) \right) + \text{c.c.} \\
&= -\frac{1}{2c^2} \left(\sum_{\omega_\ell} \int_{-\infty}^{+\infty} \frac{d\omega'}{2\pi} (\omega_\ell + \omega')^2 \left[\mathbf{I} + \underline{\underline{\chi}}^{(1)}(\omega_\ell + \omega') \right] \right. \\
&\quad \left. \cdot \tilde{\mathcal{E}}_{\omega_\ell}(\mathbf{r}, \omega') \exp\left(-i(\omega_\ell + \omega')t\right) \right) + \text{c.c.}
\end{aligned} \tag{A.52}$$

To maintain consistency with the electric field description in equation (A.39), we can express the inverse Fourier transform of $\mathbf{P}^{\text{NL}}(\mathbf{r}, t)$ in (A.47) as follows:

$$\mathbf{P}^{\text{NL}}(\mathbf{r}, t) = \frac{1}{2\pi} \left(\sum_{\omega_\ell} \int_{-\infty}^{+\infty} d\omega' \frac{1}{2} \tilde{\mathcal{P}}_{\omega_\ell}^{\text{NL}}(\mathbf{r}, \omega') \exp\left(-i\omega' t\right) \right) \exp(-i\omega_\ell t) + \text{c.c.} \tag{A.53}$$

Drawing upon the expression for the nonlinear polarization derived from the inverse Fourier transform (equation (A.53)), we can now elaborate on the final term on the right-hand side of equation (A.51):

$$\begin{aligned}
\frac{\partial^2}{\partial t^2} \mathbf{P}^{\text{NL}}(\mathbf{r}, t) &= \frac{1}{2} \frac{\partial^2}{\partial t^2} \left(\sum_{\omega_\ell} \int_{-\infty}^{+\infty} \frac{d\omega'}{2\pi} \tilde{\mathcal{P}}_{\omega_\ell}^{\text{NL}}(\mathbf{r}, \omega') \exp(-i(\omega_\ell + \omega')t) \right) + \text{c.c.} \\
&= \frac{1}{2} \left(- \sum_{\omega_\ell} \int_{-\infty}^{+\infty} \frac{d\omega'}{2\pi} (\omega_\ell + \omega')^2 \tilde{\mathcal{P}}_{\omega_\ell}^{\text{NL}}(\mathbf{r}, \omega') \exp(-i(\omega_\ell + \omega')t) \right) + \text{c.c.} \\
&= \frac{1}{2} \left(- \sum_{\omega_\ell} \omega_\ell^2 \int_{-\infty}^{+\infty} \frac{d\omega'}{2\pi} \tilde{\mathcal{P}}_{\omega_\ell}^{\text{NL}}(\mathbf{r}, \omega') \exp(-i(\omega_\ell + \omega')t) \right. \\
&\quad - 2\omega_\ell \int_{-\infty}^{+\infty} \frac{d\omega'}{2\pi} \omega' \tilde{\mathcal{P}}_{\omega_\ell}^{\text{NL}}(\mathbf{r}, \omega') \exp(-i(\omega_\ell + \omega')t) \\
&\quad \left. - \int_{-\infty}^{+\infty} \frac{d\omega'}{2\pi} \omega'^2 \tilde{\mathcal{P}}_{\omega_\ell}^{\text{NL}}(\mathbf{r}, \omega') \exp(-i(\omega_\ell + \omega')t) \right) + \text{c.c.} \tag{A.54}
\end{aligned}$$

Under the assumption that deviations from the carrier frequency are small (i.e., $|\omega'| \ll |\omega_\ell|$), equation (A.54) simplifies. This is because the higher-order terms containing products of ω' become negligible compared to the terms with only ω_ℓ . Consequently, only the leading term is retained in (A.54):

$$\frac{\partial^2}{\partial t^2} \mathbf{P}^{\text{NL}}(\mathbf{r}, t) \approx \frac{1}{2} \left(- \sum_{\omega_\ell} \omega_\ell^2 \int_{-\infty}^{+\infty} \frac{d\omega'}{2\pi} \tilde{\mathcal{P}}_{\omega_\ell}^{\text{NL}}(\mathbf{r}, \omega') \exp(-i(\omega_\ell + \omega')t) \right) + \text{c.c.} \tag{A.55}$$

Regarding the left-hand side of equation (A.51), substituting equation (A.39) into it, we obtain the following:

$$\nabla \times \nabla \times \mathbf{E}(\mathbf{r}, t) = \nabla \times \nabla \times \left(\frac{1}{2\pi} \sum_{\omega_\ell} \int_{-\infty}^{+\infty} d\omega' \frac{1}{2} \tilde{\mathcal{E}}_{\omega_\ell}(\mathbf{r}, \omega') \exp(-i(\omega_\ell + \omega')t) + \text{c.c.} \right) \tag{A.56}$$

Combining equations (A.52), (A.55), and (A.56) into the wave equation (A.51), we obtain:

$$\begin{aligned}
&\nabla \times \nabla \times \left(\frac{1}{2\pi} \sum_{\omega_\ell} \int_{-\infty}^{+\infty} d\omega' \frac{1}{2} \tilde{\mathcal{E}}_{\omega_\ell}(\mathbf{r}, \omega') \exp(-i(\omega_\ell + \omega')t) + \text{c.c.} \right) \\
&= -\frac{1}{2c^2} \left(\sum_{\omega_\ell} \int_{-\infty}^{+\infty} \frac{d\omega'}{2\pi} (\omega_\ell + \omega')^2 [\mathbf{I} + \underline{\chi}^{(1)}(\omega_\ell + \omega')] \cdot \tilde{\mathcal{E}}_{\omega_\ell}(\mathbf{r}, \omega') \exp(-i(\omega_\ell + \omega')t) \right) + \text{c.c.} \tag{A.57} \\
&\quad - \frac{\mu_0}{2} \left(- \sum_{\omega_\ell} \omega_\ell^2 \int_{-\infty}^{+\infty} \frac{d\omega'}{2\pi} \tilde{\mathcal{P}}_{\omega_\ell}^{\text{NL}}(\mathbf{r}, \omega') \exp(-i(\omega_\ell + \omega')t) \right) + \text{c.c.}
\end{aligned}$$

To isolate and analyze the behavior of each frequency component within equation (A.57), we can utilize the concept of Fourier transforms. This involves multiplying the equation by $\exp(i\omega t)$ and integrating with respect to t :

$$\begin{aligned} & \nabla \times \nabla \times \left(\frac{1}{2\pi} \sum_{\omega_\ell} \int_{-\infty}^{+\infty} d\omega' \frac{1}{2} \tilde{\mathcal{E}}_{\omega_\ell}(\mathbf{r}, \omega') \int_{-\infty}^{+\infty} dt \exp(i(\omega - \omega_\ell - \omega')t) + \text{c.c.} \right) \\ &= -\frac{1}{2c^2} \left(\sum_{\omega_\ell} \int_{-\infty}^{+\infty} \frac{d\omega'}{2\pi} (\omega_\ell + \omega')^2 [\mathbf{I} + \underline{\underline{\chi}}^{(1)}(\omega_\ell + \omega')] \cdot \tilde{\mathcal{E}}_{\omega_\ell}(\mathbf{r}, \omega') \int_{-\infty}^{+\infty} dt \exp(i(\omega - \omega_\ell - \omega')t) \right) \\ & \quad - \frac{\mu_0}{2} \left(- \sum_{\omega_\ell} \omega_\ell^2 \int_{-\infty}^{+\infty} \frac{d\omega'}{2\pi} \tilde{\mathcal{P}}_{\omega_\ell}^{\text{NL}}(\mathbf{r}, \omega') \int_{-\infty}^{+\infty} dt \exp(i(\omega - \omega_\ell - \omega')t) \right) + \text{c.c.} \end{aligned}$$

$$\begin{aligned} & \nabla \times \nabla \times \left(\frac{1}{2\pi} \sum_{\omega_\ell} \int_{-\infty}^{+\infty} d\omega' \frac{1}{2} \tilde{\mathcal{E}}_{\omega_\ell}(\mathbf{r}, \omega') \delta(\omega - \omega_\ell - \omega') + \text{c.c.} \right) \\ &= -\frac{1}{2c^2} \left(\sum_{\omega_\ell} \int_{-\infty}^{+\infty} \frac{d\omega'}{2\pi} (\omega_\ell + \omega')^2 [\mathbf{I} + \underline{\underline{\chi}}^{(1)}(\omega_\ell + \omega')] \cdot \tilde{\mathcal{E}}_{\omega_\ell}(\mathbf{r}, \omega') \delta(\omega - \omega_\ell - \omega') \right) \\ & \quad - \frac{\mu_0}{2} \left(- \sum_{\omega_\ell} \omega_\ell^2 \int_{-\infty}^{+\infty} \frac{d\omega'}{2\pi} \tilde{\mathcal{P}}_{\omega_\ell}^{\text{NL}}(\mathbf{r}, \omega') \delta(\omega - \omega_\ell - \omega') \right) + \text{c.c.} \end{aligned}$$

$$\begin{aligned} & \nabla \times \nabla \times \left(\sum_{\omega_\ell} \frac{1}{2} \tilde{\mathcal{E}}_{\omega_\ell}(\mathbf{r}, \omega - \omega_\ell) + \text{c.c.} \right) = -\frac{1}{2c^2} \left(\sum_{\omega_\ell} \omega_\ell^2 [\mathbf{I} + \underline{\underline{\chi}}^{(1)}(\omega)] \cdot \tilde{\mathcal{E}}_{\omega_\ell}(\mathbf{r}, \omega - \omega_\ell) \right) \\ & \quad - \frac{\mu_0}{2} \left(- \sum_{\omega_\ell} \omega_\ell^2 \tilde{\mathcal{P}}_{\omega_\ell}^{\text{NL}}(\mathbf{r}, \omega - \omega_\ell) \right) + \text{c.c.} \end{aligned}$$

To simplify the equation, we can equate terms with the same label ω_ℓ on both sides. This leads to:

$$\nabla \times \nabla \times \tilde{\mathcal{E}}_{\omega_\ell}(\mathbf{r}, \omega - \omega_\ell) = -\frac{1}{c^2} \omega_\ell^2 [\mathbf{I} + \underline{\underline{\chi}}^{(1)}(\omega)] \tilde{\mathcal{E}}_{\omega_\ell}(\mathbf{r}, \omega - \omega_\ell) - \frac{\omega_\ell^2}{\epsilon_0 c^2} \tilde{\mathcal{P}}_{\omega_\ell}^{\text{NL}}(\mathbf{r}, \omega - \omega_\ell)$$

To represent the spatial dependence explicitly, we can re-write this equation in terms of vector components:

$$\nabla^2 \tilde{\mathcal{E}}_{i\omega_\ell}(\mathbf{r}, \omega - \omega_\ell) - \frac{\partial}{\partial x_i} \left(\frac{\partial \tilde{\mathcal{E}}_{j\omega_\ell}}{\partial x_j} \right) = -\frac{1}{c^2} \omega_\ell^2 [\delta_{ij} + \chi_{ij}^{(1)}(\omega)] \tilde{\mathcal{E}}_{j\omega_\ell}(\mathbf{r}, \omega - \omega_\ell) - \frac{\omega_\ell^2}{\epsilon_0 c^2} \tilde{\mathcal{P}}_{i\omega_\ell}^{\text{NL}}(\mathbf{r}, \omega - \omega_\ell) \quad (\text{A.58})$$

where a sum over repeated indices is implied.

To account for the spatial propagation of the field, we apply the methodology developed by Eimerl et al.⁶⁵ to handle the spatial operators. Within the principal coordinate system XYZ , this approach leads to the following simplified

form of equation (A.58) for each vector component:

$$\begin{aligned} \nabla^2 \tilde{\mathcal{E}}_{X\omega_\ell}(\mathbf{r}, \omega - \omega_\ell) + \frac{\omega^2}{c^2} \left[1 + \chi_{XX}^{(1)}(\omega) \right] \tilde{\mathcal{E}}_{X\omega_\ell}(\mathbf{r}, \omega - \omega_\ell) - \beta'_\omega \frac{\partial^2}{\partial X \partial Z} \tilde{\mathcal{E}}_{Z\omega_\ell}(\mathbf{r}, \omega - \omega_\ell) \\ = -\frac{\omega_\ell^2}{\epsilon_0 c^2} \tilde{\mathcal{P}}_{X\omega_\ell}^{\text{NL}}(\mathbf{r}, \omega - \omega_\ell) \end{aligned} \quad (\text{A.59a})$$

$$\begin{aligned} \nabla^2 \tilde{\mathcal{E}}_{Y\omega_\ell}(\mathbf{r}, \omega - \omega_\ell) + \frac{\omega^2}{c^2} \left[1 + \chi_{YY}^{(1)}(\omega) \right] \tilde{\mathcal{E}}_{Y\omega_\ell}(\mathbf{r}, \omega - \omega_\ell) - \beta'_\omega \frac{\partial^2}{\partial Y \partial Z} \tilde{\mathcal{E}}_{Z\omega_\ell}(\mathbf{r}, \omega - \omega_\ell) \\ = -\frac{\omega_\ell^2}{\epsilon_0 c^2} \tilde{\mathcal{P}}_{Y\omega_\ell}^{\text{NL}}(\mathbf{r}, \omega - \omega_\ell) \end{aligned} \quad (\text{A.59b})$$

$$\begin{aligned} \nabla^2 \tilde{\mathcal{E}}_{Z\omega_\ell}(\mathbf{r}, \omega - \omega_\ell) + \frac{\omega^2}{c^2} \left[1 + \chi_{ZZ}^{(1)}(\omega) \right] \tilde{\mathcal{E}}_{Z\omega_\ell}(\mathbf{r}, \omega - \omega_\ell) - \beta'_\omega \frac{\partial^2}{\partial Z^2} \tilde{\mathcal{E}}_{Z\omega_\ell}(\mathbf{r}, \omega - \omega_\ell) \\ = -\frac{\omega_\ell^2}{\epsilon_0 c^2} \tilde{\mathcal{P}}_{Z\omega_\ell}^{\text{NL}}(\mathbf{r}, \omega - \omega_\ell) \end{aligned} \quad (\text{A.59c})$$

where

$$\beta'_\omega = 1 - \frac{n_e^2(\omega)}{n_o^2(\omega)} \quad (\text{A.60})$$

This parameter β_ω differs from β_{ω_ℓ} (equation A.11) in its dependence on the angular frequency ω . While β_{ω_ℓ} represents discrete values specific to each frequency ω_ℓ , β_ω captures the continuous variation across the frequency range.

The parameter β_ω differs from β_{ω_ℓ} (refer to equation A.11) in its treatment of the angular frequency ω . β_{ω_ℓ} depends discretely on frequency ω_ℓ . In contrast, β_ω captures the continuous behavior of this parameter across the entire frequency range. Moreover, to describe this continuous dependence on ω in equations (A.59), it is standard practice to use the following relationships between the linear susceptibility $\chi^{(1)}$ and the ordinary wave number k_o and extraordinary k_e wave number (corresponding to the refractive indices, n_o and n_e):

$$1 + \chi_{XX}^{(1)}(\omega) = \frac{k_o^2(\omega) c^2}{\omega^2} = n_o^2(\omega) \quad (\text{A.61a})$$

$$1 + \chi_{YY}^{(1)}(\omega) = \frac{k_o^2(\omega) c^2}{\omega^2} = n_o^2(\omega) \quad (\text{A.61b})$$

$$1 + \chi_{ZZ}^{(1)}(\omega) = \frac{k_e^2(\omega) c^2}{\omega^2} = n_e^2(\omega) \quad (\text{A.61c})$$

In (A.61c), $k_e(\omega)$ refers specifically to the case where $\theta = \pi/2$, where θ represents the angle between the wave vector \mathbf{k} and the optic axis Z ; see equation (A.28).

Furthermore, to account for the variation of k_o and k_e with frequency, we can expand them in a Taylor series around a chosen carrier frequency ω_ℓ (which can be the fundamental ω_0 or the second harmonic $2\omega_0$):

$$k_{o,e}(\omega) = k_{o,e}(\omega_\ell) + \left. \frac{\partial k_{o,e}}{\partial \omega} \right|_{\omega=\omega_\ell} (\omega - \omega_\ell) + \frac{1}{2} \left. \frac{\partial^2 k_{o,e}}{\partial \omega^2} \right|_{\omega=\omega_\ell} (\omega - \omega_\ell)^2 + \dots \quad (\text{A.62})$$

The partial derivatives are related to the group velocity³ so that equation A.62 is written as:

$$k_{o,e}(\omega) = k_{o,e}(\omega_\ell) + \left. \frac{1}{v_g^{o,e}} \right|_{\omega=\omega_\ell} (\omega - \omega_\ell) - \frac{1}{2(v_g^{o,e})^2} \left. \frac{\partial v_g^{o,e}}{\partial \omega} \right|_{\omega=\omega_\ell} (\omega - \omega_\ell)^2 + \dots \quad (\text{A.63})$$

where $v_g^{o,e}$ stands for either the ordinary (o) or the extraordinary (e) group velocity.

Using equations (A.61), and (A.63), β'_{ω_ℓ} is re-defined:

$$\beta'_{\omega_\ell} = 1 - \frac{k_e^2(\omega_\ell) + 2k_e(\omega_\ell) \frac{1}{v_g^e(\omega_\ell)} (\omega - \omega_\ell) + \frac{1}{v_g^e(\omega_\ell)^2} \left(1 - k_e(\omega_\ell) \frac{\partial v_g^e}{\partial \omega} \Big|_{\omega=\omega_\ell} \right) (\omega - \omega_\ell)^2 + \dots}{k_o^2(\omega_\ell) + 2k_o(\omega_\ell) \frac{1}{v_g^o(\omega_\ell)} (\omega - \omega_\ell) + \frac{1}{v_g^o(\omega_\ell)^2} \left(1 - k_o(\omega_\ell) \frac{\partial v_g^o}{\partial \omega} \Big|_{\omega=\omega_\ell} \right) (\omega - \omega_\ell)^2 + \dots} \quad (\text{A.64})$$

Only terms up to the second order in the Taylor expansion are shown. Finally, (A.59) becomes:

$$\begin{aligned} & \nabla^2 \tilde{\mathcal{E}}_{X \omega_\ell}(\mathbf{r}, \omega - \omega_\ell) + \left[k_o^2(\omega_\ell) + 2k_o(\omega_\ell) \frac{1}{v_g^o(\omega_\ell)} (\omega - \omega_\ell) \right. \\ & \left. + \frac{1}{v_g^o(\omega_\ell)^2} \left(1 - k_o(\omega_\ell) \frac{\partial v_g^o}{\partial \omega} \Big|_{\omega=\omega_\ell} \right) (\omega - \omega_\ell)^2 + \dots \right] \tilde{\mathcal{E}}_{X \omega_\ell}(\mathbf{r}, \omega - \omega_\ell) \\ & - \beta'_{\omega_\ell} \frac{\partial^2}{\partial X \partial Z} \tilde{\mathcal{E}}_{Z \omega_\ell}(\mathbf{r}, \omega - \omega_\ell) = - \frac{\omega_\ell^2}{\epsilon_0 c^2} \tilde{\mathcal{P}}_{X \omega_\ell}^{\text{NL}}(\mathbf{r}, \omega - \omega_\ell) \end{aligned} \quad (\text{A.65a})$$

$$\begin{aligned} & \nabla^2 \tilde{\mathcal{E}}_{Y \omega_\ell}(\mathbf{r}, \omega - \omega_\ell) + \left[k_o^2(\omega_\ell) + 2k_o(\omega_\ell) \frac{1}{v_g^o(\omega_\ell)} (\omega - \omega_\ell) \right. \\ & \left. + \frac{1}{v_g^o(\omega_\ell)^2} \left(1 - k_o(\omega_\ell) \frac{\partial v_g^o}{\partial \omega} \Big|_{\omega=\omega_\ell} \right) (\omega - \omega_\ell)^2 + \dots \right] \tilde{\mathcal{E}}_{Y \omega_\ell}(\mathbf{r}, \omega - \omega_\ell) \\ & - \beta'_{\omega_\ell} \frac{\partial^2}{\partial Y \partial Z} \tilde{\mathcal{E}}_{Z \omega_\ell}(\mathbf{r}, \omega - \omega_\ell) = - \frac{\omega_\ell^2}{\epsilon_0 c^2} \tilde{\mathcal{P}}_{Y \omega_\ell}^{\text{NL}}(\mathbf{r}, \omega - \omega_\ell) \end{aligned} \quad (\text{A.65b})$$

$$\begin{aligned} & \nabla^2 \tilde{\mathcal{E}}_{Z \omega_\ell}(\mathbf{r}, \omega - \omega_\ell) + \left[k_e^2(\omega_\ell) + 2k_e(\omega_\ell) \frac{1}{v_g^e(\omega_\ell)} (\omega - \omega_\ell) \right. \\ & \left. + \frac{1}{v_g^e(\omega_\ell)^2} \left(1 - k_e(\omega_\ell) \frac{\partial v_g^e}{\partial \omega} \Big|_{\omega=\omega_\ell} \right) (\omega - \omega_\ell)^2 + \dots \right] \tilde{\mathcal{E}}_{Z \omega_\ell}(\mathbf{r}, \omega - \omega_\ell) \\ & - \beta'_{\omega_\ell} \frac{\partial^2}{\partial Z^2} \tilde{\mathcal{E}}_{Z \omega_\ell}(\mathbf{r}, \omega - \omega_\ell) = - \frac{\omega_\ell^2}{\epsilon_0 c^2} \tilde{\mathcal{P}}_{Z \omega_\ell}^{\text{NL}}(\mathbf{r}, \omega - \omega_\ell) \end{aligned} \quad (\text{A.65c})$$

A.3 More about Second-order Susceptibility tensor and Polarization

We will now reexamine the allowed entries for the second-order susceptibility tensor, $\underline{\underline{\chi}}^{(2)}$ (in index notation $\chi_{ijk}^{(2)}$, where $i, j, k = X, Y, Z$), applicable to crystals belonging to the $3m$ point group. Neumann's principle²⁹ establishes that the symmetry operations governing the structure of a crystal also dictate its material properties. This principle extends to the second-order susceptibility tensor, $\chi_{ijk}^{(2)}(-2\omega; \omega, \omega)$. As a consequence, for crystals like lithium

niobate (LiNbO_3) belonging to the $3m$ class, the non-zero elements of the $\chi_{ijk}^{(2)}$ are the following:

$$\begin{aligned}\chi_{YXX}^{(2)} &= \chi_{XYX}^{(2)} = \chi_{XXY}^{(2)} = -\chi_{YYY}^{(2)} \\ &\quad \chi_{ZZZ}^{(2)} \\ \chi_{ZXX}^{(2)} &= \chi_{ZYY}^{(2)} \\ \chi_{YYZ}^{(2)} &= \chi_{XXZ}^{(2)} = \chi_{YZY}^{(2)} = \chi_{XZX}^{(2)}\end{aligned}$$

These non-zero elements are defined within the principal coordinate system, denoted as XYZ . Notably, under the assumption of Kleinman symmetry: only three of these elements are truly independent, unlike the four independent elements encountered in the absence of Kleinman symmetry:

$$\begin{aligned}\chi_{YXX}^{(2)} &= \chi_{XYX}^{(2)} = \chi_{XXY}^{(2)} = -\chi_{YYY}^{(2)} \\ &\quad \chi_{ZZZ}^{(2)} \\ \chi_{ZXX}^{(2)} &= \chi_{ZYY}^{(2)} = \chi_{YYZ}^{(2)} = \chi_{XXZ}^{(2)} = \chi_{YZY}^{(2)} = \chi_{XZX}^{(2)}\end{aligned}$$

With the non-zero elements of the second-order susceptibility tensor established, we can now delve deeper into the development of expression (A.50), which describes the second harmonic polarization:

$$\mathcal{P}_{i2\omega_0}^{\text{NL}}(\mathbf{r}, t) = \frac{\epsilon_0}{2} \chi_{ijk}^{(2)}(-\omega_\sigma; \omega_0, \omega_0) \mathcal{E}_{j\omega_0}(\mathbf{r}, t) \mathcal{E}_{k\omega_0}(\mathbf{r}, t)$$

We will first analyze the case where $i = X$, then present the general solution:

$$\begin{aligned}\frac{\epsilon_0}{2} \chi_{Xjk}^{(2)} \mathcal{E}_{j\omega_0}(\mathbf{r}, t) \mathcal{E}_{k\omega_0}(\mathbf{r}, t) &= \epsilon_0 \chi_{XXY}^{(2)} \mathcal{E}_{X\omega_0}(\mathbf{r}, t) \mathcal{E}_{Y\omega_0}(\mathbf{r}, t) + \epsilon_0 \chi_{XXZ}^{(2)} \mathcal{E}_{X\omega_0}(\mathbf{r}, t) \mathcal{E}_{Y\omega_0}(\mathbf{r}, t) \\ &= \epsilon_0 2d_{15} \mathcal{E}_{X\omega_0}(\mathbf{r}, t) \mathcal{E}_{Y\omega_0}(\mathbf{r}, t) - \epsilon_0 2d_{22} \mathcal{E}_{X\omega_0}(\mathbf{r}, t) \mathcal{E}_{Y\omega_0}(\mathbf{r}, t)\end{aligned}\quad (\text{A.68})$$

Purposely, the second-order susceptibility tensor $\frac{1}{2}\chi_{ijk}^{(2)}(-\omega_\sigma; \omega_0, \omega_0)$ is also denoted as $d_{mk}(-\omega_\sigma; \omega_0, \omega_0)$ as defined in Table 2.1. Finally, carrying out such a similar procedure for Y , and Z , we can obtain the following expression for $\tilde{\mathcal{P}}_{2\omega_0}^{\text{NL}}(\mathbf{r}, t)$:

$$\mathcal{P}_{2\omega_0}^{\text{NL}}(\mathbf{r}, t) = \epsilon_0 \begin{pmatrix} 0 & 0 & 0 & 0 & d_{15} & -d_{22} \\ -d_{22} & d_{22} & 0 & d_{15} & 0 & 0 \\ d_{15} & d_{15} & d_{33} & 0 & 0 & 0 \end{pmatrix} \begin{pmatrix} \mathcal{E}_{X\omega_0}^2(\mathbf{r}, t) \\ \mathcal{E}_{Y\omega_0}^2(\mathbf{r}, t) \\ \mathcal{E}_{Z\omega_0}^2(\mathbf{r}, t) \\ 2\mathcal{E}_{Y\omega_0}(\mathbf{r}, t) \mathcal{E}_{Z\omega_0}(\mathbf{r}, t) \\ 2\mathcal{E}_{X\omega_0}(\mathbf{r}, t) \mathcal{E}_{Z\omega_0}(\mathbf{r}, t) \\ 2\mathcal{E}_{X\omega_0}(\mathbf{r}, t) \mathcal{E}_{Y\omega_0}(\mathbf{r}, t) \end{pmatrix}\quad (\text{A.69})$$

In this expression, the d -matrix elements are evaluated at the twice the carrier frequency, $(2\omega_0)$.

Building upon Chapter 3, the d -matrix alone does not capture the nonlinear optical response within the X -cut LiNbO_3 . Consequently, we must perform specific transformations to obtain the appropriate second-order susceptibility tensor. Since the quantity of interest is a tensor, these transformations must adhere to the rules governing

tensor transformations²⁵:

$$\chi_{ijk}^{(2)\text{new}} = \sum_l \sum_m \sum_n R_{il} R_{jm} R_{kn} \chi_{lmn}^{(2)\text{old}} \quad (\text{A.70})$$

In this context, $\underline{\underline{\mathbf{R}}}$ denotes a rotation matrix, and $\chi_{lmn}^{(2)\text{old}}$ represents the initial components of the second-order susceptibility tensor. These initial components, $\chi_{lmn}^{(2)\text{old}}$, are provided in Table 2.1 for the crystal class $3m$. The rotation matrix is given by the following expression:

$$\underline{\underline{\mathbf{R}}} = \underline{\underline{\mathbf{R}}}_X \underline{\underline{\mathbf{R}}}_Y \quad (\text{A.71})$$

A general rotation can be constructed by sequentially applying elemental rotations about the axes of the coordinate system. In this specific case, we perform a first rotation about the Y -axis, followed by a rotation about the X -axis. $\underline{\underline{\mathbf{R}}}_Y$ and $\underline{\underline{\mathbf{R}}}_X$ are given by¹⁰⁶:

$$\underline{\underline{\mathbf{R}}}_Y(\theta = -\frac{1}{2}\pi) = \begin{pmatrix} \cos(\theta) & 0 & \sin(\theta) \\ 0 & 1 & 0 \\ -\sin(\theta) & 0 & \cos(\theta) \end{pmatrix} = \begin{pmatrix} 0 & 0 & -1 \\ 0 & 1 & 0 \\ 1 & 0 & 0 \end{pmatrix} \quad (\text{A.72a})$$

$$\underline{\underline{\mathbf{R}}}_X(\theta = -\frac{7}{6}\pi) = \begin{pmatrix} 1 & 0 & 0 \\ 0 & \cos(\theta) & -\sin(\theta) \\ 0 & \sin(\theta) & \cos(\theta) \end{pmatrix} = \begin{pmatrix} 1 & 0 & 0 \\ 0 & -\frac{\sqrt{3}}{2} & -\frac{1}{2} \\ 0 & \frac{1}{2} & -\frac{\sqrt{3}}{2} \end{pmatrix} \quad (\text{A.72b})$$

By expanding equation (A.70) and taking into account that the second-order susceptibility tensor components are zero in the majority of the cases, we obtain a simplified version of equation (A.70) given as follows:

$$\begin{aligned} \chi_{ijk}^{(2)\text{new}} &= (R_{i1}R_{j1}R_{k2} + R_{i1}R_{j2}R_{k1} + R_{i2}R_{j1}R_{k1} - R_{i2}R_{j2}R_{k2}) \chi_{112}^{(2)\text{old}} \\ &+ (R_{i3}R_{j1}R_{k1} + R_{i3}R_{j2}R_{k2}) \chi_{311}^{(2)\text{old}} \\ &+ (R_{i1}R_{j1}R_{k3} + R_{i1}R_{j3}R_{k1} + R_{i2}R_{j2}R_{k3} + R_{i2}R_{j3}R_{k2}) \chi_{113}^{(2)\text{old}} \\ &+ R_{i3}R_{j3}R_{k3} \chi_{333}^{(2)\text{old}} \end{aligned} \quad (\text{A.73})$$

Finally, we use equation (A.71) to compute equation (A.73). Equation (A.73) can be easily implemented in any programming language in order to calculate the new components.

Overall, the expressions developed in detail in this Appendix are outlined in the main text of this work.

A.4 Visible Regime: Intermediate Calculations for Wave Propagation and Intensity

This section elaborates on the calculations presented in equation (3.45) from Chapter 3, Section 3.3. Specifically, it provides insights into the derivations of equations (3.49). To begin with, the slowly varying envelopes are

parameterized as follows:

$$\tilde{\mathcal{E}}_{Y\omega_0}^o(\mathbf{r}, \omega - \omega_0) = \Theta(R^{(b)} - R_{YZ}) \tilde{F}_{Y\omega_0}^o(X, \omega - \omega_0) \exp(i k_o(\omega_0) X) \quad (\text{A.74a})$$

$$\tilde{\mathcal{E}}_{Z2\omega_0}^e(\mathbf{r}, \omega - 2\omega_0) = \Theta(R^{(b)} - R_{YZ}) \tilde{F}_{Z2\omega_0}^e(X, \omega - 2\omega_0) \exp(i k_e(2\omega_0) X) \quad (\text{A.74b})$$

For the parameterization, the laser beam is modeled as a finite-diameter rigid cylinder propagating in the X -direction (see Fig. 3.6). A Heaviside function, $\Theta(R^{(b)} - R_{YZ})$, is used to define the beam profile. This function equals 1 within the beam radius ($R^{(b)}$) and zero outside, representing the presence and absence of the field, respectively:

$$\Theta(R^{(b)} - R_{YZ}) = \begin{cases} 1 & , \text{ for } R^{(b)} \geq R_{YZ} \text{ where } R_{YZ} = \sqrt{Y^2 + Z^2} \\ 0 & , \text{ otherwise} \end{cases} \quad (\text{A.75})$$

This simplified model adopts a different approach to spatial coordinate dependence compared to the previously established method in Ref. 30. For example, in the prior approach, $F_{Z2\omega_0}^e(\mathbf{r}, \omega - 2\omega_0)$ as a function of three spatial coordinates. In contrast, this model treats $F_{Z2\omega_0}^e(X, \omega - \omega_\ell)$ as a function of the longitudinal coordinate (X) only. However, the transverse coordinates (Y and Z) are still incorporated through the inclusion of a Heaviside function. With this description of the envelopes, we will now derive the coupled amplitude equations for our simplified model. For the ordinary wave, we will use equation (3.46). With respect to the extraordinary wave, equation (3.45) is employed. For reference, equation (3.45) is provided below:

$$\begin{aligned} \hat{Z} \cdot \left[\nabla^2 \tilde{\mathcal{E}}_{\omega_\ell}(\mathbf{r}, \omega - \omega_\ell) + \underline{\mathbf{K}} \cdot \tilde{\mathcal{E}}_{\omega_\ell}(\mathbf{r}, \omega - \omega_\ell) - \beta'_{\omega_\ell} \nabla \left(\hat{Z} \cdot \nabla \right) \left(\tilde{\mathcal{E}}_{\omega_\ell}(\mathbf{r}, \omega - \omega_\ell) \cdot \hat{Z} \right) \right] \\ = \hat{Z} \cdot \left[-\frac{\omega_\ell^2}{c^2} \tilde{\mathcal{P}}_{\omega_\ell}^{\text{NL}}(\mathbf{r}, \omega - \omega_\ell) \right] \end{aligned} \quad (\text{A.76})$$

For $\omega_\ell = 2\omega_0$, this equation becomes:

$$\nabla_{Z2\omega_0}^2 \tilde{\mathcal{E}}^e(\mathbf{r}, \omega - 2\omega_0) + K_Z \tilde{\mathcal{E}}^e(\mathbf{r}, \omega - 2\omega_0) - \beta'_{2\omega_0} \frac{\partial^2}{\partial Z^2} \tilde{\mathcal{E}}^e(\mathbf{r}, \omega - 2\omega_0) = -\frac{4\omega_0^2}{\epsilon_0 c^2} \tilde{\mathcal{P}}_{Z2\omega_0}^{\text{NL}}(\mathbf{r}, \omega - 2\omega_0) \quad (\text{A.77})$$

where K_Z is given by:

$$K_Z = k_e^2(2\omega_0) + 2k_e(2\omega_0) \frac{1}{v_g^e(2\omega_0)} (\omega - 2\omega_0) - \frac{1}{v_g^e(2\omega_0)^2} \left(1 - k_e(2\omega_0) \frac{\partial v_g^e}{\partial \omega} \Big|_{\omega=2\omega_0} \right) (\omega - 2\omega_0)^2 + \dots$$

The first term on the left-hand side of equation (A.77) is developed as follows:

$$\begin{aligned}
& \nabla^2 \left[\Theta(R^{(b)} - R_{YZ}) \frac{\tilde{F}^e(X, \omega - 2\omega_0)}{Z2\omega_0} \exp(i k_e(2\omega_0) X) \right] \\
&= \nabla^2 \left[\Theta(R^{(b)} - R_{YZ}) \frac{\tilde{F}^e(X, \omega - 2\omega_0)}{Z2\omega_0} \exp\left(i n_e(2\omega_0) \frac{2\omega_0}{c} X\right) \right] \\
&= \Theta(R^{(b)} - R_{YZ}) \exp\left(i n_e(2\omega_0) \frac{2\omega_0}{c} X\right) \left[\frac{\partial^2}{\partial X^2} \frac{\tilde{F}^e(X, \omega - 2\omega_0)}{Z2\omega_0} + \right. \\
& \quad \left. i 2 \frac{2\omega_0}{c} n_e(2\omega_0) \frac{\partial}{\partial X} \frac{\tilde{F}^e(X, \omega - 2\omega_0)}{Z2\omega_0} - \frac{4\omega_0^2}{c^2} n_e^2(2\omega_0) \frac{\tilde{F}^e(X, \omega - 2\omega_0)}{Z2\omega_0} \right] \\
& \quad \quad \quad (A.78) \\
&\approx \Theta(R^{(b)} - R_{YZ}) \exp\left(i n_e(2\omega_0) \frac{2\omega_0}{c} X\right) \left[i 2 \frac{2\omega_0}{c} n_e(2\omega_0) \frac{\partial}{\partial X} \frac{\tilde{F}^e(X, \omega - 2\omega_0)}{Z2\omega_0} \right. \\
& \quad \left. - \frac{4\omega_0^2}{c^2} n_e^2(2\omega_0) \frac{\tilde{F}^e(X, \omega - 2\omega_0)}{Z2\omega_0} \right] \\
&\approx \Theta(R^{(b)} - R_{YZ}) \exp(i k_e(2\omega_0) X) \left[i 2 k_e(2\omega_0) \frac{\partial}{\partial X} \frac{\tilde{F}^e(X, \omega - 2\omega_0)}{Z2\omega_0} \right. \\
& \quad \left. - k_e^2(2\omega_0) \frac{\tilde{F}^e(X, \omega - 2\omega_0)}{Z2\omega_0} \right]
\end{aligned}$$

Under the assumption of a rigid cylindrical-shaped beam, the action of ∇_Y^2 and ∇_Z^2 on Θ is neglected. Furthermore, in expression (A.78), the slowly varying envelope (SVE) approximation is used.

Regarding the second term on the left-hand side of equation (A.77), we neglect higher-order dispersion terms:

$$\begin{aligned}
& \left[k_e^2(2\omega_0) + 2k_e(2\omega_0) \frac{1}{v_g^e(2\omega_0)} (\omega - 2\omega_0) \right. \\
& \quad \left. + \frac{1}{(v_g^e(2\omega_0))^2} \left(1 - k_e(2\omega_0) \frac{\partial v_g^e}{\partial \omega} \Big|_{\omega=2\omega_0} \right) (\omega - 2\omega_0)^2 + \dots \right] \frac{\tilde{\mathcal{E}}^e(\mathbf{r}, \omega - 2\omega_0)}{Z2\omega_0} \approx k_e^2(2\omega_0) \frac{\tilde{\mathcal{E}}^e(\mathbf{r}, \omega - 2\omega_0)}{Z2\omega_0} \\
& \quad \quad \quad (A.79)
\end{aligned}$$

In this approximation, higher-related dispersion terms are disregarded, such as ordinary /extraordinary group velocity. The last term in the left-hand side of equation A.77 yields zero because Θ is constant with respect to derivatives and \tilde{F} does not depend on Z .

One can derive the corresponding propagation equation for the Y -component of the ordinary wave through analogous

steps. Finally, we obtain the following equations:

$$\frac{\partial}{\partial X} \tilde{F}_{Y\omega_0}^o(X, \omega - \omega_0) = \Theta(R^{(b)} - R_{YZ}) \frac{i(\omega_0)^2}{2k_o(\omega_0)\epsilon_0 c^2} \tilde{\mathcal{P}}_{Y\omega_0}^{\text{NL}}(\mathbf{r}, \omega - \omega_0) \exp(-ik_o(\omega_0)X) \quad (\text{A.80a})$$

$$\frac{\partial}{\partial X} \tilde{F}_{Z2\omega_0}^e(X, \omega - 2\omega_0) = \Theta(R^{(b)} - R_{YZ}) \frac{i(2\omega_0)^2}{2k_e(2\omega_0)\epsilon_0 c^2} \tilde{\mathcal{P}}_{Z2\omega_0}^{\text{NL}}(\mathbf{r}, \omega - 2\omega_0) \exp(-ik_e(2\omega_0)X) \quad (\text{A.80b})$$

They are the coupled amplitude equations for the cylindrical-shaped beam model.

Hereunder, we present detailed, step-by-step calculations for the equations introduced in Chapter 3, Section 3.3 of the main text.

A.5 Study Case: calculations

Solution of equation (3.52a) and its representation in the time domain

$$\begin{aligned} \tilde{F}_{Y\omega_0}^o(X, \omega - \omega_0) &= \tilde{C}_{Y\omega_0}^o(\omega - \omega_0) \\ \int_{-\infty}^{+\infty} \frac{d\omega}{2\pi} \exp(-i(\omega - \omega_0)t) \tilde{F}_{Y\omega_0}^o(X, \omega - \omega_0) &= \int_{-\infty}^{+\infty} \frac{d\omega}{2\pi} \exp(-i(\omega - \omega_0)t) \tilde{C}_{Y\omega_0}^o(\omega - \omega_0) \\ \tilde{F}_{Y\omega_0}^o(X, \omega - \omega_0) &= C_{Y\omega_0}^o(t) \end{aligned} \quad (\text{A.81})$$

Time-averaged fundamental intensity: equation (3.55)

We aim to evaluate the following equation:

$$\langle I_{\omega_0} \rangle = \left\| \frac{1}{T_{P\omega_0}} \int_{-\frac{1}{2}T_{P\omega_0}}^{+\frac{1}{2}T_{P\omega_0}} dt \frac{1}{2} \text{Re} \{ \boldsymbol{\mathcal{E}}_{\omega_0}(\mathbf{r}, t) \times \boldsymbol{\mathcal{H}}_{\omega_0}^*(\mathbf{r}, t) \} \right\| \quad (\text{A.82})$$

We know that the fundamental slowly varying envelope is given by the following expression within the nonlinear medium:

$$\boldsymbol{\mathcal{E}}_{\omega_0}^o(\mathbf{r}, t) = \Theta(R^{(b)} - R_{YZ}) \exp(ik_o(\omega_0)X) \begin{pmatrix} 0 \\ F_{Y\omega_0}^o(t) \\ 0 \end{pmatrix} \quad (\text{A.83})$$

This expression is obtained by plugging the solution of equation (3.52a) into (3.47a). We can use expression (C.10) to obtain an expression for $\boldsymbol{\mathcal{H}}_{\omega_0}$:

$$\boldsymbol{\mathcal{H}}_{\omega_0}^o(\mathbf{r}, t) = \Theta(R^{(b)} - R_{YZ}) n_o(\omega_0) c\epsilon_0 \exp(ik_o(\omega_0)X) \begin{pmatrix} 0 \\ 0 \\ F_{Y\omega_0}^o(t) \end{pmatrix} \quad (\text{A.84})$$

With these expressions plugged into equation (A.82), we arrive at:

$$\begin{aligned}
\langle I_{\omega_0} \rangle &= \left\| \hat{X} \frac{1}{T_{P\omega_0}} \int_{-\frac{1}{2}T_{P\omega_0}}^{+\frac{1}{2}T_{P\omega_0}} dt \frac{1}{2} \operatorname{Re} \left\{ n_o(\omega_0) \epsilon_0 c |F_{Y\omega_0}^o(0, t)|^2 \right\} \right\| \\
&= \frac{1}{2} n_o(\omega_0) \epsilon_0 c \frac{1}{T_{P\omega_0}} \int_{-\frac{1}{2}T_{P\omega_0}}^{+\frac{1}{2}T_{P\omega_0}} dt |F_{Y\omega_0}^o(0, t)|^2 \\
&= \frac{1}{2} n_o(\omega_0) \epsilon_0 c \frac{1}{T_{P\omega_0}} \int_{-\frac{1}{2}T_{P\omega_0}}^{+\frac{1}{2}T_{P\omega_0}} dt |K f(t)|^2 \\
&= \frac{1}{2} n_o(\omega_0) \epsilon_0 c |K|^2 \frac{1}{T_{P\omega_0}} \int_{-\frac{1}{2}T_{P\omega_0}}^{+\frac{1}{2}T_{P\omega_0}} dt |f(t)|^2 \tag{A.85} \\
&= I_{\text{peak}} \frac{1}{T_{P\omega_0}} \int_{-\frac{1}{2}T_{P\omega_0}}^{+\frac{1}{2}T_{P\omega_0}} dt \exp(-t^2/\tau^2) \\
&= I_{\text{peak}} \frac{1}{T_{P\omega_0}} \sqrt{\pi} \tau \operatorname{erf}\left(\frac{T_P}{2\tau}\right) \\
&= I_{\text{peak}} \frac{1}{T_{P\omega_0}} \sqrt{\pi} \tau
\end{aligned}$$

Here, $C(t) = K f(t)$, where K is a constant with units of V/m (i.e., SI units for electric field), and $f(t)$ represents a temporal profile. This constant is introduced to align with equation (A.81), where $C(t)$ is equivalent to the amplitude function $F_{Z,\omega_0}^e(0, t)$, which is also measured in units of V/m. In this case, we assume that $f(t)$ follows a Gaussian function: $f(t) = \exp(-t^2/2\tau^2)$, which is generally a first good approximation²⁸. Moreover, $I_{\text{peak}} = \frac{1}{2} n_e(\omega_0) \epsilon_0 c |K|^2$ is the peak intensity. Additionally, $\operatorname{erf}\left(\frac{T_{P\omega_0}}{2\tau}\right)$ is the error function evaluated at $\frac{T_{P\omega_0}}{2\tau}$, and τ is the pulse length. Given that the pulse length is 0.112 ps, the error function tends to unity since $\frac{T_P}{2\tau}$ is a large number.

Calculations regarding Intensity

This integral appears in the main text (Chapter 3, Section 3.3):

$$\begin{aligned}
\tilde{\mathcal{P}}_{Z2\omega_0}^{\text{NL}}(X, \omega - 2\omega_0) &= \int_{-\infty}^{+\infty} dt \mathcal{P}_{Z2\omega_0}^{\text{NL}}(X, t) \exp(i(\omega - 2\omega_0)t) \\
&= \Theta(R^{(b)} - R_{YZ}) \epsilon_0 d_{22} \exp(i2k_o(\omega_0)X) \int_{-\infty}^{+\infty} dt F_{Y\omega_0}^o(0, t) F_{Y\omega_0}^o(0, t) \\
&= \Theta(R^{(b)} - R_{YZ}) \epsilon_0 d_{22} \exp(i2k_o(\omega_0)X) \\
&\quad \int_{-\infty}^{+\infty} dt \left(\int_{-\infty}^{+\infty} \frac{d\omega_1}{2\pi} \exp(-i(\omega_1 - \omega_0)t) \tilde{C}_{Y\omega_0}^o(\omega_1 - \omega_0) \right) \\
&\quad \left(\int_{-\infty}^{+\infty} \frac{d\omega_2}{2\pi} \exp(-i(\omega_2 - \omega_0)t) \tilde{C}_{Y\omega_0}^o(\omega_2 - \omega_0) \right) \exp(i(\omega - 2\omega_0)t) \\
&= \Theta(R^{(b)} - R_{YZ}) \epsilon_0 d_{33} \exp(i2k_o(\omega_0)X) \\
&\quad \int_{-\infty}^{+\infty} \frac{d\omega_1}{2\pi} \int_{-\infty}^{+\infty} \frac{d\omega_2}{2\pi} \tilde{C}_{Y\omega_0}^o(\omega_1 - \omega_0) \tilde{C}_{Y\omega_0}^o(\omega_2 - \omega_0) \int_{-\infty}^{+\infty} dt \exp(i(\omega - \omega_1 - \omega_2)t) \\
&= \Theta(R^{(b)} - R_{YZ}) \epsilon_0 d_{33} \exp(i2k_o(\omega_0)X) \\
&\quad \int_{-\infty}^{+\infty} \frac{d\omega_1}{2\pi} \int_{-\infty}^{+\infty} \frac{d\omega_2}{2\pi} \tilde{C}_{Y\omega_0}^o(\omega_1 - \omega_0) \tilde{C}_{Y\omega_0}^o(\omega_2 - \omega_0) \delta(\omega - \omega_1 - \omega_2) \\
&= \Theta(R^{(b)} - R_{YZ}) \epsilon_0 d_{22} \exp(i2k_o(\omega_0)X) \int_{-\infty}^{+\infty} \frac{d\omega_1}{(2\pi)^2} \tilde{C}_{Y\omega_0}^o(\omega_1 - \omega_0) \tilde{C}_{Y\omega_0}^o(\omega - \omega_1 - \omega_0)
\end{aligned} \tag{A.86}$$

Through the variable substitution $\xi = \omega_1 - \omega_0$, this equation can be re-expressed as follows:

$$\tilde{\mathcal{P}}_{Z2\omega_0}^{\text{NL}}(X, \omega - 2\omega_0) = \Theta(R^{(b)} - R_{YZ}) \epsilon_0 d_{22} \exp(i2k_o(\omega_0)X) \int_{-\infty}^{+\infty} \frac{d\xi}{(2\pi)^2} \tilde{C}_{Y\omega_0}^o(\xi) \tilde{C}_{Y\omega_0}^o(\omega - 2\omega_0 - \xi) \tag{A.87}$$

Furthermore, the following integral appears in the main text (Chapter 3, Section 3.3) in equation (3.62):

$$\begin{aligned}
& \int_{-\infty}^{+\infty} \frac{d\omega}{2\pi} G^o(\omega - 2\omega_0) \exp(-i(\omega - 2\omega_0)t) \\
&= \int_{-\infty}^{+\infty} \frac{d\omega}{2\pi} \left(\int_{-\infty}^{+\infty} \frac{d\xi}{(2\pi)^2} \tilde{C}_{Y\omega_0}^o(\xi) \tilde{C}_{Y\omega_0}^o(\omega - 2\omega_0 - \xi) \right) \exp(-i(\omega - 2\omega_0)t) \\
&= \int_{-\infty}^{+\infty} \frac{d\omega}{2\pi} \int_{-\infty}^{+\infty} \frac{d\xi}{(2\pi)^2} \left(\int_{-\infty}^{+\infty} dt_1 C_{Y\omega_0}^o(t_1) \exp(i\xi t_1) \right) \\
&\quad \left(\int_{-\infty}^{+\infty} dt_2 C_{Y\omega_0}^o(t_2) \exp(i(\omega - 2\omega_0 - \xi)t_2) \right) \exp(-i(\omega - 2\omega_0)t) \\
&= \frac{1}{2\pi} \int_{-\infty}^{+\infty} dt_1 \int_{-\infty}^{+\infty} dt_2 C_{Y\omega_0}^o(t_1) C_{Y\omega_0}^o(t_2) \left(\int_{-\infty}^{+\infty} \frac{d\omega}{2\pi} \exp(-i\omega(t - t_2)) \right) \\
&\quad \times \left(\int_{-\infty}^{+\infty} \frac{d\xi}{2\pi} \exp(-i\xi(t_2 - t_1)) \right) \exp(i2\omega_0 t) \exp(-i2\omega_0 t_2) \\
&= \frac{1}{2\pi} \int_{-\infty}^{+\infty} dt_1 \int_{-\infty}^{+\infty} dt_2 C_{Y\omega_0}^o(t_1) C_{Y\omega_0}^o(t_2) \delta(t - t_2) \delta(t_2 - t_1) \exp(i2\omega_0 t) \exp(-i2\omega_0 t_2) \\
&= \frac{1}{2\pi} (C_{Y\omega_0}^o(t))^2 \\
&= \frac{1}{2\pi} (F_{Y\omega_0}^o(0, t))^2
\end{aligned} \tag{A.88}$$

Time-averaged second-harmonic intensity: equation (3.63)

We aim to evaluate the following equation:

$$\langle I_{2\omega_0} \rangle = \left\| \frac{1}{T_{P\omega_0}} \int_{-\frac{1}{2}T_{+P\omega_0}}^{\frac{1}{2}T_{P\omega_0}} dt \frac{1}{2} \operatorname{Re} \{ \mathcal{E}_{2\omega_0}(\mathbf{r}, t) \times \mathcal{H}_{2\omega_0}^*(\mathbf{r}, t) \} \right\| \tag{A.89}$$

We know that the second-harmonic slowly varying envelope is given by the following expression within the nonlinear medium:

$$\mathcal{E}_{2\omega_0}^e(\mathbf{r}, t) = \Theta(R^{(b)} - R_{YZ}) \exp(i k_e(2\omega_0) X) \begin{pmatrix} 0 \\ 0 \\ F_{Z2\omega_0}^e(X, t) \end{pmatrix} \tag{A.90}$$

This expression is obtained by plugging the solution of equation (3.52b) into equation (3.47b). We can use expression (C.10) to obtain an expression for $\mathcal{H}_{2\omega_0}$:

$$\mathcal{H}_{2\omega_0}^e(\mathbf{r}, t) = \Theta(R^{(b)} - R_{YZ}) n_e(2\omega_0) c \epsilon_0 \exp(i k_e(2\omega_0) X) \begin{pmatrix} 0 \\ -F_{Z2\omega_0}^e(X, t) \\ 0 \end{pmatrix} \quad (\text{A.91})$$

Here, we use the following approximation: $|\frac{\partial}{\partial X} F_{Z2\omega_0}^e| \ll k_e(2\omega_0) |F_{Z2\omega_0}^e|$. With this approximation, we assume that over many wavelengths the envelope of the wave is nearly constant. With expressions (A.90) and (A.91) plugged into equation (A.82), we arrive at:

$$\begin{aligned} \langle I_{2\omega_0} \rangle &= \left\| \hat{X} \frac{1}{T_{P\omega_0}} \int_{-\frac{1}{2}T_{P\omega_0}}^{+\frac{1}{2}T_{P\omega_0}} dt \frac{1}{2} \operatorname{Re} \left\{ n_e(2\omega_0) \epsilon_0 c |F_{Z2\omega_0}^e(X, t)|^2 \right\} \right\| \\ &= \frac{1}{2} n_e(2\omega_0) \epsilon_0 c \frac{1}{T_{P\omega_0}} \int_{-\frac{1}{2}T_{P\omega_0}}^{+\frac{1}{2}T_{P\omega_0}} dt |F_{Z2\omega_0}^e(X, t)|^2 \end{aligned} \quad (\text{A.92})$$

Using expression (3.61), equation (A.92) becomes:

$$\langle I_{2\omega_0} \rangle = \frac{\omega_0^2 L^2 |d_{22}|^2}{\sqrt{8\pi^5} n_e(2\omega_0) n_o^2(\omega_0) \epsilon_0 c^3} \frac{T_{P\omega_0}}{\tau} \langle I_{\omega_0} \rangle^2 \operatorname{sinc}^2 \left(\frac{\Delta k}{2} L \right) \quad (\text{A.93})$$

This is the light intensity of the extraordinary wave after a propagation distance $X = L$. Regarding the integral, we provide the details on the calculation below:

$$\begin{aligned} \frac{1}{T_{P\omega_0}} \int_{-\frac{1}{2}T_{P\omega_0}}^{+\frac{1}{2}T_{P\omega_0}} dt |F_{Z2\omega_0}^e(X, t)|^2 &= \frac{(2\omega_0)^4 X^2}{4k_e^2(2\omega_0) c^4} |d_{22}|^2 \operatorname{sinc}^2 \left(\frac{\Delta k}{2} X \right) \frac{1}{4\pi^2} \frac{1}{T_{P\omega_0}} \int_{-\frac{1}{2}T_{P\omega_0}}^{+\frac{1}{2}T_{P\omega_0}} dt |F_{Y\omega_0}^o(t)|^4 \\ &= \frac{\omega_0^2 X^2}{n_e^2(2\omega_0) c^2} |d_{22}|^2 \operatorname{sinc}^2 \left(\frac{\Delta k}{2} X \right) \frac{1}{4\pi^2} |K|^4 \frac{1}{T_{P\omega_0}} \int_{-\frac{1}{2}T_{P\omega_0}}^{+\frac{1}{2}T_{P\omega_0}} dt |f(t)|^4 \\ &= \frac{\omega_0^2 X^2}{n_e^2(2\omega_0) c^2} |d_{22}|^2 \operatorname{sinc}^2 \left(\frac{\Delta k}{2} X \right) \frac{1}{4\pi^2} \frac{4I_{\text{peak}}^2}{n_o^2(\omega_0) c^2 \epsilon_0^2} \frac{1}{T_{P\omega_0}} \\ &\quad \int_{-\frac{1}{2}T_{P\omega_0}}^{+\frac{1}{2}T_{P\omega_0}} dt \exp(2t^2/\tau^2) \\ &= \frac{\omega_0^2 X^2}{n_o^2(\omega_0) n_e^2(2\omega_0) c^4 \epsilon_0} |d_{22}|^2 \operatorname{sinc}^2 \left(\frac{\Delta k}{2} X \right) \frac{I_{\text{peak}}^2}{\pi^2} \frac{1}{T_{P\omega_0}} \sqrt{\frac{\pi}{2}} \tau \\ &= \frac{\omega_0^2 X^2}{n_o^2(\omega_0) n_e^2(2\omega_0) c^4 \epsilon_0} |d_{22}|^2 \operatorname{sinc}^2 \left(\frac{\Delta k}{2} X \right) \sqrt{\frac{1}{2\pi}} \frac{\tau}{T_{P\omega_0}} \\ &\quad \left(\frac{\langle \mathbb{P}_{\omega_0} \rangle}{\sqrt{\pi} A_{\text{beam}}} \left(\frac{T_{P\omega_0}}{\tau} \right) \right)^2 \\ &= \frac{\omega_0^2 X^2}{\pi^2 n_o^2(\omega_0) n_e^2(2\omega_0) c^4 \epsilon_0} |d_{22}|^2 \operatorname{sinc}^2 \left(\frac{\Delta k}{2} X \right) \sqrt{\frac{1}{2\pi}} \frac{T_{P\omega_0}}{\tau} \langle I_{\omega_0} \rangle^2 \end{aligned} \quad (\text{A.94})$$

Appendix B

Absorption & Wave Propagation

This appendix supplements Chapter 4 by providing additional details and explanations, such as those for omitted intermediate steps in formula derivations.

B.1 Absorption Criterion

In this section, we derive a criterion to estimate the impact of neglecting higher-order terms in the Taylor expansion of $g_{o,e}$ around the carrier frequency, ω_ℓ :

$$\frac{1}{4} \frac{\partial}{\partial \hbar \omega} \left[\log_e \left(\text{Im} \{ \chi_{jk}^{(1)} \} \right) \right] \Big|_{\hbar \omega = \hbar \omega_\ell} \ll 1$$

Here, jk corresponds to either XX or YY for ordinary (o) waves, and jk corresponds to ZZ for extraordinary (e) waves. To derive this expression, we start with the following equation:

$$g_{o,e}(\omega) = g_{o,e}(\omega_\ell) + \frac{\partial g_{o,e}}{\partial \omega} \Big|_{\omega=\omega_\ell} (\omega - \omega_\ell) + \frac{\partial^2 g_{o,e}}{\partial \omega^2} \Big|_{\omega=\omega_\ell} (\omega - \omega_\ell)^2 + \dots$$

where the derivatives are given by the following expressions:

$$\frac{\partial g_{o,e}}{\partial \omega} \Big|_{\omega=\omega_\ell} = g_{o,e}(\omega_\ell) \left(\frac{1}{\omega_\ell} + \frac{1}{2} \frac{\partial}{\partial \omega} \left[\log_e \left(\text{Im} \{ \chi_{jk}^{(1)}(\omega_\ell) \} \right) \right] \Big|_{\omega=\omega_\ell} \right) \quad (\text{B.1a})$$

$$\begin{aligned} \frac{\partial^2 g_{o,e}}{\partial \omega^2} \Big|_{\omega=\omega_\ell} = g_{o,e}(\omega_\ell) & \left(\frac{1}{\omega_\ell} \frac{\partial}{\partial \omega} \left[\log_e \left(\text{Im} \{ \chi_{jk}^{(1)}(\omega_\ell) \} \right) \right] \Big|_{\omega=\omega_\ell} - \frac{1}{4} g_{o,e}(\omega_\ell) \frac{\partial}{\partial \omega} \left[\text{Im} \{ \chi_{jk}^{(1)}(\omega_\ell) \} \right] \Big|_{\omega=\omega_\ell} \right. \\ & \left. + \frac{1}{2} \frac{1}{\text{Im} \{ \chi_{jk}^{(1)}(\omega_\ell) \}} \frac{\partial^2}{\partial \omega^2} \left[\text{Im} \{ \chi_{jk}^{(1)}(\omega_\ell) \} \right] \Big|_{\omega=\omega_\ell} \right) \quad (\text{B.1b}) \end{aligned}$$

In estimating the relative importance of the second term in the Taylor expansion compared to the first, we can exploit the narrow bandwidth assumption (i.e., $\Delta\omega \ll \omega_\ell$). This allows us to approximate the maximum absolute difference from the center frequency, $\max(|\omega - \omega_\ell|)$, by $\Delta\omega/2$ (i.e., $\max(|\omega - \omega_\ell|) \approx \Delta\omega/2$). So, we can compare the following terms:

$$|g_{o,e}(\omega)| = \frac{\omega_\ell}{c} \sqrt{\text{Im}\{\chi_{jk}^{(1)}\}} \quad (\text{B.2a})$$

$$\left| \frac{\partial g_{o,e}}{\partial \omega} \Big|_{\omega=\omega_\ell} \frac{\Delta\omega}{2} \right| = |g_{o,e}(\omega)| \left| \frac{1}{2} \frac{\Delta\omega}{\omega_\ell} + \frac{1}{2} \frac{\partial}{\partial \omega} \left[\log_e \left(\text{Im}\{\chi_{jk}^{(1)}(\omega_\ell)\} \right) \right] \Big|_{\omega=\omega_\ell} \frac{\Delta\omega}{2} \right| \quad (\text{B.2b})$$

Given the relation $\mathbb{E} = \hbar\omega$ between energy (\mathbb{E}) and angular frequency (ω), we can rewrite expressions (B.2) as follows:

$$|g_{o,e}(\omega)| = \frac{\mathbb{E}_l}{\hbar c} \sqrt{\text{Im}\{\chi_{jk}^{(1)}\}} = \frac{\hbar\omega_\ell}{\hbar c} \sqrt{\text{Im}\{\chi_{jk}^{(1)}\}} \quad (\text{B.3a})$$

$$\left| \frac{\partial g_{o,e}}{\partial \mathbb{E}} \Big|_{\hbar\omega=\mathbb{E}_l} \frac{\Delta\mathbb{E}}{2} \right| = \left| \frac{\partial g_{o,e}}{\partial \hbar\omega} \Big|_{\hbar\omega=\hbar\omega_\ell} \frac{\hbar\Delta\omega}{2} \right| \quad (\text{B.3b})$$

$$\begin{aligned} &= |g_{o,e}(\omega)| \left| \frac{1}{2} \frac{\Delta\mathbb{E}}{\mathbb{E}_l} + \frac{1}{2} \frac{\partial}{\partial \mathbb{E}} \left[\log_e \left(\text{Im}\{\chi_{jk}^{(1)}\} \right) \right] \Big|_{\mathbb{E}=\mathbb{E}_l} \frac{\Delta\mathbb{E}}{2} \right| \\ &= |g_{o,e}(\omega)| \left| \frac{1}{2} \frac{\hbar\Delta\omega}{\hbar\omega_\ell} + \frac{1}{2} \frac{\partial}{\partial \hbar\omega} \left[\log_e \left(\text{Im}\{\chi_{jk}^{(1)}\} \right) \right] \Big|_{\hbar\omega=\hbar\omega_\ell} \frac{\hbar\Delta\omega}{2} \right| \end{aligned} \quad (\text{B.3c})$$

where $\mathbb{E}_l = \hbar\omega_\ell$, $\Delta\mathbb{E} = \hbar\Delta\omega$. Since $\Delta\omega \ll \omega_\ell$, the first term in the expression (B.3c) is negligible. Therefore, we can focus on the next term in that expression:

$$|g_{o,e}(\omega)| \left| \frac{1}{2} \frac{\partial}{\partial \hbar\omega} \left[\log_e \left(\text{Im}\{\chi_{jk}^{(1)}\} \right) \right] \Big|_{\hbar\omega=\hbar\omega_\ell} \frac{\hbar\Delta\omega}{2} \right| \quad (\text{B.4})$$

The second term in the Taylor series expansion typically plays a lesser role because the change in frequency, $\Delta\omega$, is much smaller than the base frequency, ω_ℓ . However, the presence of $g_{o,e}$ within this term, which depends on ω_ℓ , can counteract this diminishing effect. Hence, from expression (B.4), this influence gets diminished if the following condition holds:

$$\left| \frac{1}{4} \frac{\partial}{\partial \hbar\omega} \left[\log_e \left(\text{Im}\{\chi_{jk}^{(1)}\} \right) \right] \Big|_{\hbar\omega=\hbar\omega_\ell} \right| \ll 1$$

B.2 Solutions of equations (4.22)

We aim to solve the following equations:

$$\frac{\partial}{\partial X} \tilde{F}_{Y\omega_0}^o(X, \omega - \omega_0) + \frac{1}{2} \alpha_o(\omega_0) \tilde{F}_{Y\omega_0}^o(X, \omega - \omega_0) - \frac{i(\omega - \omega_0)}{v_g^o} \tilde{F}_{Y\omega_0}^o(X, \omega - \omega_0) \approx 0 \quad (\text{B.5a})$$

$$\begin{aligned} \frac{\partial}{\partial X} \tilde{F}_{Z2\omega_0}^e(X, \omega - 2\omega_0) + \frac{1}{2} \alpha_e(2\omega_0) \tilde{F}_{Z2\omega_0}^e(X, \omega - 2\omega_0) - \frac{i(\omega - 2\omega_0)}{v_g^e} \tilde{F}_{Z2\omega_0}^e(X, \omega - 2\omega_0) \\ = \frac{i(2\omega_0)^2}{2k_e(\omega_0)\epsilon_0 c^2} \tilde{\mathcal{P}}^{\text{NL}}(\mathbf{r}, \omega - 2\omega_0) \exp(-i k_e(2\omega_0) X) \end{aligned} \quad (\text{B.5b})$$

Additionally, the boundary conditions are the following:

$$F_{Y\omega_0}^o(0, t) = K \exp\left(-\frac{t^2}{2\tau^2}\right) \quad (\text{B.6a})$$

$$F_{Z2\omega_0}^e(0, t) = 0 \quad (\text{B.6b})$$

The solution to equation (B.5a) is given by:

$$\tilde{F}_{Y\omega_0}^o(X, \omega - \omega_0) = \tilde{C}_{Y\omega_0}^o(\omega - \omega_0) \exp\left(-\frac{\alpha_o(\omega_0)}{2} X\right) \exp\left(\frac{i(\omega - \omega_0)}{v_g^o} X\right) \quad (\text{B.7})$$

where C is a constant with respect to spatial coordinate. We can use the following expression in order to incorporate the boundary condition (B.6a):

$$\begin{aligned} F_{Y\omega_0}^o(X, t) &= \frac{1}{2\pi} \int_{-\infty}^{+\infty} d\omega \tilde{F}_{Y\omega_0}^o(X, \omega - \omega_0) \exp(-i(\omega - \omega_0)t) \quad \text{when } X = 0 \\ F_{Y\omega_0}^o(0, t) &= \frac{1}{2\pi} \int_{-\infty}^{+\infty} d\omega \tilde{C}_{Y\omega_0}^o(\omega - \omega_0) \exp(-i(\omega - \omega_0)t) \\ &= C_{Y\omega_0}^o(t) \\ &= K \exp\left(-\frac{t^2}{2\tau^2}\right) \end{aligned} \quad (\text{B.8})$$

From equation (B.8), we can obtain an expression for $C_{Y\omega_0}^o(\omega - \omega_0)$ as follows:

$$\begin{aligned} \tilde{C}_{Y\omega_0}^o(\omega - \omega_0) &= \int_{-\infty}^{+\infty} dt C_{Y\omega_0}^o(t) \exp(i(\omega - \omega_0)t) \\ &= \int_{-\infty}^{+\infty} dt K \exp\left(-\frac{t^2}{2\tau^2}\right) \exp(i(\omega - \omega_0)t) \\ &= K \sqrt{2\pi} \exp\left(-\frac{\tau^2}{2} (\omega - \omega_0)^2\right) \end{aligned} \quad (\text{B.9})$$

With this result, we can calculate an expression for $F_{Y\omega_0}^o(X, t)$ as follows:

$$\begin{aligned}
F_{Y\omega_0}^o(X, t) &= \frac{1}{2\pi} \int_{-\infty}^{+\infty} d\omega \tilde{F}_{Y\omega_0}^o(X, \omega - \omega_0) \exp(-i(\omega - \omega_0)t) \\
&= \frac{1}{2\pi} \int_{-\infty}^{+\infty} d\omega \tilde{C}_{Y\omega_0}^o(\omega - \omega_0) \exp\left(-\frac{\alpha_o(\omega_0)}{2}X\right) \exp\left(\frac{i(\omega - \omega_0)}{v_g^o}X\right) \\
&\quad \exp(-i(\omega - \omega_0)t) \\
&= K \exp\left(-\frac{\alpha_o(\omega_0)}{2}X\right) \exp\left(-\frac{1}{2\tau^2}\left(t - \frac{1}{v_g^o}X\right)^2\right)
\end{aligned} \tag{B.10}$$

The integration turns out to be simple since the absorption coefficient is only evaluated at the carrier frequency of the fundamental.

We can obtain an expression for the time-averaged fundamental intensity through the following expression which is derived in Appendix C:

$$\langle I_{\omega_0} \rangle = \left\| \frac{1}{T_{P\omega_0}} \int_{-\frac{1}{2}T_{P\omega_0}}^{+\frac{1}{2}T_{P\omega_0}} dt \frac{1}{2} \operatorname{Re}\{\mathcal{E}_{\omega_0}(X, t) \times \mathcal{H}_{\omega_0}^*(X, t)\} \right\| \tag{B.11}$$

Here, $T_{P\omega_0}$ stands for the period-repetition time. In this case, $\mathcal{E}_{\omega_0}(X, t)$ is given by the following expression:

$$\mathcal{E}_{\omega_0}^o(X, t) = \exp(i k_o(\omega_0)X) \begin{pmatrix} 0 \\ F_{Y\omega_0}^o(X, t) \end{pmatrix} \tag{B.12}$$

where $F_{Y\omega_0}^o(X, t)$ is described by equation (B.10). The magnetic field can be written as follows*:

$$\mathcal{H}_{\omega_0}^o(X, t) = n_o(\omega_0) c \epsilon_0 \exp(i k_o(\omega_0)X) \begin{pmatrix} 0 \\ 0 \\ F_{Y\omega_0}^o(X, t) \end{pmatrix} \tag{B.13}$$

Plugging equations (B.12) and (B.13) into (B.11), we obtain the following expression:

$$\begin{aligned}
\langle I_{\omega_0} \rangle &= I_{\text{peak}} \exp(-\alpha_o(\omega_0)X) \frac{1}{T_{P\omega_0}} \int_{-\frac{1}{2}T_{P\omega_0}}^{+\frac{1}{2}T_{P\omega_0}} dt \exp\left(-\frac{1}{\tau^2}\left(t - \frac{1}{v_g^o}X\right)^2\right) \\
&= I_{\text{peak}} \exp(-\alpha_o(\omega_0)X) \frac{1}{T_{P\omega_0}} \frac{1}{2} \sqrt{\pi}\tau \left(\operatorname{erf}\left(\frac{\frac{T_{P\omega_0}}{2} + \frac{X}{v_g^o}}{\tau}\right) + \operatorname{erf}\left(\frac{\frac{T_{P\omega_0}}{2} - \frac{X}{v_g^o}}{\tau}\right) \right) \\
&= I_{\text{peak}} \exp(-\alpha_o(\omega_0)X) \frac{1}{T_{P\omega_0}} \sqrt{\pi}\tau
\end{aligned} \tag{B.14}$$

*The magnetic field is calculated using equation (C.10): $\nabla \times \mathcal{E}_{\omega_\ell} = i\mu_0\omega_\ell \mathcal{H}_{\omega_\ell}$. Additionally, we use the following approximation: $\left| \frac{\partial}{\partial X} F_{Y\omega_0}^o \right| \ll k_o(\omega_0) \left| F_{Y\omega_0}^o \right|$. With this approximation, we assume that over many wavelengths the envelope of the wave is nearly constant.

where I_{peak} is given by:

$$I_{\text{peak}} = \frac{1}{2} n_o(\omega_0) c \epsilon_0 |K|^2 \quad (\text{B.15})$$

Both error functions (denoted by erf) approach unity as their arguments become large numbers.

As we are interested in the fundamental intensity at the beginning of the nonlinear medium, we set $X = 0$, and equation (B.14) becomes:

$$\langle I_{\omega_0} \rangle = I_{\text{peak}} \frac{1}{T_{\text{P}\omega_0}} \sqrt{\pi\tau} \quad (\text{B.16})$$

We arrive at an expression (B.16) that is identical to the one derived in Chapter 3, equation (3.55). This suggests that we can approximation equation (B.10) as follows:

$$F_{Y\omega_0}^o(X, t) \approx K \exp\left(-\frac{\alpha_o(\omega_0)}{2} X\right) \exp\left(-\frac{t^2}{2\tau^2}\right) \quad (\text{B.17})$$

Or equivalently, we can write it as follows:

$$F_{Y\omega_0}^o(X, t) \approx \exp\left(-\frac{\alpha_o(\omega_0)}{2} X\right) C_{Y\omega_0}^o(t) \quad (\text{B.18})$$

Both the original function $\exp\left(-\frac{1}{2\tau^2}\left(t - \frac{1}{v_g^o} X\right)^2\right)$ and its approximation $\exp(-t^2/2\tau^2)$ are symmetrical around $t = 0$. This means the positive and negative deviations from the average value due to the position (i.e., X) term in the original function tend to cancel out when integrated over the entire pulse period. Essentially, the errors introduced by the approximation (ignoring position dependence) tend to cancel out when integrating over the entire symmetrical pulse period.

To solve equation (B.5b), we require the nonlinear polarization in the frequency domain. We can obtain this by performing a Fourier transform on equation (4.18c), leading to:

$$\tilde{\mathcal{P}}_{Z2\omega_0}^{\text{NL}}(X, \omega - 2\omega_0) = \epsilon_0 d_{22} G^o(\omega - 2\omega_0) \exp(-\alpha_o(\omega_0) X) \exp(i2k_o(2\omega_0) X) \quad (\text{B.19})$$

where $G^o(\omega - 2\omega_0)$ is given by:

$$G^o(\omega - 2\omega_0) = \int_{-\infty}^{+\infty} \frac{d\xi}{(2\pi)^2} \tilde{C}_{Y\omega_0}^o(\xi) \tilde{C}_{Y\omega_0}^o(\omega - 2\omega_0 - \xi)$$

In this context, we leverage the approximation (B.18) because the narrow-band nature of the scenario concentrates the time-averaged value in the central region of the pulse.

Equation (B.5b) is a non-homogeneous differential equation. This implies that the general solution can be expressed as the sum of two components: the homogeneous solution, which satisfies the equation when the nonlinear polarization term is zero (i.e., $\tilde{F}_{Z2\omega_0}^{\text{NL}} = 0$), and a particular solution that accounts for the driving force of the nonlinearities. The homogeneous solution of equation (4.22b) is given by:

$$\tilde{y}_h = \tilde{D}_{Z2\omega_0}^e(\omega - 2\omega_0) \exp\left(-\frac{\alpha_e(\omega_0)}{2} X\right) \exp\left(\frac{i(\omega - 2\omega_0)}{v_g^e} X\right) \quad (\text{B.20})$$

We will now aim to solve equation (B.5b):

$$\begin{aligned} \frac{\partial}{\partial X} \tilde{F}_{Z2\omega_0}^e(X, \omega - 2\omega_0) + \frac{1}{2} \alpha_e(2\omega_0) \tilde{F}_{Z2\omega_0}^e(X, \omega - 2\omega_0) - \frac{i(\omega - 2\omega_0)}{v_g^e} \tilde{F}_{Z2\omega_0}^e(X, \omega - 2\omega_0) = \\ \frac{i\omega_0}{n_e(2\omega_0) c} d_{22} \exp(-\alpha_o(\omega_0) X) G^o(\omega - 2\omega_0) \exp(-i \Delta k X) \end{aligned} \quad (\text{B.21})$$

where the phase-matching term Δk is given by:

$$\begin{aligned} \Delta k &= k_e(2\omega_0) - 2k_o(\omega_0) \\ &= \frac{2\omega_0}{c} (n_e(2\omega_0) - n_o(\omega_0)) \end{aligned} \quad (\text{B.22})$$

The terms $k_o(\omega_0)$ and $k_e(2\omega_0)$ are given by equation (4.4a) evaluated at the fundamental and second-harmonic frequency ($\omega = \omega_0, 2\omega_0$). There are several ways of solving this differential equation, we use the integrating factor method. The integrating factor, in this case, is given by $\mu = \exp\left(\left[\frac{\alpha_e(2\omega_0)}{2} - \frac{i(\omega - 2\omega_0)}{v_g^e}\right] X\right)$. By multiplying both sides of equation (B.21) by μ and integrating, this equation reduces to:

$$\begin{aligned} \tilde{F}_{Z2\omega_0}^e(X, \omega - 2\omega_0) = \frac{i\omega_0}{n_e(2\omega_0) c} d_{22} \exp\left(-\left[\frac{\alpha_e(2\omega_0)}{2} - \frac{i(\omega - 2\omega_0)}{v_g^e}\right] X\right) \\ \int_0^X dx' G^o(\omega - 2\omega_0) \exp\left(\left[\frac{\alpha_e(2\omega_0)}{2} - \alpha_o(\omega_0) - i\left(\Delta k + \frac{(\omega - 2\omega_0)}{v_g^e}\right)\right] x'\right) \end{aligned} \quad (\text{B.23})$$

We can make the following approximation:

$$\begin{aligned} \tilde{F}_{Z2\omega_0}^e(X, \omega - 2\omega_0) \approx \frac{i\omega_0}{n_e(2\omega_0) c} d_{22} \exp\left(-\left[\frac{\alpha_e(2\omega_0)}{2} - \frac{i(\omega - 2\omega_0)}{v_g^e}\right] X\right) \\ \int_0^X dx' G^o(\omega - 2\omega_0) \exp\left(\left[\frac{\alpha_e(2\omega_0)}{2} - \alpha_o(\omega_0) - i\Delta k\right] x'\right) \end{aligned} \quad (\text{B.24})$$

This is based on the fact that the wave is a narrow-band signal. We can focus on the terms $\Delta k + \frac{(\omega - 2\omega_0)}{v_g^e}$ to understand this approximation:

$$\begin{aligned} \Delta k + \frac{(\omega - 2\omega_0)}{v_g^e} &= (n_e(2\omega_0) - n_o(\omega_0)) \frac{2\omega_0}{c} + \frac{(\omega - 2\omega_0)}{v_g^e} \\ &\approx (n_e(2\omega_0) - n_o(\omega_0)) \frac{2\omega_0}{c} \end{aligned} \quad (\text{B.25})$$

In the narrow-band regime, we have the following scenario $|\omega - 2\omega_0| \ll 2\omega_0$. Additionally, the group velocity (v_g^e) generally falls on the same order of magnitude as the speed of light (c). These conditions lead to equation (B.25). As $G^o(\omega - 2\omega_0)$ is independent of spatial coordinates, equation (B.24) is now primed for integration:

$$\begin{aligned} \tilde{F}_{Z2\omega_0}^e(X, \omega - 2\omega_0) = \frac{i\omega_0 d_{22} G^o(\omega - 2\omega_0)}{n_e(2\omega_0) c \left(\frac{\alpha_e(2\omega_0)}{2} - \alpha_o(\omega_0) - i\Delta k\right)} \\ \left(\exp\left([- \alpha_o(\omega_0) - i\Delta k] X\right) - \exp\left(-\frac{1}{2} \alpha_e(2\omega_0) X\right)\right) \exp\left(\frac{i(\omega - 2\omega_0)}{v_g^e} X\right) \end{aligned} \quad (\text{B.26})$$

After simple but extended algebraic manipulations, equation (B.26) reduces to:

$$\begin{aligned} \tilde{F}_{Z2\omega_0}^e(X, \omega - 2\omega_0) &= \frac{i\omega_0 d_{22} G^o(\omega - 2\omega_0) \exp(i\theta)}{n_e(2\omega_0) c \sqrt{\frac{\alpha_e(2\omega_0)}{2} - \alpha_o(\omega_0) - i\Delta k}} \\ &\left[\exp\left([- \alpha_o(\omega_0) - i\Delta k] X\right) - \exp\left(-\frac{1}{2}\alpha_e(2\omega_0) X\right) \right] \exp\left(\frac{i(\omega - 2\omega_0)}{v_g^e} X\right) \end{aligned} \quad (\text{B.27})$$

where θ is given by:

$$\theta = \pi + \arctan \left[\left(\frac{\alpha_e(2\omega_0)}{2} - \alpha_o(\omega_0) \right) (\Delta k)^{-1} \right] \quad (\text{B.28})$$

Equation (B.27) is the particular solution for equation (B.21). The general solution is the combination of equations (B.20) and (B.27):

$$\begin{aligned} \tilde{F}_{Z2\omega_0}^e(X, \omega - 2\omega_0) &= \tilde{D}_{Z2\omega_0}^e(\omega - 2\omega_0) \exp\left(-\frac{\alpha_e(\omega_0)}{2} X\right) \exp\left(\frac{i(\omega - 2\omega_0)}{v_g^e} X\right) \\ &+ \frac{i\omega_0 d_{22} G^o(\omega - 2\omega_0) \exp(i\theta)}{n_e(2\omega_0) c \sqrt{\frac{\alpha_e(2\omega_0)}{2} - \alpha_o(\omega_0) - i\Delta k}} \\ &\left[\exp\left([- \alpha_o(\omega_0) - i\Delta k] X\right) - \exp\left(-\frac{1}{2}\alpha_e(2\omega_0) X\right) \right] \exp\left(\frac{i(\omega - 2\omega_0)}{v_g^e} X\right) \end{aligned} \quad (\text{B.29})$$

Under the initial condition (B.6b), this equation reduces to[†]:

$$\begin{aligned} \tilde{F}_{Z2\omega_0}^e(X, \omega - 2\omega_0) &= \frac{i\omega_0 d_{22} G^o(\omega - 2\omega_0) \exp(i\theta)}{n_e(2\omega_0) c \sqrt{\frac{\alpha_e(2\omega_0)}{2} - \alpha_o(\omega_0) - i\Delta k}} \\ &\left[\exp\left([- \alpha_o(\omega_0) - i\Delta k] X\right) - \exp\left(-\frac{1}{2}\alpha_e(2\omega_0) X\right) \right] \exp\left(\frac{i(\omega - 2\omega_0)}{v_g^e} X\right) \end{aligned} \quad (\text{B.30})$$

$\tilde{D}_{Z2\omega_0}^e(\omega - 2\omega_0)$ turns out to be equal to zero. We can express equation (B.30) in the time-domain, as follows:

$$\begin{aligned} F_{Z2\omega_0}^e(X, t) &= \int_{-\infty}^{\infty} \frac{d\omega}{2\pi} \tilde{F}_{Z2\omega_0}^e(X, \omega - 2\omega_0) \exp(-i(\omega - 2\omega_0)t) \\ &= \frac{i\omega_0 d_{22} G^o(\omega - 2\omega_0) \exp(i\theta)}{n_e(2\omega_0) c \sqrt{\frac{\alpha_e(2\omega_0)}{2} - \alpha_o(\omega_0) - i\Delta k}} \\ &\left[\exp\left([- \alpha_o(\omega_0) - i\Delta k] X\right) - \exp\left(-\frac{1}{2}\alpha_e(2\omega_0) X\right) \right] \\ &\int_{-\infty}^{+\infty} \frac{d\omega}{2\pi} G^o(\omega - 2\omega_0) \exp\left(\frac{i(\omega - 2\omega_0)}{v_g^e} X\right) \exp(-i(\omega - 2\omega_0)t) \end{aligned} \quad (\text{B.31})$$

[†]Although the boundary condition is defined in the time domain, it is also compatible in the frequency domain: $F_{Z,2\omega_0}^e(\mathbf{r} = 0, t) = F_{Z,2\omega_0}^e(\mathbf{r} = 0, \omega - 2\omega_0) = 0$.

In the integral, the space-related term can be neglected because the integration focuses on a smaller range (i.e., focus on the narrow-band approximation) of ω where the phase factor variation is minimal:

$$F_{Z2\omega_0}^e(X, t) \approx \frac{i \omega_0 d_{22} G^o(\omega - 2\omega_0) \exp(i\theta)}{n_e(2\omega_0) c \sqrt{\frac{\alpha_e(2\omega_0)}{2} - \alpha_o(\omega_0) - i\Delta k}} \left[\exp\left([- \alpha_o(\omega_0) - i\Delta k] X\right) - \exp\left(-\frac{1}{2} \alpha_e(2\omega_0) X\right) \right] \int_{-\infty}^{+\infty} \frac{d\omega}{2\pi} G^o(\omega - 2\omega_0) \exp(-i(\omega - 2\omega_0)t) \quad (\text{B.32})$$

This integral is already developed in expression (B.33):

$$\int_{-\infty}^{+\infty} \frac{d\omega}{2\pi} G^o(\omega - 2\omega_0) e^{-i(\omega - 2\omega_0)t} = \frac{1}{2\pi} (F_{Y\omega_0}^o(t))^2 \quad (\text{B.33})$$

With this result, equation (B.33) becomes:

$$F_{Z2\omega_0}^e(X, t) = \frac{i \omega_0 d_{22} G^o(\omega - 2\omega_0) \exp(i\theta)}{n_e(2\omega_0) c \sqrt{\frac{\alpha_e(2\omega_0)}{2} - \alpha_o(\omega_0) - i\Delta k}} \left[\exp\left([- \alpha_o(\omega_0) - i\Delta k] X\right) - \exp\left(-\frac{1}{2} \alpha_e(2\omega_0) X\right) \right] \frac{1}{2\pi} (F_{Y\omega_0}^o(t))^2 \quad (\text{B.34})$$

B.3 Reflection Geometry

We will provide a step-by-step derivation for a and b in equation (4.75a). We use this relation $\mathbf{k}'_s(2\omega_0) \cdot \mathbf{k}'_s(2\omega_0) = 4(\gamma'_{\parallel, \omega_0})^2$ as follows

$$\begin{aligned} (k'_{s,\bar{x}}(2\omega_0))^2 + (k'_{s,\bar{z}}(2\omega_0))^2 &= \mathbf{k}'_s(2\omega_0) \cdot \mathbf{k}'_s(2\omega_0) \\ (2k_{i,\bar{x}}(\omega_0))^2 + (a_{\omega_0} + ib_{\omega_0})^2 &= 4(\gamma'_{\parallel, \omega_0})^2 \end{aligned} \quad (\text{B.35})$$

where we use expressions (4.73) and (4.75a). Since $\gamma'_{\parallel, \omega_0}$ is given by equation (4.48), the next step revolves around equating the corresponding real and imaginary parts of equation (B.35):

$$\begin{aligned} (2k_{i,\bar{x}}(\omega_0))^2 + (a_{\omega_0} + ib_{\omega_0})^2 &= 4(\gamma'_{\parallel, \omega_0})^2 \\ &= 4 \left(\beta'_{\parallel, \omega_0} + i\alpha'_{\parallel, \omega_0} \right)^2 \\ &= \frac{4\omega_0^2}{c^2} \epsilon'_{\parallel}(\omega_0) \\ &= \frac{4\omega_0^2}{c^2} \left[\text{Re}\left\{ \epsilon'_{\parallel}(\omega_0) \right\} + i \text{Im}\left\{ \epsilon'_{\parallel}(\omega_0) \right\} \right] \end{aligned} \quad (\text{B.36})$$

The real part of equation (B.36) is the following:

$$a_{\omega_0}^2 - b_{\omega_0}^2 = 4 \left(\beta'_{\parallel, \omega_0} \right)^2 - 4 \left(\alpha'_{\parallel, \omega_0} \right)^2 - 4(k_{i,\bar{x}}(\omega_0))^2 = \frac{4\omega_0^2}{c^2} \text{Re}\left\{ \epsilon'_{\parallel}(\omega_0) \right\} - 4(k_{i,\bar{x}}(\omega_0))^2 \quad (\text{B.37})$$

Through using the following relation $(2k_{i,\bar{x}}(\omega_0))^2 = (2\gamma'_{\parallel,\omega_0} \sin(\theta_i))^2 = \frac{4\omega_0^2}{c^2} \epsilon_{\parallel}(\omega_0) \sin(\theta_i)$, equation (B.37) reduces to:

$$\begin{aligned} a_{\omega_0}^2 - b_{\omega_0}^2 &= 4 \left(\beta'_{\parallel,\omega_0} \right)^2 - 4 \left(\alpha'_{\parallel,\omega_0} \right)^2 - 4 \left(k_{i,\bar{x}}(\omega_0) \right)^2 \\ &= \frac{4\omega_0^2}{c^2} \left(\text{Re} \left\{ \epsilon'_{\parallel}(\omega_0) \right\} - \epsilon_{\parallel}(\omega_0) \sin(\theta_i) \right) \\ &= A_{\parallel,\omega_0} \end{aligned} \quad (\text{B.38})$$

Regarding the imaginary part, we have the following expression:

$$\begin{aligned} 8\beta'_{\parallel,\omega_0} \alpha'_{\parallel,\omega_0} &= 2a_{\omega_0} b_{\omega_0} \\ &= \frac{4\omega_0^2}{c^2} \text{Im} \left\{ \epsilon'_{\parallel}(\omega_0) \right\} \\ &= B_{\parallel,\omega_0} \end{aligned} \quad (\text{B.39})$$

From these two equations (B.38) and (B.39), we can solve for a and b :

$$a_{\omega_0} = \left(\frac{\sqrt{A_{\parallel,\omega_0}^2 + B_{\parallel,\omega_0}^2} + A_{\parallel,\omega_0}}{2} \right)^{1/2} \quad (\text{B.40a})$$

$$b_{\omega_0} = \left(\frac{\sqrt{A_{\parallel,\omega_0}^2 + B_{\parallel,\omega_0}^2} - A_{\parallel,\omega_0}}{2} \right)^{1/2} \quad (\text{B.40b})$$

Following an analogous procedure with the relation $\mathbf{k}'_{\Gamma}(2\omega_0) \cdot \mathbf{k}'_{\Gamma}(2\omega_0) = (\gamma'_{\perp,2\omega_0})^2$, we find the following expressions for c and d :

$$c_{2\omega_0} = \left(\frac{\sqrt{A_{\perp,2\omega_0}^2 + B_{\perp,2\omega_0}^2} + A_{\perp,2\omega_0}}{2} \right)^{1/2} \quad (\text{B.41a})$$

$$d_{2\omega_0} = \left(\frac{\sqrt{A_{\perp,2\omega_0}^2 + B_{\perp,2\omega_0}^2} - A_{\perp,2\omega_0}}{2} \right)^{1/2} \quad (\text{B.41b})$$

where:

$$\begin{aligned}
c_{2\omega_0}^2 - d_{2\omega_0}^2 &= \left(\beta'_{\perp,2\omega_0}\right)^2 - \left(\alpha'_{\perp,2\omega_0}\right)^2 - 4 \left(k_{i,\bar{x}}(\omega_0)\right)^2 \\
&= \frac{(2\omega_0)^2}{c^2} \left(\operatorname{Re}\left\{\epsilon'_{\perp}(2\omega_0)\right\} - \epsilon_{\parallel}(\omega_0) \sin(\theta_i) \right) \\
&= A_{\perp,2\omega_0}
\end{aligned} \tag{B.42a}$$

$$\begin{aligned}
2\beta'_{\perp,2\omega_0} \alpha'_{\perp,2\omega_0} &= 2c_{2\omega_0} d_{2\omega_0} \\
&= \frac{(2\omega_0)^2}{c^2} \operatorname{Im}\left\{\epsilon'_{\perp}(2\omega_0)\right\} \\
&= B_{\perp,2\omega_0}
\end{aligned} \tag{B.42b}$$

Reflected time-averaged second-harmonic intensity

We aim to develop the following equation:

$$\langle I_{2\omega_{0R}}(\mathbf{r}) \rangle = \left\| \frac{1}{T_{P\omega_0}} \int_{-\frac{1}{2}T_{P\omega_0}}^{\frac{1}{2}T_{P\omega_0}} dt \frac{1}{2} \operatorname{Re}\left\{ \underset{2\omega_{0R}}{\mathcal{E}}(\mathbf{r}, t) \times \underset{2\omega_{0R}}{\mathcal{H}}^*(\mathbf{r}, t) \right\} \right\| \tag{B.43}$$

$\mathcal{E}_{2\omega_{0R}}$ and $\mathcal{H}_{2\omega_{0R}}$ are given by the following expressions:

$$\mathcal{E}_{2\omega_{0R}}(\mathbf{r}, t) = \begin{pmatrix} 0 \\ 1 \\ 0 \end{pmatrix} \exp(i\mathbf{k}_R(2\omega_0) \cdot \mathbf{r}) F_{2\omega_{0R}}(t) \tag{B.44a}$$

$$\mathcal{H}_{2\omega_{0R}}^*(\mathbf{r}, t) = \begin{pmatrix} \cos(\theta_R) \\ 0 \\ \sin(\theta_R) \end{pmatrix} \frac{1}{\mu_0 2\omega_0} \gamma_{\perp,2\omega_0} \exp(-i\mathbf{k}_R(2\omega_0) \cdot \mathbf{r}) F_{2\omega_{0R}}^*(t) \tag{B.44b}$$

Using these expressions, we can obtain the following term:

$$\frac{1}{2} \operatorname{Re}\left\{ \underset{2\omega_{0R}}{\mathcal{E}}(\mathbf{r}, t) \times \underset{2\omega_{0R}}{\mathcal{H}}^*(\mathbf{r}, t) \right\} = \frac{1}{2} \begin{pmatrix} \sin(\theta_R) \\ 0 \\ -\cos(\theta_R) \end{pmatrix} \frac{1}{\mu_0 2\omega_0} \gamma_{\perp,2\omega_0} \left| F_{2\omega_{0R}}(t) \right|^2 \tag{B.45}$$

We will now focus on $\left|F_{2\omega_0}(t)\right|^2$ ($F_{2\omega_0}(t)$ is given by equation (4.89)):

$$\begin{aligned}
\left|F_{2\omega_0}(t)\right|^2 &= \left[\frac{(2\omega_0)^2}{c^2} \frac{a+ib}{2\gamma'_{\parallel,\omega_0}} \frac{d_{22} [t\{p\}]^2}{(2\gamma'_{\parallel,\omega_0})^2 - (\gamma'_{\perp,2\omega_0})^2} \left(\frac{(c-a) + i(d-b)}{\gamma_{\perp,2\omega_0} \cos(\theta_R) + c + id} \right) \frac{1}{2\pi} F_{\omega_0}(t) \right] \\
&\quad \left[\frac{(2\omega_0)^2}{c^2} \frac{a+ib}{2\gamma'_{\parallel,\omega_0}} \frac{d_{22} [t\{p\}]^2}{(2\gamma'_{\parallel,\omega_0})^2 - (\gamma'_{\perp,2\omega_0})^2} \left(\frac{(c-a) + i(d-b)}{\gamma_{\perp,2\omega_0} \cos(\theta_R) + c + id} \right) \frac{1}{2\pi} F_{\omega_0}(t) \right]^* \\
&= \frac{(2\omega_0)^4}{4c^4} \frac{(a^2 + b^2)}{(\beta'_{\parallel,\omega_0})^2 + (\alpha'_{\parallel,\omega_0})^2} \frac{|d_{22}|^2 |t\{p\}|^4}{p^2 + q^2} \frac{(c-a)^2 + (d-b)^2}{(\gamma_{\perp,2\omega_0} \cos(\theta_R) + c)^2 + d^2} \frac{1}{4\pi^2} \left|F_{\omega_0}(t)\right|^4 \quad (\text{B.46}) \\
&= \frac{(2\omega_0)^4}{4c^4} \frac{(a^2 + b^2)}{(\beta'_{\parallel,\omega_0})^2 + (\alpha'_{\parallel,\omega_0})^2} \frac{|d_{22}|^2 (2n_{\parallel}(\omega_0) \cos(\theta_i))^4}{p^2 + q^2 (p'^2 + q'^2)^2} \frac{(c-a)^2 + (d-b)^2}{(\gamma_{\perp,2\omega_0} \cos(\theta_R) + c)^2 + d^2} \\
&\quad \frac{1}{4\pi^2} \left|F_{\omega_0}(t)\right|^4
\end{aligned}$$

We introduce new variables (i.e., p, q, p', q') for the sake of readability. We obtain these variables as follows:

$$\begin{aligned}
\frac{1}{(2\gamma'_{\parallel,\omega_0})^2 - (\gamma'_{\perp,2\omega_0})^2} &= \frac{1}{4(\beta'_{\parallel,\omega_0})^2 + (\alpha'_{\perp,2\omega_0})^2 - (\beta'_{\perp,2\omega_0})^2 - 4(\alpha'_{\parallel,\omega_0})^2 + i(8\beta'_{\parallel,\omega_0}\alpha'_{\parallel,\omega_0} - 2\beta'_{\perp,2\omega_0}\alpha'_{\perp,2\omega_0})} \\
&= \frac{1}{q + ip} \quad (\text{B.47})
\end{aligned}$$

Here, we introduce q and p , which are given by the following expressions:

$$q = 4(\beta'_{\parallel,\omega_0})^2 + (\alpha'_{\perp,2\omega_0})^2 - (\beta'_{\perp,2\omega_0})^2 - 4(\alpha'_{\parallel,\omega_0})^2 \quad (\text{B.48a})$$

$$p = 8\beta'_{\parallel,\omega_0}\alpha'_{\parallel,\omega_0} - 2\beta'_{\perp,2\omega_0}\alpha'_{\perp,2\omega_0} \quad (\text{B.48b})$$

We can develop the expression for the transmission coefficient $t\{p\}$ as follows:

$$\begin{aligned}
t\{p\} &= \frac{2n_{\parallel}(\omega_0) \cos(\theta_i)}{n_{\parallel}(\omega_0) \frac{a+ib}{2\gamma'_{\parallel,\omega_0}} + n'_{\parallel}(\omega_0) \cos(\theta_i)} \\
&= \frac{2n_{\parallel}(\omega_0) \cos(\theta_i)}{q' + ip'} \quad (\text{B.49})
\end{aligned}$$

Here, we develop the denominator (i.e., we mainly rationalize the complex quantities):

$$q' = \frac{1}{2} \frac{n_{\parallel}(\omega_0)}{(\beta'_{\perp,2\omega_0})^2 + (\alpha'_{\parallel,\omega_0})^2} (a\beta'_{\parallel,\omega_0} + b\alpha'_{\parallel,\omega_0}) + \text{Re}\{n'_{\parallel}(\omega_0)\} \cos(\theta_i) \quad (\text{B.50a})$$

$$p' = \left[\frac{1}{2} \frac{n_{\parallel}(\omega_0)}{(\beta'_{\perp,2\omega_0})^2 + (\alpha'_{\parallel,\omega_0})^2} (b\beta'_{\parallel,\omega_0} - a\alpha'_{\parallel,\omega_0}) + \text{Im}\{n'_{\parallel}(\omega_0)\} \cos(\theta_i) \right] \quad (\text{B.50b})$$

The next operation is the integration, which yields the following:

$$\begin{aligned} \frac{1}{T_{P\omega_0}} \int_{-\frac{1}{2}T_{P\omega_0}}^{+\frac{1}{2}T_{P\omega_0}} |F_{2\omega_0 i}(t)|^4 &= \frac{1}{T_{P\omega_0}} |K|^2 \int_{-\frac{1}{2}T_{P\omega_0}}^{+\frac{1}{2}T_{P\omega_0}} \exp\left(-2\frac{t^2}{\tau^2}\right) \\ &= \frac{1}{T_{P\omega_0}} \frac{4I_{\bar{z} \rightarrow 0^-}^2}{\epsilon_0^2 c^2 n_{\parallel}^2(\omega_0)} \sqrt{\frac{\pi}{2}} \tau \end{aligned} \quad (\text{B.51})$$

Here, we use the relation (4.84):

$$I_{\bar{z} \rightarrow 0^-} = \frac{\epsilon_0 c}{2} n_{\parallel}(\omega_0) |K|^2$$

Finally, we gather together all these calculations and take the Euclidean norm, which yields the following expression:

$$\begin{aligned} \langle I_{2\omega_0 R} \rangle &= \frac{16 \omega_0^3 \gamma_{\perp, 2\omega_0} (a_{\omega_0}^2 + b_{\omega_0}^2) |d_{22}|^2 n_{\parallel}^2(\omega_0) \cos^4(\theta_i)}{\epsilon_0 c^4 \sqrt{2\pi^3} (\beta'_{\parallel, \omega_0})^2 + (\alpha'_{\parallel, \omega_0})^2} \frac{(c_{2\omega_0} - a_{\omega_0})^2 + (d_{2\omega_0} - b_{\omega_0})^2}{\left[p'^2 + q'^2\right]^2} \frac{(\gamma_{\perp, 2\omega_0} \cos_{2\omega_0}(\theta_i) + c_{2\omega_0})^2 + d_{2\omega_0}^2}{\frac{1}{p^2 + q^2} \frac{\tau}{T_{P\omega_0}} I_{\bar{z} \rightarrow 0^-}^2} \end{aligned} \quad (\text{B.52})$$

Appendix C

Time-averaged Poynting vector

To compute an intensity observable (e.g. for the second harmonic generation intensity) we use the time-averaged Poynting vector. The Poynting vector revolves around the energy flow, but its rapid fluctuations make it challenging for detectors to track. However, detectors are capable of responding to the energy accumulated within a characteristic time scale, such as the period-repetition time (T_p) of a pulsed field, or the period (T) of a field of a continuous-wave field. Therefore, averaging over T_p (or T) is sensible.

The electric and magnetic fields for a frequency mode ω_ℓ is characterized by the following expression:

$$\mathbf{E}_{\omega_\ell}(\mathbf{r}, t) = \frac{1}{2} \left[\mathcal{E}_{\omega_\ell}(\mathbf{r}, t) \exp(-i\omega_\ell t) + \mathcal{E}_{\omega_\ell}^*(\mathbf{r}, t) \exp(i\omega_\ell t) \right] \quad (\text{C.1a})$$

$$\mathbf{H}_{\omega_\ell}(\mathbf{r}, t) = \frac{1}{2} \left[\mathcal{H}_{\omega_\ell}(\mathbf{r}, t) \exp(-i\omega_\ell t) + \mathcal{H}_{\omega_\ell}^*(\mathbf{r}, t) \exp(i\omega_\ell t) \right] \quad (\text{C.1b})$$

where the subscript ω_ℓ corresponds to either the fundamental frequency ω_0 or the second-harmonic frequency $2\omega_0$. \mathcal{E} and \mathcal{H} are slowly-varying complex envelope in space and time for the electric field and magnetic field, respectively. The time-averaged intensity is given by the magnitude of the Poynting vector as follows:

$$\langle I_{\omega_\ell} \rangle = \|\langle \mathbf{S}_{\omega_\ell} \rangle\| = \|\langle \mathbf{E}_{\omega_\ell} \times \mathbf{H}_{\omega_\ell} \rangle\| \quad (\text{C.2})$$

Let's further developed the Poynting vector using equations (C.1a) and (C.1b):

$$\begin{aligned}
\mathbf{S}_{\omega_\ell} &= \mathbf{E}_{\omega_j} \times \mathbf{H}_{\omega_j} \\
&= \frac{1}{2} \left[\mathcal{E}_{\omega_\ell}(\mathbf{r}, t) \exp(-i\omega_j t) + \mathcal{E}_{\omega_\ell}^*(\mathbf{r}, t) \exp(i\omega_j t) \right] \\
&\times \frac{1}{2} \left[\mathcal{H}_{\omega_\ell}(\mathbf{r}, t) \exp(-i\omega_j t) + \mathcal{H}_{\omega_\ell}^*(\mathbf{r}, t) \exp(i\omega_j t) \right] \\
&= \frac{1}{4} \left[\mathcal{E}_{\omega_\ell} \times \mathcal{H}_{\omega_\ell}^* + \mathcal{E}_{\omega_\ell}^* \times \mathcal{H}_{\omega_\ell} + \mathcal{E}_{\omega_\ell} \times \mathcal{H}_{\omega_\ell} \exp(-2i\omega_j t) + \mathcal{E}_{\omega_\ell}^* \times \mathcal{H}_{\omega_\ell}^* \exp(2i\omega_j t) \right] \\
&= \frac{1}{2} \operatorname{Re}\{\mathcal{E}_{\omega_\ell}(\mathbf{r}, t) \times \mathcal{H}_{\omega_\ell}^*(\mathbf{r}, t)\} + \frac{1}{2} \operatorname{Re}\{\mathcal{E}_{\omega_\ell}(\mathbf{r}, t) \times \mathcal{H}_{\omega_\ell}(\mathbf{r}, t) \exp(-2i\omega_j t)\}
\end{aligned} \tag{C.3}$$

For the case of a pulsed radiation, the time-averaged of the Poynting vector over time is given by:

$$\begin{aligned}
\langle \mathbf{S}_{\omega_\ell} \rangle &= \frac{1}{T_{P_{\omega_\ell}}} \int_{-T_{P_{\omega_\ell}}/2}^{+T_{P_{\omega_\ell}}/2} dt \mathbf{S}_{\omega_\ell} \\
&= \frac{1}{T_{P_{\omega_\ell}}} \int_{-T_{P_{\omega_\ell}}/2}^{+T_{P_{\omega_\ell}}/2} dt \left[\frac{1}{2} \operatorname{Re}\{\mathcal{E}_{\omega_\ell} \times \mathcal{H}_{\omega_\ell}^*\} + \frac{1}{2} \operatorname{Re}\{\mathcal{E}_{\omega_\ell} \times \mathcal{H}_{\omega_\ell} \exp(-2i\omega_j t)\} \right] \\
&\approx \frac{1}{T_{P_{\omega_\ell}}} \int_{-T_{P_{\omega_\ell}}/2}^{+T_{P_{\omega_\ell}}/2} dt \frac{1}{2} \operatorname{Re}\{\mathcal{E}_{\omega_\ell}(\mathbf{r}, t) \times \mathcal{H}_{\omega_\ell}^*(\mathbf{r}, t)\}
\end{aligned} \tag{C.4}$$

where $T_{P_{\omega_\ell}}$ is the period-repetition time for frequency ω_ℓ involved in the nonlinear process. The final step is based on the fact that $\exp\{-i2\omega_j t\}$ is a rapid oscillating function within the timescale $T_{P_{\omega_\ell}}$, resulting in effectively negligible contribution to the integral, despite being multiplied by slowly-varying functions. Finally, the time-averaged intensity is given as follows:

$$\langle I_{\omega_\ell} \rangle = \left\| \frac{1}{T_{P_j}} \int_{-T_{P_{\omega_\ell}}/2}^{+T_{P_{\omega_\ell}}/2} dt \frac{1}{2} \operatorname{Re}\{\mathcal{E}_{\omega_\ell}(\mathbf{r}, t) \times \mathcal{H}_{\omega_\ell}^*(\mathbf{r}, t)\} \right\| \tag{C.5}$$

In order to compute equation (C.5), we need to calculate the magnetic field. We can use the following equation to calculate the magnetic field:

$$\nabla \times \mathbf{E}_{\omega_\ell} = -\mu_0 \frac{\partial}{\partial t} \mathbf{H}_{\omega_\ell} \tag{C.6}$$

Plugging equations (C.1) into this equation, we obtain the following expression:

$$\nabla \times \mathcal{E}_{\omega_\ell} = i\mu_0 \omega_\ell \mathcal{H}_{\omega_\ell} - \mu_0 \frac{\partial \mathcal{H}_{\omega_\ell}}{\partial t} \tag{C.7}$$

From equation (3.21) in Chapter 3, we can express the slowly-varying envelopes as follows:

$$\mathcal{E}_{\omega_\ell}(\mathbf{r}, t) = \frac{1}{2\pi} \int_{-\infty}^{+\infty} d\omega' \tilde{\mathcal{E}}_{\omega_\ell}(\mathbf{r}, \omega') \exp(-i\omega' t) \tag{C.8a}$$

$$\mathcal{H}_{\omega_\ell}(\mathbf{r}, t) = \frac{1}{2\pi} \int_{-\infty}^{+\infty} d\omega' \tilde{\mathcal{H}}_{\omega_\ell}(\mathbf{r}, \omega') \exp(-i\omega' t) \tag{C.8b}$$

Then, by plugging these expressions into equation (C.7), we obtain the following:

$$\begin{aligned} \nabla \times \frac{1}{2\pi} \int_{-\infty}^{+\infty} d\omega' \tilde{\mathcal{E}}_{\omega_\ell}(\mathbf{r}, \omega') \exp(-i\omega' t) &= \frac{\mu_0}{2\pi} \int_{-\infty}^{+\infty} d\omega' [i(\omega_\ell + \omega')] \tilde{\mathcal{H}}_{\omega_\ell}(\mathbf{r}, \omega') \exp(-i\omega' t) \\ &\approx \frac{i\mu_0\omega_\ell}{2\pi} \int_{-\infty}^{+\infty} d\omega' \tilde{\mathcal{H}}_{\omega_\ell}(\mathbf{r}, \omega') \exp(-i\omega' t) \end{aligned} \quad (\text{C.9})$$

Here, we take into consideration the fact that $\omega' \ll \omega_\ell$ for narrow bandwidth fields used when deriving the wave equation for the electric field. Finally, by Fourier transforming back, equation (C.9) becomes:

$$\nabla \times \mathcal{E}_{\omega_\ell} = i\mu_0\omega_\ell \mathcal{H}_{\omega_\ell} \quad (\text{C.10})$$

Using this equation, we can obtain the magnetic field after calculating the second-harmonic electric field.

Appendix D

Two approaches towards problems in linear and nonlinear optics

Generally, the field is assumed to be of infinite extent and constant in amplitude and phase in a plane transverse to the direction of propagation. Under this approximation, envelope solely depends on z (in general, longitudinal coordinate) and t as follows: $F \exp(i(kz - \omega t))$. Such a wave is called an infinite plane wave.

When transverse effects are not longer neglected, a common form of a finite beam is the TEM₀₀ mode of a circular Gaussian beam. The field of this type of wave is written as follows:

$$\begin{aligned}\mathbf{E}(\mathbf{r}, t) &= \mathbf{E}(r_{\perp}, z, t) = \frac{1}{2} \hat{e} F(r_{\perp}, z) \exp(i(kz - \omega t)) + \text{c.c.} \\ F(r_{\perp}, z) &= F(z, t) \frac{W_0}{W(z)} \exp\left(i \left[\frac{kr^2}{2q(z)} - \tan^{-1} \left(\frac{z}{z_R} \right) \right]\right) \\ F(r_{\perp}, z) &= F(z, t) \frac{W_0}{W(z)} \exp\left(\frac{-r^2}{W^2(z)}\right) \exp\left(i \left[\frac{kr^2}{2R(z)} - \tan^{-1} \left(\frac{z}{z_R} \right) \right]\right)\end{aligned}\tag{D.1}$$

Remarkably, the beam has a Gaussian cross section with a variable radius $W(z)$, which is defined as the half-width of the Gaussian curve at the point r (the radial coordinate), where the curve is at $1/e$ of its maximum value. $W(z)$ is given by:

$$W(z) = W_0 \left[1 + \left(\frac{z}{z_R} \right)^2 \right]^{1/2}\tag{D.2}$$

where W_0 is minimum radius at $z = 0$. The diameter of the beam at $z = 0$ is $2W_0$, which is called the beam waist. The quantity $q(z)$ is called a complex radius of curvature:

$$q(z) = z - i z_R\tag{D.3}$$

Finally, the quantity z_R is called the Rayleigh range, and is defined by

$$z_R = \frac{n \pi W_0^2}{\lambda} \quad (\text{D.4})$$

where n is the index of refraction of the medium, and λ is the wavelength. The distance between the points $\pm z_R$ about the waist is called the confocal parameter b of the beam, $b = 2z_R$. These sets of parameters prove valuable for estimating solutions when assessing propagation equations within the context of the plane-wave approximation¹¹, pp.91–98.

Appendix E

Computational Details: DFT

This section complements the computational details provided in Chapter 4, Section 4.5.

There are several parameters that one must properly choose in order to run simulations. These parameters are selected based on convergence tests regarding the total energy of the system in both codes: GPAW and `Exciting`. For instance, we evaluate the number of plane waves utilized to study the system, distinguished by the flags “`ecut`” (see equation (2.67) in Chapter 2, Section 2.3.1) and “`rgkmax`” (see Chapter 2, Section 2.3.1, page 29) in GPAW and `exciting`, respectively. Additionally, we assess the sampling of the Brillouin zone, characterized by “`kpt`” and “`ngridk`” in GPAW and `exciting`, respectively (for an explanation of the role of \mathbf{k} -point sampling, see pages 21 and 22). The units of `ecut` are chosen to be electronvolts (eV), while `rgkmax` is a dimensionless parameter⁴⁷. Based on these simple convergence tests, the chosen parameters are: 1200 eV for “`ecut`” and a $5 \times 5 \times 5$ Monkhorst-Pack grid for “`kpts`” (See Fig. E.1); 7 for “`rgkmax`” and a $9 \times 9 \times 9$ size mesh for “`ngridk`” (See Fig. E.2). The relaxed structure is computed from computing the total energy of the system with respect to different material volumes (see Fig. E.3). We find the optimal volume (consequently the lattice parameter*) using the Birch-Murnaghan equation of state¹⁰⁷ (see Fig. E.3):

$$E(V) = E_0 + \frac{9V_0B_0}{16} \left(\left[\left(\frac{V_0}{V} \right)^{2/3} - 1 \right]^3 B'_0 + \left[6 - 4 \left(\frac{V_0}{V} \right)^{2/3} \right] \right) \quad (\text{E.1})$$

where B_0 is the bulk modulus at equilibrium V_0 , and B'_0 is the first derivative of the bulk modulus with respect to pressure.

Finally, with the relaxed structure, we compute the dielectric functions with GPAW while second-order susceptibility tensor with `Exciting`. Regarding the former, we calculate the dielectric matrix using equation (2.101), where the cut-energy value is 200 eV. We increase the sample of the reciprocal space, using a $19 \times 19 \times 19$ \mathbf{k} -mesh. Comparing with previous DFT calculations on LiNbO_3 , Husin et al.¹⁰⁸ performed geometric optimization and calculated

*We obtain the lattice parameter by solving for a_0 in the following equation: $|a_0 \hat{\mathbf{a}} \cdot (a_0 \hat{\mathbf{b}} \times a_0 \hat{\mathbf{c}})| = V_0$, where a_0 is the optimal lattice parameter.

the optical properties of LiNbO_3 using the Monkhorst-Pack method with a Vanderbilt-type ultrasoft pseudopotential. They employed a plane-wave cut-off energy of 500 eV and a $3 \times 3 \times 2$ \mathbf{k} -mesh size. They determined the ordinary and extraordinary dielectric functions of LiNbO_3 crystals for photon energies up to 40 eV.

However, Mamoun et al.¹⁰⁹ calculated the dielectric functions of LiNbO_3 crystals for photon energies up to 30 eV, but they sampled the reciprocal space by a larger Monkhorst-Pack mesh: $11 \times 11 \times 11$. Therefore, as we aim to calculate at higher energies (72 eV), we use a $19 \times 19 \times 19$ \mathbf{k} -mesh.

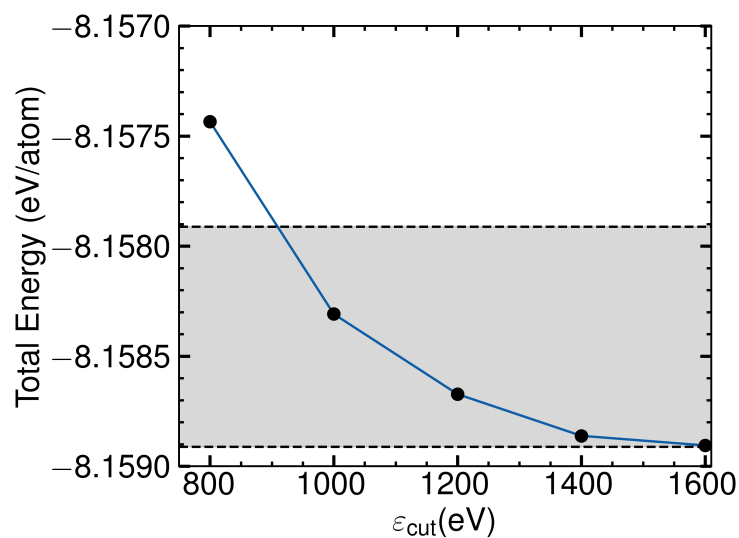
To compute the second-order susceptibility tensor, we employed equations (2.105) and (2.106) along with a $15 \times 15 \times 15$ \mathbf{k} -mesh for sampling the reciprocal space. This specific \mathbf{k} -mesh selection aligns with previous studies on materials like LiNbO_3 ¹⁵ and LiOsO_3 ¹⁸, which used the same \mathbf{k} -mesh density ($15 \times 15 \times 15$) to calculate the second-order susceptibility tensor in the XUV range.

Our choice of the GGA-PBE functional is motivated by two factors. Firstly, as shown by Husin et al.¹⁰⁸, it reproduces the lattice parameters of LiNbO_3 crystals more accurately than the LDA functional. This justifies its use for the subsequent calculations throughout this thesis. Secondly, we employ the scissor operator to better represent the energy levels compared to those obtained from DFT calculations. To achieve this, we shift the conduction energy levels by the band gap value computed using a higher-level theories, such as G_0W_0 . As noted by Husin et al.¹⁰⁸, these high-level theories typically rely on GGA-PBE functionals. For consistency in applying the scissor operator, we therefore perform our DFT calculations using the GGA-PBE functional as well.

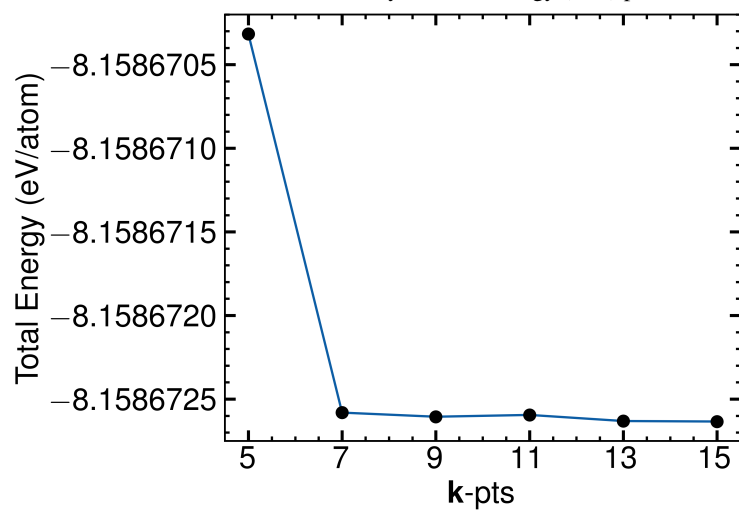
We acknowledge that we were unable to perform a convergence test on the \mathbf{k} -mesh size due to limitations in computational resources. Therefore, the chosen parameters represent the maximum achievable resolution within our computational constraints. A more comprehensive study incorporating convergence tests is recommended for future investigations.

There are additional computational details regarding the `Exciting` code. The wave functions, potential, and charge density are expanded into two different bases. They are expanded in spherical harmonics within the atomic spheres, while outside the spheres (interstitial region) they are expanded in a plane wave basis (See Chapter 2, Section 2.3). Inside the sphere, the maximum value of the angular momentum number l for wave functions, potential, and density is $l_{max} = 8$. For the muffin-tin radii, we choose $r_{\text{Li}} = 1,7$ Bohr, $r_{\text{O}} = 1.45$ Bohr and $r_{\text{Nb}} = 2$ Bohr. Additionally, local orbitals are incorporated into the calculations for each atomic species: s for Li, s and p for O, and s , p and d for Nb. All this information is contained within the species file for each atomic species that `Exciting` needs for running calculations. We use default species files provided by `Exciting` developers⁴⁷.

Since GPAW utilizes the Atomic Simulation Environment (ASE)⁷⁴, a Python package for managing atomic simulations, it adopts the unit conventions of ASE. These primarily consist of electron volts (eV) for energy and angstroms (Å) for lengths. However, `Exciting` uses atomic units; relevant units include Hartree (Ha) for energies and Bohr for lengths. When working with `Exciting` results, it is often necessary to convert these units to electron volts (eV) and angstroms (Å) for consistency with GPAW calculations.

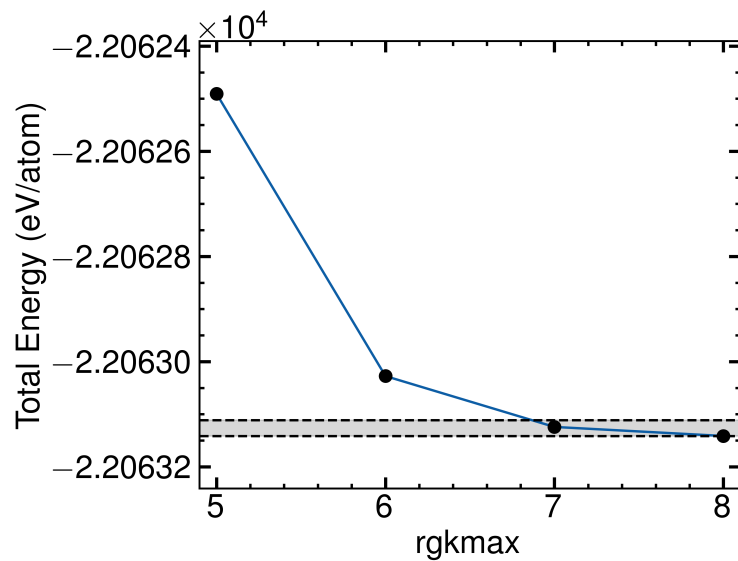


(a) Change of the the total energy per atom with respect to the size of the plane-wave basis set, which is characterized by a cut-off energy (ϵ_{cut}) parameter.

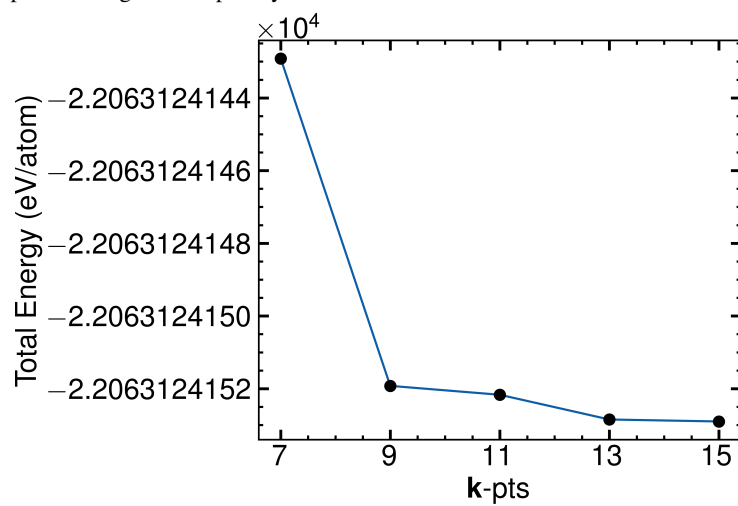


(b) Change of the total energy per atom with respect to the k-point grid size. For example, k-point = 11 corresponds to the case where $11 \times 11 \times 11$ points are used to sample the reciprocal space.

Figure E.1: Total energy per atom as a function of various DFT parameters, calculated using the GPAW code. The gray region represents a 1 meV energy window. Points within this region indicate a difference of less than 1 meV between them.



(a) Change of the the total energy per atom with respect to $rgkmax$. The parameter $rgkmax$ implicitly determines the number of basis functions.



(b) Change of the total energy per atom with respect to the k -point grid size.

Figure E.2: Total energy per atom as a function of various DFT parameters, calculated using the `Exciting` code. The gray region represents a 30 meV energy window. Points within this region indicate a difference of less than 30 meV between them.

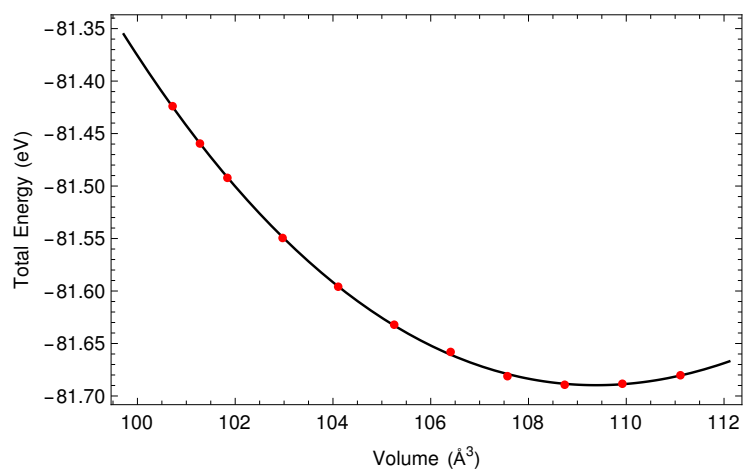


Figure E.3: GGA-PBE computed equation of state for bulk LiNbO_3 , which is fitted with a polynomial equation.

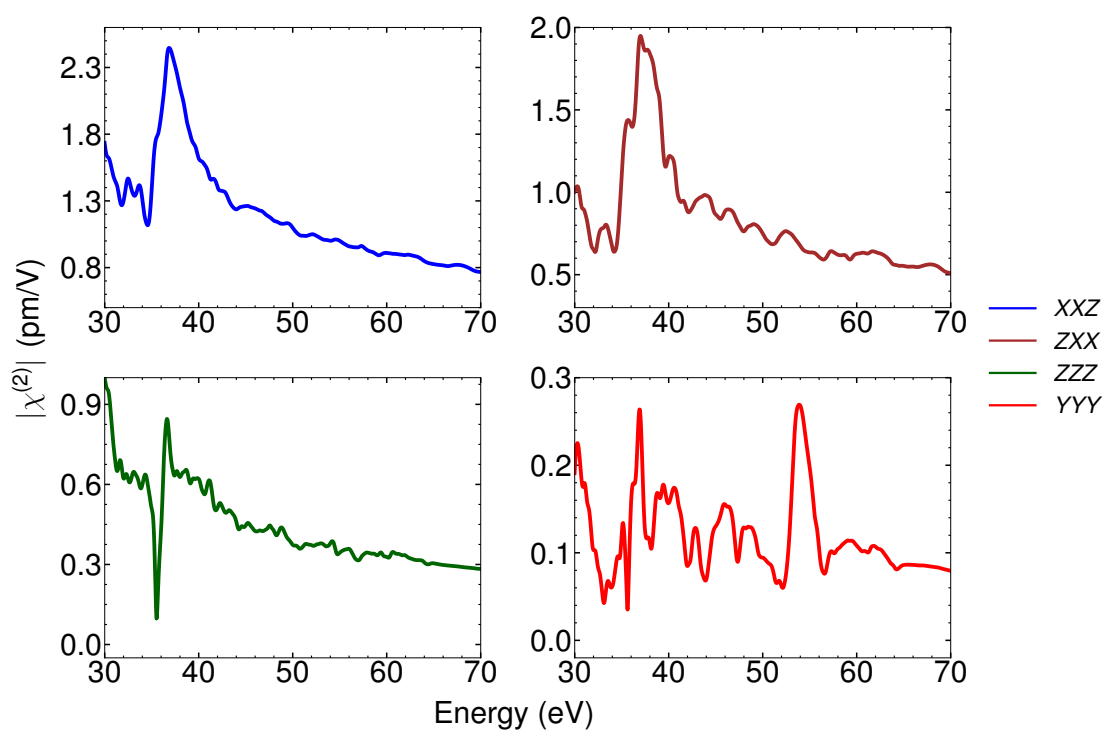


Figure E.4: Visualization of the non-zero second-order nonlinear susceptibility components of LiNbO_3 . Shown in a clockwise direction from the upper left quadrant are the components: XXZ , ZXX , YYY , and ZZZ .

Bibliography

- [1] Landau, L.; Lifshitz, E. *Electrodynamics of continuous media*; Pergamon Press, 1984; Vol. 8.
- [2] Weinberger, P. John Kerr and his effects found in 1877 and 1878. *Philosophical Magazine Letters* **2008**, *88*, 897–907.
- [3] Powers, P. E.; Haus, J. W. *Fundamentals of nonlinear optics*; CRC press, 2017.
- [4] Zhao, X.; Ji, L.; Liu, D.; Gao, Y.; Rao, D.; Cui, Y.; Feng, W.; Li, F.; Shi, H.; Shan, C.; Ma, W.; Sui, Z. Second-harmonic generation of temporally low-coherence light. *APL Photonics* **2020**, *5*, 091301.
- [5] Franken, P. A.; Hill, A. E.; Peters, C. W.; Weinreich, G. Generation of Optical Harmonics. *Phys. Rev. Lett.* **1961**, *7*, 118–119.
- [6] Ma, J.; Sun, M. Nonlinear optical microscopies (NOMs) and plasmon-enhanced NOMs for biology and 2D materials. *Nanophotonics* **2020**, *9*, 1341–1358.
- [7] Ho, P. C.; Wang, J. Z.; Meloni, F.; Vargas-Baca, I. Chalcogen bonding in materials chemistry. *Coordination Chemistry Reviews* **2020**, *422*, 213464.
- [8] Rodríguez, C.; Booth, M. J.; Turcotte, R. Adaptive optics for in vivo brain imaging. *Frontiers in Neuroscience* **2023**, *17*, 1188614.
- [9] Hoy, C. L.; Ferhanoğlu, O.; Yildirim, M.; Kim, K. H.; Karajanagi, S. S.; Chan, K. M. C.; Kobler, J. B.; Zeitels, S. M.; Ben-Yakar, A. Clinical Ultrafast Laser Surgery: Recent Advances and Future Directions. *IEEE Journal of Selected Topics in Quantum Electronics* **2014**, *20*, 242–255.
- [10] Rizzuto, A. M.; Irgen-Giuro, S.; Eftekhari-Bafrooei, A.; Saykally, R. J. Broadband deep UV spectra of interfacial aqueous iodide. *The journal of physical chemistry letters* **2016**, *7*, 3882–3885.
- [11] Boyd, R. W. *Nonlinear Optics*, third edition ed.; Academic Press, 2008.
- [12] Heinz, T. F.; Loy, M. M. T.; Thompson, W. A. Study of Si(111) Surfaces by Optical Second-Harmonic Generation: Reconstruction and Surface Phase Transformation. *Phys. Rev. Lett.* **1985**, *54*, 63–66.

- [13] Sekikawa, T.; Kosuge, A.; Kanai, T.; Watanabe, S. Nonlinear optics in the extreme ultraviolet. *Nature* **2004**, *432*, 605–608.
- [14] Tanaka, T.; Kato, M.; Saito, N.; Owada, S.; Tono, K.; Yabashi, M.; Ishikawa, T. Absolute laser-intensity measurement and online monitor calibration using a calorimeter at a soft X-ray free-electron laser beamline in SACLA. *Nuclear Instruments and Methods in Physics Research Section A: Accelerators, Spectrometers, Detectors and Associated Equipment* **2018**, *894*, 107–110.
- [15] Berger, E. *et al.* Extreme Ultraviolet Second Harmonic Generation Spectroscopy in a Polar Metal. *Nano Letters* **2021**, *21*, 6095–6101, PMID: 34264679.
- [16] Vivek, P.; Suvitha, A.; Jauhar, R. M.; Steephen, A.; Arunkumar, R.; Karunakaran, N.; Kowsalya, M.; Rekha, M. Determination of SHG d eff by Maker fringes studies on unidirectional grown guanidinium chlorochromate single crystal for NLO device applications. *Journal of Optics* **2021**, *50*, 77–82.
- [17] Sharma, S.; Ambrosch-Draxl, C. Second-harmonic optical response from first principles. *Physica Scripta* **2004**, *2004*, 128.
- [18] Uzundal, C. B. *et al.* Polarization-Resolved Extreme-Ultraviolet Second-Harmonic Generation from LiNbO₃. *Phys. Rev. Lett.* **2021**, *127*, 237402.
- [19] Griffiths, D. *Introduction to Electrodynamics*; Pearson Education, 2014.
- [20] Lafrentz, M.; Brunne, D.; Kaminski, B.; Pavlov, V. V.; Henriques, A. B.; Pisarev, R. V.; Yakovlev, D. R.; Springholz, G.; Bauer, G.; Abramof, E.; Rappl, P. H. O.; Bayer, M. Optical third-harmonic spectroscopy of the magnetic semiconductor EuTe. *Phys. Rev. B* **2010**, *82*, 235206.
- [21] Lam, R. K. *et al.* Soft X-Ray Second Harmonic Generation as an Interfacial Probe. *Phys. Rev. Lett.* **2018**, *120*, 023901.
- [22] Wikipedia, the free encyclopedia, Bidirectional scattering distribution function. 2006; https://upload.wikimedia.org/wikipedia/commons/d/d8/BSDF05_800.png, [Online; accessed May 11, 2024].
- [23] Liu, Z.; Wang, J.; Chen, B.; Wei, Y.; Liu, W.; Liu, J. Giant enhancement of continuous wave second harmonic generation from few-layer GaSe coupled to high-Q quasi bound states in the continuum. *Nano Letters* **2021**, *21*, 7405–7410.
- [24] Kittel, C. *Introduction to Solid State Physics*; Wiley, 2004.
- [25] IEEE Standard on Piezoelectricity. *ANSI/IEEE Std 176-1987* **1988**,
- [26] Guha, S.; Gonzalez, L. P. *Laser Beam Propagation in Nonlinear Optical Media*; CRC Press, 2013.
- [27] Fleck, J. A.; Feit, M. D. Beam propagation in uniaxial anisotropic media. *J. Opt. Soc. Am.* **1983**, *73*, 920–926.

- [28] Sutherland, R. L. *Handbook of nonlinear optics*; CRC press, 2003.
- [29] Butcher, P. N.; Cotter, D. *The Elements of Nonlinear Optics*; Cambridge Studies in Modern Optics; Cambridge University Press, 1990.
- [30] Schrödinger, E. An Undulatory Theory of the Mechanics of Atoms and Molecules. *Phys. Rev.* **1926**, 28, 1049–1070.
- [31] Griffiths, D. J.; Schroeter, D. F. *Introduction to quantum mechanics*, third edition ed.; Cambridge University Press: Cambridge ; New York, NY, 2018.
- [32] Hohenberg, P.; Kohn, W. Inhomogeneous Electron Gas. *Phys. Rev.* **1964**, 136, B864–B871.
- [33] Gross, A. Theoretical surface science. *A Microscopic Perspective. Originally published in the series: Advanced Texts in Physics*, **2009**, 132.
- [34] Kohn, W.; Sham, L. J. Self-Consistent Equations Including Exchange and Correlation Effects. *Phys. Rev.* **1965**, 140, A1133–A1138.
- [35] Sholl, D. S.; Steckel, J. A. *Density functional theory: a practical introduction*; John Wiley & Sons, 2022.
- [36] Perdew, J. P.; Burke, K.; Ernzerhof, M. Generalized Gradient Approximation Made Simple. *Phys. Rev. Lett.* **1996**, 77, 3865–3868.
- [37] Monkhorst, H. J.; Pack, J. D. Special points for Brillouin-zone integrations. *Phys. Rev. B* **1976**, 13, 5188–5192.
- [38] Chadi, D. J.; Cohen, M. L. Special Points in the Brillouin Zone. *Phys. Rev. B* **1973**, 8, 5747–5753.
- [39] Cárdenas, J. R.; Bester, G. Atomic effective pseudopotentials for semiconductors. *Phys. Rev. B* **2012**, 86, 115332.
- [40] Slater, J. In *Energy Band Calculations by the Augmented Plane Wave Method***The research reported in this paper has been assisted by the National Science Foundation and the Office of Naval Research, as well as by the Army, Navy, and Air Force.; Löwdin, P.-O., Ed.; Advances in Quantum Chemistry; Academic Press, 1964; Vol. 1; pp 35–58.
- [41] Blöchl, P. E.; Först, C. J.; Schimpl, J. Projector augmented wave method: ab initio molecular dynamics with full wave functions. *Bulletin of Materials Science* **2003**, 26, 33–41.
- [42] Kresse, G.; Joubert, D. From ultrasoft pseudopotentials to the projector augmented-wave method. *Phys. Rev. B* **1999**, 59, 1758–1775.
- [43] Abramowitz, M.; Stegun, I. A. *Handbook of Mathematical Functions with Formulas, Graphs, and Mathematical Tables*, ninth dover printing, tenth gpo printing ed.; Dover: New York, 1964.

- [44] Giustino, F. *Materials modelling using density functional theory: properties and predictions*; Oxford University Press, 2014.
- [45] Andersen, O. K. Linear methods in band theory. *Phys. Rev. B* **1975**, *12*, 3060–3083.
- [46] Sjöstedt, E.; Nordström, L.; Singh, D. An alternative way of linearizing the augmented plane-wave method. *Solid state communications* **2000**, *114*, 15–20.
- [47] Gulans, A.; Kontur, S.; Meisenbichler, C.; Nabok, D.; Pavone, P.; Rigamonti, S.; Sagmeister, S.; Werner, U.; Draxl, C. exciting: a full-potential all-electron package implementing density-functional theory and many-body perturbation theory. *Journal of Physics: Condensed Matter* **2014**, *26*, 363202.
- [48] Hohenberg, P.; Kohn, W. Density functional theory (DFT). *Phys. Rev* **1964**, *136*, B864.
- [49] Johnson, K. A.; Ashcroft, N. W. Corrections to density-functional theory band gaps. *Phys. Rev. B* **1998**, *58*, 15548–15556.
- [50] Giantomassi, M.; Stankovski, M.; Shaltaf, R.; Grüning, M.; Bruneval, F.; Rinke, P.; Rignanese, G.-M. Electronic properties of interfaces and defects from many-body perturbation theory: Recent developments and applications. *physica status solidi (b)* **2011**, *248*, 275–289.
- [51] Rehr, J. J. Lars Hedin and the quest for a theory of excited states. *Physica Scripta* **2005**, *2005*, 19.
- [52] Hüser, F.; Olsen, T.; Thygesen, K. S. Quasiparticle GW calculations for solids, molecules, and two-dimensional materials. *Phys. Rev. B* **2013**, *87*, 235132.
- [53] Sham, L. J.; Schlüter, M. Density-Functional Theory of the Energy Gap. *Phys. Rev. Lett.* **1983**, *51*, 1888–1891.
- [54] Riefer, A.; Friedrich, M.; Sanna, S.; Gerstmann, U.; Schindlmayr, A.; Schmidt, W. G. LiNbO₃ electronic structure: Many-body interactions, spin-orbit coupling, and thermal effects. *Phys. Rev. B* **2016**, *93*, 075205.
- [55] Raciti, R.; Bahariqushchi, R.; Summonte, C.; Aydinli, A.; Terrasi, A.; Mirabella, S. Optical bandgap of semiconductor nanostructures: Methods for experimental data analysis. *Journal of Applied Physics* **2017**, *121*, 234304.
- [56] Marques, M.; Gross, E. TIME-DEPENDENT DENSITY FUNCTIONAL THEORY. *Annual Review of Physical Chemistry* **2004**, *55*, 427–455.
- [57] Runge, E.; Gross, E. K. U. Density-Functional Theory for Time-Dependent Systems. *Phys. Rev. Lett.* **1984**, *52*, 997–1000.
- [58] Wang, C.-Y.; Elliott, P.; Sharma, S.; Dewhurst, J. K. Real time scissor correction in TD-DFT. *Journal of Physics: Condensed Matter* **2019**, *31*, 214002.

- [59] Sottile, F. Response functions of semiconductors and insulators: from the Bethe-Salpeter equation to time-dependent density functional theory. PhD thesis, CNRS-CEA/DSM, École Polytechnique, Palaiseau, France, 2003; Available at https://etsf.polytechnique.fr/system/files/Tesi_dot.pdf.
- [60] Hübener, H.; Luppi, E.; Véliard, V. Ab initio calculation of second harmonic generation in solids. *physica status solidi (b)* **2010**, *247*, 1984–1991.
- [61] Adler, S. L. Quantum Theory of the Dielectric Constant in Real Solids. *Phys. Rev.* **1962**, *126*, 413–420.
- [62] Wisner, N. Dielectric Constant with Local Field Effects Included. *Phys. Rev.* **1963**, *129*, 62–69.
- [63] Tancogne-Dejean, N. Ab initio description of second-harmonic generation from crystal surfaces. PhD thesis, Polytech Paris-Saclay - Université Paris-Saclay, Gif-sur-Yvette, France, 2015; Available at <https://pastel.hal.science/tel-01235611v2/document>.
- [64] Sharma, S.; Dewhurst, J. K.; Ambrosch-Draxl, C. Linear and second-order optical response of III-V monolayer superlattices. *Phys. Rev. B* **2003**, *67*, 165332.
- [65] D. Eimerl, J. A.; Milonni, P. Paraxial Wave Theory of Second and Third Harmonic Generation in Uniaxial Crystals. *Journal of Modern Optics* **1995**, *42*, 1037–1067.
- [66] Leidinger, M.; Fieberg, S.; Waasem, N.; Kühnemann, F.; Buse, K.; Breunig, I. Comparative study on three highly sensitive absorption measurement techniques characterizing lithium niobate over its entire transparent spectral range. *Opt. Express* **2015**, *23*, 21690–21705.
- [67] Schlarb, U.; Betzler, K. Refractive indices of lithium niobate as a function of temperature, wavelength, and composition: A generalized fit. *Phys. Rev. B* **1993**, *48*, 15613–15620.
- [68] Schlarb, U.; Betzler, K. Refractive indices of lithium niobate as a function of temperature, wavelength, and composition: A generalized fit. *Physical Review B* **1993**, *48*, 15613.
- [69] Sánchez-Dena, O.; Fierro-Ruiz, C. D.; Villalobos-Mendoza, S. D.; Carrillo Flores, D. M.; Elizalde-Galindo, J. T.; Farías, R. Lithium Niobate Single Crystals and Powders Reviewed—Part I. *Crystals* **2020**, *10*.
- [70] Gettemy, D.; Harker, W.; Lindholm, G.; Barnes, N. Some optical properties of KTP, LiIO/sub 3/, and LiNbO/sub 3/. *IEEE Journal of Quantum Electronics* **1988**, *24*, 2231–2237.
- [71] Khan, K.; Akbar, M. A.; Koppelaar, H. Study of coupled nonlinear partial differential equations for finding exact analytical solutions. *Royal Society open science* **2015**, *2*, 140406.
- [72] Paschotta, R. Velocity of Light. RP Photonics Encyclopedia, https://www.rp-photonics.com/velocity_of_light.html.

- [73] Mortensen, J. J. *et al.* GPAW: An open Python package for electronic structure calculations. *The Journal of Chemical Physics* **2024**, *160*, 092503.
- [74] Larsen, A. H. *et al.* The atomic simulation environment—a Python library for working with atoms. *Journal of Physics: Condensed Matter* **2017**, *29*, 273002.
- [75] Center for X-Ray Optics, *X-Ray Interactions With Matter*. 1995-2024; https://henke.lbl.gov/optical_constants/.
- [76] Hafner, J. Ab-initio simulations of materials using VASP: Density-functional theory and beyond. *Journal of Computational Chemistry* **2008**, *29*, 2044–2078.
- [77] Elk: Electrons in k-space. <http://elk.sourceforge.net/>.
- [78] Mortensen, J. J.; Hansen, L. B.; Jacobsen, K. W. Real-space grid implementation of the projector augmented wave method. *Phys. Rev. B* **2005**, *71*, 035109.
- [79] Larsen, A. H.; Vanin, M.; Mortensen, J. J.; Thygesen, K. S.; Jacobsen, K. W. Localized atomic basis set in the projector augmented wave method. *Phys. Rev. B* **2009**, *80*, 195112.
- [80] Yan, J.; Mortensen, J. J.; Jacobsen, K. W.; Thygesen, K. S. Linear density response function in the projector augmented wave method: Applications to solids, surfaces, and interfaces. *Phys. Rev. B* **2011**, *83*, 245122.
- [81] Singh, D. J.; Nordstrom, L. *Planewaves, Pseudopotentials, and the LAPW method*; Springer Science & Business Media, 2006.
- [82] Kirklin, S.; Saal, J. E.; Meredig, B.; Thompson, A.; Doak, J. W.; Aykol, M.; Rühl, S.; Wolverton, C. The Open Quantum Materials Database (OQMD): assessing the accuracy of DFT formation energies. *npj Computational Materials* **2015**, *1*.
- [83] Saal, J. E.; Kirklin, S.; Aykol, M.; Meredig, B.; Wolverton, C. Materials Design and Discovery with High-Throughput Density Functional Theory: The Open Quantum Materials Database (OQMD). *JOM* **2013**, *65*, 1501–1509.
- [84] Schmidt, W. G.; Albrecht, M.; Wippermann, S.; Blankenburg, S.; Rauls, E.; Fuchs, F.; Rödl, C.; Furthmüller, J.; Hermann, A. LiNbO₃ ground- and excited-state properties from first-principles calculations. *Phys. Rev. B* **2008**, *77*, 035106.
- [85] Thierfelder, C.; Sanna, S.; Schindlmayr, A.; Schmidt, W. G. Do we know the band gap of lithium niobate? *physica status solidi c* **2010**, *7*, 362–365.
- [86] Veithen, M.; Ghosez, P. First-principles study of the dielectric and dynamical properties of lithium niobate. *Phys. Rev. B* **2002**, *65*, 214302.

- [87] Riefer, A.; Sanna, S.; Gavrilenko, A. V.; Schmidt, W. G. Linear and nonlinear optical response of LiNbO₃ calculated from first principles. *IEEE Transactions on Ultrasonics, Ferroelectrics, and Frequency Control* **2012**, *59*, 1929–1933.
- [88] Fox, A. *Optical Properties of Solids*; Oxford master series in condensed matter physics; Oxford University Press, 2001.
- [89] You, D. *et al.* Multi-particle momentum correlations extracted using covariance methods on multiple-ionization of diiodomethane molecules by soft-X-ray free-electron laser pulses. *Phys. Chem. Chem. Phys.* **2020**, *22*, 2648–2659.
- [90] Way For Light, *Free Electron laser Radiation for Multidisciplinary Investigations*. <https://www.wayforlight.eu/facility/23325>.
- [91] Elettra Sincrotrone Trieste, 2023; <https://www.elettra.eu/lightsources/fermi.html>.
- [92] Sorokin, A. A.; Bican, Y.; Bonfigt, S.; Brachmanski, M.; Braune, M.; Jastrow, U. F.; Gottwald, A.; Kaser, H.; Richter, M.; Tiedtke, K. An X-ray gas monitor for free-electron lasers. *Journal of Synchrotron Radiation* **2019**, *26*, 1092–1100.
- [93] Poletto, L.; Frassetto, F.; Miotti, P.; Di Cicco, A.; Finetti, P.; Grazioli, C.; Iesari, F.; Kivimäki, A.; Stagira, S.; Coreno, M. Spectrometer for X-ray emission experiments at FERMI free-electron-laser. *Review of Scientific Instruments* **2014**, *85*, 103112.
- [94] Vakulov, Z.; Ivonin, M.; Zamburg, E. G.; Klimin, V. S.; Volik, D. P.; Golosov, D. A.; Zavadskiy, S. M.; Dostanko, A. P.; Miakonkikh, A. V.; Clemente, I. E.; Rudenko, K. V.; Ageev, O. A. Size effects in LiNbO₃ thin films fabricated by pulsed laser deposition. *Journal of Physics: Conference Series* **2018**, *1124*, 022032.
- [95] Geiss, R. Micro and nanostructured lithium niobate for integrated nonlinear optics. Ph.D. thesis, Friedrich-Schiller-Universität Jena, 2016.
- [96] Herman, W. N.; Hayden, L. M. Maker fringes revisited: second-harmonic generation from birefringent or absorbing materials. *J. Opt. Soc. Am. B* **1995**, *12*, 416–427.
- [97] Jerphagnon, J.; Kurtz, S. K. Maker Fringes: A Detailed Comparison of Theory and Experiment for Isotropic and Uniaxial Crystals. *Journal of Applied Physics* **2003**, *41*, 1667–1681.
- [98] Bloembergen, N.; Pershan, P. S. Light Waves at the Boundary of Nonlinear Media. *Phys. Rev.* **1962**, *128*, 606–622.
- [99] Shen, Y. *The Principles of Nonlinear Optics*; Wiley classics library; Wiley, 2003.
- [100] Orfanidis, S. J. Electromagnetic waves and antennas. **2002**,

-
- [101] Sanna, S.; Schmidt, W. G. Lithium niobate *X*-cut, *Y*-cut, and *Z*-cut surfaces from ab initio theory. *Phys. Rev. B* **2010**, *81*, 214116.
- [102] Rams, J.; Cabrera, J. M. Second harmonic generation in the strong absorption regime. *Journal of Modern Optics* **2000**, *47*, 1659–1669.
- [103] Bringuier, E.; Bourdon, A.; Piccioli, N.; Chevy, A. Optical second-harmonic generation in lossy media: Application to GaSe and InSe. *Phys. Rev. B* **1994**, *49*, 16971–16982.
- [104] Guyot-Sionnest, P.; Chen, W.; Shen, Y. R. General considerations on optical second-harmonic generation from surfaces and interfaces. *Phys. Rev. B* **1986**, *33*, 8254–8263.
- [105] Glenn, W. Second-harmonic generation by picosecond optical pulses. *IEEE Journal of Quantum Electronics* **1969**, *5*, 284–290.
- [106] Strang, G. *Introduction to Linear Algebra*, 4th ed.; Wellesley-Cambridge Press: Wellesley, MA, 2009.
- [107] Birch, F. Finite Elastic Strain of Cubic Crystals. *Phys. Rev.* **1947**, *71*, 809–824.
- [108] Husin, R.; Badrudin, F. W.; Taib, M. F. M.; Yahya, M. Z. A. Effects of strain on electronic and optical properties of LiNbO₃: a first principles study. *Materials Research Express* **2019**, *6*, 114002.
- [109] Mamoun, S.; Merad, A.; Guilbert, L. Energy band gap and optical properties of lithium niobate from ab initio calculations. *Computational Materials Science* **2013**, *79*, 125–131.

Abbreviations & Symbols

XYZ Crystal physics coordinate system 11

$\underline{\chi}^{(2)}(-\omega_\sigma; \omega_1, \omega_2)$ Second-order susceptibility tensor ix, 17

$\underline{\epsilon}$ Linear dielectric tensor 13

$\mathcal{E}(\mathbf{r}, t)$ Temporal slowly varying envelope of an electric field 9, 37

\mathbf{k} (Wave vector) Electric field propagation vector 9

\mathbb{P} Power 9

$\mathbf{E}(\mathbf{r}, t)$ Electric field 7

$\mathbf{H}(\mathbf{r}, t)$ Magnetic field 7

\mathbf{k} Crystal momentum of the electrons within periodic structures 21

$\varepsilon_{n\mathbf{k}}$ Eigenvalue (energy) of the independent-particle Kohn-Sham Hamiltonian 24

$\tilde{F}_{j\omega_l}^e(\mathbf{r}, \omega - \omega_l)$ Spatially slowly varying Envelope of an extraordinary wave in the frequency domain 45

$\tilde{F}_{j\omega_l}^o(\mathbf{r}, \omega - \omega_l)$ Spatially slowly varying envelope of an ordinary wave in the frequency domain 45

$x_1x_2x_3$ Principal (dielectric) coordinate system 11

LiNbO₃ Lithium Niobate 2, 37

DFT Density Functional Theory 2, 7

SHG Second Harmonic Generation 1, 7, 37, 68, 107

UV Ultraviolet 1

XUV Extreme Ultraviolet 2